ASTROPHYSICAL AND COSMOLOGICAL PROBES OF NEW PHYSICS

By

MITCHELL J. WEIKERT

A dissertation submitted to the

School of Graduate Studies

Rutgers, The State University of New Jersey

In partial fulfillment of the requirements

For the degree of

Doctor of Philosophy

Graduate Program in Physics & Astronomy

Written under the direction of

Matthew R. Buckley

And approved by

New Brunswick, New Jersey

October 2025

ABSTRACT OF THE DISSERTATION

Astrophysical and Cosmological Probes of New Physics

by MITCHELL J. WEIKERT

Dissertation Director: Matthew R. Buckley

Cosmological and astrophysical phenomena give important clues about the fundamental nature of the Universe. The vast length and time scales, as well as the extremely high energies and densities of the early universe and astrophysical objects provide unique circumstances that are difficult to reproduce in laboratories. Cosmological and astrophysical observations currently provide some of the most overwhelming evidence of physics beyond the Standard Model and they will likely play a pivotal role in our quest to continue extending our understanding of nature. The first part of this thesis will focus on observations of the early universe that can be used to test cosmological models that make implications about extensions of the Standard Model. We focus on cosmological scenarios where there is significant isocurvature in the initial conditions of the universe, which can arise from a range of plausible particle physics scenarios. We show how these scenarios can be constrained due to the lack of a signal of isocurvature in cosmological data. The second part of this thesis uses radio emission from the Andromeda galaxy to search for and constrain a well-motivated theory of dark matter with weak-scale couplings to the SM. Both of these searches provided null results, setting competitive constraints on extensions of the Standard Model that are of interest to the field.

ACKNOWLEDGMENTS

I have been extremely grateful for my time at Rutgers as a part of the NHETC. I am fortunate to have had the opportunity to hone my technical skills and knowledge while exploring some of the most profound questions about the Universe. Writing this thesis has felt bitter-sweet to me at times. I have been cherishing the opportunity to recount what I have learned and discovered about the Universe during my time as a PhD student, but I am also under the realization that this is likely my last paper about cosmology for the foreseeable future. I love doing science and will miss it, but I have decided that I love my family more. Based on the timing of my graduation this spring and the arrival of our first child in September 2024, I decided to leave academia to pursue a career in industry.

In addition to my appreciation for the NHETC as a whole, I owe gratitude to several specific people who have made a significant impact on me. First, I want to thank my advisory Matthew Buckley. You have been a very supportive guide for me through showing me how to write scientific papers, how to assess ideas at rough level before getting into the weeds, and through casual conversations about interesting new ideas. You encouraged me to explore ideas that I found interesting as well and that is valuable to me. I would also like to thank David Shih. Though you weren't my advisor, I still learned a great deal from you in your classes, in journal club, and during the times that I worked with you on research projects. I appreciated your decisive approach to research and the knowledge and enthusiasm you shared with me about machine learning. I will be sure to bring that with me to industry. Also, thanks to Scott Thomas for sharing your passion and knowledge about quantum field theory and the Standard Model with me.

Thanks also to the PhD students that supported me. I want to give a special thanks to Edward Ramirez and Eric Putney for our regular meetings to study QFT. I had a lot of fun diligently keeping track of the ϵ in the path integral formalism. Beyond that, I appreciated our long discussions about our confusions and understandings about the material (confusions became more common near the end of the book). I also want to give a special thanks to Ranit Das. Thanks for teaching how to

implement neural networks and understand the many bugs that I experienced. I enjoyed getting to work with you on research in both cosmology and machine learning. Thanks as well to Ian Pang, Sam Huang, Ranit, and Eric for making my last Pheno conference one for the books. I had a lot of fun with you guys and appreciated getting to support one another through our preparation for our talks and our attempts to network. I enjoyed our intriguing conversation one of the nights about Grassmann-valued neural networks among other things.

Thanks as well to the postdocs that I overlapped with: Claudius Krause, Marat Freytsis, Sung Hak Lim, Darius Faroughy, Nico Fernandez, and Peizhi Du. I learned a great deal from you all and I appreciated how friendly you were to me. I want to especially thank Peizhi for our long discussions about technical details on our cosmology projects. I really valued working with you for your curiosity and desire to understand things carefully. I felt like we were both helping each other understand things more completely, which benefited the projects greatly and was an enriching experience for my life. Good luck as a faculty member in China.

Thanks to Ron Gilman for helping me navigate the program, answering questions I had, and securing funding for me for travel and my fellowship in my final semester. Thanks also to our administrative and IT staff for helping to ease the burden of logistical challenges.

Thanks to my collaborators on Refs. [1, 2]: Peizhi, Nico, and Matt. I enjoyed getting work with you three. In regards to those works, we thank Subhajit Ghosh, Soubhik Kumar and Chen Sun for useful discussions. Those works were supported by DOE grant DOE-SC0010008 and National Natural Science Foundation of China (Grants No. T2388102). I appreciate the guidance that Matt provided for our work in Ref. [3]. We thank Andrew Baker for helpful advice and discussion. We also thank the authors of Ref. [4] for providing the data for our analysis. This work was supported by DOE grant DOE-SC001000.

Last and most importantly, I will forever be grateful for my wife Nicole Shadowen. She has been incredibly supportive of my PhD journey since when we met in 2017. Over the years, she consistently provided a safe place for me to reflect on what I was learning about myself and the challenges of being a PhD student where I could be met with empathy and a listening ear. She

wasn’t (and still isn’t) afraid to hold me accountable when I can do better. She inspires me to be my best self in all of my endeavors. She is also extremely talented and I learn a lot from her. During my PhD, she graciously worked and earned us a living well beyond a PhD student income so that we didn’t have live a graduate student lifestyle. Most recently, she gave birth to our first child, Noa, and has been working tirelessly to protect her, nurture her, and bond with her. She is extremely generous and committed to her family. Nicole and Noa make my career pursuits even more meaningful than they would be otherwise.

To my wife Nicole, for loving and supporting me. Also, to my daughter Noa, for being such a beam of happiness in my life

TABLE OF CONTENTS

LIST OF TABLES

LIST OF FIGURES

CHAPTER 1

INTRODUCTION AND BACKGROUND

The Standard Model (SM) of Particle Physics is a comprehensive theory of fundamental particles and interactions. The theory was completed in 1973 when David Gross, Frank Wilczek, and David Politzer formulated Quantum Chromodynamics (QCD) [5, 6] as the theory of the interaction between quarks and gluons, also known as the strong interaction. Since its creation, the SM has been empirically tested to high precision, and is consistent with the results of almost all terrestrial experiments.[1] Since the theory was completed, the parameters have been refined from experimental input, but the major theory structure is the same as it was in 1973.

However, astrophysical and cosmological observations suggest a picture of the universe that presents a number of puzzles that may require physics beyond the SM to explain. In Section 1.1, we will review the many observations that contributed to our current standard cosmological theory, ΛCDM. Assuming that ΛCDM is correct, the most recent observations of the Cosmic Microwave Background (CMB) [18] and large-scale structure [19, 20, 21] provide precise measurements of the details of the theory, including the highly fine-tuned initial conditions that are required. The puzzling configuration of the Universe at early times is most commonly explained by a dynamic mechanism called inflation [22, 23]. Another puzzling feature of the universe, required to fit the CMB and large-scale structure measurements, is that about 85% of the matter is dark matter, an unknown substance that is stable, massive, cold, and does not interact significantly with SM particles. The existence of dark matter is also supported by convincing astrophysical evidence [24]. ΛCDM employs the cold dark matter model [25], which is a model of dark matter as a substance that is pressureless and non-interacting for the entire evolution of the universe.

---

[1] There are several phenomena from such experiments that point to the possibility of physics beyond the SM. One such example is neutrino oscillations from reactor [7, 8] and accelerator [9, 10, 11] experiments which demonstrate definitive evidence that the masses of at least 2 of the neutrino states are non-zero. The SM does not account for neutrino masses, but it can be relatively easily extended to accommodate them [12, 13, 14]. Also, there are unexplained anomolies in measurements of the muon magnetic moment [15, 16] and the W boson mass [17].

This thesis will have two parts, each of which addresses one of these puzzles. Part I is composed of two studies that use cosmological data to explore the possibility of new physics operating in the very early universe. We set constraints on cosmological parameters that can be applied to a variety of new physics scenarios and we study a specific version of inflation with additional physics beyond the SM. Part II presents one study that sets constraints on dark matter interactions with the SM using astrophysical data. In this introductory chapter, we will provide the necessary background information and the motivation of our work. In Section 1.1, we will review the cosmological model ΛCDM by discussing the theory and the evidence of its various features. After establishing the features of ΛCDM, we will point out puzzles that suggest the existence of physics beyond the SM. The first of these puzzles is that the initial conditions of the universe appear to be highly fine-tuned, which we will discuss in Section 1.2. In Section 1.3, we will discuss the second puzzle which is that there is overwhelming evidence for the existence of dark matter, but we do not know its particle physics nature.

1.1 Modern Cosmology

The early universe is well-described by the cosmological model ΛCDM, which is supported by many independent sources of evidence [18, 19, 20, 21, 26, 27, 28, 29]. The model is based on General Relativity in an approximately homogeneous and isotropic expanding universe with a stress-energy tensor that is made up of dark energy, dark matter and all particle species in the SM. The various features of ΛCDM were established over the course of decades from many independent observations. This led to the construction of different possible cosmological models, which could be tested by fitting them to data and determining the values of their parameters. Ultimately, ΛCDM was found to be the simplest one that successfully fit the data.

Modern cosmology was born from a series of discoveries starting in the 1920s. In 1929 Edwin Hubble showed that the distances and radial velocities of nearby galaxies exhibited a trend that could be fit by [30]

$$v_r = H_0 r, \tag{1.1}$$

where r is the distance from Earth, v_r is the radial velocity with respect to Earth, and H_0 is the proportionality constant that Hubble found which is now known as the Hubble constant. This trend would be expected if the galaxies were exhibiting isotropic random motion in a universe that is expanding at a rate H_0. In the 1930s, early galaxy surveys [31, 32] suggested that the distribution of galaxies was approximately homogeneous over scales of order $100\,\mathrm{Mpc}$. As time went on, the galaxy catalogs got larger and more rigorous statistical tests [33] revealed the same finding.

The metric of a homogeneous isotropic universe can be solved for exactly and is given by the FLRW metric [34, 35, 36, 37]

$$ds^2 = a(\tau)^2\left(-d\tau^2 + dx^i dx^j \gamma_{ij}\right), \tag{1.2}$$

where a is the scale factor of the universe which depends on conformal time τ. Another way of quantifying cosmological time is through the redshift of light emitted at a particular moment as measured today, defined as $z \equiv \frac{\lambda_0}{\lambda_{\mathrm{em}}} - 1 = a^{-1} - 1$, where λ_{em} is the wavelength when the light was emitted and λ_0 is the wavelength today. γ_{ij} depends on the spatial geometry of the universe and is defined by

$$dx^i dx^j \gamma_{ij} = \frac{dr^2}{1-kr^2} + r^2(d\theta^2 + d\phi^2 \sin^2\theta) \tag{1.3}$$

where k is the spatial curvature which can be positive (closed universe), negative (open universe), or 0 (flat universe). Physical time and distance increments are defined as

$$\begin{aligned} dt &= a d\tau \\ d\mathbf{x}^2_{\mathrm{phys}} &= a^2 dx^i dx^j \gamma_{ij}, \end{aligned} \tag{1.4}$$

such that the geometry is locally described by the Minkowski metric in canonical form. Using Einstein's equation for the FLRW metric in the presence of a set of homogeneous and isotropic fluids, one can find

$$H^2 = \frac{8\pi G}{3}\bar{\rho} - \frac{k}{a^2}, \tag{1.5}$$

where $H \equiv \dot{a}/a$ is the Hubble parameter, which is the time dependent extension of H_0 in Eq. (1.1), and $\bar{\rho} = \sum_i \bar{\rho}_i$ is the spatially averaged energy density which can be written as a sum over each fluid component indexed by i. Based on Hubble's observations, that nearby galaxies are moving away, the scale factor must be growing in size and therefore H is positive.

One of the most important pieces of evidence in cosmology is the CMB, which was first discovered in 1965 when Penzias and Wilson measured excess isotropic blackbody radiation with a temperature of $3.5 \pm 1.0\,\mathrm{K}$ [38]. Today we understand that the CMB is a nearly homogeneous and isotropic blackbody with an average temperature $T_0 \approx 2.35 \times 10^{-4}\,\mathrm{eV}$ with spatially and angularly dependent deviations that are of order $\delta T/T_0 \sim 10^{-5}$. These deviations can be seen today as anisotropies and have been measured and studied in extraordinary detail [18]. The observation of the CMB suggests that photons were in equilibrium with an almost homogeneous and isotropic distribution at early times and now they are freely propagating from their last scattering event. We will explain this in more detail in the rest of this section.

The existence of the CMB can be understood in modern cosmology by considering the influence of interactions on particle species in the expanding universe. The rate for a particle to interact with a species with number density n can be written as

$$\Gamma = n\langle\sigma v\rangle, \tag{1.6}$$

where $\langle\sigma v\rangle$ is the thermally averaged cross section for the process, which can be determined from particle physics. Due to the expansion of the universe, the various particle species lost energy and became more dilute, causing this rate to decrease with time. The cosmological influence of the interaction depends on how this rate compares to the Hubble parameter. When $\Gamma \gtrsim H$, the interaction rate is large enough to establish equilibrium. When $\Gamma \lesssim H$, the particle's mean free time is more than a Hubble time H^{-1} and the interaction stops having a cosmological influence.

The process that kept photons in equilibrium in the early universe was Compton scattering:

$$\gamma + e^- \to \gamma + e^-. \tag{1.7}$$

While this process was in equilibrium, the scattering rate for photons was

$$\Gamma_\gamma(T) = n_e(T)\langle\sigma v\rangle \approx n_e(T)\sigma_T, \tag{1.8}$$

where σ_T is the Thompson scattering cross section and $n_e(T)$ is the number density of free electrons at temperature T. This temperature was shared between photons and all particles in thermal equilibrium with them, known as the thermal bath. For $T < 0.1\,\mathrm{MeV}$, the thermal bath is composed of photons, electrons and protons. The number density of free electrons is influenced by the formation of neutral hydrogen:

$$p^+ + e^- \leftrightarrow H + \gamma. \tag{1.9}$$

As the universe expands, the temperature of the thermal bath drops as $1/a$. When the temperature is above the binding energy of hydrogen ($B_H = 13.6\,\mathrm{eV}$), an average photon has enough energy to free an electron from a hydrogen atom so almost all of the electrons in the universe are free. When the temperature drops below B_H, the energetics begin to favor the production of hydrogen. The free electron fraction $X_e \equiv n_e/n_{e,\mathrm{tot}}$ drops to 0.1 when the temperature of photons drops to $0.3\,\mathrm{eV}$ [39].[2] As the number density of free electrons drops, so does the photon scattering rate, leading to the decoupling of photons when $\Gamma_\gamma(T_\mathrm{dec}) \sim H(T_\mathrm{dec})$ which is satisfied at $T_\mathrm{dec} \approx 0.27\,\mathrm{eV}$ [39]. After the photons decouple, they propagate freely and lose energy with the expansion of the universe, remaining in a blackbody distribution with a temperature that continues to drop as $T \propto a^{-1}$. The CMB photons that we observe today all come from the spherical shell around us that our past light cone intersects at the time of decoupling called the *surface of last-scattering*.

In addition to the characteristic temperature of the CMB, there is a pattern of directionally dependent fluctuations of the temperature, shown in Figure 1.1, which are a sign of small deviations from the approximation of homogeneity and isotropy. COBE [42] made the first detection of these anisotropies and found that they had a magnitude of $\delta T/\bar{T} \sim 10^{-5}$. These observations were

---

[2] This temperature is significantly lower than the binding energy of hydrogen because there are many more photons than electrons in the universe: $n_{e,\mathrm{tot}}/n_\gamma \sim n_b/n_\gamma \equiv \eta \approx 10^{-9}$. Here n_b is the number density of baryons which is of order the total number of electrons since the universe is electrically neutral and most baryons in the universe are protons.

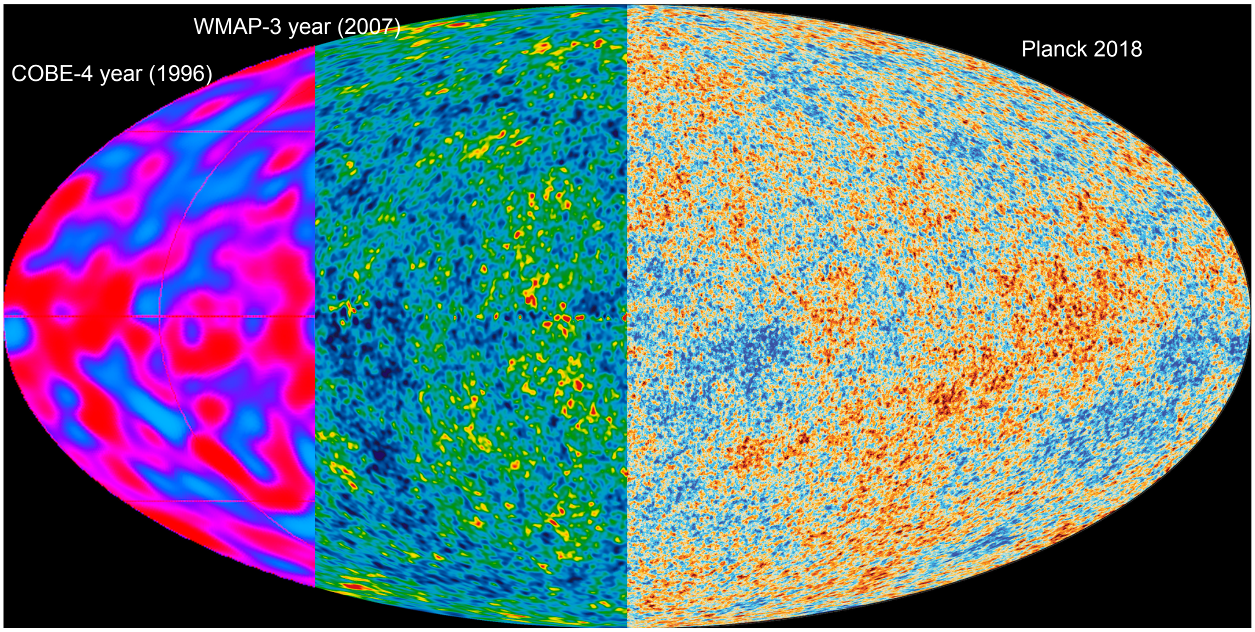

Figure 1.1: A composite image showing the CMB sky from 3 different missions including COBE [40], WMAP [41], and Planck [18] from left to right. Note, figure adapted from https://lambda.gsfc.nasa.gov/, https://wmap.gsfc.nasa.gov/, and https://www.esa.int.

consistent with initial density perturbations of order $\delta\rho/\bar{\rho} \equiv (\rho - \bar{\rho})/\bar{\rho} \sim 10^{-5}$ that were adiabatic and Gaussian with a scale-invariant power spectrum. These initial conditions were compatible with theories of structure formation [43, 44, 45], which successfully explained the observed distribution of galaxies [46]. After the observation of the accelerating expansion of the universe [28, 29], which suggested a non-zero cosmological constant, all of the ingredients for ΛCDM were established:[3] an expanding universe with baryons, cold dark matter, and a cosmological constant with Gaussian distributed adiabatic scalar perturbations and a nearly scale-invariant primordial power spectrum.

For adiabatic initial conditions, the density perturbations of each pair of particles a and b satisfy

$$\frac{\delta\rho_a}{\rho'_a} = \frac{\delta\rho_b}{\rho'_b} \tag{1.10}$$

at all locations, where $' \equiv d/d\tau$. In this case, the amplitude of the initial conditions is fully specified by the comoving curvature perturbation $\mathcal{R}$, which is a gauge invariant quantity defined

---

[3] The only feature of the universe that wasn't constrained by observations at this point was the spatial curvature of the Universe k. For simplicity, the Universe was assumed to be flat in ΛCDM, which would be tested quantitatively later on [47].

to be equal to the spatial curvature perturbation in the comoving gauge. Unless noted otherwise, we will use the synchronous gauge for the remainder of this thesis. In this gauge, the comoving curvature can be written as

$$\mathcal{R} = \eta - \mathcal{H}v \xrightarrow[k\tau \ll 1]{} \eta. \tag{1.11}$$

Here $\mathcal{H} \equiv a'/a$ is the conformal Hubble parameter and v is the velocity perturbation defined through $T^0{}_i \equiv ik_i(\bar{\rho} + \bar{P})v$ where $T^\mu{}_\nu$ is the stress energy tensor. η is the traceless component of the synchronous gauge metric perturbation:

$$h_{ij} = \frac{1}{k^2}\left[k_i k_j h + \left(k_i k_j - \frac{k^2}{3}\delta_{ij}\right) 6\eta\right], \tag{1.12}$$

which is related to the full metric (in a spatially flat background cosmology)[4] as

$$ds^2 = -dt^2 + a^2(\delta_{ij} + h_{ij})dx^i dx^j. \tag{1.13}$$

For initial conditions that are Gaussian, rotationally invariant, and translationally invariant, the statistics are fully determined from the two point function, which can be written as

$$\langle \mathcal{R}(\mathbf{k})\mathcal{R}(\mathbf{k}')\rangle \equiv 2\pi^2 \frac{(2\pi)^3\delta^3(\mathbf{k}+\mathbf{k}')}{k^3} P_{\mathcal{R}}(k), \tag{1.14}$$

where

$$P_{\mathcal{R}}(k) = A_s \left(\frac{k}{k_{\text{pivot}}}\right)^{n_s - 1} \tag{1.15}$$

is the curvature power spectrum. Here A_s and n_s are the scalar amplitude and index respectively and $k_{\text{pivot}} \equiv 0.05\,\text{Mpc}$ is the pivot wavenumber.

It is conventional to describe the abundances of substances relative to one another in terms of

---

[4] In a non-flat background cosmology, the metric must be modified such that $\delta_{ij} \to \gamma_{ij}$ and partial derivatives (in position space) become covariant derivatives. This includes in Eq. (1.12) where factors of ik_i represent a partial derivative in position space.

the time-dependent density parameters

$$\Omega_i^{\mathrm{TD}}(a) \equiv \frac{8\pi G\rho_i(a)}{3H(a)^2} \qquad i \in \{c, b, \Lambda\}. \tag{1.16}$$

For extensions of ΛCDM with $k \neq 0$, there is also a parameter

$$\Omega_k^{\mathrm{TD}}(a) \equiv -\frac{k}{a^2 H(a)^2}, \tag{1.17}$$

constructed such that

$$1 = \sum_i \Omega_i^{\mathrm{TD}}(a), \tag{1.18}$$

where the subscript i takes on the values $\{c, b, \Lambda, k\}$ which represent cold dark matter, baryons, dark energy, and spatial curvature, respectively. Eq. (1.18) can be verified using Eqs. (1.5), (1.16) & (1.17). To fully determine the density parameters as a function of scale factor, we need to specify the values of all but one of the Ω_i^{TD} parameters evaluated today. The density parameters today are defined as $\Omega_i \equiv \Omega_i^{\mathrm{TD}}(1)$ while the Hubble parameter today is $H(1) \equiv H_0 \equiv h \times 100\,\mathrm{km\,s^{-1}\,Mpc^{-1}}$. In ΛCDM, the spatial curvature parameter is fixed to $\Omega_k = 0$ by assumption, but the next generation of CMB observations after COBE would be able to measure the value of the spatial curvature, putting ΛCDM to the test.

The next CMB anisotropy survey was called WMAP [47], which produced its first results in 2003. WMAP had significantly higher resolution and sensitivity than its predecessor, and its measurement of the pattern of CMB anisotropies could be compared to detailed predictions from different possible cosmological models. The predictions depend on the initial conditions, the abundances of different substances and the physics of the early universe. The physics of the early universe is captured by the Boltzmann and Einstein equations which can be customized to include the effect of any relevant particle interactions. By modeling this physics, one can arrive at a detailed prediction for the CMB anisotropies that we observe today, which depend on the combination of parameters selected for ΛCDM. By performing Bayesian inference with Markov Chain Monte Carlo, WMAP

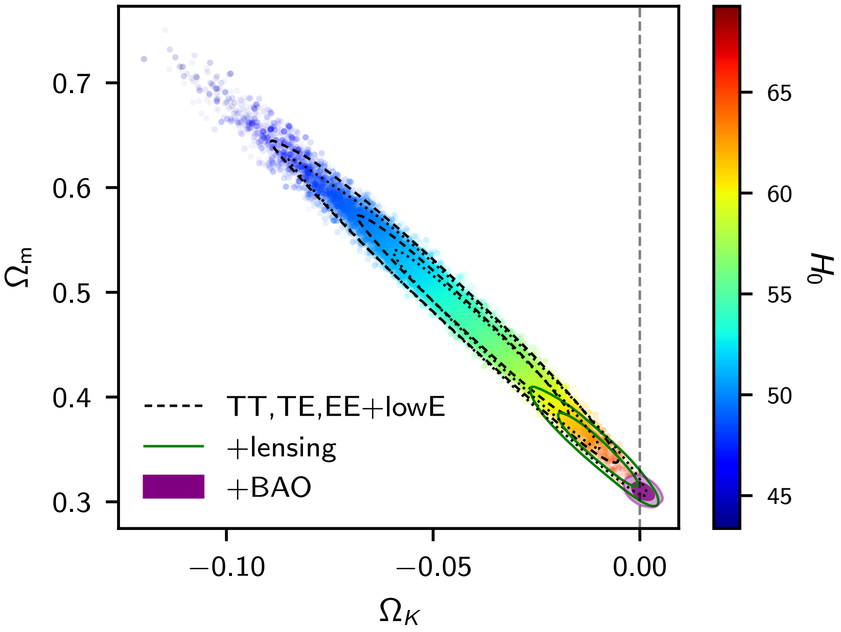

Figure 1.2: Samples and 1 and 2σ contours (black dashed) from the posterior for an extension of ΛCDM with spatial curvature from CMB data only. The green contours show the 1 and 2σ posterior with lensing data added and the filled contours show the same result with BAO data added. Note, figure reprinted from Planck 2018 [18].

[47] found that ΛCDM was the simplest model that successfully fit the data and they inferred the parameters to a precision of $5-10\%$.

The current state of the art full sky CMB anisotropy survey is Planck [18], which had yet higher resolution and could determine the values of cosmological parameters even more precisely than the previous surveys. In the analysis of this survey as well as for WMAP, the cosmological models under investigation were fit to a combination of CMB and large-scale structure data. Figure 1.2 shows that if only CMB data are used to constrain an extension of ΛCDM that allows for spatial curvature, there is a strong degeneracy between H_0, Ω_k, and $\Omega_m \equiv \Omega_b + \Omega_c$ (called the *geometric degeneracy*).

The reason for this degeneracy is that observations can precisely measure the angular size of various features in the CMB, but the angular size depends on their physical size at decoupling and the distance of the last-scattering surface. By changing the parameters within the dashed contour in Figure 1.2, the physical size and distance can change in just the right way that the observable angular sizes remain the same. An important scale in the CMB is the angular size of the sound horizon at decoupling, which is given by

$$\theta_{\rm dec} = \frac{r_s(z_{\rm dec})}{D_A(z_{\rm dec})}, \tag{1.19}$$

where $r_s(z_{\rm dec})$ is the sound horizon at decoupling and $D_A(z_{\rm dec})$ is the angular diameter distance to the surface of last scattering, which is at a redshift $z_{\rm dec}$. The sound horizon gets imprinted onto the CMB through the process of baryon acoustic oscillations (BAO) which are sound waves of all different wavelengths fluctuating in the photon-baryon plasma. The largest wavelength of a standing wave that undergoes a half integer number of cycles from the start of the radiation domination era to the time of decoupling (returning to maximum amplitude) is $2r_s(z_{\rm dec})$. Therefore, modes of this wavelength (or harmonics of it) are at maximum amplitude at the time of last scattering leading to an increase in the probability of CMB anisotropies on angular scales $\theta_{\rm dec}/j$ where $j \in \mathbb{N}$.

BAO also leaves an imprint of the sound horizon on the baryons after decoupling, leading to variations in the distribution of galaxies over a length-scale[5] $\sim r_s(z_{\rm dec})$. These fluctuations have an angular scale

$$\theta_{\rm BAO} \approx \frac{r_s(z_{\rm dec})}{D_A(z_{\rm BAO})} \tag{1.20}$$

where $z_{\rm BAO} \lesssim 1$ for the relevant galaxy surveys that measure BAO [19, 20, 21]. Figure 1.3 shows a visual representation of the distribution of galaxies from Sloan Digital Sky Survey (SDSS) [52]. By measuring $\theta_{\rm BAO}$, the value of D_A at decoupling can be calibrated with respect to its values at much lower redshifts, breaking the geometric degeneracy. Therefore, the strongest cosmological constraints come from the combined dataset of Planck [18] and BAO (from galaxy surveys) [19, 20, 21], leading to the 1σ and 2σ results shown with the purple contours in Figure 1.2. This analysis tightly constrains the curvature parameter to $\Omega_k = 0.0007 \pm 0.0037$ at 95% confidence, which is consistent with a flat universe and the assumptions of ΛCDM. We will further discuss the smallness of Ω_k in Section 1.2.

---

[5] The actual length-scale relevant for BAO is the sound horizon at the baryon drag epoch $r_s(z_{\rm drag})$ where $z_{\rm drag} \approx 1059 < z_{\rm dec}$. This is the time when baryons are released from Compton drag by photons

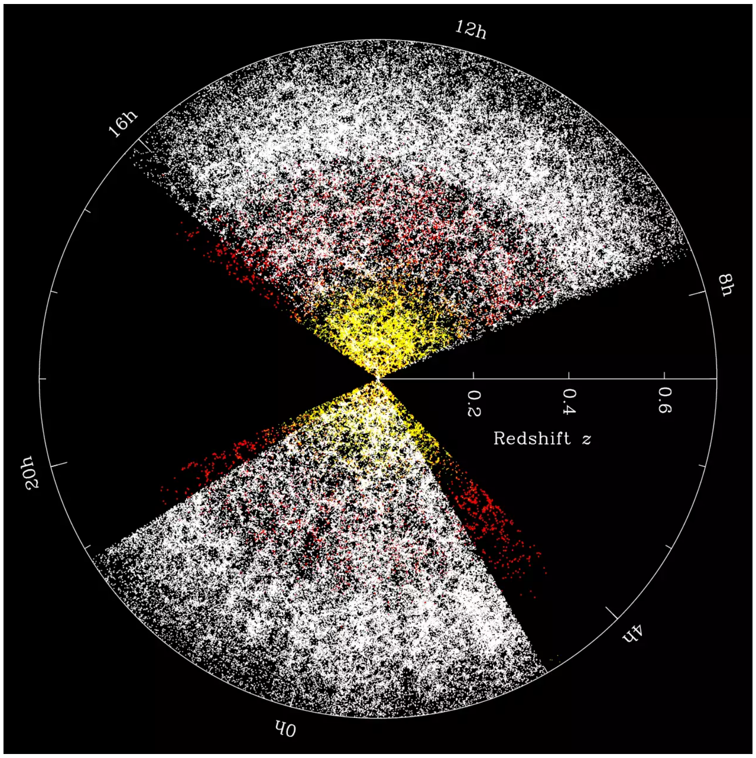

Figure 1.3: Distribution of three different samples of galaxies from SDSS including the main galaxy sample [48] (yellow), the luminous red galaxy sample [49] (red), and the BOSS CMASS sample [50] (white). The visualization method follows the approach of [51] and this figure is reprinted from www.mpa-garching.mpg.de.

Table 1.1: 68% intervals for parameters of ΛCDM from Planck CMB angular power spectra (TT, EE, TE, lowE) [18], Planck lensing [53], and BAO [19, 20, 21]. The top entries are primary parameters of the model, while the bottom ones are derived from the primary parameters. $\Omega_m \equiv \Omega_c + \Omega_b$ is the density parameter for matter and $z_{\rm dec}$ and $z_{\rm eq}$ are the redshifts of decoupling and matter-radiation equality, respectively. Note, table adapted from [18].

Parameter	Value
$\Omega_b h^2$	0.02242 ± 0.00014
$\Omega_c h^2$	0.11933 ± 0.00091
$100\theta_{\rm MC}$	1.04101 ± 0.00029
τ	0.0561 ± 0.0071
$\ln(10^{10} A_s)$	3.047 ± 0.014
n_s	0.9665 ± 0.0038
h	0.6766 ± 0.0042
Ω_Λ	0.6889 ± 0.0056
Ω_m	0.3111 ± 0.0056
$z_{\rm dec}$	1089.80 ± 0.21
$z_{\rm eq}$	3387 ± 21

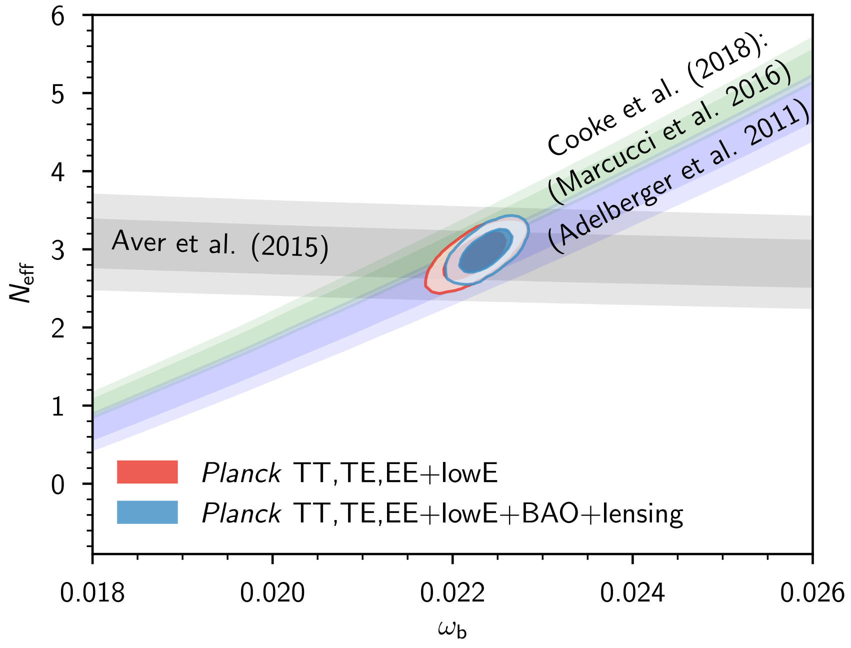

Figure 1.4: Constraints on $\omega_b \equiv \Omega_b h^2$ and the effective number of neutrino species $N_{\rm eff}$ from Planck [18] and BBN. For the Planck constraints, $N_{\rm eff}$ is included in addition to the standard ΛCDM parameters. BBN constraints are from measurements of the primordial helium [26] and deuterium [27] abundances. Note, this figure is reprinted from Ref. [18].

These constraints on the geometry of the universe provide justification for setting $\Omega_k = 0$ in ΛCDM. The results of the fit to ΛCDM from Planck [18] and BAO [19, 20, 21] data is shown in Table 1.1, with the primary parameters listed in the top section. $\theta_{\rm MC}$ is an approximation for the sound horizon at decoupling that depends on the density parameters and the Hubble constant. Since there is an additional constraint given by Eq. (1.18), the first 3 primary parameters in the table provide enough information to determine Ω_b, Ω_c, Ω_Λ, and h. A_s and n_s are defined in Eq. (1.15) and lastly, τ is the optical depth of reionization, which we will not discuss in detail. This model provides a good fit to the data, but the result suggests several puzzles that need to be investigated.

1.2 The Initial Conditions Puzzles

The observational constraints on Ω_k tell us that it is very close to zero. Combining this constraint with the known expansion history of the universe, it was even closer to zero in the past. We have observational evidence of the expansion history back to the start of Big Bang Nucleosynthesis

(BBN), which began when the temperature of the Universe was $\sim 1\,\mathrm{MeV}$. BBN is the process by which the universe produced light nuclei such as helium and deuterium. Its predictions, which depend on the expansion history of the universe back to this early time, agree with observations of the light element abundances [26, 27], as shown in Figure 1.4. If the bound on Ω_k is extrapolated back to this early moment, the 95% limit on the magnitude of the curvature becomes $|\Omega_k^{\mathrm{TD}}(a(T = 1\,\mathrm{MeV}))| \lesssim 2.4\times 10^{-30}$ and, hypothetically, it was even smaller earlier provided that the expansion history continues to be accurate. The apparent coincidence that the early universe was so nearly flat is called the *flatness problem* and may be a hint at new physics.

There is a second problem involving the fine-tuning of the conditions in the early universe. The nearly perfect blackbody spectrum and uniform temperature of the CMB suggests that before the universe cooled to T_{dec}, the electrons and photons were in equilibrium with approximately the same temperature everywhere over at least the region that we can observe in the CMB today. The radius of this region is much larger than the region of the universe that could have previously been in causal contact at decoupling as can be seen by considering the particle horizon.

The comoving particle horizon between times $t_1 < t_2$ is given by

$$\Delta\tau_{12} = \int_{t_1}^{t_2} \frac{dt}{a(t)} = \int_{\ln a_1}^{\ln a_2} d(\ln a)(aH)^{-1} \tag{1.21}$$

where $(aH)^{-1}$ is known as the comoving horizon and is the furthest comoving distance that a particle can travel in the future based on the instantaneous expansion of the universe. Here $\Delta\tau_{12} = \tau(a_2) - \tau(a_1)$ where $\tau(a)$ is the conformal time (defined differentially in Eq. (1.2)) as a function of scale factor. By convention the conformal time parameter is defined such that $\tau \to 0$ as $a \to 0$. Thus, the conformal time parameter can be defined (as a function of a) as

$$\tau(a) = \lim_{a_1\to 0} \int_{\ln a_1}^{\ln a} d(\ln a)(aH)^{-1} \tag{1.22}$$

as long as the limit exists. For a universe made up of energy density with a single equation of state

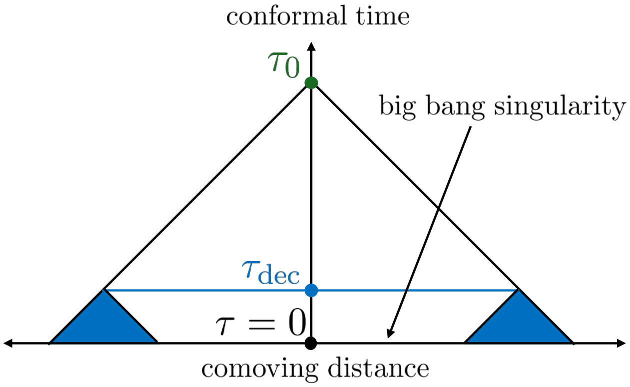

Figure 1.5: Conformal diagram including our past light-cone from extrapolating ΛCDM back to $\tau = 0$. The past light-cones of points on the surface of last-scattering are shown in blue. These are non-overlapping, suggesting that the photons we observe from different parts of the CMB sky could not have interacted with one another from $\tau = 0$ to $\tau = \tau_{\text{dec}}$.

$w \equiv P/\rho$, the comoving horizon goes as

$$(aH)^{-1} \propto a^{(1+3w)/2} \tag{1.23}$$

In this simplified scenario, the particle horizon is given by

$$\Delta\tau_{12} = \frac{2}{1+3w}\left[(a_2H_2)^{-1} - (a_1H_1)^{-1}\right] \qquad w \neq -1/3 \tag{1.24}$$

In ΛCDM, the universe starts out in radiation domination ($w = 1/3$) and transitions to matter domination ($w = 0$) before decoupling. During both of these epochs, $(aH)^{-1}$ increases with a so $\Delta\tau_{12} \approx \tau(a_2) \sim (a_2H_2)^{-1}$ if $a_2 \gg a_1$. Ignoring the effect of dark energy whose density is small for most of the expansion history, the region that we can observe in the CMB has an approximate radius[6]

$$\Delta\tau_{\text{dec},0} = \tau_0 - \tau(a_{\text{dec}}) \approx \tau_0 \sim H_0^{-1} \approx 4\,\text{Gpc}, \tag{1.25}$$

where τ_0 is the conformal time today. This region can be seen in Figure 1.5 by tracing the light-cone back to decoupling. On the other hand, the region over which photons could have traveled

---

[6] Note, this is an underestimate because the comoving horizon started to get smaller when dark energy started to dominate the energy density of the universe. Therefore in the calculation that includes dark energy, the integrand in Eq. (1.21) is near its maximum value for more time than it is under the approximation of no dark energy.

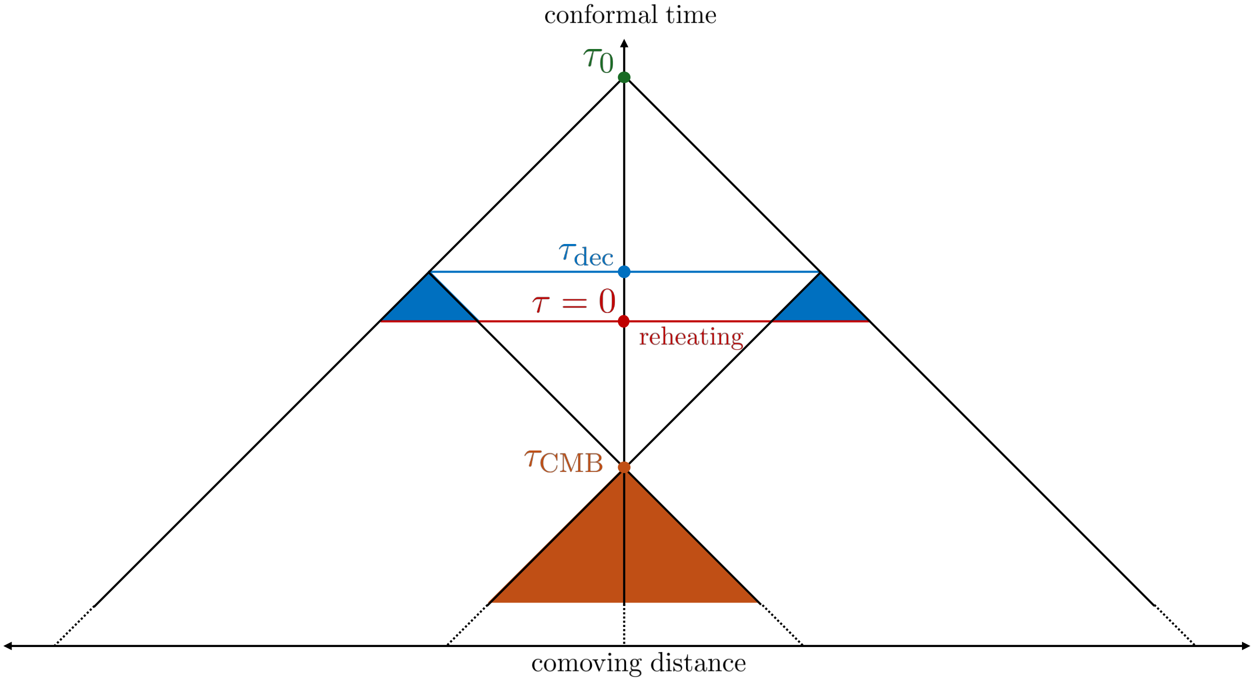

Figure 1.6: Just as in Figure 1.5 but with a hypothetical period before $\tau = 0$, where the comoving horizon is decreasing. If this period lasts long enough, the entire CMB could have been in causal contact at sufficiently early times as is the case for the orange region. $\tau_{\rm CMB}$ is the conformal time of the hypothetical moment that the entire CMB was inside the horizon during inflation.

from the start of radiation domination to decoupling has a comoving length

$$\tau_{\rm dec} \sim (a_{\rm dec} H_{\rm dec})^{-1} \approx 400\,{\rm Mpc}. \tag{1.26}$$

This distance is depicted with the blue light-cones in Figure 1.5. Since the past light-cones from different points of the CMB (the blue regions) are not overlapping ($\tau_{\rm dec} \ll \tau_0$), photons from those different points on the surface of last-scattering could not have interacted with one another from the start of the radiation era to decoupling. Regardless, the entire CMB has nearly the same temperature. This apparent coincidence of the conditions of the early universe is called the *horizon problem* and may also be a hint at new physics.

To solve the flatness and horizon problems, we need a dynamic mechanism that causes generic initial conditions to be converted into the flat and uniform configuration that was present early on. From Eqs. (1.16), (1.17), (1.23) & (1.24), we can see that this can be accomplished if there is a period of time before radiation domination with $w < -1/3$. During this time, the comoving horizon decreases so $\Delta\tau_{12} \sim (a_1 H_1)^{-1}$ if $a_1 \ll a_2$. If a_2 is the scale factor at the start of radiation domination, then $\tau(a_2) \approx 0$ so $\Delta\tau_{12} \approx -\tau(a_1)$. Thus during a hypothetical period with $w < -1/3$ that precedes radiation domination, conformal time is defined as[7]

$$\tau(a) = -\lim_{a_2 \to \infty} \int_{\ln a}^{\ln a_2} d(\ln a)(aH)^{-1}. \tag{1.27}$$

Therefore, conformal time can start out negative and large in magnitude, allowing for additional time for points on the surface of last-scattering to be in causal contact with one another early on (see Figure 1.6).

A satisfactory solution would require that the process starts when $-\tau = -\tau_i \sim (a_i H_i)^{-1}$ is large enough that $|\Omega_k(a_i)|$ was $\mathcal{O}(1)$ and the entire CMB was in causal contact. The condition to alleviate the flatness problem is

$$\Omega_k(a_i) = \Omega_k \left(\frac{H_0}{a_i H(a_i)} \right)^2 \sim \mathcal{O}(1). \tag{1.28}$$

A solution to the horizon problem would require that the comoving horizon at a_i be at least as large as it is today, so that correlations over length-scales the size of the observable universe or larger could have been established. If these conditions were met, then natural initial conditions at a_i would lead to the homogeneous distribution of energy that was present at decoupling if

$$(a_i H_i)^{-1} \gg H_0^{-1}. \tag{1.29}$$

A popular realization of this solution is the mechanism of inflation [22, 23], which in its sim-

---

[7] It should be understood that Eq. (1.27) is a formal definition and when taking the limit, the expansion history before radiation domination should artificially continue infinitely into the future. In practice, this formal definition is a good approximation for $\tau \leq \tau_{\text{end}} < 0$ where τ_{end} is the end of the $w < -1/3$ epoch. Similarly, the formal definition in Eq. (1.22) is a good approximation for $\tau > \tau_{\text{start}}$ where τ_{start} is the start of the radiation domination epoch. For $\tau_{\text{end}} < \tau < \tau_{\text{start}}$, the evolution is non-trivial and is not described well by either definition. Fortunately, this time interval is typically very small and often can be taken to be zero.

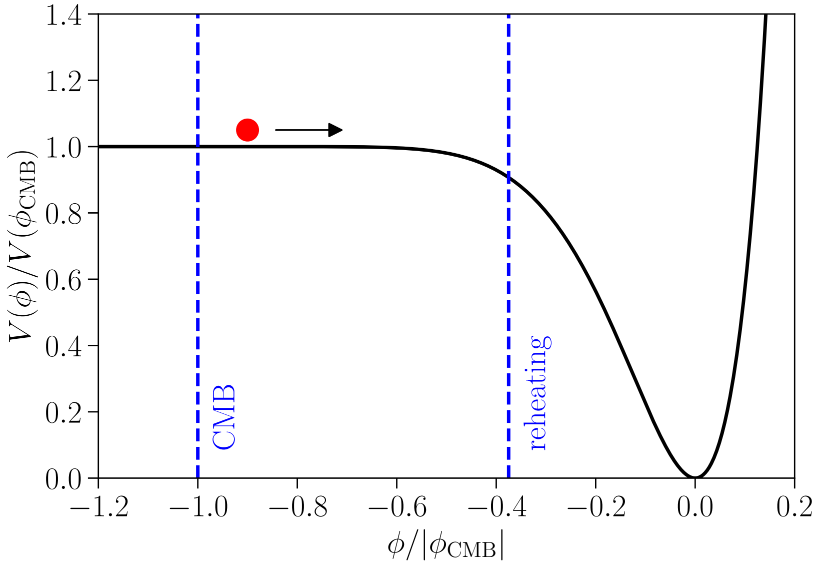

Figure 1.7: Example of an inflationary potential for slow-roll inflation with the inflaton field visualized as a ball rolling on the potential. In this example, $\dot{\phi}$ is positive and at a time $t_{\rm CMB}$ (when the conformal time is $\tau_{\rm CMB}$), the field reaches $\phi_{\rm CMB} \equiv \phi(t_{\rm CMB})$ and the horizon is the same as it was at decoupling. When the field reaches the second dashed line, inflation ends and the remaining energy density in the inflaton is converted into radiation through reheating.

plest form involves a new scalar field ϕ called the inflaton which dominated the energy density of the universe before the radiation domination era. Under the approximation of homogeneity and isotropy the equation of motion for a scalar is given by

$$\ddot{\phi} + 3H\dot{\phi} + V_\phi = 0, \tag{1.30}$$

where $V(\phi)$ is the potential experienced by the scalar field and $V_\phi \equiv \partial_\phi V$. The energy density and pressure can be written as

$$\begin{aligned} \rho &= \frac{1}{2}\dot{\phi}^2 + V(\phi) \\ p &= \frac{1}{2}\dot{\phi}^2 - V(\phi) \end{aligned} \tag{1.31}$$

and the equation of state is given by

$$w = \frac{1 - 2V/\dot{\phi}^2}{1 + 2V/\dot{\phi}^2}, \tag{1.32}$$

which satisfies $w < -1/3$ if $V > \dot{\phi}^2$. A plausible example of $V(\phi)$ is sketched in Figure 1.7.

During inflation, the comoving horizon needs to decrease from $> H_0^{-1} \approx 4\,\mathrm{Gpc}$ to $< (aH)^{-1}|_{T=1\,\mathrm{MeV}} \approx 2 \times 10^{-4}\,\mathrm{Mpc}$, which can only happen if inflation lasts for much longer than a Hubble time H^{-1}. This is only possible if the solution to Eq. (1.30) is overdamped which occurs if

$$\frac{\dot{\phi}^2}{V}\left|\frac{V_\phi}{H\dot{\phi}}\right| \ll 1. \tag{1.33}$$

If this condition is met then $\ddot{\phi}$ is small compared the the other two terms in Eq. (1.30) so $3H\dot{\phi} \approx -V_\phi$. Substituting this into Eq. (1.33) tells us $\dot{\phi}^2/V \ll 1$ which implies that $w \approx -1$ and the inflaton behaves as vacuum energy. This can also be written as the condition on the slope of the potential given by

$$M_{\mathrm{pl}}^2 \left(\frac{V_\phi}{V}\right)^2 \ll 1, \tag{1.34}$$

which says that the potential must be very flat. Provided that these conditions are met, the comoving horizon at the start of inflation can be large enough to satisfy Eqs. (1.28) & (1.29). In this case, the Universe can go from $\Omega_k^{\mathrm{TD}}(a_i) \sim \mathcal{O}(1)$ at the start of inflation to being flat enough to be consistent with observations at the end of inflation. Also, the inflaton field can be highly homogeneous over the region of the universe that we can observe today. The flatness and homogeneity at the end of inflation can then be imprinted on the particle species at the start of the radiation era.

Inflation ends when $\dot{\phi}^2 \sim V$, at which point the inflaton oscillates in the bottom of its potential producing particle excitations of the field. These inflaton particles then decay into a variety of particle species that can populate the SM and dark matter. Assuming that the inflaton is approximately homogeneous with small perturbations, it is convenient to write it as $\phi(\tau, \mathbf{x}) = \bar{\phi}(\tau) + \delta\phi(\tau, \mathbf{x})$, where we have switched to using τ as the time parameter. The process of inflation only depends on the local value of ϕ. In an arbitrary gauge, the value of ϕ varies over space so inflation will end at different times at each location in space. If we do the gauge transformation

$$\tau \to \hat{\tau}(\tau, \mathbf{x}) = \tau + \frac{\delta\phi(\tau, \mathbf{x})}{\bar{\phi}'}, \tag{1.35}$$

then $\phi(\tau, \mathbf{x}) = \phi(\hat{\tau}(\tau, \mathbf{x}))$ which is uniform if we use $\hat{\tau}$ as our time parameter. In this gauge, the energy density of one of the inflaton's decay products, species a, is also uniform

$$\rho_a(\hat{\tau}, \mathbf{x}) = \bar{\rho}_a(\hat{\tau}). \tag{1.36}$$

Switching back to the original gauge gives us

$$\rho_a(\hat{\tau}) = \rho_a(\tau) + \rho_a'(\tau)\frac{\delta\phi(\tau, \mathbf{x})}{\bar{\phi}'} \tag{1.37}$$

so

$$\frac{\delta\rho_a(\tau, \mathbf{x})}{\bar{\rho}_a'} = \frac{\delta\phi(\tau, \mathbf{x})}{\bar{\phi}'}. \tag{1.38}$$

Therefore, a small value of $\delta\phi$ leads to a small value of $\delta\rho_a$ implying that the energy density of species a is nearly homogeneous. Since the right-hand-side of Eq. (1.38) is independent of a, we find that all pairs of particle species a and b, produced from the decay of the inflaton, satisfy the adiabatic condition given in Eq. (1.10). Therefore, inflation predicts adiabatic initial conditions for all particle species that are produced by the decay of the inflaton.

Inflation also gives a prediction for the statistics of the inhomogeneous part of the initial conditions which can be seen by studying the evolution of $\delta\phi$. Here, we review this result following the approach of Ref. [39]. The classical equation of motion for $\delta\phi$ in the spatially flat gauge in Fourier space is given by

$$u_k'' + \left(k^2 - \frac{a''}{a}\right) u_k = 0, \tag{1.39}$$

where $u_k \equiv a\delta\phi(\tau, k)$. Therefore, each mode of u_k behaves as a harmonic oscillator with a time dependent frequency $\omega_k(\tau) = (k^2 - a''/a)^{1/2} \approx k\left[1 - 2/(k\tau)^2\right]^{1/2}$. When all modes of interest are significantly smaller than the horizon, the system is made up of a set of approximately time-independent harmonic oscillators with $\omega_k^2 \approx k^2$. The oscillators start in their asymptotic quantum vacuum state at early times and the field $\hat{u}_k$ evolves according to the quantum version of Eq. (1.39). Due to quantum uncertainty, each mode of $\hat{u}_k$ has non-zero variance and as the universe expands, the quantum state decoheres into a statistical ensemble. The variance of the field value in position space can be written as

$$\langle 0|\hat{u}(\tau, \mathbf{x})^2|0\rangle = \int d\ln k P_u(k, \tau), \tag{1.40}$$

where

$$P_u(k, \tau) = \left(\frac{aH}{2\pi}\right)^2 \left(1 + \left(\frac{k}{aH}\right)^2\right) \tag{1.41}$$

is the power spectrum for u.

After a mode exits the horizon, it remains outside of the horizon until after the end of inflation. For modes that are significantly outside of the horizon ($k \ll aH$), the comoving curvature perturbation is approximately conserved. Therefore it can be used to relate perturbations in the inflaton to the perturbations of the particle species after reheating. In the spatially flat gauge, the inflaton perturbation is related to the comoving curvature perturbation by

$$\mathcal{R} \approx -\frac{H}{\dot{\bar{\phi}}}\delta\phi. \tag{1.42}$$

Based on this relation, the power spectrum of $\mathcal{R}$ is given by

$$P_{\mathcal{R}}(k, \tau) = \left(\frac{H^2}{2\pi\dot{\bar{\phi}}}\right)^2 \left(1 + \left(\frac{k}{aH}\right)^2\right), \tag{1.43}$$

and for $k|\tau| \approx k/(aH) \ll 1$, the curvature power spectrum approaches

$$P_{\mathcal{R}}(k) = \left(\frac{H^2}{2\pi\dot{\bar{\phi}}}\right)^2 \Bigg|_{aH=k}. \tag{1.44}$$

Since H and $\dot{\phi}$ are slowly changing, the scale-dependence of the power spectrum can be approximated by evaluating the right-hand-side at the time that the mode crosses the horizon during inflation. Thus, the power spectrum predicted by inflation is nearly scale invariant, as suggested by the fit of n_s in Table 1.1, with the slight scale-dependence telling us about the time dependence of H and $\dot{\phi}$.

Thus, inflation provides a solution to the flatness and horizon problems and it also predicts that the primordial perturbations should be adiabatic with a nearly scale-invariant power spectrum. During inflation, gravitational degrees of freedom also undergo quantum fluctuations, leading to the production of gravitational waves in the frequency range $10^{-18} - 10^{-16}\,\mathrm{Hz}$. These gravitational waves have not been detected and searches for them [54, 55] have led to an upper bound on the tensor-to-scalar ratio at $k = 0.002\,\mathrm{Mpc}^{-1}$ given by $r_{0.002} < 0.0056$. This implies an upper bound on the energy-scale of the inflationary potential

$$V^{1/4} < 1.6 \times 10^{16}\,\mathrm{GeV}. \tag{1.45}$$

Future gravitational wave searches, such as CMB-S4 [56], will have even more sensitivity, probing down to $r \approx 0.003$.

Other signals of inflation may be detectable if there are additional dynamics during inflation. A broad class of models with exotic dynamics during inflation lead to the production of primordial isocurvature in addition to the adiabatic mode. Isocurvature is defined as any deviation from the adiabatic condition in Eq. (1.10). In Part I, we study these scenarios, setting generic cosmological constraints on isocurvature using the CMB and large-scale structure. We also investigate a specific scenario where a subdominant field during inflation undergoes a cosmological first order phase transition, producing isocurvature.

1.3 The Dark Matter Puzzle

Dark matter was first proposed in 1933 by Fritz Zwicky, who inferred the mass of the Coma cluster using the virial theorem and found that the visible matter could not account for all of its mass [57, 58]. However, his ideas were dismissed for decades because the evidence wasn't very strong and other explanations involving baryonic sources of non-luminous matter seemed plausible. The idea of dark matter became more compelling in the 1970s when Vera Rubin discovered that the rotation curves of spiral galaxies remained flat beyond the extent of the baryonic matter [59, 60]. These flat rotation curves were suggested the presence of large halos of non-baryonic dark matter [61] that hosted the spiral galaxies. Using the mass to light ratio of previously observed spiral galaxies and the luminosity function of previously observed galaxies, Ref. [62] inferred the matter abundance in the Universe to be $\Omega_m \approx 0.2$.

The cosmological role of dark matter began to be appreciated when Ref. [43] suggested a two-stage model of structure formation that could simultaneously account for the approximately scale-free structure on large scales and the dissipative dynamics needed to form galaxies. This model required that approximately 80% of the total matter in the universe was collisionless and dissipationless dark matter. The dark matter formed halos that baryonic matter could collapse into, forming galaxies. For this to produce the structure we see today, the initial density perturbations of dark matter had to be of order $\delta\rho_c/\rho_c \sim 10^{-5}$ [44, 45]. Structure formation also required dark matter to be non-relativistic when galaxy-sized halos entered the horizon [25, 63, 64], which could be achieved most straightforwardly by hypothesizing that dark matter particles have negligible velocities for the entire evolution of the universe. This was called the cold dark matter hypothesis.

The first measurement of CMB anisotropies by COBE [42] detected that the temperature perturbations were of order $\delta T/T \sim 10^{-5}$. This implied that $\delta\rho/\rho$ was of the same order initially, supporting models of structure formation that required cold, non-interacting dark matter for structure formation. Using the initial amplitude of perturbations inferred from COBE, N-body cosmological simulations that only included cold dark matter led to robust predictions [66, 67] for the dark

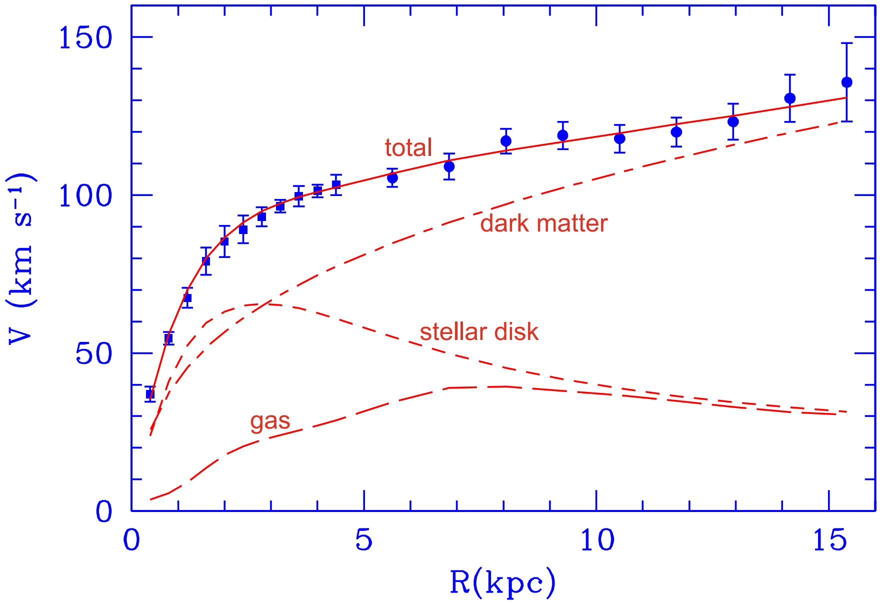

Figure 1.8: Observed circular velocities (blue) from M33 vs. distance from the center R compared to the best fit 3-component model, adapted from Ref. [65].

matter density profile of galaxies. The dark matter profile inferred from measured rotation curves of galaxies [68, 69, 65] (see Figure 1.8) agreed with these simulations on large scales. Also, the distribution of galaxies in the Universe observed by the 2dF Galaxy Redshift Survey [70] was in agreement with mock observations from CDM simulations [71], suggesting $\Omega_m h = 0.20 \pm 0.03$ and $\Omega_b/\Omega_m = 0.15 \pm 0.07$.

Perhaps the strongest model-independent evidence for the existence of collisionless dark matter is observations of the Bullet Cluster [24], which is shown in Figure 1.9. The Bullet Cluster consists of two galaxy clusters that recently collided. The gas of each cluster interacted during the collision leading to the production of X-rays that can be observed from where the clusters collided. Most of the matter of each cluster did not interact significantly, however, as can be seen through weak gravitational lensing. Since the stars and gas only make up a small fraction of the total matter, the rest must be a substance that is invisible and does not interact with itself significantly. This is direct evidence that most of the matter in these two clusters is effectively collisionless dark matter.

Certain features of the CMB anisotropies themselves depend on the dark matter abundance. WMAP [47] was the first CMB survey with the resolution necessary to detect these features. Com-

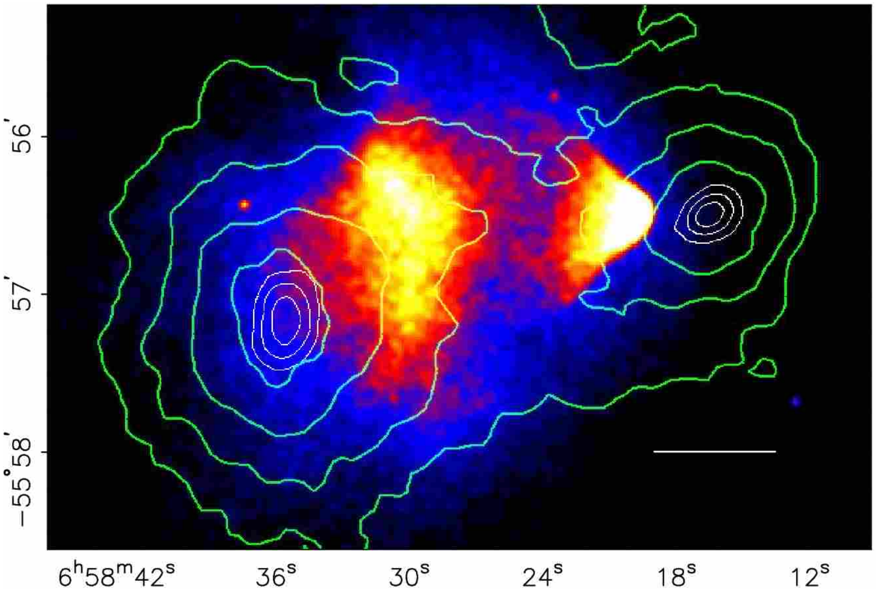

Figure 1.9: Image of the Bullet Cluster in X-rays [72] from Chandra [73] overlaid with a contour plot of the projected surface mass density from weak gravitational lensing analysis [24]. Note, figure reprinted from Ref. [24].

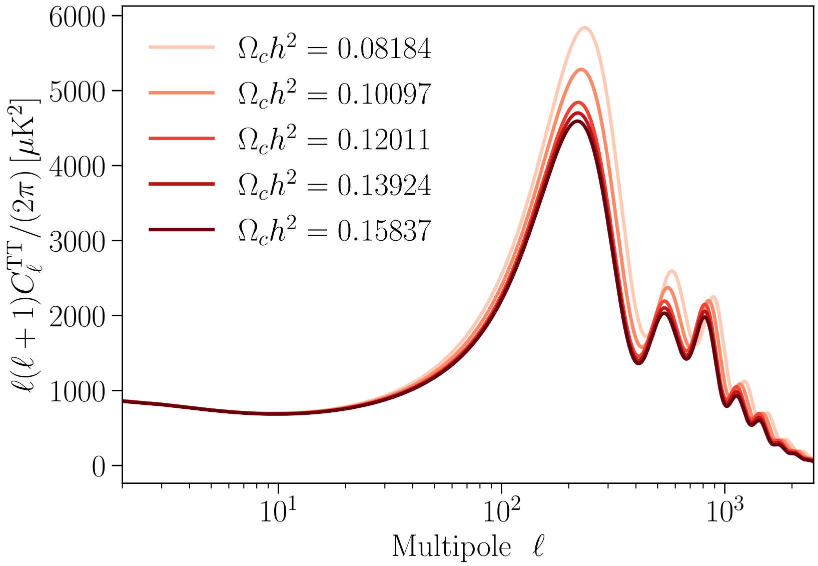

Figure 1.10: The predicted temperature anisotropy angular power spectrum for different values of $\Omega_c h^2$ produced from CLASS [74]. The run with the middle value of $\Omega_c h^2$ uses the best-fit values of all parameters from Planck 2018 [18]. For the other runs, everything is held fixed except for h and $\Omega_c h^2$ which are varied together such that the redshifts of matter-radiation equality and matter-dark energy equality remain fixed.

bining their CMB observations [47] with the 2dFGRS large-scale structure dataset [70], they derived precise constraints on the parameters of ΛCDM and found $\Omega_c \neq 0$. The sensitivity of the predicted angular power spectrum on $\Omega_c h^2$ is shown in Figure 1.10. The state of the art in CMB observations and cosmological parameter estimation is Planck [18]. The value of $\Omega_c h^2$ from their fit to CMB [18] and BAO [19, 20, 21], shown in Table 1.1, can be used to derive constraints on Ω_c. This provides the most precise measurement of the dark matter abundance available.

Based on all of the above evidence, no particle within the SM has the necessary properties to make up all of the dark matter, so there must be new physics beyond the SM to explain the nature of dark matter. To learn about the particle physics properties of dark matter, we look for evidence of subtle dark matter-SM interactions. We have not observed evidence of such interactions, implying that dark matter does not interact significantly with the SM. There are three general types of interaction processes that we search for. One type of process is dark matter-SM scattering, which is the target of direct detection experiments [75, 76, 77, 78]. Another is dark matter production from collisions of SM particles which is a potential signal in collider experiments [79, 80, 81, 82]. Lastly, there is the phenomenon of dark matter annihilation into SM particles in the universe today, which is the aim of indirect detection studies and the focus of Part II.

Interactions that allow dark matter to annihilate into SM particles are a generic feature of well-motivated models [84, 85] of thermally-produced dark matter. In these scenarios, a number-changing interaction between dark matter and the SM allows dark matter to be produced in the early universe. In Figure 1.11, we show the dark matter abundance as a function of time for a 2-2 annihilation process between the SM and dark matter for a variety of values of the interaction strength. These scenarios can be further classified into two main production mechanisms.

The first is freeze-out [86, 87, 88, 89], where dark matter starts in chemical equilibrium with SM particles, and eventually decouples when the annihilation rate drops below the Hubble rate (as discussed in Section 1.1). After dark matter decouples, the number of dark matter particles in the universe approaches a constant which depends on the time when it decouples. The time when it decouples depends on the thermally averaged annihilation cross section $\langle \sigma v \rangle$ and depends mildly

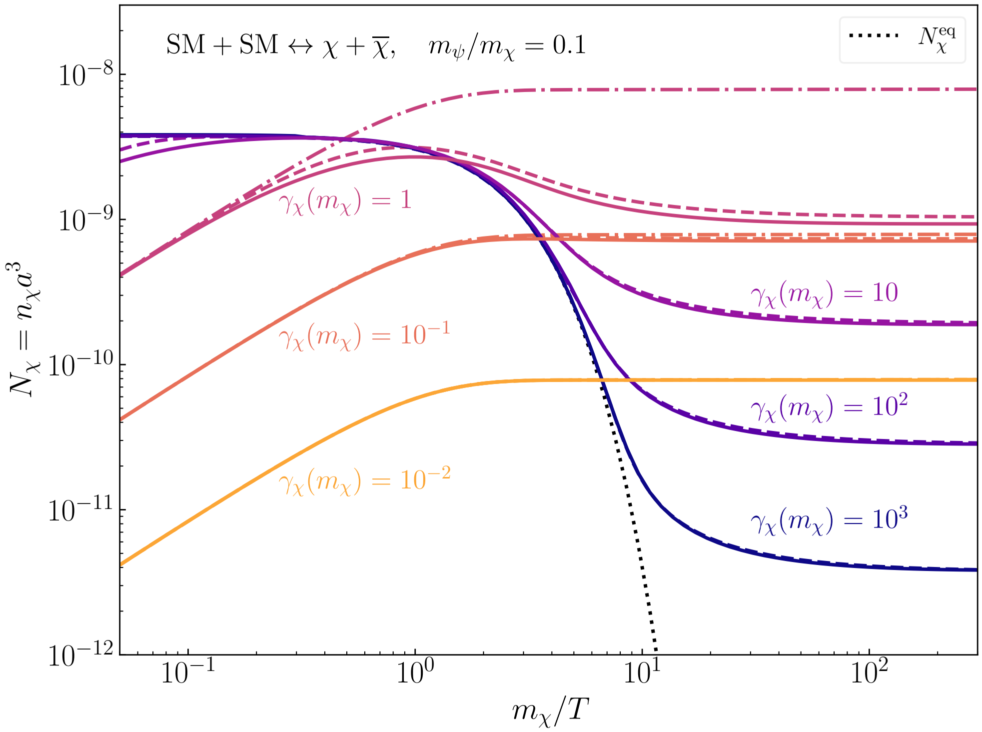

Figure 1.11: Evolution of dark matter abundance for a variety of values of the interaction strength, parameterized by $\gamma_\chi(m_\chi)$, where $\gamma_\chi(T) \equiv \Gamma(T)/H(T)$ and $\Gamma(T)$ is defined in Eq. (1.6). The curves with $\gamma_\chi(m_\chi) \geq 10$ show the freeze-out scenario while the curves with $\gamma_\chi(m_\chi) \leq 1$ show the freeze-in scenario. The solid curves are the exact result and the dashed and dash-dotted make various approximations, that will not be of interest in this work. Lastly, the black dotted curve is the abundance of dark matter in the equilibrium distribution. Note, this figure is reprinted from Ref. [83].

on the dark matter mass m_χ. This process produces the observed amount of dark matter in the universe if $\langle\sigma v\rangle \sim 3 \times 10^{-26}\,\mathrm{cm}^2/\mathrm{s}$ for dark matter in the mass range $m_\chi \sim 1 - 10^3\,\mathrm{GeV}$ [90]. In this scenario, larger cross sections lead to production of a sub fraction of the total dark matter. The second scenario is freeze-in [91, 92, 93], where dark matter is produced out of equilibrium through SM annihlations. For freeze-in, the dark matter annihilation cross-section that is needed to produce the full amount of dark matter is smaller than in the freeze-out scenario. In any situation, the strength of indirect detection signals is proportional to $\langle\sigma v\rangle$, so the thermal production mechanisms suggest a variety of targets for indirect detection studies to aim for, the most achievable one being $\langle\sigma v\rangle \sim 3 \times 10^{-26}\,\mathrm{cm}^2/\mathrm{s}$.

This thesis is organized as follows. Part I consists of two chapters that explore the effect of isocurvature initial conditions on cosmological data. In Chapter 2 we calculate generic constraints on isocurvature from CMB and large-scale structure data for a variety of types of modes, based on Ref. [2]. Next, in Chapter 3, we constrain a class of models of inflationary cosmological phase transitions that produce dark radiation isocurvature and we present an extension of the SM that would lead to this phenomenology. This work is based on Ref. [1]. Part II consists of one chapter (Chapter 4), where we probe dark matter annihilation into $b\bar{b}$ using radio observations of Andromeda (M31). This chapter is based on Ref. [3]. Lastly, in Chapter 5 we conclude.

Part I

Cosmological Constraints on Isocurvature

CHAPTER 2

GENERAL CONSTRAINTS ON ISOCURVATURE FROM THE CMB AND LY-α FOREST

Current cosmological data are well-described by the Lambda-Cold Dark Matter (ΛCDM) model, which assumes adiabatic initial conditions for the primordial density perturbations. This agreement between data and theory enables strong constraints on new physics that generates isocurvature perturbations. Existing constraints typically assume a simple power law form for the isocurvature power spectrum. However, many new physics scenarios – such as cosmological phase transitions and gravitational particle production – can deviate from this assumption.

This chapter is based on Ref. [2], where we derive general constraints which apply to a wide variety of new physics scenarios. To accomplish this, we consider four types of isocurvature modes (dark matter, baryon, dark radiation and neutrino density isocurvature) and parametrize the isocurvature power spectrum using two general forms: a delta function and a broken power law. Using data from the cosmic microwave background (CMB), baryon acoustic oscillations, the Lyman-α forest, and CMB spectral distortions, we place constraints on the isocurvature power spectrum across a wide range of scales, from $10^{-4}\,\mathrm{Mpc}^{-1}$ to $10^{4}\,\mathrm{Mpc}^{-1}$.

2.1 Introduction

At present, cosmological data from a wide variety of sources, from the Cosmic Microwave Background (CMB) to large-scale structure and galaxy formation, can be well-described by the standard Lambda-Cold Dark Matter (ΛCDM) model. Within this model, the initial conditions for the primordial density fluctuations are adiabatic [18]. However, some extensions of this model add new physics in the early Universe with isocurvature initial conditions. Such models typically have some component of the initial perturbations which are not sourced by the inflaton.

Current constraints on isocurvature [54] typically assume its power spectrum follows a simple power law as a function of perturbation wavenumber, as is naturally expected in axion or curvaton models (for reviews, see e.g., [94, 95]). However, numerous well-motivated new physics scenarios – such as cosmological phase transitions [96, 97, 1] and gravitational particle production during inflation [98, 99, 100, 101, 102, 103, 104, 105] – predict isocurvature power spectra that deviate from this assumption. Limits derived under the assumption of a power law cannot straightforwardly be applied to models with different power spectra.

In this work, we develop general limits on isocurvature initial conditions by using two complementary parameterizations of the isocurvature power spectrum. Such limits can be straightforwardly applied to a wide variety of new physics scenarios, removing the need for time-consuming and challenging analyses for each new modification to ΛCDM.

For the first parameterization of the power spectrum we use a delta-function in wavenumber. Although no models produce an exact delta function, this choice captures the primary characteristics of a peaked spectrum. Additionally, the delta-function power spectrum allows us to decompose the experimental limits on an arbitrary isocurvature power spectrum as a function of wavenumber. Up to $\mathcal{O}(1)$ factors, the limits on the delta-function power spectrum can be applied to an arbitrary extended power spectrum for each wavenumber.[1] A similar approach has been used for constraints on the curvature power spectrum and the density of primordial black holes (see, for example, [106, 107]).

To complement the delta-function approach, we also set limits on a broken power law spectrum behaving as $\propto k^3$ for small k and $\propto k^0$ for large k. This form of power spectrum is generic to many isocurvature production mechanisms operating during inflation, with the break in the power law corresponding to the horizon at the start of isocurvature production. For example, this spectrum can arise from inflationary non-thermal cosmological phase transitions (see e.g., Ref. [1, 108]).

At large scales ($k \lesssim 0.1\,\mathrm{Mpc}^{-1}$), constraints for both power spectrum models are driven primarily by measurements of the CMB angular power spectrum and Baryon Acoustic Oscillations (BAO). Future observations of large-scale structure [109] and 21-cm measurements [110, 111]

---

[1] We note that the extrapolation of limits from a delta function to an extended power spectrum is unreliable if the power spectrum amplitude is degenerate with other parameters in the cosmological fit.

are anticipated to serve as powerful tools for probing dark matter isocurvature. On galaxy scales, the matter power spectrum can be probed using Ly-α forest data, leading to strong constraints on isocurvature for $k \sim 1\,\mathrm{Mpc}^{-1}$.

To set limits in these regimes, we simulate the CMB and matter power spectrum using `CLASS` code [112], modified to incorporate our choices for the isocurvature power spectra. To derive constraints from large scale structure and the CMB multipoles, we perform Markov Chain Monte Carlo (MCMC) analyses with data from the CMB, BAO, and Lyman-α (Ly-α) forest across a range of scales from $\sim 10^{-4}$ to ~ 1 Mpc^{-1}. We employ a compressed likelihood [113, 114, 115, 116] for the Ly-α data, which provides the most stringent constraint at this scale. Notably, the compressed likelihood encodes information from both the amplitude and slope of the matter power spectrum, making our constraint stronger than previous analyses that only considered the amplitude. However, these constraints can only be applied to the broken power law spectrum, as the assumption of a constant slope in the compressed likelihood is not realized in the delta function spectrum.

At even smaller scales, isocurvature perturbations induce spectral distortions in the CMB photon distribution, which appear as deviations away from a perfect blackbody spectrum. The non-observation of such distortions place further constraints on isocurvature. We calculate the isocurvature-induced amplitude of the y- and μ-type spectral distortions, and use current bounds by COBE/FIRAS [117] to set limits for isocurvature power spectra with wavenumbers in the range $1\,\mathrm{Mpc}^{-1} \lesssim k \lesssim 10^4\,\mathrm{Mpc}^{-1}$.

By combining these analyses, we map out constraints on both the delta function and broken power law parametrization of the isocurvature power spectrum as a function of wavenumber, from $10^{-4}\,\mathrm{Mpc}^{-1}$ to $10^4\,\mathrm{Mpc}^{-1}$. In Section 2.2, we describe the types of isocurvature modes considered and the two generic power spectrum parameterizations. In Section 2.3, we present constraints from the CMB angular power spectrum and BAO data. Constraints from the Ly-α forest are discussed in Section 2.4, and CMB spectral distortions in Section 2.5. We conclude in Section 2.6.

2.2 General Parameterizations of Isocurvature Power Spectrum

The effects of isocurvature on cosmological observables depend on the isocurvature power spectrum and the type of isocurvature mode present. Both of these quantities depend on detailed assumptions made within a specific cosmological model containing physics beyond ΛCDM. The goal of this study is to set constraints on isocurvature that can be applied to a variety of models.

The power spectrum quantifies the statistics of the initial conditions of the isocurvature mode and itself depends on the isocurvature production mechanism. To obtain model-independent limits, we parameterize the isocurvature power spectrum in two generic ways.

The first parameterization is a delta-function in wavenumber:

$$P_{\text{iso}}(k) = A_{\text{iso}}\delta(\ln k - \ln k_0). \tag{2.1}$$

This power spectrum allows us to isolate the effect of isocurvature on relevant observables at each wavenumber. Second, we study a realistic (but still generic) parameterization of the power spectrum given by a broken power law:

$$P_{\text{iso}}(k) = A_{\text{iso}} \begin{cases} (k/k_0)^3 & k \leq k_0 \\ 1 & k > k_0 \end{cases} . \tag{2.2}$$

The features of this power spectrum can arise from many models. Length scales over which there are no correlations in the isocurvature modes have a $\propto k^3$ dependence in the power spectrum (also known as white noise spectrum, see e.g., [101, 118, 119, 104, 120, 121, 110]). Such vanishing correlations are expected for modes that are outside the horizon for the entirety of the isocurvature production, independent of the mechanism. Isocurvature production mechanisms operating during inflation (e.g., non-thermal cosmological phase transitions [1]) can lead to an approximately scale-invariant k^0 power spectrum for wavenumbers that were inside the horizon during the production of isocurvature.

For this study, we focus on isocurvature effects only and so we assume there is no new physics contribution in adiabatic modes. Therefore, we adopt the standard ΛCDM adiabatic power spectrum:

$$P_{\mathrm{ad}}(k) = A_s \left(\frac{k}{k_{\mathrm{pivot}}} \right)^{n_s - 1}, \tag{2.3}$$

where the free parameters A_s and n_s are the scalar amplitude and spectral index. k_{pivot} is the pivot scale, conventionally defined as $k_{\mathrm{pivot}} \equiv 0.05\,\mathrm{Mpc}^{-1}$ [18].

The initial conditions for `CLASS` are defined at a sufficiently early time τ_{ini} such that $k\tau_{\mathrm{ini}} \ll 1$ for all wavenumbers of interest. For the isocurvature initial conditions, we must specify which species deviates from the adiabatic condition in the limit $k\tau_{\mathrm{ini}} \to 0$ (we assume that only a single species has an initial isocurvature mode). For this work, we consider each of four different isocurvature modes: cold dark matter density isocurvature (CDI), baryon density isocurvature (BDI), neutrino density isocurvature (NDI), and free-streaming dark radiation density isocurvature (DRDI).[2] For each of these modes, we use the standard initial conditions [122, 123, 124, 125, 126, 127, 128] which are defined by setting the density perturbation $\delta \equiv (\rho - \bar{\rho})/\bar{\rho}$ for the relevant species to unity at leading order in $k\tau_{\mathrm{ini}}$. The rest of the stress-energy and metric perturbations are specified by the evolution equations in the super-horizon limit, while requiring that there is initially no curvature in the isocurvature mode.

The full set of initial conditions for these four isocurvature modes (including the adiabatic terms), in the synchronous gauge, are shown in Appendix A.1. Here we list the leading term in the density perturbation of photons δ_γ in the limit of $k\tau \to 0$:

$$\begin{aligned} \delta_\gamma^{\mathrm{CDI/BI}} &= -\frac{2}{3}\frac{\Omega_{c/b}}{\Omega_m}\omega_m \tau, \\ \delta_\gamma^{\mathrm{NDI/DRDI}} &= \frac{-R_{\nu/\mathrm{dr}}}{1 - R_{\nu/\mathrm{dr}}}, \end{aligned} \tag{2.4}$$

---

[2] There is another possible isocurvature mode: neutrino velocity isocurvature. We do not study this type of isocurvature as it lacks a well-motivated generation mechanism.

where

$$\begin{aligned} \omega_m &\equiv \sqrt{\frac{8\pi G}{3}} \frac{a(\tau_{\text{ini}})\bar{\rho}_m(\tau_{\text{ini}})}{\sqrt{\bar{\rho}_r(\tau_{\text{ini}})}}, \\ R_{\nu/\text{dr}} &\equiv \frac{\bar{\rho}_{\nu/\text{dr}}}{\bar{\rho}_r}, \end{aligned} \tag{2.5}$$

the total matter background density is $\bar{\rho}_m$, the total background radiation density is $\bar{\rho}_r$, and the fractional matter density is $\Omega_{c/b}/\Omega_m$ in CDM or baryons (for the CDI and BDI isocurvature modes, respectively).

From Eq. (2.4) and Appendix A.1, we can see that initial conditions for photons and metric perturbations in the CDI and BDI modes are the same up to a simple scaling of Ω_i/Ω_m with $i \in \{c, b\}$. Given these initial conditions as well as the forms of the metric and photon evolution equations, the evolved photon perturbation continues to be proportional to Ω_i/Ω_m. Since the CMB angular power spectra come from the two-point functions of photon density perturbations, the isocurvature contribution scales with $(\Omega_i/\Omega_m)^2 A_{\text{iso}}$ (see Eq. (2.6)). We have checked using `CLASS` that CDI and BDI provide identical CMB angular power spectra for the same P_{iso} when rescaling A_{iso} by $(\Omega_i/\Omega_m)^2$, with $i = c, b$. Therefore, for CDI and BDI we will present constraints on $(\Omega_i/\Omega_m)^2 A_{\text{iso}}$.

Another feature of note for CDI and BDI modes is that photon perturbations grow linearly with conformal time τ for super-horizon modes (see Eq. (2.4)). As a result, the size of photon perturbations for a given k mode scales inversely with k at the time of horizon entry (when $k\tau \sim 1$), with the associated suppression in the CMB observables at high k (or high ℓ).

For DRDI, the observables depend not only on the energy density of DR (usually parametrized as the effective number of neutrino species $\Delta N_{\text{eff}} \equiv 3.044 \times \bar{\rho}_{\text{dr}}/\bar{\rho}_\nu \propto R_{\text{dr}}$) through the initial photon perturbation, which is proportional to $R_{\text{dr}}/(1 - R_{\text{dr}})$ (see Eq. (2.4)), but also through changes to the background radiation energy density and thus the Hubble parameter. However, for sufficiently small ΔN_{eff} (equivalently, small R_{dr}), the modification to the total radiation density is negligible and the only effect on observables from DRDI is from isocurvature. For these small values of R_{dr}, the initial photon perturbation is proportional to R_{dr} and (using the same argument as in the CDI and BDI cases) this proportionality also holds for the evolved photon perturbation variables. Therefore, in this case the effect of DRDI on observables scales with $R_{\rm dr}^2 A_{\rm iso}$. For this reason, we assume $R_{\rm dr} \ll 1$ and show constraints on DRDI in terms of $R_{\rm dr}^2 A_{\rm iso}$.

2.3 Constraints from CMB+BAO

In this section we set constraints on $P_{\rm iso}$ at large scales, using CMB angular power spectra and BAO measurements. For the CMB, we used the angular power spectrum of the temperature (T) and polarization (E) anisotropies' two-point correlation functions. The angular power spectrum of the temperature-temperature correlation function C_ℓ^{TT} is

$$C_\ell^{TT} = 4\pi \int d(\ln k) \left(P_{\rm ad}(k) |\Delta_\ell^{\rm ad}(k)|^2 + P_{\rm iso}(k) |\Delta_\ell^{\rm iso}(k)|^2 \right) . \tag{2.6}$$

In this expression, $P_{\rm ad}(k)$ and $P_{\rm iso}(k)$ are the adiabatic and isocurvature power spectra respectively, and $\Delta_\ell^A(k)$ is the photon transfer function for $A = \{{\rm ad}, {\rm iso}\}$. The form of the transfer function for $A = {\rm iso}$ depends on the type of isocurvature mode present. Similar expressions hold for the angular power spectrum of EE and the cross-correlations between T and E.

For a specified isocurvature power spectrum, we calculate Eq. (2.6) using the Boltzmann solver `CLASS` [112]. Since `CLASS` requires a finite power spectrum, we regularize the peaked power spectrum Eq. (2.1) using the parameterization

$$P_{\rm iso}(k) = \begin{cases} A_{\rm iso}/(2\epsilon) & |\ln{(k/k_0)}| \le \epsilon \\ 0 & |\ln{(k/k_0)}| > \epsilon \end{cases} , \tag{2.7}$$

where ϵ is a constant that determines the width (in $\log k$) of the peak. This expression approaches Eq. (2.1) in the limit where $\epsilon \to 0$. In practice, it is not feasible to take ϵ to be arbitrarily small in numerical simulations. In this study, we choose the relatively small value $\epsilon = 0.05 \ln(10)$. We have verified that our constraints are insensitive to the actual value of ϵ in the range $0.01 \lesssim \epsilon \lesssim 0.1$, with at most a $\sim 20\%$ difference in the results.

The simulated fractional difference of CMB temperature anisotropy angular power spectra

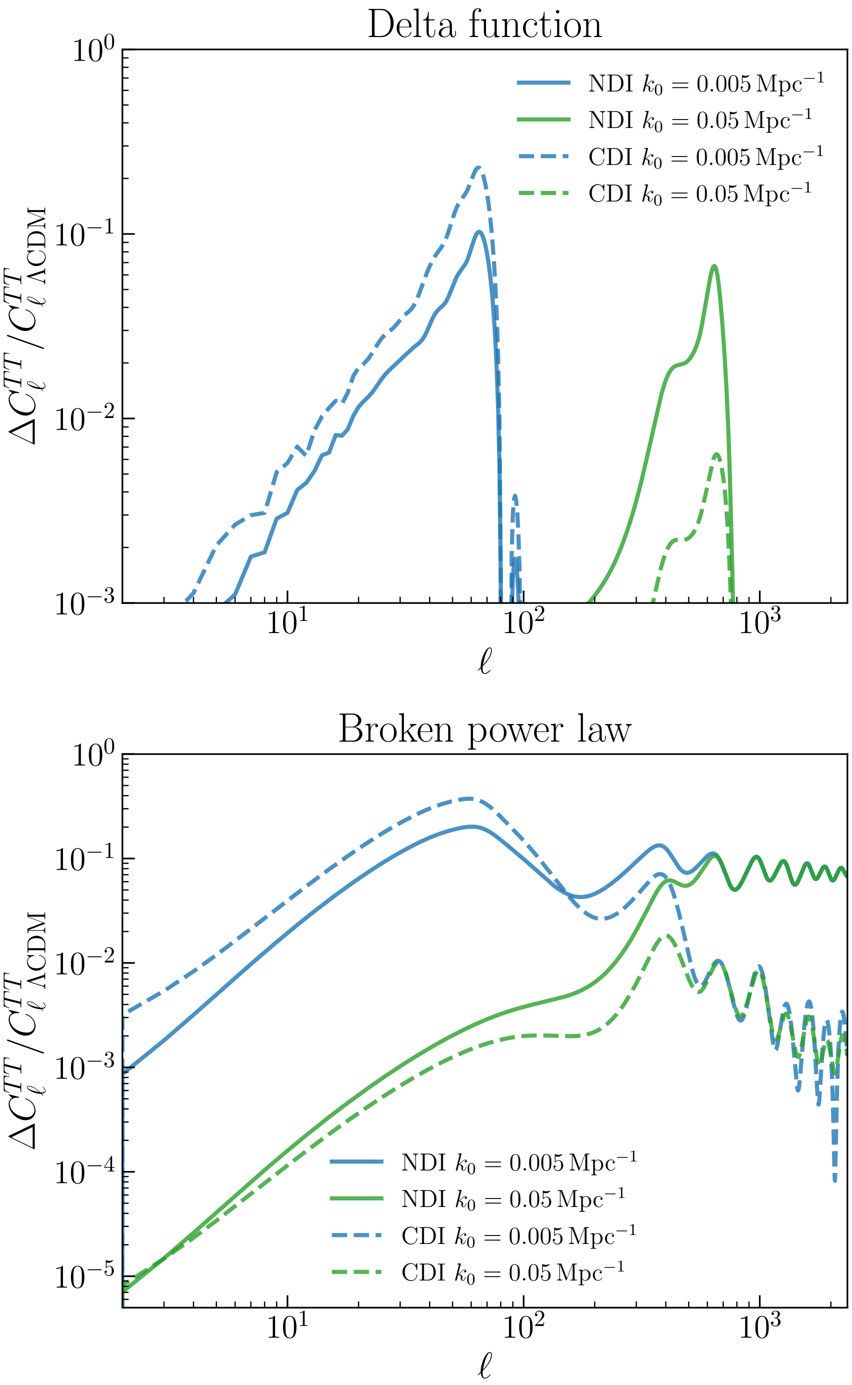

Figure 2.1: The fractional difference of the CMB angular power spectra ΔC_ℓ^{TT} with respect to the case of ΛCDM for CDI (dashed) and NDI (solid) modes with two general forms of isocurvature power spectrum: a delta function (left, see Eq. (2.7)) and a broken power law (right, see Eq. (2.2)). Here we choose $A_{\rm iso} = 2.1 \times 10^{-9}$ and two values of k_0: $0.005\,\mathrm{Mpc}^{-1}$ (blue) and $0.05\,\mathrm{Mpc}^{-1}$(green).

ΔC_ℓ^{TT} with respect to the ΛCDM case for different isocurvature modes with our two general parameterizations of $P_{\rm iso}$ are shown in Figure 2.1. We choose to show results from CDI and NDI as representative for isocurvature modes in matter and radiation respectively.

For the delta-function power spectrum peaking at k_0 (Figure 2.1, left panel), we see the fractional difference between the CMB power spectra with isocurvature and ΛCDM exhibits peaks at the spherical harmonic mode ℓ_0 corresponding to k_0 times the comoving distance to the surface of last scattering ($d_{\rm SLS} \sim 10^4$ Mpc): $\ell_0 = k_0 d_{\rm SLS}$. We note that a delta function form for $P_{\rm iso}(k)$ does not lead to a delta function in ΔC_ℓ^{TT} because the transfer function $\Delta_\ell(k_0)$ has non-zero values for a range of ℓ (see Eq. (2.6)). Moreover, we see that for fixed $A_{\rm iso}$, the ratio of height of the peaks for different k_0 is more dramatic for CDI than for NDI. This is because the CDI transfer function has additional ℓ dependence due to the time dependence in CDI initial conditions (see Eq. (2.4) and discussions below it). As a result, the peak for CDI at high ℓ is more suppressed compared to that of NDI.

The right panel of Figure 2.1 shows the CMB power spectra for the CDI and NDI isocurvature modes, assuming a broken power law $P_{\rm iso}$ (see Eq. (2.2)). We can see that for NDI, curves with different k_0 approach the same plateau (with some oscillations) for large ℓ. This is because the $P_{\rm iso}$ has same constant value for $k > k_0$ for fixed $A_{\rm iso}$, regardless of k_0. Each curve deviates from the common plateau when $\ell < \ell_0$ (corresponding to $k < k_0$), and asymptotes to $\propto \ell^3$ reflecting the $\propto k^3$ feature in $P_{\rm iso}$. The CDI cases, on the other hand, do not have a plateau for large ℓ even if $P_{\rm iso}$ is constant. This is again due to the fact that $\Delta_\ell^{\rm CDI}$ has additional scale dependence that leads to a suppression at high ℓ. The oscillations in these curves reflect the phase shift between isocurvature and adiabatic modes [129, 130].

2.3.1 Data Sets and Methodology

To assess the cosmological constraints on the isocurvature power spectrum, we conduct a comprehensive likelihood analysis using a combination of cosmological datasets. From the relevant two-point observables computed using `CLASS`, we employ `MontePython` [131] for Markov Chain

Monte Carlo (MCMC) exploration of the parameter space constraints from data. Our analysis incorporates the following experimental data:

- CMB: Planck 2018 temperature and polarization spectra, including low-ℓ TT, EE measurements and high-ℓ TTTEEE, as well as gravitational lensing reconstructions [18].
- BAO: Baryon acoustic oscillation measurements from the Six-degree Field Galaxy Survey (6dFGS) [19], the Sloan Digital Sky Survey (SDSS) Data Release 7 Main Galaxy Sample (MGS) [20], and the LOWZ galaxy sample from BOSS DR12 [21].

In each of our analyses, we assume the standard adiabatic modes for all species (with the standard power spectrum Eq. (2.3)), plus one isocurvature mode for a single species. Both of our two general parametrizations of $P_{\rm iso}$ depend on two parameters: $A_{\rm iso}$ and k_0. For each isocurvature mode, we fix values of k_0 and run an MCMC analysis to get the constraint on $A_{\rm iso}$ at 95% confidence level (CL). Our MCMC analysis therefore has seven scanning parameters: $A_{\rm iso}$ and the six standard ΛCDM parameters $\{\omega_{\rm b}, \omega_{\rm c}, H_0, \log_{10}(10^{10}A_{\rm s}), n_{\rm s}, \tau\}$. All cosmological parameters are assigned flat priors. Following the convention adopted by the Planck Collaboration [18], we model free-streaming neutrinos as two massless species and one massive species with $m_\nu = 0.06$ eV.

2.3.2 Results

The 95% CL constraints from CMB data on $A_{\rm iso}$ for different k_0 and isocurvature modes are summarized in Figure 2.4. For NDI, we place constraints directly on $A_{\rm iso}$, while we rescale the constraint on $A_{\rm iso}$ for CDI/BDI with $(\Omega_{c/b}/\Omega_m)^2$ in order to show the constraints on different species in the same plot. For DRDI, we choose to run the analysis for a single value of $\Delta N_{\rm eff} = 0.01$ and extrapolate limits on the combination of $R_{\rm dr}^2 A_{\rm iso}$ from this. We have checked using `CLASS` simulation that this result can be applied generally to DRDI for $R_{\rm dr} \ll 1$.

For both the delta-function and broken power law parametrization of $P_{\rm iso}$, the MCMC analysis chain is used to a set a constraint on $A_{\rm iso}$ for $k_0 \in [10^{-4}, 0.2]\ \mathrm{Mpc}^{-1}$. As seen in the left panels of Figure 2.4, for the delta-function power spectrum the strongest constraint on $A_{\rm iso}$ occurs for k_0

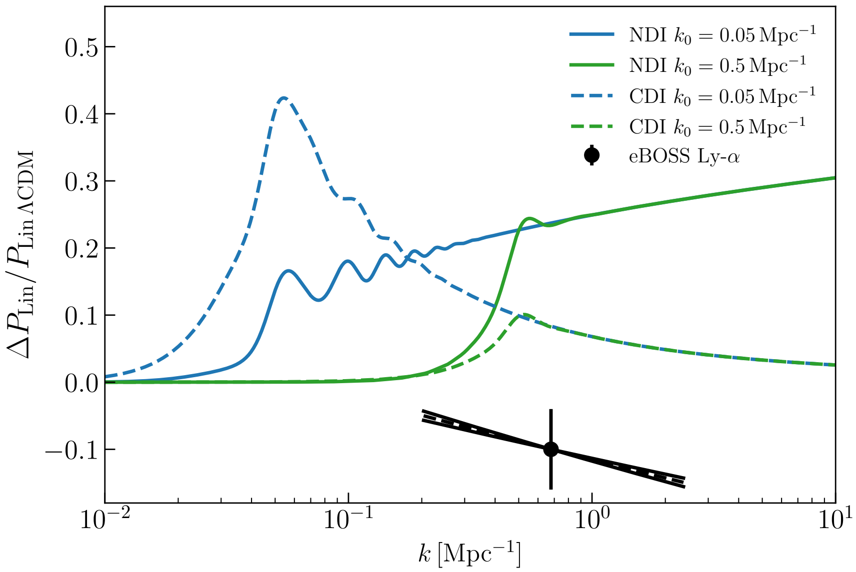

Figure 2.2: The fractional difference of the linear matter power spectrum ΔP_{lin} between ΛCDM and the broken power law isocurvature power spectrum assuming CDI (dashed) and NDI (solid). Here we choose $A_{\mathrm{iso}} = 1.05 \times 10^{-8}$ and two values of k_0: $0.05\,\mathrm{Mpc}^{-1}$ (blue) and $0.5\,\mathrm{Mpc}^{-1}$(green). We also show the compressed likelihood from eBOSS Ly-α data [132, 133].

around the CMB pivot scale $k_{\mathrm{pivot}} = 0.05\,\mathrm{Mpc}^{-1}$. The constraints weaken for both smaller and larger k_0. The strong constraints at the CMB pivot scale can be traced to the fact that the Planck data has the smallest error bars around this wavenumber.

The broken power law spectrum results are shown in the right panels of Figure 2.4. Here, we find that the constraints on A_{iso} for all isocurvature modes roughly remain constant for $k_0 \lesssim k_{\mathrm{pivot}}$ and scale as k_0^3 for $k_0 \gtrsim k_{\mathrm{pivot}}$. This behavior again arises from the strong constraining power of Planck data at k_{pivot}. Therefore, the limit on the continuous isocurvature power spectrum is mostly set by its amplitude at this pivot scale. For $k_0 \lesssim k_{\mathrm{pivot}}$, the isocurvature spectrum (see Eq. (2.2)) is at its plateau at the pivot scale and thus the constraint is roughly constant. For $k_0 \gtrsim k_{\mathrm{pivot}}$, the size of $P_{\mathrm{iso}}(k_{\mathrm{pivot}})$ scales as $A_{\mathrm{iso}}(k_{\mathrm{pivot}}/k_0)^3$. Therefore the constraint on A_{iso} scales as k_0^3. Given this k_0^3 scaling, we show the MCMC results up to $k_0 = 0.5\,\mathrm{Mpc}^{-1}$ and then extrapolate the constraints for $k_0 \geq 0.5\,\mathrm{Mpc}^{-1}$ (denoted as dashed lines).

2.4 Constraints from Ly-α Forest

Traditional analyses of the Ly-α forest flux power spectrum rely on hydrodynamical simulations that scan a multi-dimensional parameter space of cosmology and astrophysical inputs. Although accurate, these analyses are computationally intensive. Instead, it has been shown [113, 114, 115, 116] that most of the cosmological information in the Ly-α forest can be captured in only two parameters describing the amplitude and tilt of the linear matter power spectrum $P_{\rm lin}$ at a specific pivot redshift z_p and wavenumber k_p:

$$\Delta_L^2 \equiv \frac{k_p^3 \, P_{\rm lin}(k_p, z_p)}{2\pi^2}, \quad n_L \equiv \left. \frac{d \ln P_{\rm lin}(k, z)}{d \ln k} \right|_{(k_p, z_p)} . \tag{2.8}$$

Following Refs. [113, 114, 115, 116], we compress the cosmological information from the Ly-α forest flux power spectrum into the amplitude and tilt of the linear matter power spectrum. We evaluate these parameters at a pivot redshift of $z_p = 3$ and a pivot wavenumber $k_p = 0.009\,{\rm s\,km^{-1}}$ in velocity units, which corresponds to the comoving scale $k_p a(z_p) H(z_p) \approx 1 h\,{\rm Mpc}^{-1}$. This procedure significantly reduces the computational burden compared to full hydrodynamical simulations. However as the compressed likelihood is only accurate if the matter power spectrum is approximately described by an amplitude and slope near k_p, this technique can only be applied when the primordial power spectrum is smooth without oscillations and sharp change in slope around this scale. We therefore set Ly-α forest constraint on isocurvature only when assuming the broken power law. The delta function power spectrum is not constrained by this analysis.

We use the eBOSS (SDSS DR14) Ly-α forest flux power spectrum measurements [132], adopting the 2D Gaussian likelihood presented in Ref. [133]. This likelihood is marginalized over astrophysical uncertainties in the flux power modeling (e.g., thermal history and feedback processes), and its use has been validated for a wide range of cosmological models, including non-standard scenarios. The best-fit parameters for the compressed likelihood are $\bar{\Delta}_L^2 = 0.310$, $\sigma_{\Delta_L^2} = 0.020$, $\bar{n}_L = -2.340$, $\sigma_{n_L} = 0.006$ and $\rho = 0.512$ [116].[3] Here ρ is the correlation coefficient between Δ_L^2

---

[3] There is an updated version of compressed likelihood [134, 135]. We leave the study with this likelihood to future

and n_L. Examples of the fractional change in the matter power spectrum relative to the ΛCDM result for both NDI and CDI isocurvature are shown in Figure 2.2. We show the constraints from the compressed likelihood on the amplitude and slope of the linear power spectrum across the range of applicable wavenumbers $[0.3, 3.5]\ h\,\mathrm{Mpc}^{-1}$. As can be seen, for both CDI and NDI cases, if the transition in the broken power law occurs away from pivot wavenumber k_p, the resulting linear matter power spectrum is smooth through the region where the compressed likelihood is used to set bounds. Transitions near k_p lead to more rapidly changing slopes in the power spectrum, making the limits extracted from the compressed likelihood less robust.

In particular, the compressed Ly-α likelihood allows one to isolate the power-spectrum amplitude and tilt, mitigating biases that might arise when projecting higher-dimensional parameter constraints. This approach ensures consistency across different cosmic epochs and scales, thereby improving our overall cosmological parameter inferences. The compressed likelihood is added to that of the CMB, BAO, and SNe measurements described in Section 2.3, again using `MontePython` to explore the parameter space via MCMC. In this combination, we evaluate the log-likelihood of each dataset independently and derive joint posteriors in parameter space.

The resulting constraints on the isocurvature model parameters are shown in Figure 2.4. The joint constraints with CMB+BAO and Ly-α are approximately the same as the CMB+BAO ones for $k_0 \lesssim 0.2\,\mathrm{Mpc}^{-1}$. This occurs because the plateau of the power spectrum extends to scales that the CMB is sensitive to and thus constraints are dominated by CMB+BAO. For $k_0 \gtrsim 1\,\mathrm{Mpc}^{-1}$, CMB constraints weaken, while Ly-α constraints are stronger as the slope of P_{lin} deviates from the preferred value of the compressed likelihood near the pivot scale k_p because $P_{\mathrm{iso}} \propto (k/k_0)^3$. In this regime, the constraints scale as k_0^3, and we extrapolated the results for $k_0 \geq 3\,\mathrm{Mpc}^{-1}$ with this scaling (denoted as dashed lines). There is an intermediate region around $k_0 \sim 1\,h\,\mathrm{Mpc}^{-1}$ (corresponding to k_p) where the constraints exhibit a sharp transition. This feature is due to the rapid change in slope of the isocurvature power spectrum and the resulting linear matter power spectrum around k_p. Since the slope of P_{lin} quickly changes near k_p for these values of k_0, we

---

work.

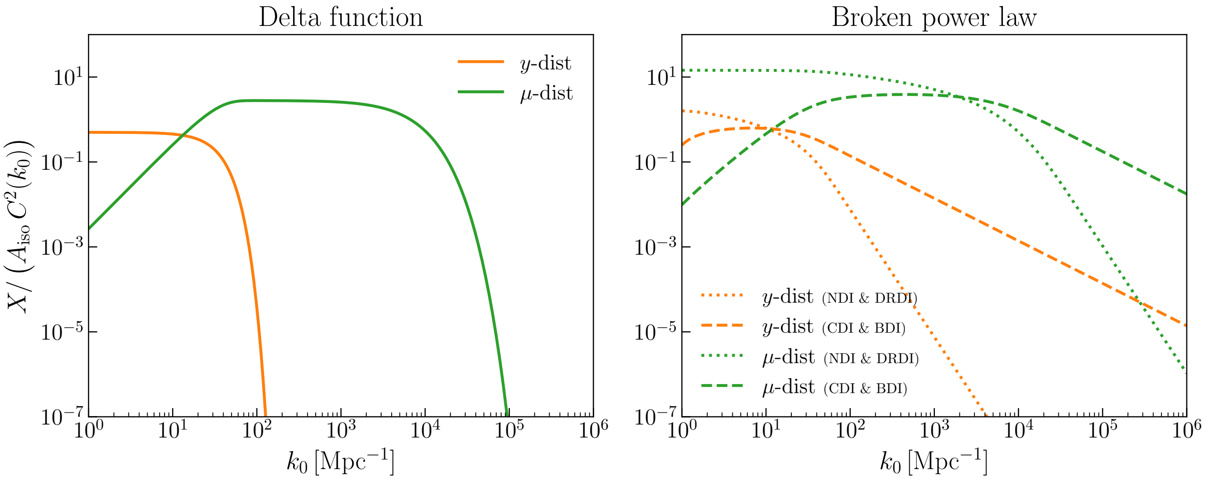

Figure 2.3: Spectral distortions of type $X \in \{y, \mu\}$ normalized to $A_{\rm iso}C^2(k_0)$ for the delta function power spectrum (left) and the broken power law spectrum (right). For the delta function power spectrum, each type of isocurvature mode leads to spectral distortions that are the same up to the proportionality factor $A_{\rm iso}C^2(k_0)$. We therefore show a single curve for all modes. For the broken power law spectrum, the distortions for NDI and DRDI modes only differ by the proportionality factor $A_{\rm iso}C^2(k_0)$ and are shown with dotted curves. The distortions for CDI and BDI mode as functions of k_0 do not have the same form and are shown with the dashed curves.

again note that the constraints in this regime are less robust due to limitations in the compressed likelihood approach.

2.5 Constraints from CMB Spectral Distortions

In this section we consider constraints on isocurvature modes from CMB spectral distortions. These constraints apply for wavenumbers in the range $1\,\text{Mpc}^{-1} \lesssim k \lesssim 10^4\,\text{Mpc}^{-1}$, complementary to the sensitivity range of CMB anisotropies and BAO data.

The observed CMB frequency spectrum is consistent with a blackbody distribution with zero chemical potential. Therefore, any dynamics (e.g., energy injection) that causes distortions in the CMB spectrum (that is, deviations from the blackbody distribution), will be constrained by current and future data (for earlier studies, see e.g., [136, 137, 138, 139, 140, 141, 142]). Depending on the time of the energy injection and the relevant processes in the photon and baryon bath that are active, the spectral distortion can be parametrized by different forms. At very early times,

$z \gtrsim 2 \times 10^6$, the rates of photon number-changing processes (such as double Compton scattering and Bremsstrahlung) are much larger than the Hubble expansion rate. Therefore, any kind of energy injection to the photon and baryon bath will be quickly thermalized, creating a blackbody spectrum at a different temperature with a vanishing chemical potential. This change can be fully absorbed into the measurement of CMB temperature, leaving no spectral distortions.

For redshifts $5 \times 10^4 \lesssim z \lesssim 2 \times 10^6$, photon number-changing processes are inefficient. However, Compton scattering is still active, keeping the photon and electron plasma in thermal equilibrium. In this epoch the photon phase space density follows a Bose-Einstein distribution and exotic energy injection will in general change the temperature and generate a non-zero chemical potential. This creates a difference Δf_γ between the phase space density and a blackbody spectrum:

$$\Delta f_\gamma(\omega, T) = \frac{1}{e^{\omega/(T+\Delta T)+\mu} - 1} - f_{\gamma,0}(\omega/T)\,. \tag{2.9}$$

Here $f_{\gamma,0}(x) \equiv 1/(e^x - 1)$ is the blackbody distribution with zero chemical potential, ΔT is the change in temperature relative to T, and μ is the size of the $\mu-$type spectral distortion and is proportional to the chemical potential. In our analysis, we treat both μ and $\Delta T/T$ as small perturbations and work at linear order in these parameters. Δf is defined such that the new phase space density has the same number density as the blackbody at temperature T but a different energy density[4]. Using this condition the relation between μ and the change in photon energy density is

$$\frac{\Delta n_\gamma}{n_\gamma} \equiv \frac{\int d\omega\, \omega^2 \Delta f_\gamma}{\int d\omega\, \omega^2 f_{\gamma,0}} = 0 \;\Rightarrow\; \mu \approx 1.4 \frac{\Delta \rho_\gamma}{\rho_\gamma}, \tag{2.10}$$

where

$$\frac{\Delta \rho_\gamma}{\rho_\gamma} \equiv \frac{\int d\omega\, \omega^3 \Delta f_\gamma}{\int d\omega\, \omega^3 f_{\gamma,0}}. \tag{2.11}$$

---

[4] For the dissipation of acoustic modes that we consider in this work, the change in photon number density at second order in perturbation theory can be fully absorbed into the definition of the temperature T in Eq. (2.9). After this redefinition, a net change in photon energy density remains.

Below $z \lesssim 5 \times 10^4$, Compton scattering is inefficient at maintaining a Bose-Einstein distribution for the photons after energy injection. However, photons can still interact with electrons via Compton scattering before recombination, making the resulting photon phase space distribution a mixture of blackbody spectra with slightly different temperatures. This kind of distribution can not be described by a single blackbody with a new temperature, instead creating a spectral distortion in photon phase space called a y-distortion:

$$\Delta f_\gamma(\omega, T) = y\,\mathcal{Y}(\omega/T), \tag{2.12}$$

where

$$\mathcal{Y}(x) = [x(1 + 2f_{\gamma,0}(x)) - 4]\,\mathcal{G}(x) \tag{2.13}$$

with

$$\mathcal{G}(x) \equiv x f_{\gamma,0}(x)(1 + f_{\gamma,0}(x)). \tag{2.14}$$

The coefficient y in Eq. (2.12) denotes the size of the y-distortion and is related to the energy release as

$$y = \frac{1}{4}\frac{\Delta\rho_\gamma}{\rho_\gamma}. \tag{2.15}$$

As seen in Eqs. (2.10) and (2.15), the key quantity to determine the size of the spectral distortion (both μ or y) is the change in the photon energy density $\Delta\rho_\gamma/\rho_\gamma$. The main source of such energy injection from primordial density perturbations with $k \geq 1\,\mathrm{Mpc}^{-1}$ is the dissipation of acoustic modes through photon diffusion [140]. This process generates spectral distortions when $z \gtrsim z_* = 1100$. As a result, in our calculations we can assume that photons and baryons are always tightly coupled. With this assumption, the energy injection rate from acoustic modes Q_{ac} is given by [140]

$$\frac{1}{a^4\rho_\gamma}\frac{d(a^4 Q_{\mathrm{ac}})}{dz} = \frac{64}{15}\frac{1}{\kappa H(1+z)}\int d(\ln k) k^2 P_{\mathrm{iso}}(k)(\Theta_1^{\mathrm{iso}})^2, \tag{2.16}$$

where $\kappa = \sigma_T n_e$ is the rate of Thomson scattering and Θ_1^{iso} is the dipole moment of the photon temperature perturbation in the isocurvature mode. As the size of isocurvature power spectra we consider are much larger than that of curvature $P_{\text{iso}} \gg P_{\text{ad}}$, we only keep the contribution from isocurvature perturbations in Eq. (2.16).

For the dissipation of an acoustic mode with wavenumber k, the energy injection rate is non-negligible only when the diffusion scale $k_D(z)$ is of order k. For $z \gtrsim z_{\text{eq}}$, baryon loading is small as $\rho_b \ll \rho_\gamma$ and the diffusion scale can be approximated by

$$\partial_z k_D^{-2} \approx -\frac{8}{45}\frac{1+z}{H\kappa}. \tag{2.17}$$

To find k_D^{-2} as a function of redshift z, we integrate Eq. (2.17) from $z = \infty$ to z and obtain the following analytic result which is valid for $z \gtrsim z_{\text{eq}}$:

$$\begin{aligned} k_D^{-2} = (0.35\,\text{Mpc})^2 \times \left(\frac{0.143}{\Omega_m h^2}\right)^{1/2} \left(\frac{0.022}{\Omega_b h^2}\right) \left(\frac{0.88}{1-Y_p/2}\right) \\ \times \left(\frac{1+z}{10^4}\right)^{-5/2} f_D\left(\frac{1+z_{\text{eq}}}{1+z}\right), \end{aligned} \tag{2.18}$$

where z_{eq} is the redshift of matter-radiation equality and

$$f_D(y) \equiv \frac{1}{3y^{5/2}}\left[\sqrt{1+y}\left(3y^2-4y+8\right)-8\right]. \tag{2.19}$$

Therefore, the diffusion scale is well inside the horizon at all redshifts and it satisfies $k_D(z) \gtrsim 1\,\text{Mpc}^{-1}$ for $z \gtrsim z_{\text{eq}}$. This means that the modes we are considering ($k \gtrsim 1\,\text{Mpc}^{-1}$) will only inject energy when $z \gtrsim z_{\text{eq}}$, implying that we are justified in neglecting baryon loading. Under these circumstances, the photon dipole moment can be approximated for modes inside the horizon as

$$\Theta_1^{\text{iso}} \approx c_s\left[A(k)\sin(kr_s) - B(k)\cos(kr_s)\right] e^{-k^2/k_D^2}, \tag{2.20}$$

where $r_s = \int dt\, c_s/a$ is the sound horizon and $c_s^2 \approx 1/3$ is the sound speed.

From Eqs. (2.10), (2.15) and (2.16), the μ and y distortions in the CMB today can be calculated

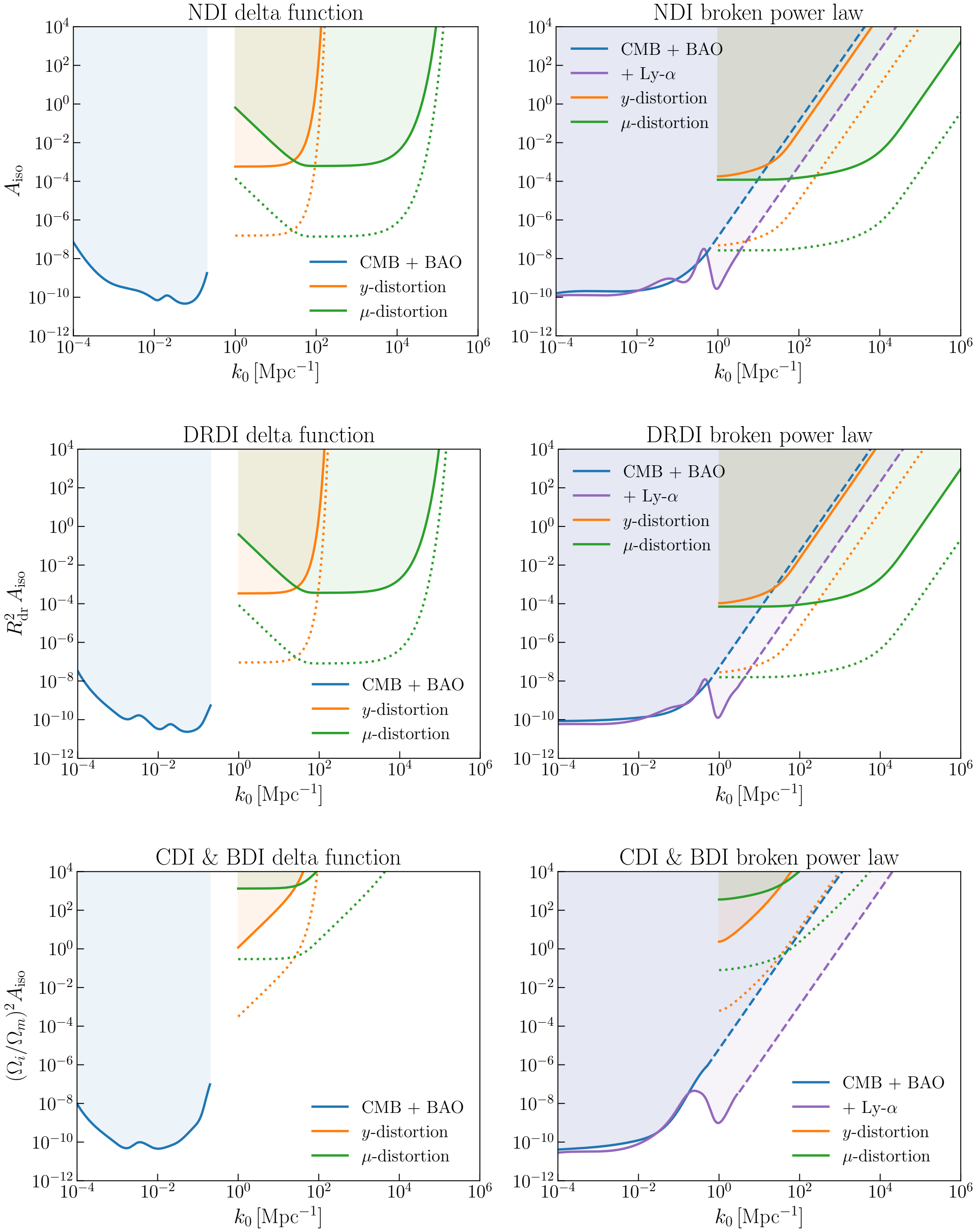

Figure 2.4: Limits on isocurvature power spectrum amplitude as a function of k_0 for NDI, DRDI, CDI and BDI from various observations. The left column shows limits on the delta-function power spectrum (Eq. (2.1)) and the right column shows limits on the broken power law spectrum (Eq. (2.2)). Limits from CMB and BAO are shown in blue while joint constraints with Ly-α are shown in purple. The dashed lines indicate the extrapolation that is proportional to k_0^3. Limits from y-type and μ-type spectral distortions are in orange and green, respectively. For each type of spectral distortion we show current limits (solid) from COBE/FIRAS [117] and projected limits (dotted) for PIXIE [143].

in terms of the energy release during two different epochs[5] [140]:

$$\begin{aligned} \mu &\approx 1.4 \left.\frac{\Delta\rho_\gamma}{\rho_\gamma}\right|_\mu \approx 1.4 \int\limits_{z_{\mu,y}}^{\infty} dz \mathcal{J}_{bb}(z) \frac{1}{a^4\rho_\gamma} \frac{d(a^4 Q_{ac})}{dz} \\ y &\approx \frac{1}{4} \left.\frac{\Delta\rho_\gamma}{\rho_\gamma}\right|_y \approx \frac{1}{4} \int\limits_{z_*}^{z_{\mu,y}} dz \mathcal{J}_{bb}(z) \frac{1}{a^4\rho_\gamma} \frac{d(a^4 Q_{ac})}{dz}, \end{aligned} \tag{2.21}$$

where $z_{\mu,y} = 5 \times 10^4$ and $\mathcal{J}_{bb}(z) = \exp\left[-(z/z_\mu)^{5/2}\right]$ which is the visibility function[6] which erases contributions to μ distortions at redshifts $z \gtrsim z_\mu = 1.98 \times 10^6$. Note that $\mathcal{J}_{bb}(z) \to 1$ in the redshift range over which the integral for the y distortion is taken.

Substituting Eq. (2.16) into the expressions for μ and y in Eq. (2.21), we see that Θ_1 (defined in Eq. (2.20)) will oscillate with z much faster than any other factor in the integrand. As a result, the integrals in Eq. (2.21) can be approximated by averaging the integrands over many oscillation periods, allowing us to replace $\sin^2(kr_s)$ and $\cos^2(kr_s)$ each with $1/2$ and to omit the cross-term. After these approximations, the fractional energy density due to spectral distortions can be written as

$$\frac{\Delta\rho_\gamma}{\rho_\gamma} = 2 \int d(\ln k) C(k)^2 P_{\rm iso}(k) \int dz \mathcal{J}_{bb}(z) \partial_z e^{-2k^2/k_D^2}, \tag{2.22}$$

where $C(k)^2 \equiv A(k)^2 + B(k)^2$ (with $A(k)$ and $B(k)$ defined in Eq. (2.20)). This expression can be evaluated for μ and y distortion by using the appropriate limits of the z integral.

As we are interested in limits on four different isocurvature modes (CDI, BDI, NDI and DRDI), we must calculate the coefficient $C(k)^2$ in Eq. (2.22) for each of those modes. In each case, the coefficients $A(k)$ and $B(k)$ – and from them, $C(k)$ – can be found by simulating the Boltzmann Einstein equations for the appropriate initial conditions and fitting Eq. (2.20) to the numerical result during the radiation domination era for modes inside the horizon.

---

[5] In principle, y distortions can be generated from energy release at any redshift after $z_{\mu,y}$. However, the y distortion from photon diffusion considered in this work contributes only before recombination. Therefore, we set the lower limit of the second integral in Eq. (2.21) to z_*.

[6] A refined visibility function is considered in Ref. [144]. We have verified that the difference between the spectral distortions obtained in this work and the result from using the refined visibility function is less than 10%.

For NDI, the k-independent value of $C(k)^2$ was found in a previous numerical study [140]:

$$C(k)^2 \approx 0.052 \quad (\text{NDI}). \tag{2.23}$$

For both CDI and BDI, analytic considerations [145] imply that $\{A, B\} \propto (\Omega_i/\Omega_m)(k_{\text{eq}}/k)$ where Ω_i is the density parameter for matter species i and $k_{\text{eq}} = 9.56 \times 10^{-3}\,\text{Mpc}^{-1}$ is the wavenumber that crosses the horizon at matter-radiation equality. This form for A and B was fit to the numerical result [140] leading to

$$C(k)^2 \approx 0.28 \left(\frac{\Omega_i}{\Omega_m}\right)^2 \left(\frac{k_{\text{eq}}}{k}\right)^2 \quad (\text{CDI/BDI}). \tag{2.24}$$

For free-streaming dark radiation, the analogous result does not exist in the literature. We used `CLASS` to extract the A and B coefficients for the DR isocurvature mode with different energy densities of dark radiation. We found that the coefficients are well approximated by the k-independent values

$$\begin{aligned} A \approx& -0.28 \times \frac{R_{\text{dr}}}{1-R_{\text{dr}}} \\ B \approx& -0.1 \times \frac{R_{\text{dr}}}{1-R_{\text{dr}}} \end{aligned} \tag{2.25}$$

for $R_{\text{dr}} \ll 1$. This leads to

$$C(k)^2 = 0.088 \left(\frac{R_{\text{dr}}}{1-R_{\text{dr}}}\right)^2 \quad (\textbf{DRDI}\,,\ R_{\text{dr}} \ll 1). \tag{2.26}$$

From these results, we calculate the y and μ distortions for each mode and power spectrum. According to Eqs. (2.21) and (2.22), y distortions have the form

$$y \approx \frac{1}{2} \int\limits_{k_{\min}}^{\infty} d(\ln k) C(k)^2 P_{\text{iso}}(k)\ e^{-2k^2/k_D^2}\Big|_{z_*}^{z_{\mu,y}}\,, \tag{2.27}$$

where we set a lower limit on the k integral given by $k_{\rm min} = 1\,{\rm Mpc}^{-1}$. This choice ensures that the approximation of small baryon loading is satisfied and it is a conservative choice as any contributions to the integral from lower k are positive. For the μ distortions, we find

$$\mu \approx 2.8 \int\limits_{k_{\rm min}}^{\infty} d(\ln k) C(k)^2 P_{\rm iso}(k) \int\limits_{z_{\mu,y}}^{\infty} dz \mathcal{J}_{bb}(z) \partial_z e^{-2k^2/k_D(z)^2}, \tag{2.28}$$

which must be numerically integrated for each choice of power spectrum.

Using the delta-function power spectrum, the k integrals are trivial and both spectral distortions are proportional to $C(k_0)^2 A_{\rm iso}$ for all isocurvature modes. We show the y and μ distortions normalized to this product in the left panel of Figure 2.3.

Using the broken power law spectrum, the k integral is non-trivial and the result depends on the full k dependence of $C(k)^2$ for each mode. We show the y and μ distortions for each case in the right panel of Figure 2.3, again with the results normalized to $A_{\rm iso} C(k_0)^2$. Since NDI and DRDI both have a $C(k)^2$ which is independent of k, the results for these modes are the same (shown with the dotted curves). On the other hand, CDI and BDI modes have $C(k)^2 \propto k^{-2}$. The results for these modes are shown with dashed curves.

The 2σ upper bounds on μ and y from COBE/FIRAS are given by [117]

$$\begin{aligned} |y| &\leq 1.5 \times 10^{-5} \\ |\mu| &\leq 9 \times 10^{-5}. \end{aligned} \tag{2.29}$$

The projected limits for PIXIE are [143]

$$\begin{aligned} |y| &\leq 4 \times 10^{-9} \\ |\mu| &\leq 2 \times 10^{-8}. \end{aligned} \tag{2.30}$$

The resulting existing and projected limits on isocurvature from spectral distortions are shown in Figure 2.4. For the delta function power spectrum (the left panels of Figure 2.4), the strongest constraints are from y-distortions for $1\,\mathrm{Mpc}^{-1} \lesssim k_0 \lesssim 40\,\mathrm{Mpc}^{-1}$ and from μ-distortions for $40\,\mathrm{Mpc}^{-1} \lesssim k_0 \lesssim 10^4\,\mathrm{Mpc}^{-1}$. Constraints weaken for $k_0 \gtrsim 10^4\,\mathrm{Mpc}^{-1}$ because these modes are within the photon diffusion length ($k_0 \gtrsim k_D(z)$) for the whole period ($z \lesssim 10^6$) during which spectral distortions can be produced. For NDI and DRDI modes, the dominant constraints between $1\,\mathrm{Mpc}^{-1} \lesssim k_0 \lesssim 10^4\,\mathrm{Mpc}^{-1}$ are almost flat due to $C(k)^2$ being independent of k (see Eqs. (2.23) and (2.26)). In comparison, CDI and BDI results exhibit k_0^2 dependence as a result of the $C(k)^2 \propto k^{-2}$ dependence in Eq. (2.24).

For the case of broken power law (the right panels of Figure 2.4), the constraint is always dominated by the μ-distortion for NDI and DRDI, and behaves as $\propto k_0^3$ for $k_0 \gtrsim 10^4\,\mathrm{Mpc}^{-1}$ due to the k^3 part of P_{iso}. For the broken power law constraints on CDI and BDI, the results are similar to that from delta function: the y-distortion dominates for $1\,\mathrm{Mpc}^{-1} \lesssim k_0 \lesssim 40\,\mathrm{Mpc}^{-1}$ and the combined constraint shows k_0^2 dependence for $1\,\mathrm{Mpc}^{-1} \lesssim k_0 \lesssim 10^4\,\mathrm{Mpc}^{-1}$. In principle, the limits would apply for $k_0 < 1\,\mathrm{Mpc}^{-1}$ as well since the power spectrum still has support for $k > 1\,\mathrm{Mpc}^{-1}$. However, the CMB and Ly-α limits are significantly stronger for this range of k_0 so we do not show the constraints from spectral distortions in the regime.

2.6 Conclusions

New physics models can generate isocurvature signatures in cosmological observables in any species (CDM, baryons, neutrinos and dark radiation) with a wide variety of primordial isocurvature power spectra. Existing cosmological constraints on the isocurvature power spectrum generally assume a simple power law, limiting the applicability. In this work, we derive general constraints that can be applied to a broad class of new physics models by parametrizing the isocurvature power spectrum with two forms: a delta-function and a broken power law, and consider four types of isocurvature modes (CDI, BDI, NDI, and DRDI).

We place constraints on the isocurvature power spectrum across a wide range of scales with data from the CMB+BAO, the Ly-α forest, and CMB spectral distortions. From our MCMC analysis, we find that CMB+BAO sets the strongest constraints at large scales ($k \lesssim 0.1\,\mathrm{Mpc}^{-1}$), while Ly-$\alpha$

puts the most stringent constraint at $k \sim 1\,\mathrm{Mpc}^{-1}$. CMB spectral distortions constrain the isocurvature spectrum at $1\,\mathrm{Mpc}^{-1} \lesssim k \lesssim 10^4\,\mathrm{Mpc}^{-1}$. Note that the Ly-$\alpha$ constraints assume a continuous power spectrum and so are only applied in this work to the broken power law parametrization of isocurvature.

Other observables can also place constraint on isocurvature spectrum at different scales. The presence of isocurvature can affect the Big Bang Nucleosynthesis (BBN) and the primordial abundance of light elements (see e.g., Ref. [146] for DRDI). Isocurvature perturbations can source gravitational waves as they enter the horizon and thus will be constrained by gravitational wave observations (see Refs. [147, 148] for CDI). Large isocurvature perturbations can also form primordial black holes (For CDI, see Ref. [149]). We leave the study of general constraints on different isocurvature modes from these effects to future work.

CHAPTER 3

DARK RADIATION ISOCURVATURE FROM COSMOLOGICAL PHASE TRANSITIONS

Cosmological first order phase transitions are typically associated with physics beyond the Standard Model, and thus of great theoretical and observational interest. Models of phase transitions where the energy is mostly converted to dark radiation can be constrained through limits on the dark radiation energy density (parameterized by $\Delta N_{\rm eff}$). However, the current constraint ($\Delta N_{\rm eff} < 0.3$) assumes the perturbations are adiabatic.

This chapter is based off of Ref. [1], where we point out that a broad class of non-thermal first order phase transitions that start during inflation but do not complete until after reheating leave a distinct imprint in the scalar field from bubble nucleation. Dark radiation inherits the perturbation from the scalar field when the phase transition completes, leading to large-scale isocurvature that would be observable in the CMB. We perform a detailed calculation of the isocurvature power spectrum and derive constraints on $\Delta N_{\rm eff}$ based on CMB+BAO data. For a reheating temperature of $T_{\rm rh}$ and a nucleation temperature T_*, the constraint is approximately $\Delta N_{\rm eff} \lesssim 10^{-5}(T_*/T_{\rm rh})^{-4}$, which can be much stronger than the adiabatic result. We also point out that since perturbations of dark radiation have a non-Gaussian origin, searches for non-Gaussianity in the CMB could place a stringent bound on $\Delta N_{\rm eff}$ as well.

3.1 Introduction

Extensions of the Standard Model of particle physics often result in first order phase transitions (FOPT) in the early Universe. For example, the phase transition (PT) in models of electroweak baryogenesis is predicted to be first order [150, 151, 152, 153, 154, 155, 156, 157]. New physics that postulates new confining gauge groups – such as in composite Higgs/Randall Sundrum models which address the Planck-Weak Hierarchy problem [158, 159, 160, 161, 162, 163, 164, 165, 166, 167, 168, 169, 170, 171, 172, 173, 174, 175, 176], or in dark matter models with dark QCD or dark $SU(N)$ gauge theories [177, 178, 179, 180, 181, 182, 183, 184, 185, 186, 187, 187] – can also result in FOPT. A class of Early Dark Energy models [188, 189, 190], introduced to relieve the tension between the early- and late-time measurements of H_0 [18, 191], generally require PTs in their dark sector [192, 193, 194]. Probing cosmological FOPTs is therefore a problem of wide applicability to physics beyond the Standard Model.

Cosmological FOPTs create gravitational waves through bubble collisions, shock waves, and turbulence produced during the transition [195, 196, 197, 198, 199, 200, 201, 202]. For phase transitions at $\mathcal{O}(10-100)$ MeV temperatures, these gravitational waves have frequencies accessible to the Pulsar Timing Array (PTA) [203, 204, 205, 206, 207]. Future experiments, including LISA [208, 209], DECIGO [210, 211], and BBO [212], will be able to probe transition temperature around the TeV scale or above.

In addition to these direct probes of the stochastic gravitational wave background generated by the FOPT, precision measurements of the Cosmic Microwave Background (CMB) can constrain phase transitions that generate massless or low-mass dark radiation (DR) [185, 213].[1] The energy density of DR is typically parameterized in terms of the extra number of effective neutrino species ΔN_{eff} above the Standard Model expectation $N_{\text{eff}} = 3.044$ [214, 215, 216]. For free-streaming DR, the CMB sets the upper bound $\Delta N_{\text{eff}} < 0.3$ at 95% confidence level (CL) [18].

Importantly, this constraint on the number of light degrees of freedom assumes the initial density perturbations of the dark radiation are *adiabatic*: with over- and under-densities proportional to those of the other radiation species. If the DR is sourced by a FOPT that undergoes violent bubble nucleation, the initial spatial distribution of the perturbations will contain additional *isocurvature* modes.[2] However, for FOPTs with energy scales far above the $\sim$ eV scales of recombination and decoupling, the isocurvature perturbations are typically highly suppressed for modes that can leave observable imprints within the CMB [96, 97]. As a result – even though isocurvature per-

---

[1] In this context, gravitational waves are also a form of dark radiation.

[2] For general discussions of isocurvature, see for example [122, 123, 124, 125, 126, 127].

turbations are tightly constrained by CMB measurements [54, 217, 128][3] – these limits typically cannot be applied to the high-scale FOPTs, and the dominant constraint comes from the standard measurements on the number of relativistic degrees of freedom.

In this paper, we consider a broad class of high-scale FOPT models which generate large-scale isocurvature perturbations whose imprint *would* be visible within the CMB. These models have non-thermal (vacuum) phase transitions, where the scalar potential that triggers the transition is independent of temperature and couples to the inflaton field. As a result of this coupling, the FOPT can begin during inflation, with a bubble nucleation rate per volume $\Gamma_{\rm PT}$ which we assume to satisfy

$$\Gamma_{\rm PT} \ll H_{\rm inf}^4, \tag{3.1}$$

during the inflationary epoch (when the Hubble parameter is $H_{\rm inf}$). This hierarchy of scales can be chosen so that the PT does *not* complete by the end of inflation and instead completes only after reheating. In the scenario we consider in this paper, the energy density in the scalar field undergoing the FOPT is mostly converted into dark radiation when the PT completes, with perturbations inherited from the scalar field.

Bubbles nucleated in the scalar field during inflation will expand to the horizon size in a Hubble time and remain frozen in comoving coordinates afterwards. As the comoving horizon is rapidly changing during inflation, this results in a wide range of bubble sizes, with the largest bubbles corresponding to the earliest nucleation events. The bubble distribution will later be imprinted in DR when the PT completes. A schematic of cosmological history during and after inflation is shown in Figure 3.1. For phase transitions that start when the inflationary horizon is of order the comoving scale at recombination or larger, stochastic perturbations in DR can leave an observable imprint on the CMB.[4] As the bubbles are randomly distributed, the DR perturbations are uncorrelated with the fluctuations of the inflaton and behave as isocurvature. Since the CMB is consistent with adiabatic initial conditions with zero isocurvature [54], we can place constraints on $\Delta N_{\rm eff}$ from this class of

---

[3] There are also constraints on dark radiation isocurvature from Big Bang nucleosynthesis [146].

[4] For earlier works on effects of large bubbles from phase transitions during inflation, see Refs. [218, 219, 220, 221, 222, 108].

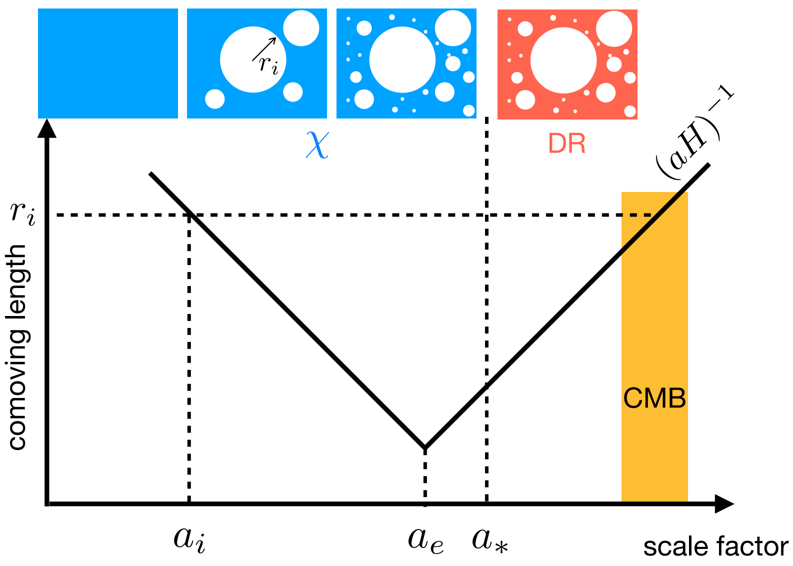

Figure 3.1: A schematic plot of comoving horizon size $(aH)^{-1}$ (black line) as a function of scale factor a. Three scale factors have been listed: a_i denotes the start of the FOPT, a_e shows the end of inflation, and a_* corresponds to the nucleation temperature T_* when phase transition completes. The shaded orange region shows the time window when modes that CMB can probe enter the horizon. The upper part of the plot shows the evolution of perturbations in the χ field due to nucleation of bubbles. $r_i \equiv (a_i H_{\text{inf}})^{-1}$ is the size of the earliest and largest bubble, nucleated at a_i. After the completion of the PT around a_*, χ converts into DR with the same large-scale perturbations, which will imprint DR isocurvature signals on the CMB after re-entering the horizon. (We note that the distribution of bubbles shown in this plot are schematic. We will present more realistic bubble distributions from simulations in Section 3.3.)

FOPTs that are much stronger than in the adiabatic scenario.

In this work, we present a detailed calculation of the DR isocurvature power spectrum from non-thermal PTs that start during inflation. We implement this model in CLASS [112, 74, 223], appropriately modified to include DR isocurvature. Using numerical simulations, we show how the CMB power spectra would change in the presence of DR isocurvature. We then perform a Markov Chain Monte Carlo (MCMC) scan using CMB and Baryon Acoustic Oscillation (BAO) data to constrain the DR energy density (written in terms of ΔN_{eff}) and other parameters related to the phase transition. We find that when the temperature T_* at which the phase transition completes (estimated from $\Gamma_{\text{PT}} = H(T_*)^4$), is close to the reheating temperature T_{rh}, the isocurvature perturbations set a limit of $\Delta N_{\text{eff}} \lesssim 10^{-5}(T_*/T_{\text{rh}})^{-4}$. This limit weakens as T_*/T_{rh} decreases and approaches the adiabatic constraint of $\Delta N_{\text{eff}} < 0.3$ when $T_* \ll T_{\text{rh}}$. In addition to the isocurvature, a FOPT which begins during inflation will also result in non-Gaussianity in the CMB. While we defer a full analysis of such constraints to a future work, here we estimate the expected limits by analogy with neutrino density isocurvature non-Gaussianity [224, 225, 226].

This paper is organized as follows. In Section 3.2, we introduce a model of non-thermal phase transitions and calculate the transition rate. In Section 3.3 we describe the dynamics of the phase transition during inflation and the resulting distribution of nucleated bubbles. In Section 3.4, we calculate the two quantities that will lead to observational constraints on the model: the DR isocurvature power spectrum and bispectrum. Next, we implement the model in CLASS and show the effects of DR isocurvature on the CMB angular power spectra in Section 3.5. In Section 3.6 we describe the datasets we use to set our limits and the details of our MCMC parameter scans. The resulting constraints on the DR isocurvature parameters from the CMB angular power spectra and bispectra are shown in Section 3.7. We conclude in Section 3.8.

3.2 Models of Non-thermal Phase Transitions

In this work, we consider models containing a scalar field χ that undergoes a FOPT that imprints significant isocurvature perturbations into the CMB. The minimum requirements for such models are:

i. The FOPT starts during inflation, at a moment when the comoving horizon (r_i) is above the minimum comoving length scale that the CMB can probe.

ii. The PT rate remains small during inflation ($\gamma_{\rm PT} \equiv \Gamma_{\rm PT}/H_{\rm inf}^4 \ll 1$).

iii. After reheating, the PT completes (at a temperature T_*, defined by $\Gamma_{\rm PT}/H(T_*)^4 = 1$) and the energy density in the χ field converts into DR.

The interesting isocurvature effects we consider in this paper are present as long as these three requirements are met.

As a specific implementation, we realize these features with a scalar potential that is non-thermal – that is, independent of the temperature T of the Universe. This non-thermality can be simply achieved if there are no sizeable couplings between the scalar field χ and the Standard Model fields. Without temperature dependence in the potential, the parameters of the model can be chosen such that the phase transition rate $\Gamma_{\rm PT}$ is constant and satisfies $\Gamma_{\rm PT} \ll H_{\rm inf}^4$. The phase transition in our study is triggered by the slow roll of the inflaton field ϕ, through couplings between ϕ and χ.[5] We further assume that the energy density of the χ field is subdominant to that of ϕ during inflation, and couplings between χ and other light fields in the dark sector allow the eventual conversion of vacuum energy into dark radiation after the phase transition completes. The example potential we consider is described in Section 3.2.1 along with the resulting phase transition rate. The phase transition trigger during inflation is discussed in Section 3.2.2.

3.2.1 Temperature-Independent Phase Transition

The temperature-independence of the scalar potential $V(\chi)$ can be achieved by requiring that V is dominated by a bare tree-level potential. For this paper, we consider the simple example:

$$V(\chi) = -\frac{1}{2}m^2\chi^2 + \frac{\mu}{3}\chi^3 + \frac{\lambda}{4}\chi^4. \tag{3.2}$$

The Z_2 symmetry of the potential is broken by μ, which we assume to be small ($\mu \ll m$) and positive. This condition implies that the two vacuum states at $\chi_\pm \approx \pm m/\sqrt{\lambda}$ are nearly degenerate. That is, the vacuum energy difference $\Delta V \sim \mu m^3/\lambda^{3/2}$ is much smaller than the potential barrier $V_{\rm max} \sim m^4/\lambda$.

We assume the field is in the false vacuum state χ_+ early in the inflationary phase. When the comoving horizon is r_i, the FOPT starts as χ tunnels to the true vacuum χ_-. In Section 3.2.2, we present one example of a dynamical mechanism for this transition, achieved by coupling χ and the inflaton ϕ through the Z_2-breaking μ term.

For $\Delta V \ll V_{\rm max}$, the thin-wall approximation is applicable and the quantum tunneling rate can

---

[5] For other ways of triggering non-thermal FOPTs, see for example [227].

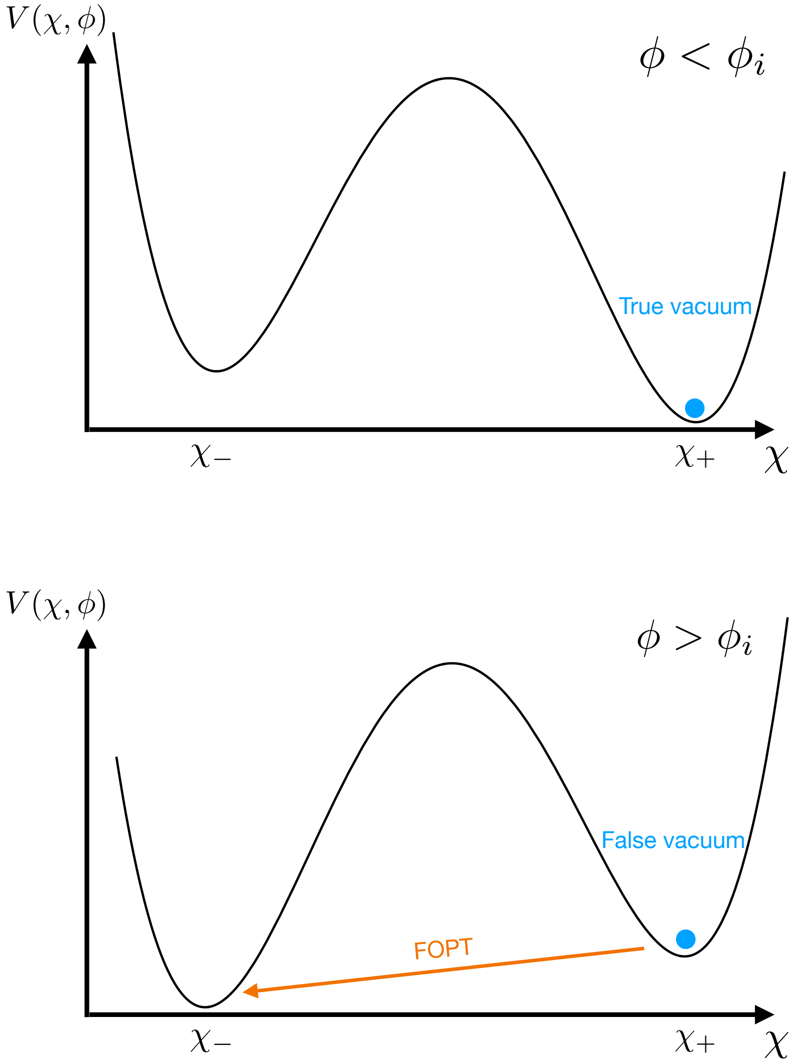

Figure 3.2: Schematic plot of the scalar potential $V(\chi, \phi)$ in Eq. (3.6). When $\phi < \phi_i$, χ stays in the true vacuum near χ_+. Soon after $\phi > \phi_i$, it turns into the false vacuum because $\mu(\phi)$ changes sign. Therefore, the FOPT starts and χ tunnels to true vacuum near χ_-.

be calculated in terms of the $O(4)$ symmetric bounce action [228, 229, 230]

$$S_4 = \frac{27\pi^2 S_1^4}{2\Delta V^3} \sim \lambda^{1/2}\left(\frac{m}{\mu}\right)^3 \gg 1, \tag{3.3}$$

where $S_1 \sim m^3/\lambda$ is the bounce action along the radial direction. The quantum phase transition rate per volume is

$$\Gamma_{\rm PT} \sim r_c^{-4} S_4^2 e^{-S_4}, \tag{3.4}$$

where $r_c = 3S_1/\Delta V$ is the size of the critical bubble for the $O(4)$ symmetric bubble under the thin-wall approximation. Since $\Gamma_{\rm PT}$ is exponentially sensitive to S_4, one can easily achieve the requisite small $\Gamma_{\rm PT}/H_{\rm inf}^4$ for a reasonable choice of parameters. Under these assumptions, and with the additional requirement that the number of e-folds after the tunneling begins is small enough (see Section 3.3 for details), the phase transition does not complete by the end of inflation. That is, at the end of inflation there are regions where the scalar field is in the false vacuum, separating bubbles of true vacuum nucleated during inflation.

After inflation, we assume the Universe instantaneously reheats to a radiation-dominated state with a temperature $T_{\rm rh}$. We assume $\Gamma_{\rm PT}$ remains constant after inflation, and that the PT completes at a temperature T_*. As the horizon changes after inflation, a constant $\Gamma_{\rm PT}$ requires that the critical bubble size r_c is less than the physical horizon size at any time. Otherwise, the bounce action will acquire horizon dependent corrections from the curved spacetime [231]. That is, we require

$$r_c^{-1} \sim \frac{\mu}{\lambda^{1/2}} \gg H_{\rm inf}. \tag{3.5}$$

This and all other requirements stated in this section can be satisfied by choosing appropriate values of m, λ, μ, and $H_{\rm inf}$.

3.2.2 Inflaton-Triggered Phase Transition

Our scenario requires a phase transition that is triggered during inflation, rather than by a coupling to a thermalized Standard Model bath. While more complex examples might be motivated by other theoretical considerations, a simple realization of this phenomenon is to couple the χ field to the ϕ through the small Z_2-breaking μ term in Eq. (3.2):

$$V(\chi, \phi) = -\frac{1}{2}m^2\chi^2 + \frac{\mu(\phi)}{3}\chi^3 + \frac{\lambda}{4}\chi^4. \tag{3.6}$$

To trigger the FOPT, $\mu(\phi)$ must be some function of ϕ that switches sign as ϕ slow-rolls past some critical value of ϕ_i. To simplify the later discussion, we focus on a specific form of $\mu(\phi)$ that behaves like a step function when ϕ passes ϕ_i. One simple realization of such a $\mu(\phi)$ function is

$$\mu(\phi) = \mu \tanh\left(\frac{\phi - \phi_i}{\Delta\phi}\right), \tag{3.7}$$

where the mass scale $\Delta\phi$ is chosen to be much smaller than change of ϕ in a Hubble time. We also require μ to be small such that the $\frac{1}{3}\mu(\phi)\chi^3$ term has a negligible contribution to the inflaton potential.[6] We note that isocurvature signals we consider in this work are insensitive to the specific choice of $\mu(\phi)$, provided that it behaves like a step function with a quick transition.

For choices of $\mu(\phi)$ that have the necessary temperature-independent trigger behavior, this model has the novel feature that the phase transition begins during inflation when ϕ rolls past a critical value ϕ_i. When this happens, χ_+ is no longer the global minimum of the potential and a FOPT can occur as χ tunnels to the true minimum at χ_- (see Figure 3.2). This tunneling occurs stochastically; as bubbles of true vacuum form at random times and locations, they expand to the horizon size and inflate along with it (as we will discuss in detail in the next section). Therefore, the largest bubbles after inflation are those that nucleated earliest, when $\phi \approx \phi_i$ and the comoving horizon size was r_i. Therefore, the distribution of bubbles has a characteristic feature around r_i.

---

[6] The small μ parameter is technically natural because Z_2 symmetry ($\chi \to -\chi$) is restored when $\mu \to 0$. Since this coupled term $\frac{1}{3}\mu(\phi)\chi^3$ is small, the inflaton dynamics and the FOPT in the χ field can be studied independently.

In our simple scenario, the PT rate remains constant and the phase transition can be fully specified by $\gamma_{\rm PT} \equiv \Gamma_{\rm PT}/H_{\rm inf}^4$ and r_i.

We emphasize that all the interesting large-scale isocurvature effects considered in this paper are present as long as the three requirements stated at the beginning of this section are satisfied. To demonstrate the resulting constraints from the CMB data, we restrict ourselves to the simple toy model parameterized by $\gamma_{\rm PT}$ and r_i.

3.3 Stochastic Bubble Distribution from Incomplete Phase Transition during inflation

In this section, we discuss the dynamics of bubbles nucleated during inflation and describe their stochastic distribution. From the distribution of bubbles, we will calculate density perturbations in the χ field, which will lead to DR isocurvature with non-Gaussian statistics discussed in Section 3.4.

For this calculation, we work in the homogeneous inflationary background, neglecting the effect of metric perturbations on the dynamics of the χ field during inflation. This approximation is valid if $\bar{\rho}_\chi/(\bar{\rho}_\phi + \bar{\rho}_\chi) \ll 1$ and $\delta\rho_\chi/\bar{\rho}_\chi \gg \delta\rho_\phi/\bar{\rho}_\phi$. Here $\bar{\rho}$ denotes the averaged energy density of the corresponding field and $\delta\rho$ its perturbation. These conditions will be satisfied for all model parameters considered in this work that lead to constraints driven by DR isocurvature. Under this approximation, each bubble will expand with spherical symmetry.

The bubble wall dynamics are calculated in detail in Appendix B.1: for the model parameters and approximations under which we are working, within a Hubble time the wall accelerates to a terminal velocity which is close to the speed of light. Given the short acceleration time, we can take the bubble wall velocity to be $v_w \approx 1$ immediately after nucleation. Under this approximation, a bubble that nucleates at time t' has a comoving radius at time t:

$$\begin{aligned} r(t,t') =& \frac{1}{H_{\rm inf} a(t')}\left(1 - \frac{a(t')}{a(t)}\right) + \frac{r_c}{a(t')} \\ \approx& \frac{1}{H_{\rm inf} a(t')}. \end{aligned} \tag{3.8}$$

Here we drop the second term (as $a(t')/a(t)$ decays exponentially with time) and the third term (as $r_c \ll H_{\rm inf}^{-1}$ from Eq. (3.5)). After neglecting these terms, the radius only depends on the nucleation time t' and so we will omit the t argument: writing $r(t,t') \to r(t')$. This means that the bubble will quickly expand to the size of the comoving horizon at the time of nucleation. As the comoving horizon decreases during inflation, the bubble becomes super-horizon soon after nucleation and is fixed in size during the later evolution of the Universe.

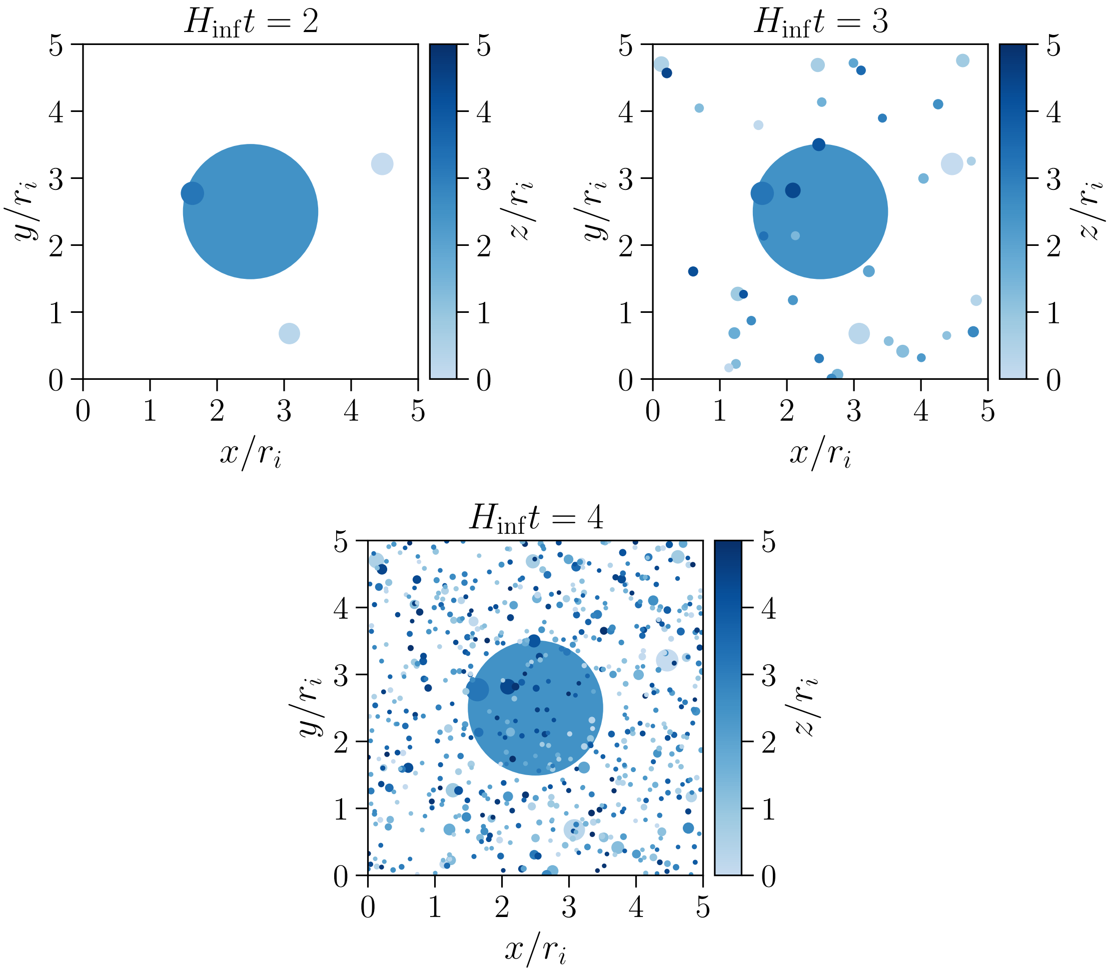

Figure 3.3: Simulated bubble distribution at different times for $\gamma_{\rm PT} = 1 \times 10^{-4}$ within a cube with side-length $5r_i$, centered on the largest (and first) bubble nucleated . r_i is the radius of a bubble nucleated at $t = 0$, when the simulation begins. The bubble distribution is projected to the x-y plane with the colors representing the z coordinate of the center of each bubble.

As the nucleation of bubbles is a stochastic process, the location and time of nucleation events are randomly distributed. Analytically, we can calculate the probability that a point in space remains in the false vacuum at a given time. Without loss of generality, we set $t = 0$ to be the moment when the inflaton rolls past the trigger value of ϕ_i (see Section 3.2.2) and bubbles can start nucleating. For a point $(\mathbf{x}, t)$ to be in false vacuum, a bubble cannot have nucleated at any time $t' < t$ in any location within a sphere of radius $r(t')$ centered at $\mathbf{x}$. In terms of the Hubble-normalized phase transition rate $\gamma_{\mathrm{PT}} \equiv \Gamma_{\mathrm{PT}}/H_{\mathrm{inf}}^4$, the expected number of nucleation events within this region of space-time is

$$\begin{aligned} I(t) =& \frac{4\pi}{3}\Gamma_{\mathrm{PT}} \int_0^t dt' a(t')^3 r(t')^3 \\ =& \frac{4\pi}{3}\gamma_{\mathrm{PT}} H_{\mathrm{inf}} t\,. \end{aligned} \tag{3.9}$$

As a result, the probability of false vacuum at $(\mathbf{x}, t)$ is

$$p_{\mathrm{false}}(t) = e^{-I(t)} = e^{-t/\tau_{\mathrm{PT}}}, \tag{3.10}$$

where

$$\tau_{\mathrm{PT}}^{-1} \equiv \frac{4\pi}{3}\gamma_{\mathrm{PT}} H_{\mathrm{inf}}\,. \tag{3.11}$$

Outside of the bubbles the χ field has an energy density of ΔV, while inside the energy density is zero. Thus, the spatially averaged energy density of the χ field at time t is

$$\bar{\rho}_\chi(t) = \Delta V p_{\mathrm{false}}(t) = \Delta V e^{-t/\tau_{\mathrm{PT}}}. \tag{3.12}$$

We are interested in the scenario where the phase transition remains incomplete when inflation ends at time t_e. This occurs if $t_e/\tau_{\mathrm{PT}} < 1$. In that case, the χ field will have a distribution of mostly non-overlapping bubbles with radii between $r_e \equiv r(t_e)$ and $r_i \equiv r(0)$. In this scenario, we can approximate the energy density of the χ field during inflation as

$$\rho_\chi(\mathbf{x},t) = \Delta V \left[1 - \sum_{I:t_I<t} \Theta(r_I - |\mathbf{x} - \mathbf{x_I}|)\right], \tag{3.13}$$

where $r_I \equiv r(t_I)$ and $\mathbf{x}_I$ are the comoving radius and center location of bubble I, respectively, and the sum runs over all bubbles nucleated before t.

To provide an illustrative example of the time evolution of the distribution of bubbles, we perform a simulation of bubble nucleation for an incomplete FOPT during inflation. We simulate a cubic region of space with comoving volume $(50\, r_i)^3$ and $\gamma_{\rm PT} = 10^{-4}$. We start our simulation at $t = 0$, nucleating bubbles at a rate given by

$$\frac{dN}{dt} = \mathcal{V}_{\rm false}(t) a(t)^3 \Gamma_{\rm PT}, \tag{3.14}$$

where $\mathcal{V}_{\rm false}(t)$ is the volume of space in the false vacuum at t. When a bubble is nucleated, the location of its center is sampled uniformly from the region of space that is in the false vacuum. We show the resulting spatial distribution of bubbles at three different times in Figure 3.3. For illustrative purposes, we show only the $(5r_i)^3$ volume that contains the first (and largest) bubble nucleated in the original volume. The pattern of bubbles shown in Figure 3.3 is only one iteration of the stochastic nucleation process that would be active during inflation. To extract limits from the cosmological data, we must calculate the statistical properties of the inhomogeneities caused by the bubbles.

The observable that captures the inhomogeneous effects of the phase transition at the end of inflation is the density contrast parameter, which is defined as

$$\delta_\chi(\mathbf{x}, t_e) \equiv \frac{\rho_\chi(\mathbf{x}, t_e) - \bar{\rho}_\chi(t_e)}{\bar{\rho}_\chi(t_e)}. \tag{3.15}$$

In Fourier space this is

$$\delta_\chi(\mathbf{k}, t_e) = -e^{t_e/\tau_{\rm PT}} \frac{4\pi}{k^3} \sum_{I:t_I<t_e} e^{-i\mathbf{k}\cdot\mathbf{x_I}} \mathcal{A}(kr_I) + \mathcal{C} \times \delta^3(\mathbf{k}), \tag{3.16}$$

where $\mathcal{A}(y) \equiv \sin y - y\cos y$. We ignore the term proportional to the delta function in Eq. (3.16) in our analysis, as the $\mathbf{k} = 0$ Fourier mode will not contribute to CMB observables with multipoles $\ell > 0$.

The two point function of δ_χ is then given by

$$\begin{aligned} \langle \delta_\chi(\mathbf{k})\delta_\chi(\mathbf{k}')\rangle &= e^{2t_e/\tau_{\rm PT}} \frac{(4\pi)^2}{k'^3 k^3} \\ &\quad \times \sum_{IJ} \langle e^{-i(\mathbf{k}\cdot\mathbf{x_I}+\mathbf{k}'\cdot\mathbf{x_J})} \mathcal{A}(kr_I)\mathcal{A}(k'r_J)\rangle. \end{aligned} \tag{3.17}$$

The double sum can be split into terms where $I = J$ and those where $I \neq J$. We will neglect the terms where $I \neq J$, as their sum is suppressed by a factor $\gamma_{\rm PT}$ relative to the sum over $I = J$ (see Appendix B.2). We can replace the ensemble average of the $I = J$ terms with an integral over bubble coordinates:

$$\langle \delta_\chi(\mathbf{k})\delta_\chi(\mathbf{k}')\rangle = e^{2t_e/\tau_{PT}} \frac{(4\pi)^2}{k^3 k'^3} N \int d^4x\, p_1(x) e^{-i(\mathbf{k}+\mathbf{k}')\cdot\boldsymbol{x}} \mathcal{A}(kr(t))\mathcal{A}(k'r(t))\,. \tag{3.18}$$

Here, $p_1(x)$ is the single-bubble probability distribution function over nucleation coordinates $x = (\mathbf{x}, t)$, and is given by

$$p_1(x) = \frac{1}{\mathcal{V}}\left(\frac{1}{N}\frac{dN}{dt}\right), \tag{3.19}$$

where N is the total number of bubbles nucleated in a comoving volume $\mathcal{V}$ before t_e and dN/dt is given by Eq. (3.14) with

$$\mathcal{V}_{\rm false}(t) = \mathcal{V}p_{\rm false}(t) = \mathcal{V}e^{-t/\tau_{\rm PT}}. \tag{3.20}$$

After performing the $\mathbf{x}$ integral of Eq. (3.18), the two point function can be written in terms of

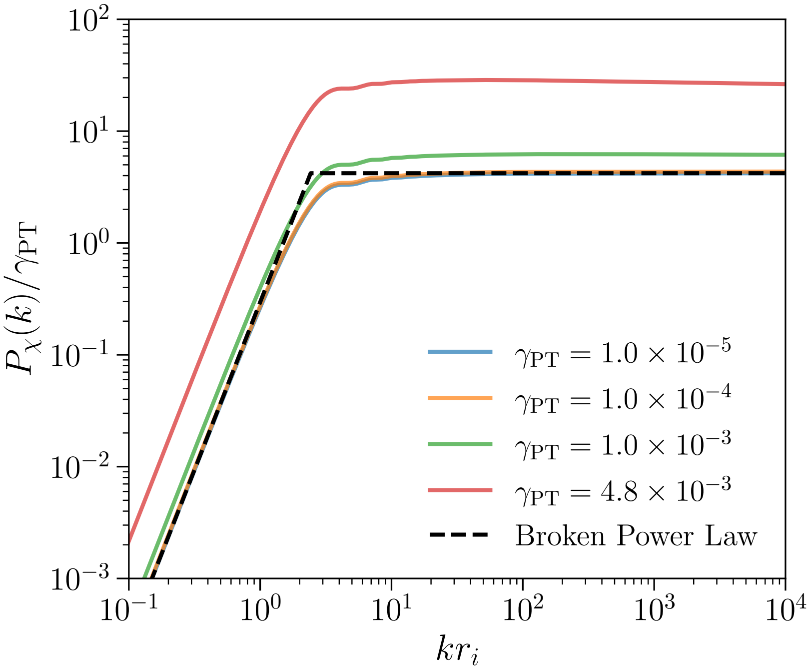

Figure 3.4: Power Spectra of the density contrast of χ normalized by $\gamma_{\rm PT}$ for different values of $\gamma_{\rm PT}$ and $H_{\rm inf}t_e = 50$. The largest value of $\gamma_{\rm PT}$ is chosen such that the incomplete PT condition $4\pi\gamma_{\rm PT}H_{\rm inf}t_e/3 < 1$ is barely satisfied. The dashed line is a broken power law with the same asymptotic behavior as the power spectrum in the limit of $\gamma_{\rm PT}H_{\rm inf}t_e \ll 1$ (see Eq. (3.22)) .

the dimensionless power spectrum $P_\chi(k)$ as

$$\langle \delta_\chi(\mathbf{k})\delta_\chi(\mathbf{k}')\rangle \equiv 2\pi^2 \frac{(2\pi)^3\delta^3(\mathbf{k}+\mathbf{k}')}{k^3} P_\chi(k). \tag{3.21}$$

where

$$\begin{aligned} P_\chi(k) &= 8\gamma_{\rm PT} e^{(8\pi\gamma_{\rm PT}H_{\rm inf}t_e)/3}(kr_i)^{-4\pi\gamma_{\rm PT}/3} \\ &\quad \times \int\limits_{kr_e}^{kr_i} du\, u^{-4+4\pi\gamma_{\rm PT}/3}\mathcal{A}(u)^2 \qquad (3.22) \\ &\approx \gamma_{\rm PT} \begin{cases} \frac{8}{27}(kr_i)^3 & kr_i \ll 1 \\ 4.2 & kr_i \gg 1 \end{cases} \end{aligned}$$

to leading order of $\gamma_{\rm PT}$ in the limit $\gamma_{\rm PT}H_{\rm inf}t_e \ll 1$. The result for small kr_i is calculated analytically by Taylor-expanding the integrand and the result for large kr_i is found by numerically calculating the limit as $kr_i \to \infty$.[7] As there are no bubbles larger than r_i, the k^3 dependence when $kr_i \ll 1$ is a consequence of the fact that the two-point function of δ_χ is constant for modes larger than r_i. The flat power spectrum when $kr_i \gg 1$ can be understood as follows: when the nucleation rate is low, the majority of the Universe is in the false vacuum at all times $0 < t < t_e$, and thus the rate of bubble nucleation in any physical volume of fixed size is the same at all times resulting in a scale invariant distribution of bubbles. In Figure 3.4, we show numerical results for the power spectrum as a function of k for various values of $\gamma_{\rm PT}$ along with a broken power law with the same asymptotic behavior as Eq. (3.22). The broken power law provides a good approximation to the power spectrum provided $\gamma_{\rm PT}H_{\rm inf}t_e \ll 1$. Therefore, assuming $H_{\rm inf}t_e \sim 50$, the approximation is valid for $\gamma_{\rm PT} \lesssim 10^{-3}$.

---

[7] We numerically integrate Eq. (3.22) for a series of values of kr_i until the integral converges to a constant asymptotic value at 1% precision.

3.4 Imprints of a non-thermal FOPT

After inflation and reheating, we assume the Universe is radiation dominated. As the Hubble parameter drops as $\propto T^2$, $\Gamma_{\rm PT}/H(T)^4$ will increase rapidly and reach unity at the nucleation temperature T_*, when the phase transition completes. We assume the energy density in the χ field will be converted to DR at T_* by couplings between DR and the χ field. As a result, the DR will inherit the χ field's inhomogeneities, which, on large scales, follow the stochastic distribution of bubbles nucleated during inflation. This process will generate a relative entropy perturbation between DR and photons as well as a curvature perturbation which is distinct from the curvature perturbation produced by quantum fluctuations of the inflaton. The relative entropy perturbation will contribute to the DR isocurvature mode, while both curvature perturbations will contribute to the adiabatic mode. The isocurvature mode also has a non-negligible 3-point function and therefore has non-Gaussian statistics.

We begin this section by calculating the angular power spectrum of CMB temperature anisotropies in terms of the adiabatic and isocurvature power spectra. We then identify the super-horizon initial conditions for the DR isocurvature and adiabatic modes and calculate the power spectra. We show in Appendix B.3 that – for the class of models considered in this work – the FOPT-induced curvature [108] has a negligible impact on cosmological observables compared to the DR isocurvature. The DR isocurvature therefore sets the relevant constraints on these models of FOPTs. Finally, we calculate the isocurvature bispectrum from the non-Gaussian statistics.

In the synchronous gauge, the perturbed FRW metric is written as

$$ds^2 = a(\tau)^2 \left[-d\tau^2 + (\delta_{ij} + h_{ij})dx^i dx^j\right], \tag{3.23}$$

where τ is the conformal time.[8] The metric perturbation h_{ij} can be written in Fourier space as

$$h_{ij}(\mathbf{k},\tau) = \left[\hat{k}_i\hat{k}_j h(\mathbf{k},\tau) + \left(\hat{k}_i\hat{k}_j - \frac{1}{3}\delta_{ij}\right) 6\eta(\mathbf{k},\tau)\right], \tag{3.24}$$

where h and η denote the trace and traceless longitudinal part of h_{ij} respectively.

In general, we can split a perturbation $X \in \{h, \eta, \delta_a, \theta_a, \sigma_a, ...\}$ into a sum of isocurvature and adiabatic modes. Here δ_a, θ_a, and σ_a correspond to the $\ell = 0, 1$, and 2 moments of the phase-space perturbation of species a. In particular, $\delta \equiv \delta\rho/\bar{\rho}$. For radiation species, moments $\ell > 2$ are needed, and it is useful to define $F_{a,\ell}$ as the ℓ^{th} moment of the phase-space perturbation of relativistic species a.

For the FOPT we study in this paper, there are two linearly independent modes: the adiabatic mode that contains the curvature perturbation, and the isocurvature mode that contains the relative entropy perturbation. Therefore each perturbation variable can be written as a sum over these two modes using the decomposition

$$X(\mathbf{k},\tau) = c^{\text{ad}}(\mathbf{k})X^{\text{ad}}(k,\tau) + c^{\text{iso}}(\mathbf{k})X^{\text{iso}}(k,\tau). \tag{3.25}$$

Here $c^A(\mathbf{k})$ is a time-independent coefficient (where $A \in \{\text{ad}, \text{iso}\}$) which is common for all perturbation variables, and $X^A(k,\tau)$ is perturbation-specific but independent of the direction $\hat{\mathbf{k}}$. The initial conditions for the modes of $X^A(k,\tau)$ are obtained by solving the Boltzmann and Einstein equations in the super-horizon limit $(k\tau \ll 1)$.

The initial conditions for the adiabatic mode with DR are a straightforward extension of the adiabatic initial conditions for radiation in the standard cosmology [232]: for example, $\delta^{\text{ad}}_{\text{dr}} = \delta^{\text{ad}}_{\gamma} = \delta^{\text{ad}}_{\nu}$. The initial conditions for the DR isocurvature mode can be derived in analogy to neutrino density isocurvature [122]. As in the standard procedure, we choose a basis such that $\sum_a \delta\rho^{\text{iso}}_a = 0$, where the sum runs over the isocurvature energy density perturbations of all radiation species

---

[8] While it was natural to use physical time t during inflation, the initial conditions for CLASS are most conveniently written in terms of τ. Therefore, all functions that directly enter the CLASS calculation will be written in terms of τ rather than t.

($a = \gamma$, ν, dr). This ensures that the total energy density of radiation in the isocurvature mode is homogeneous at the initial time $\tau \to 0$ in the radiation-dominated Universe and thus does not source curvature. Since there is no isocurvature in neutrinos in our models, their density perturbations are equal to that of photons ($\delta_\gamma^{\mathrm{iso}} = \delta_\nu^{\mathrm{iso}}$). We also choose the normalization such that $\delta_{\mathrm{dr}}^{\mathrm{iso}} = 1$ when $k\tau \to 0$. These requirements fix the initial conditions for the DR isocurvature mode:

$$\delta_{\mathrm{dr}}^{\mathrm{iso}} = 1\ ,\ \delta_\gamma^{\mathrm{iso}} = \delta_\nu^{\mathrm{iso}} = \frac{-R_{\mathrm{dr}}}{1 - R_{\mathrm{dr}}} \quad (k\tau \to 0), \tag{3.26}$$

where $R_{\mathrm{dr}} \equiv \bar{\rho}_{\mathrm{dr}}/(\bar{\rho}_\gamma + \bar{\rho}_\nu + \bar{\rho}_{\mathrm{dr}})$. To be concrete, we treat DR as free-streaming in this paper. The complete initial conditions for the free-streaming DR isocurvature mode in the synchronous gauge are given in Appendix B.4. Notably, in the limit $R_{\mathrm{dr}} \ll 1$, all moments of the photon and neutrino phase-space perturbations in the isocurvature mode ($F_{\gamma,\ell}^{\mathrm{iso}}$ and $F_{\nu,\ell}^{\mathrm{iso}}$) are proportional to R_{dr}, which can be seen based on their initial conditions and time evolution controlled by the coupled Boltzmann hierarchy and Einstein equations.

The coefficients $c^A(\mathbf{k}) = \{c^{\mathrm{ad}}(\mathbf{k}), c^{\mathrm{iso}}(\mathbf{k})\}$ encode the initial random configuration of each mode. For the FOPT models of interest, the modes are approximately uncorrelated so the statistics of Gaussian observables are determined by

$$\langle c^A(\mathbf{k}) c^A(\mathbf{k}') \rangle = 2\pi^2 \frac{(2\pi)^3 \delta^3(\mathbf{k} + \mathbf{k}')}{k^3} P_A(k), \tag{3.27}$$

where $P_A(k) = \{P_{\mathrm{ad}}(k), P_{\mathrm{iso}}(k)\}$ are the power spectra of the adiabatic and isocurvature modes.

One relevant observable in the CMB is the photon temperature anisotropy $\Delta \equiv \Delta T/\bar{T}$, which can be written in a Fourier-Legendre series as

$$\Delta(\mathbf{x}, \hat{\mathbf{n}}, \tau) = \sum_{\ell=0}^{\infty} (-i)^\ell (2\ell + 1) \int \frac{d^3k}{(2\pi)^3} e^{i\mathbf{k}\cdot\mathbf{x}} \Delta_\ell(\mathbf{k}, \tau) P_\ell(\hat{\mathbf{k}} \cdot \hat{\mathbf{n}}), \tag{3.28}$$

where $\hat{\mathbf{n}}$ is the direction of the momentum and Δ_ℓ is proportional to the multipole moment of the photon phase-space density perturbation $\Delta_\ell = F_{\gamma,\ell}/4$. Its angular two-point function is

$$\langle \Delta(\mathbf{x}, \hat{\mathbf{n}}, \tau_0) \Delta(\mathbf{x}, \hat{\mathbf{n}}', \tau_0) \rangle = \frac{1}{4\pi} \sum_\ell (2\ell + 1) C_\ell^{TT} P_\ell(\hat{\mathbf{n}} \cdot \hat{\mathbf{n}}'). \tag{3.29}$$

Here C_ℓ^{TT} is the temperature anisotropy angular power spectrum:

$$\begin{aligned} C_\ell^{TT} = 4\pi \int d(\ln k) \, \big(& P_{\rm ad}(k) |\Delta_\ell^{\rm ad}(k, \tau_0)|^2 + \\ & P_{\rm iso}(k) |\Delta_\ell^{\rm iso}(k, \tau_0)|^2 \big) \, . \end{aligned} \tag{3.30}$$

In this expression, $\Delta_\ell^A(k, \tau)$ is the photon transfer function, which is obtained by solving the Boltzmann and Einstein equations for $F_{\gamma,\ell}^A(k, \tau)$ with the initial conditions for mode $A = \{\text{ad}, \text{iso}\}$. The dependence on the particle physics models is therefore encapsulated in $P_{\rm ad}(k)$ and $P_{\rm iso}(k)$.

We focus on a class of models for which the contribution of the FOPT to $P_{\rm ad}(k)$ is small compared to the adiabatic modes arising from inflation (see Appendix B.3). For this class of models, the dominant effects on CMB observables is from $P_{\rm iso}(k)$ so we can set $P_{\rm ad}(k)$ to be the standard ΛCDM adiabatic power spectrum

$$P_{\rm ad}(k) = A_s \left(\frac{k}{k_{\rm pivot}} \right)^{n_s - 1}, \tag{3.31}$$

where A_s and n_s are the scalar amplitude and spectral index. $k_{\rm pivot}$ is the pivot scale, conventionally defined as $k_{\rm pivot} \equiv 0.05\,\text{Mpc}^{-1}$ [18]. The photon transfer function in the isocurvature mode scales as $\Delta_\ell^{\rm iso} = \frac{1}{4} F_{\gamma,\ell}^{\rm iso} \propto R_{\rm dr}$ for $R_{\rm dr} \ll 1$ (see the discussion below Eq. (3.26)). Therefore, the effect of isocurvature on the angular power spectrum is determined by $R_{\rm dr}^2 P_{\rm iso}(k)$. This behavior will be manifest in our results.

3.4.1 Isocurvature

To obtain $P_{\rm iso}(k)$ in Eq. (3.30), we consider the gauge-invariant relative entropy perturbation between the DR and the photons:

$$\mathcal{S}_{\rm dr,\gamma} \equiv -3\mathcal{H}\left(\frac{\delta\rho_{\rm dr}}{\rho'_{\rm dr}} - \frac{\delta\rho_\gamma}{\rho'_\gamma}\right). \tag{3.32}$$

Here $'$ denotes $\partial/\partial\tau$, and $\mathcal{H} = aH$ is the conformal Hubble parameter. With the definition in Eq. (3.25) and the isocurvature mode relations in Eq. (3.26), as $k\tau \to 0$ this reduces to

$$\mathcal{S}_{\rm dr,\gamma} = \frac{3}{4}\frac{c^{\rm iso}(\mathbf{k})}{1 - R_{\rm dr}}. \tag{3.33}$$

Therefore, the isocurvature power spectrum $P_{\rm iso}$ can be directly related to $\langle \mathcal{S}_{\rm dr,\gamma}\, \mathcal{S}_{\rm dr,\gamma}\rangle$.

To calculate $\mathcal{S}_{\rm dr,\gamma}$, we first determine the relations between $\delta_{\rm dr}$ and δ_χ. As the DR we are interested in was generated by rapid bubble percolation around a temperature T_* (given by $H(T_*)^4 = \Gamma_{\rm PT}$), we can assume an instantaneous transfer of energy from the χ field into DR when the temperature of the Universe reaches T_*. We therefore work in the gauge where the temperature of the Universe is uniform just before the phase transition completes. This can be achieved by the following gauge transformation:

$$\delta\tau(\mathbf{x},\tau) = -\frac{\delta\rho_{\rm SM}}{\rho'_{\rm SM}}, \tag{3.34}$$

where SM means a total over particle species in the Standard Model. In this gauge, the standard model density perturbation (defined as $\delta\hat{\rho}_{\rm SM} \equiv \delta\rho_{\rm SM} + \rho'_{\rm SM}\,\delta\tau$) vanishes and the density perturbation of χ remains approximately unchanged ($\delta\hat{\rho}_\chi \approx \delta\rho_\chi$).

Since the temperature is uniform in the new gauge, the phase transition completes at the same time τ_* everywhere and the large-scale perturbations (super-horizon at T_*) in $\hat{\rho}_\chi$ will be directly converted to those in $\hat{\rho}_{\rm dr}$. The sub-horizon perturbations of DR around T_* are more complicated, and depend on the dynamics of the FOPT. However, as we are only interested in modes that are accessible to CMB, we can safely neglect contributions from sub-horizon dynamics at T_*, assuming

$T_* \gg T_{\rm CMB}$. In this paper, we can therefore approximate

$$\hat{\delta}_{\rm dr}(\mathbf{k}, \tau_*) \approx \delta_\chi(\mathbf{k}, t_*) \approx \delta_\chi(\mathbf{k}, t_e), \tag{3.35}$$

where $t = t_*$ when the phase transition completes (at proper time τ_*). The last approximation in Eq. (3.35) holds because bubbles nucleated at times $t \in [t_e, t_*]$ have radii that are subhorizon at T_*.

The Standard Model density perturbations prior to the end of the FOPT are generated from inflaton fluctuations and thus are all adiabatic, satisfying

$$\frac{\delta\rho_a}{\rho'_a} = \frac{\delta\rho_{\rm SM}}{\rho'_{\rm SM}} \tag{3.36}$$

for any standard model particle species a. Therefore density perturbations of each individual Standard Model species vanish in the new gauge as well ($\delta\hat{\rho}_a = 0$) and the relative entropy perturbation is simply

$$\mathcal{S}_{{\rm dr},\gamma} = \frac{3}{4}\hat{\delta}_{\rm dr}. \tag{3.37}$$

As $\mathcal{S}_{{\rm dr},\gamma}$ is gauge invariant, we can directly relate Eq. (3.33) and Eq. (3.37). Together with Eq. (3.35), we find

$$c^{\rm iso}(\mathbf{k}) \approx (1 - R_{\rm dr})\delta_\chi(\mathbf{k}, \tau_e). \tag{3.38}$$

Therefore, $P_{\rm iso}$ is proportional to P_χ:

$$P_{\rm iso}(k) \approx (1 - R_{\rm dr})^2 P_\chi(k). \tag{3.39}$$

As P_χ exhibits the broken power law behavior in Eq. (3.22), for the remainder of our work, we take P_{iso} as

$$P_{\text{iso}}(k) = f_{\text{iso}}^2 A_s \begin{cases} (k/k_i)^3 & k \leq k_i \\ 1 & k > k_i \end{cases} , \tag{3.40}$$

where A_s is the amplitude of the scalar curvature power spectrum and f_{iso} is a coefficient that sets the amplitude of the isocurvature power spectrum. In our model, $f_{\text{iso}}^2 A_s \approx 4.2\gamma_{\text{PT}}$. We note that we use k_i as the scale of the transition of the broken power law, which is related to r_i^{-1} by an $\mathcal{O}(1)$ factor.

3.4.2 Non-Gaussianity

The perturbations generated by the FOPT have non-Gaussian statistics that may be observable in the CMB. The CMB power spectra discussed before are based on two-point functions, which only contain Gaussian information. To quantify non-Gaussianity in the CMB, we need to examine higher point functions of the photon temperature anisotropy Δ. One example is the three-point function, which comes predominantly from the isocurvature mode for the models considered, given by

$$\begin{aligned} \langle \Delta(\hat{\mathbf{n}}_1)\Delta(\hat{\mathbf{n}}_2)\Delta(\hat{\mathbf{n}}_3)\rangle = \left(\frac{20}{3}\right)^3 & \sum_{\ell_1,\ell_2,\ell_3} (2\ell_1+1)(2\ell_2+1)(2\ell_3+1)(-i)^{\ell_1+\ell_2+\ell_3} \\ & \times \int \frac{d^3k_1}{(2\pi)^3} \int \frac{d^3k_2}{(2\pi)^3} \int \frac{d^3k_3}{(2\pi)^3} (2\pi)^3 \delta^3(\mathbf{k_1}+\mathbf{k_2}+\mathbf{k_3}) \\ & \times P_{\ell_1}(\hat{\mathbf{k}}_1 \cdot \hat{\mathbf{n}}_1) P_{\ell_2}(\hat{\mathbf{k}}_2 \cdot \hat{\mathbf{n}}_2) P_{\ell_3}(\hat{\mathbf{k}}_3 \cdot \hat{\mathbf{n}}_3) \\ & \times B_{\text{iso}}(k_1,k_2,k_3) \Delta_{\ell_1}^{\text{iso}}(k_1,\tau_0) \Delta_{\ell_2}^{\text{iso}}(k_2,\tau_0) \Delta_{\ell_3}^{\text{iso}}(k_3,\tau_0). \end{aligned} \tag{3.41}$$

We have introduced the isocurvature bispectrum B_{iso}, which we define using the convention [224]:

$$\begin{aligned} & \langle c^{\text{iso}}(\mathbf{k_1}) c^{\text{iso}}(\mathbf{k_2}) c^{\text{iso}}(\mathbf{k_3})\rangle \\ & \equiv (2\pi)^3 \delta^3(\mathbf{k_1}+\mathbf{k_2}+\mathbf{k_3}) \left(\frac{20}{3}\right)^3 B_{\text{iso}}(k_1,k_2,k_3). \end{aligned} \tag{3.42}$$

To calculate the bispectrum for our model, we use Eq. (3.38) to relate $c^{\rm iso}(\mathbf{k})$ to $\delta_\chi(\mathbf{k}, t_e)$ and perform steps similar to those for the calculation of P_χ, leading to

$$\begin{aligned} B_{\rm iso}(k_1, k_2, k_3) = &-\left(\frac{3\pi}{5}\right)^3 (1-R_{\rm dr})^3 e^{4\pi\gamma_{\rm PT} H_{\rm inf} t_e} \frac{\gamma_{\rm PT}}{k_1^3 k_2^3} \\ &\times \int\limits_{k_3 r_e}^{k_3 r_i} du u^{-4} \mathcal{A}(\alpha_1 u)\mathcal{A}(\alpha_2 u)\mathcal{A}(u), \end{aligned} \tag{3.43}$$

where $\alpha_1 \equiv k_1/k_3$, $\alpha_2 \equiv k_2/k_3$, and $\mathcal{A}(u)$ is defined below Eq. (3.16). In Section 3.7.3 we will estimate constraints by comparing this result to the equilateral and local bispectra which have been studied in the literature [224]. To simplify the comparison, we will write down expressions for $B_{\rm iso}$ evaluated at wavenumbers in the squeezed $k_1 \ll k_2 \approx k_3$) and equilateral ($k_1 \approx k_2 \approx k_3$) configurations. For $R_{\rm dr} \ll 1$ and $\gamma_{\rm PT} H_{\rm inf} t_e \ll 1$ these expressions are

$$\begin{aligned} B_{\rm iso}(k_1, k, k) = &-\left(\frac{3\pi}{5}\right)^3 \frac{\gamma_{\rm PT}}{k^6} \\ &\times \begin{cases} \frac{1}{3}\int_0^{kr_i} du u^{-1}\mathcal{A}(u)^2 & k_1 \ll k \\ \int_0^{kr_i} du u^{-4}\mathcal{A}(u)^3 & k_1 = k \end{cases} . \end{aligned} \tag{3.44}$$

Restricting to the case where $kr_i \gg 1$, the asymptotic behavior of the integrals in these expressions is

$$\begin{aligned} \frac{1}{3}\int\limits_0^{kr_i} du u^{-1}\mathcal{A}(u)^2 &\propto (kr_i)^2 \\ \int\limits_0^{kr_i} du u^{-4}\mathcal{A}(u)^3 &\propto \text{constant}, \end{aligned} \tag{3.45}$$

so

$$B_{\rm iso}(k_1, k, k) \propto \begin{cases} k^{-4} & k_1 \ll k \\ k^{-6} & k_1 = k \end{cases} . \tag{3.46}$$

3.5 Effects on CMB observations

In the previous section, we have calculated the DR isocurvature power spectrum from non-thermal FOPTs. In this section, we implement the model in CLASS, and simulate the CMB angular power spectra. As mentioned before, we can approximate the adiabatic power spectrum as unchanged compared to the standard ΛCDM model. The presence of ree-streaming DR (parameterized by ΔN_{eff}) shifts CMB observables as a result of the change in the background energy density – such shifts create the standard limit on $\Delta N_{\text{eff}} \lesssim 0.3$. In addition, DR isocurvature creates additional shifts in CMB observables which are the main focus of this work.

As explained in the introduction to Section 3.4, the effect of DR isocurvature on the CMB depends on $R_{\text{dr}}^2 P_{\text{iso}}(k)$. To simplify comparisons with limits on DR with adiabatic perturbations, we write R_{dr} in terms of the equivalent number of effective neutrino species, $\Delta N_{\text{eff}} \equiv 3.044 \times (\bar{\rho}_{\text{dr}}/\bar{\rho}_\nu)$. Around photon decoupling, $R_{\text{dr}} \approx 0.13 \times \Delta N_{\text{eff}}$. The isocurvature power spectrum (defined in Eq. (3.40)) depends on two additional parameters: f_{iso} determines the amplitude, and k_i is the wavenumber at which the broken power law transitions. This transition wavenumber also corresponds to the comoving scale at the start of the FOPT. Given the form of P_{iso}, the effect of DR isocurvature on the CMB is proportional to $\Delta N_{\text{eff}}^2 f_{\text{iso}}^2$ for fixed k_i. We express k_i in terms of multiples of $k_{\text{pivot}} \equiv 0.05\,\text{Mpc}^{-1}$, the pivot scale of the adiabatic power spectrum given in Eq. (3.31).

To show the effects of DR isocurvature on the CMB observables, we simulate the CMB power spectra with difference choices of k_i, and compare them to the case with purely adiabatic initial conditions. In Figure 3.5, we show the difference of the temperature angular power spectrum C_ℓ^{TT} between ΛCDM and three models with DR, all with $\Delta N_{\text{eff}} = 0.1$. In one case, we consider only the adiabatic effects of DR (setting $f_{\text{iso}} = 0$). In the other two we include isocurvature with $k_i = k_{\text{pivot}}$ and $0.1\,k_{\text{pivot}}$ (with $f_{\text{iso}} = 10$ in both cases). The acoustic peaks in models with isocurvature shift towards higher ℓ as compared to the adiabatic case with the same ΔN_{eff}. This result is consistent with the literature (see for example [129]). In Figure 3.6, we show the fractional difference of

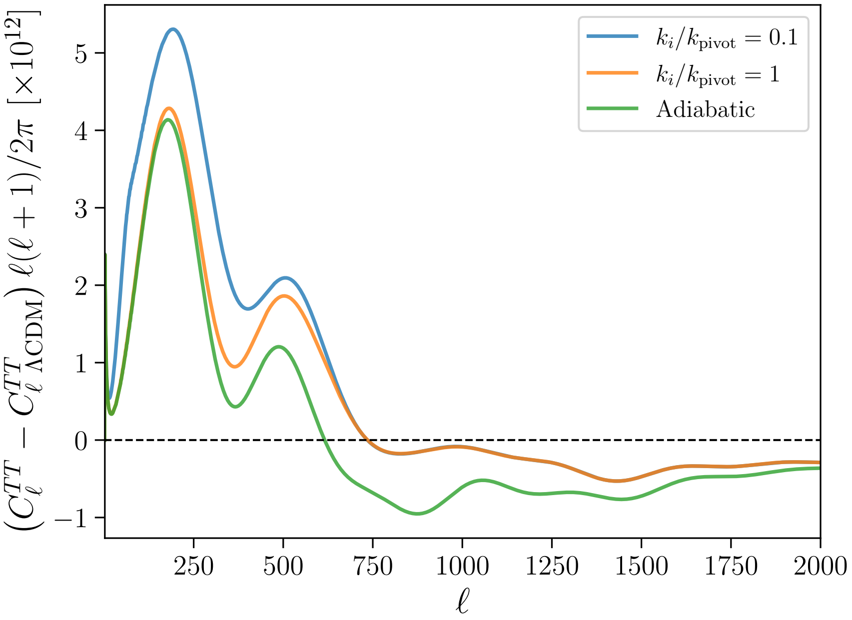

Figure 3.5: The difference of temperature anisotropy angular power spectra between cases with dark radiation ($\Delta N_{\mathrm{eff}} = 0.1$) and the ΛCDM model. The blue and orange lines denote DR isocurvature with different k_i and fixed $f_{\mathrm{iso}} = 10$. The green line shows the result with adiabatic initial conditions. The pivot scale is chosen to be $k_{\mathrm{pivot}} = 0.05\,\mathrm{Mpc}^{-1}$.

angular power spectra between the DR isocurvature and adiabatic cases (again holding $\Delta N_{\mathrm{eff}} = 0.1$) for the TT (left) and EE (right) modes. For the DR isocurvature simulations again we fix $f_{\mathrm{iso}} = 10$ and vary k_i. The oscillations seen in both panels are a consequence of the shift in the acoustic peaks due to isocurvature, as discussed.

For all DR isocurvature models shown in Figures 3.5 and 3.6, differences between the CMB power spectra disappear at large ℓ. This occurs because CMB spherical harmonics with $\ell \gtrsim \ell_i \sim k_i d_{\mathrm{SLS}}$ mostly receive contributions from wavenumbers $k \gtrsim k_i$, where the isocurvature power spectrum is flat and independent of k_i. Here $d_{\mathrm{SLS}} \sim 10^4\,\mathrm{Mpc}$ is the comoving distance to the surface of last scattering.[9] For $k_i \lesssim 2\times 10^{-3}\,k_{\mathrm{pivot}}$, the corresponding transition spherical harmonic is $\ell_i \lesssim 1$ and the entire CMB angular power spectrum can only probe the plateau of the DR isocurvature power spectrum. For such k_i, the effect of DR isocurvature saturates and the CMB becomes insensitive to further reductions in k_i.

---

[9] Thus, for $k_i = k_{\mathrm{pivot}}$, $\ell_i \sim 500$.

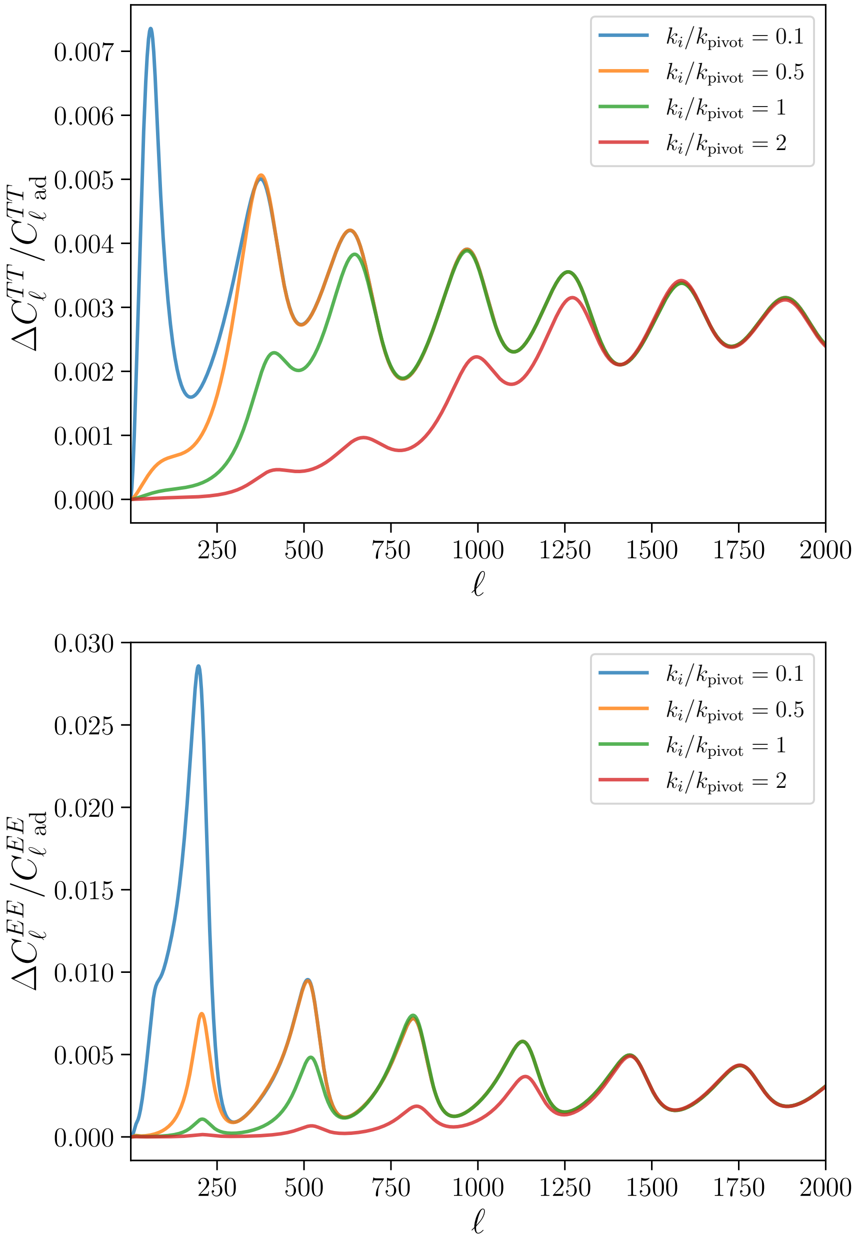

Figure 3.6: The fractional difference of CMB power spectra (C_ℓ^{TT} in the left panel, C_ℓ^{EE} in the right panel) between cases with dark radiation isocurvature and adiabatic initial conditions for different k_i. We set $f_{\rm iso} = 10$ for DR isocurvature, while $\Delta N_{\rm eff} = 0.1$ for both adiabatic and isocurvature cases. The pivot scale is chosen to be $k_{\rm pivot} = 0.05\,\text{Mpc}^{-1}$.

3.6 Methodology and Data Sets

To evaluate the cosmological constraints on the FOPT model parameters, we perform a full likelihood analysis using cosmological datasets. To compute the observables within these datasets, we employ a modified version of the `CLASS` code [128, 112] along with `MontePython` [233, 131] to perform the MCMC analysis.

We use the datasets from the following experiments to set limits on the FOPT model:

- Planck 2018 high-ℓ TTTEEE and low-ℓ TT, EE anisotropy angular power spectra and the gravitational lensing data [18].
- The BAO measurements from the Six-degree Field Galaxy Survey (6dFGS) [19], the Sloan Digital Sky Survey (SDSS) DR7 MGS [20], and the LOWZ galaxy samples of BOSS DR12 [21].

Our baseline cosmology consists of the usual six cosmological parameters of ΛCDM. To this, we add the three isocurvature parameters discussed previously: ΔN_{eff}, k_i, f_{iso}. We assume three active neutrinos species, one with mass $0.06\,\text{eV}$ and two massless. As explained in Section 3.5, the effects of DR isocurvature are sensitive to the product $\Delta N_{\text{eff}} f_{\text{iso}}$ while the effects of the background cosmology are sensitive to ΔN_{eff}. It is also convenient to express the transition wavenumber k_i in terms of the CMB pivot wavenumber k_{pivot}. Therefore we use ΔN_{eff}, k_i/k_{pivot} and $\Delta N_{\text{eff}} f_{\text{iso}}$ as the primary parameters for our MCMC runs with a log-flat prior for each parameter. The boundaries of these priors are: $\log_{10}(\Delta N_{\text{eff}}) \in [-5, -0.3]$, $\log_{10}(k_i/k_{\text{pivot}}) \in [-4, 3]$ and $\log_{10}(\Delta N_{\text{eff}} f_{\text{iso}}) \in [-2.3, 2.3]$. The ΛCDM parameters have standard wide flat priors. The FOPT isocurvature power spectrum of our simplified model (calculated in Section 3.4.1) is a good approximation provided $\gamma_{\text{PT}} \lesssim 10^{-3}$. Therefore, the particular FOPT model studied in this work maps onto the priors used in the likelihood analysis for $f_{\text{iso}} \lesssim 10^3$. We note that our cosmological model and priors are sufficiently general that other isocurvature generation mechanisms may lead to cosmologies that map onto subsets of our parameter space. With this in mind, we show the resulting posteriors for f_{iso} outside of the strict domain of validity for this class of FOPTs.

We use the Metropolis-Hastings algorithm with the Gelman-Rubin convergence criterion $R - 1 < 0.02$ [234] for the MCMC chains. To analyze MCMC chains and calculate Bayesian posteriors, we use the `GetDist` package [235]. The best-fit values are obtained using simulated annealing for the minimization of χ^2 values [236]. The procedure of simulated annealing systematically lowers the temperature during an MCMC chain run, effectively navigating and optimizing against noisy likelihood functions with numerous local maxima.

3.7 Results

Having discussed our theoretical and statistical methodology as well as the datasets that we use in our analysis, we are ready to calculate posteriors for the parameters of DR isocurvature model. The mean and best-fit values of each parameter in our fit are shown in Table 3.1. The posterior distributions (65% and 95% CL) for these new physics parameters are shown in Figure 3.7. The limits on $\Delta N_{\rm eff} f_{\rm iso}$ become approximately independent of $\Delta N_{\rm eff}$ for $\Delta N_{\rm eff} \ll 0.1$ and are also independent of k_i for $k_i \ll k_{\rm pivot}$.

As seen in Table 3.1, there is a slight preference (compared to ΛCDM) in the data for non-zero isocurvature, with best-fit parameters $k_i/k_{\rm pivot} = 0.36$, $\Delta N_{\rm eff} = 7.5 \times 10^{-3}$, and $\Delta N_{\rm eff} f_{\rm iso} = 1.58$. We show in Figure 3.8 the fractional difference in C_ℓ^{TT} between this best-fit model and the best-fit ΛCDM model compared to the Planck 2018 residuals (also normalized to the ΛCDM result). We also show the fractional difference compared to ΛCDM of an adiabatic-only model with the same parameters as the DR isocurvature best-fit other than setting $f_{\rm iso} = 0$.

To better understand the features of our posteriors, it is useful to hold one of the three new physics parameters fixed and consider posteriors over the other two. We do this in the next two subsections, holding $f_{\rm iso}$ fixed in Section 3.7.1 and k_i fixed in Section 3.7.2. Finally, we estimate limits from non-Gaussianities in Section 3.7.3, though a dedicated search is needed to derive a robust bound.

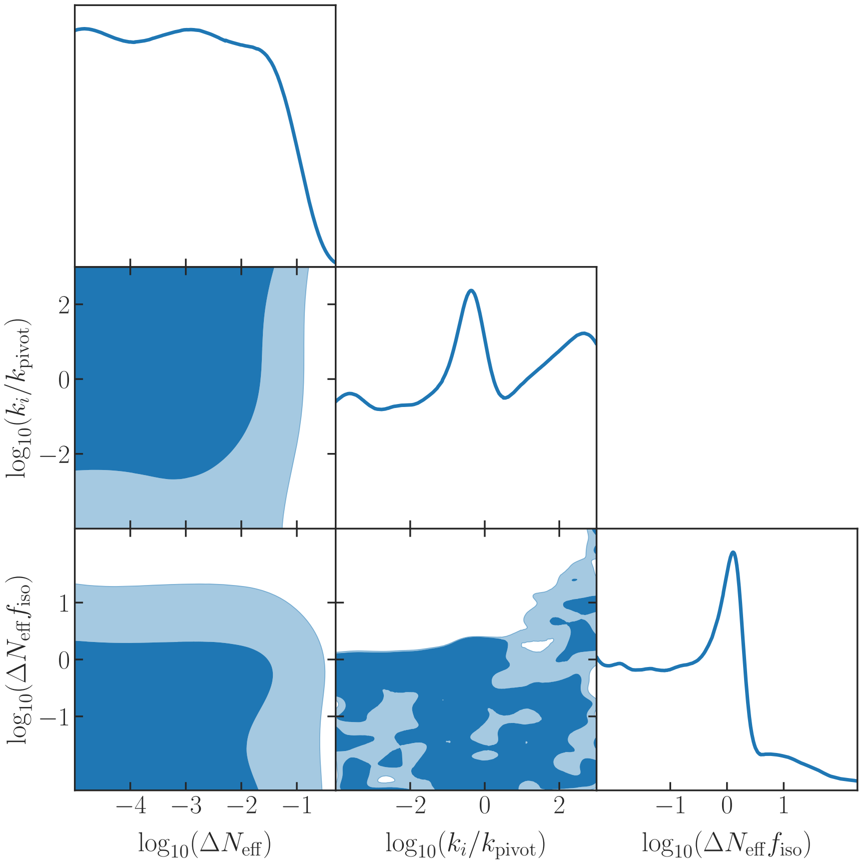

Figure 3.7: The two dimensional marginalized posterior distributions for the FOPT new physics parameters $\Delta N_{\rm eff}$, $\Delta N_{\rm eff} f_{\rm iso}$ and $k_i/k_{\rm pivot}$, when analyzing Planck+BAO (see text for details). We omit the posteriors of the six ΛCDM parameters for clarity.

Parameters	FOPT
$\Omega_{\rm b}h^2$	$0.0225\ (0.0223 \pm 0.0002)$
$\Omega_{\rm c}h^2$	$0.1199\ (0.01954 \pm 0.0011)$
$100 * \theta_s$	$1.0421\ (1.0420 \pm 0.0003)$
$\ln(10^{10}A_s)$	$3.0459\ (3.0474 \pm 0.0146)$
n_s	$0.9678\ (0.9679 \pm 0.0398)$
$\tau_{\rm reio}$	$0.0580\ (0.0564 \pm 0.0073)$
$\log_{10}(\Delta N_{\rm eff})$	$-2.1244\ (< -1.0741)$
$\log_{10}(k_i/k_{\rm pivot})$	-0.4496 (unconstrained)
$\log_{10}(\Delta N_{\rm eff} f_{\rm iso})$	$0.1974\ (< 1.1453)$
$\Delta\chi^2_{\rm tot}$	-0.68

Table 3.1: The best-fit parameters of the FOPT isocurvature model resulting from fits to the Planck+BAO datasets. The mean and 1σ variation for each parameter when fit to the data are shown in parenthesis or the 95% CL upper bound.

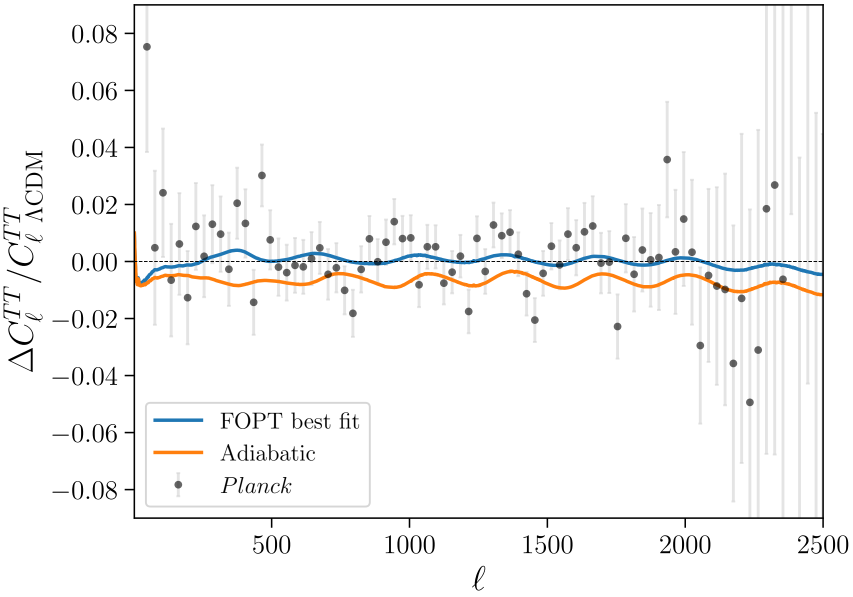

Figure 3.8: The change (relative to ΛCDM) in C_ℓ^{TT} power spectrum normalized to $C_{\ell,\Lambda\mathrm{CDM}}^{TT}$ for the FOPT best-fit model (see Table 3.1), an adiabatic model and the Planck 2018 data [18]. For the adiabatic case we use the same parameters as in the FOPT best-fit except we turn off isocurvature ($f_{\mathrm{iso}} = 0$).

3.7.1 ΔN_{eff} constraints with fixed f_{iso}

In this subsection, we fix f_{iso} and perform the scan over ΔN_{eff}, k_i and the other six ΛCDM parameters. This corresponds to a scenario where the phase transition rate $\gamma_{\mathrm{PT}} \sim f_{\mathrm{iso}}^2 A_s$ is held fixed while the horizon size at the beginning of the transition $r_i \sim k_i^{-1}$ varies. In Figure 3.9, we show posteriors for this scan for three values of f_{iso}: 10, 500 and 1000.

For the largest two values of f_{iso} we find that the 2σ contours approach the adiabatic constraint $\Delta N_{\mathrm{eff}} < 0.3$ for large k_i. This is expected as the DR isocurvature power spectrum modifies the CMB power spectrum primarily at ℓ above the range currently probed by Planck when $k_i \gtrsim 10^2\, k_{\mathrm{pivot}}$, making the CMB power spectrum observationally indistinguishable from the adiabatic-only result. As k_i decreases, the limit on ΔN_{eff} strengthens rapidly. For sufficiently small k_i, CMB data is mainly sensitive to the plateau of the isocurvature power spectrum (see Eq. (3.40)) and the constraint approaches an asymptotic value which depends on $\Delta N_{\mathrm{eff}} f_{\mathrm{iso}}$.

For $f_{\mathrm{iso}} = 10$ we find a preference for the range $k_i \sim (0.1 - 1) \times k_{\mathrm{pivot}}$. That is, models with

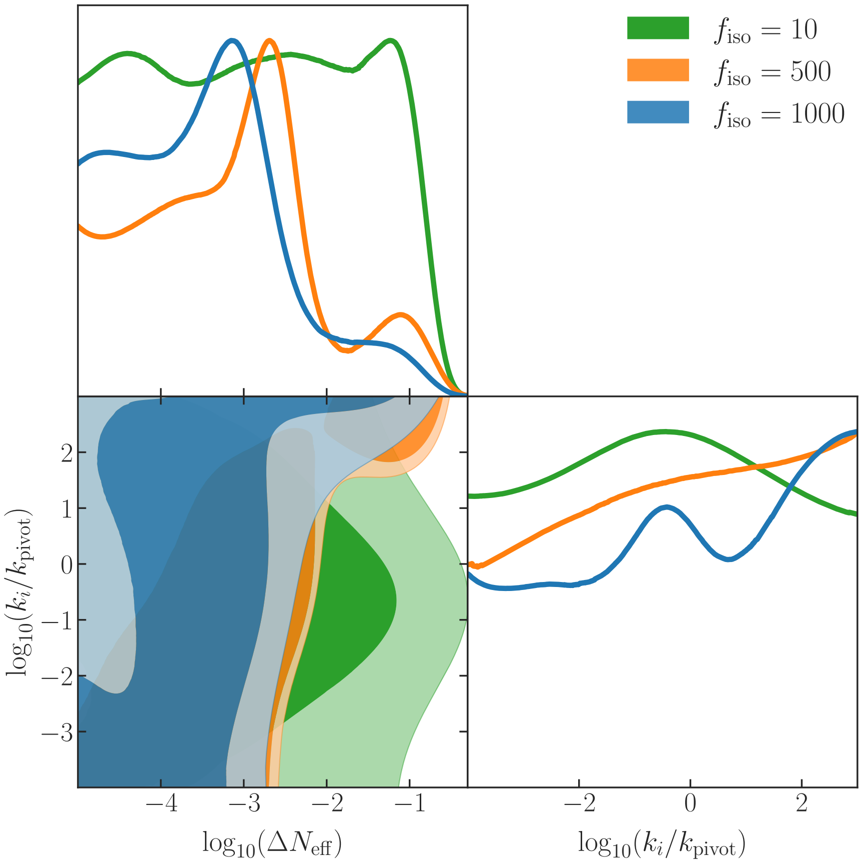

Figure 3.9: The two dimensional marginalized posterior distributions for the FOPT new physics parameters $\Delta N_{\rm eff}$ and $k_i/k_{\rm pivot}$, holding $f_{\rm iso}$ fixed.

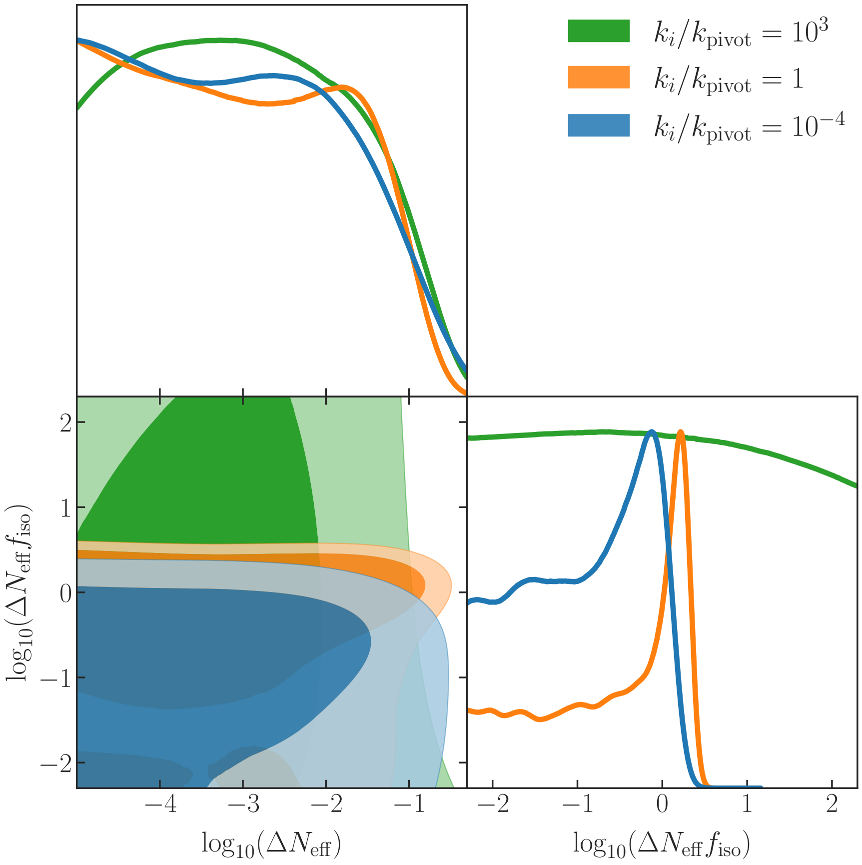

Figure 3.10: The two dimensional marginalized posterior distributions for the FOPT new physics parameters $\Delta N_{\rm eff}$ and $\Delta N_{\rm eff} f_{\rm iso}$, holding k_i fixed.

this combination of k_i and $f_{\rm iso}$ fit the data better than models with large k_i (which are themselves indistinguishable from the adiabatic model).

3.7.2 $\Delta N_{\rm eff}$ constraints with fixed k_i

Next, we fix k_i and calculate the posteriors in $\Delta N_{\rm eff}$ and $\Delta N_{\rm eff} f_{\rm iso}$. This corresponds to the scenario where the horizon size at the beginning of the PT is fixed, and the PT rate varies. The results of our MCMC fit to the data are shown in Figure 3.10 for three choices of $(k_i/k_{\rm pivot})$: 10^3, 1, and 10^{-4}.

Again, we see that when k_i is large ($k_i = 10^3\, k_{\rm pivot}$) the constraints on $\Delta N_{\rm eff}$ approximate the adiabatic result for all values of $f_{\rm iso}$ within our priors. For the other two values of k_i, isocurvature becomes important and the model can be constrained even for very small values of $\Delta N_{\rm eff}$. For $\Delta N_{\rm eff} \ll 0.1$, the adiabatic and background effects are negligible and the CMB data mainly has sensitivity to the combination $\Delta N_{\rm eff} f_{\rm iso}$ which parameterizes the strength of isocurvature effects. In this regime, we find the 95% CL constraints $\Delta N_{\rm eff} f_{\rm iso} < 1.25$ for $k_i = 10^{-4}\, k_{\rm pivot}$ and $\Delta N_{\rm eff} f_{\rm iso} < 2.09$ for $k_i = k_{\rm pivot}$. We have confirmed through explicit calculation using linear-flat priors on $\Delta N_{\rm eff}$ that these results are robust against our choice of priors.

The limits on $\Delta N_{\rm eff} f_{\rm iso}$ are stronger for the smallest value of k_i as the CMB only probes the plateau (the maximum) of the isocurvature power spectrum. For the larger value, the CMB is sensitive to the portion of the power spectrum which is proportional to k^3 and suppressed relative to the plateau. As $\Delta N_{\rm eff}$ becomes $\mathcal{O}(0.1)$, the adiabatic effects become important. At this point, the limits deviate from $\Delta N_{\rm eff} f_{\rm iso} = \mathrm{const.}$ and we (approximately) recover the adiabatic result: $\Delta N_{\rm eff} < 0.3$.

The constraint on $\Delta N_{\rm eff} f_{\rm iso}$ for $\Delta N_{\rm eff} \ll 0.1$ can be rewritten as a constraint on $\Delta N_{\rm eff}$ in terms of other quantities directly related to FOPTs. As shown below Eq. (3.40), $A_s f_{\rm iso}^2 \approx 4.2\gamma_{\rm PT}$ and $\gamma_{\rm PT} = \Gamma_{\rm PT}/H_{\rm inf}^4$. Using the definitions of nucleation temperature T_* ($\Gamma_{\rm PT} = H^4(T_*)$) and reheating temperature $T_{\rm rh}$ ($H_{\rm inf} = H(T_{\rm rh})$) for instantaneous reheating, we can rewrite $\gamma_{\rm PT} = (T_*/T_{\rm rh})^8$ in the radiation-dominated Universe. Therefore, the constraint $\Delta N_{\rm eff} f_{\rm iso} < \beta(k_i)$ is equivalent to

$$\Delta N_{\rm eff} < 2.8 \times 10^{-5} \left(\frac{T_{\rm rh}}{T_*}\right)^4 \left(\frac{\beta(k_i)}{1.25}\right). \tag{3.47}$$

for $T_*/T_{\rm rh} \gtrsim 0.1$. $\beta(k_i)$ is mildly sensitive to k_i for $k_i \lesssim k_{\rm pivot}$ as demonstrated by our limits on $\Delta N_{\rm eff} f_{\rm iso}$ for small $\Delta N_{\rm eff}$ discussed earlier this subsection.

For the two smallest values of k_i shown in Figure 3.10, there is a preference for models with isocurvature ($\Delta N_{\rm eff} f_{\rm iso} \sim 0.1 - 1$) compared to the adiabatic-only model which is well approximated by the smallest values of $\Delta N_{\rm eff} f_{\rm iso}$ allowed by our prior. This effect is more prominent for $k_i = k_{\rm pivot}$ which is close to the best-fit value of k_i.

3.7.3 ΔN_{eff} constraints from non-Gaussianity

In this section, we will estimate constraints on this class of FOPTs from non-Gaussianity in the CMB. Currently, there is no dedicated search for non-Gaussianity with DR isocurvature produced in a FOPT. The most relevant study is on non-Gaussianity with neutrino density isocurvature [224].

Based on Eq. (3.41), the effect of non-Gaussianity in our study will be comparable in size to that of neutrino density isocurvature when

$$\begin{aligned} &B_{\text{iso}}(k_1,k_2,k_3)\Delta^{\text{iso}}_{\ell_1}(k_1,\tau_0)\Delta^{\text{iso}}_{\ell_2}(k_2,\tau_0)\Delta^{\text{iso}}_{\ell_3}(k_3,\tau_0) \sim \\ &B_{\nu,\text{iso}}(k_1,k_2,k_3)\Delta^{\nu,\text{iso}}_{\ell_1}(k_1,\tau_0)\Delta^{\nu,\text{iso}}_{\ell_2}(k_2,\tau_0)\Delta^{\nu,\text{iso}}_{\ell_3}(k_3,\tau_0). \end{aligned} \tag{3.48}$$

where $B_{\nu,\text{iso}}$ and $\Delta^{\nu,\text{iso}}_{\ell}$ are the bispectrum and transfer function for the neutrino density isocurvature model. This transfer function can be simply related to the transfer function for DR isocurvature by accounting for the different energy fraction of DR and neutrinos. As discussed in Section 3.4, the transfer function for DR isocurvature is proportional to R_{dr}. Therefore, the transfer function for neutrino isocurvature can be well-approximated by

$$\Delta^{\nu,\text{iso}}_{\ell}(k,\tau) \sim \frac{R_\nu}{R_{\text{dr}}}\Delta^{\text{iso}}_{\ell}(k,\tau), \tag{3.49}$$

where $R_i \equiv \bar{\rho}_i/(\bar{\rho}_\gamma + \bar{\rho}_\nu + \bar{\rho}_{\text{dr}})$. Subsituting this result into Eq. (3.48), we find that the effect of non-Gaussianity will be similar in the two models when

$$B_{\text{iso}}(k_1,k_2,k_3) \sim \left(\frac{R_\nu}{R_{\text{dr}}}\right)^3 B_{\nu,\text{iso}}(k_1,k_2,k_3). \tag{3.50}$$

The available constraints on neutrino isocurvature non-Gaussianity [224] assume a local bispectrum which peaks in the squeeze configuration:

$$B_{\text{local}}(k_1,k,k) \propto \frac{f^{\text{local}}_{\text{NL}}}{k_1^{4-n_s}k^{4-n_s}} \quad k_1 \ll k \tag{3.51}$$

where $f_{\rm NL}^{\rm local}$ is a dimensionless parameter that quantifies the amount of non-Gaussianity present. The FOPT bispectrum, on the other hand, is independent of k_1 in the squeeze configuration (as shown in Eq. (3.46)) so the bound on $f_{\rm NL}^{\rm local}$ does not apply to our case.

The bispectrum from the FOPT is similar to the equilateral template for which the dominant effects come from the equilateral configuration [224]

$$B_{\rm equil}(k,k,k) = 6\left(\frac{2\pi^2}{25}\right)^2 A_s^2 f_{\rm NL}^{\rm equil}\frac{1}{k^6}\left(\frac{k_{\rm pivot}}{k}\right)^{2(1-n_s)}. \tag{3.52}$$

However, measurements of $f_{\rm NL}^{\rm equil}$ for isocurvature non-Gaussianity do not exist in the literature. Based on measurements of equilateral and local non-Gaussianity for curvature [224], we assume that a search for equilateral non-Gaussianity for isocurvature would find a value of $f_{\rm NL}^{\rm equil}$ within an order of magnitude of $f_{\rm NL}^{\rm local}$. Under this assumption and given the 2σ upper bound on $|f_{\rm NL}^{\rm local}|$ for neutrino density isocurvature [224], we can estimate an approximate bound $|f_{\rm NL}^{\rm equil}| \lesssim 10^3$ for the same cosmological model. This result can be translated into a bound on FOPT non-Gaussianity by evaluating Eq. (3.50) in the equilateral configuration ($k_1 \approx k_2 \approx k_3$) near the pivot scale $k_{\rm pivot}$ and taking $B_{\nu,\rm iso} = B_{\rm equil}$. After numerical integration of the second line of Eq. (3.44), the FOPT bispectrum can be written as

$$B_{\rm iso}(k,k,k) = -0.97 A_s f_{\rm iso}^2 \frac{1}{k^6}. \tag{3.53}$$

Combining Eqs. (3.50), (3.52) and (3.53) leads to the approximate constraint

$$\Delta N_{\rm eff}^3 f_{\rm iso}^2 \lesssim 2\times 10^{-4}. \tag{3.54}$$

In Section 3.7.2 we found $\Delta N_{\rm eff} f_{\rm iso} \lesssim 1$ in the regime $k_i \lesssim k_{\rm pivot}$ and $\Delta N_{\rm eff} \ll 0.3$. Therefore the dominant constraint on FOPT may come from non-Gaussianity for $\Delta N_{\rm eff} \gtrsim 2\times 10^{-4}$, though we again emphasize that a dedicated study is required to set a robust bound.

3.8 Conclusions

We have showed that for a broad class of non-thermal FOPTs, the scalar field undergoes a phase transition that nucleates bubbles during inflation. If the PT rate is small during inflation, the bubbles do not collide and their size is determined by the horizon size at the time of nucleation. The FOPT will eventually complete after reheating, at which point we assume most of the remaining energy density in the scalar field converts into dark radiation. The DR inherits the inhomogeneity of the scalar field, leading to a DR isocurvature mode.

If the PT starts sufficiently early during inflation, isocurvature in the DR can create measurable perturbations in the CMB. In this work, we performed a detailed calculation of the DR isocurvature power spectrum and implemented it in CLASS code. Using Planck 2018 and BAO data, we calculated the constraint on the energy density of DR (in terms of the effective relativistic degrees of freedom $\Delta N_{\rm eff}$). We demonstrated that the constraint on $\Delta N_{\rm eff}$ can be much stronger than the limit derived assuming adiabatic initial conditions. In particular, when the temperature T_* at which the phase transition completes, is close to the reheating temperature $T_{\rm rh}$, the isocurvature perturbations set a limit of $\Delta N_{\rm eff} \lesssim 10^{-5}(T_*/T_{\rm rh})^{-4}$. This limit weakens as T_* decreases and approaches the adiabatic constraint of $\Delta N_{\rm eff} < 0.3$ when T_* becomes much less than $T_{\rm rh}$.

Since the distribution of the perturbation caused by bubbles is intrinsically non-Gaussian, it could leave sizable non-Gaussianity signals in the CMB. We have also estimated the strength of the non-Gaussianity constraint on FOPTs from the CMB by comparing to neutrino density isocurvature. However, we showed that the bispectrum calculated for this class of FOPTs is different than those studied previously. Therefore, a dedicated search is needed to derive a robust bound on FOPTs from non-Gaussianity in the CMB.

Moreover, our study can also put a lower bound on the scale of inflation if we can determine $\Delta N_{\rm eff}$ and T_*. These quantities can be derived if we observe the direct gravitational wave spectrum from the FOPT. We will show in a follow-up paper that the recent nano-Hz gravitational wave data could already set a lower limit on the scale of the reheating temperature. In the future, it will be interesting to explore the correlation of gravitational wave signals and cosmological data to further probe FOPTs.

Part II

Dark Matter Indirect Detection

CHAPTER 4

LIMITS ON DARK MATTER ANNIHILATION FROM THE SHAPE OF RADIO EMISSION IN M31

Well-motivated models of dark matter often result in a population of electrons and positrons within galaxies produced through dark matter annihilation – usually in association with gamma rays. As they diffuse through galactic magnetic fields, these $e^{\pm}$ produce synchrotron radio emission. The intensity and morphology of this signal depends on the properties of the interstellar medium through which the $e^{\pm}$ propagate.

This chapter is based on Ref. [3]. In this work we use observations of the Andromeda Galaxy (M31) to construct a model of the gas, magnetic fields, and starlight, allowing us to calculate constraints on dark matter annihilation to $b\bar{b}$ based on the morphology of $3.6\mathrm{cm}$ radio emission. As the emission signal at the center of M31 is very sensitive to the diffusion coefficient and dark matter profile, we base our limits on the differential flux in the region between $0.9 - 6.9\mathrm{kpc}$ from the center. We exclude annihilation cross sections $\gtrsim 3 \times 10^{-25}$ cm^3/s in the mass range $10 - 500$ GeV, with a maximum sensitivity of 7×10^{-26} cm^3/s at $20 - 40$ GeV. Though these limits are weaker than those found in previous studies of M31, they are robust to variations of the diffusion coefficient.

4.1 Introduction

To date, all evidence for dark matter comes from its gravitational influence on the visible matter in the Universe. However, the majority of successful models for the production of dark matter require some level of non-gravitational interactions between the visible and dark sectors. Perhaps the best-known such scenario is that of thermally-produced dark matter, where a small interaction between dark matter and the Standard Model results in a relic population of non-relativistic particles due to thermal freeze-out during the early Universe. Weakly-Interacting Massive Particles (WIMPs) are the most well-known implementation of this class of dark matter models. In such models, the observed density of dark matter is obtained if the velocity-averaged annihilation cross section is $\langle \sigma v \rangle \sim 3 \times 10^{-26}\,\mathrm{cm}^3/\mathrm{s}$, for dark matter in the mass range $\sim 1 - 10^3\mathrm{GeV}$ [237].[1]

Thermal relics, as well as other models with dark matter-Standard Model interactions of similar magnitude, result in a number of possible experimental signatures. Of particular interest to this work is indirect detection, where present-day residual annihilation or decay of dark matter into Standard Model particles gives visible signatures that can be detected here on Earth. Annihilation to Standard Model particles will generically result in cascade decays terminating in stable $e^{\pm}$, photons, neutrinos, and $p/\bar{p}$, evidence of which can reach Earth-based detectors from their astronomical point of origin. As the strength of these signals increases with dark matter density squared and decreases with the distance to target squared, the indirect detection targets with the greatest signal rate are the largest and closest conglomerations of dark matter. The highest intensity signals are therefore expected to be seen from our own Milky Way Galactic Center, but other nearby galaxies – such as Andromeda (M31) [238, 239], the Large Magellanic Cloud (LMC) [240], the Small Magellanic Cloud (SMC) [241], and local dwarf galaxies [242, 243, 244, 245, 246, 247, 248, 249] – can have significant signals too. As the backgrounds and systematics for these systems differ from the Milky Way, they can be compelling targets despite the lower signal rate.

High-energy prompt photons, which can either come directly from the annihilation of dark matter or the cascade decays of annihilation products, travel largely unimpeded from where they were produced to Earth. Such photons are therefore the most straightforward indirect detection signal, with a morphology that is set only by the dark matter distribution. Interestingly, many groups have identified an excess of gamma rays in the energy range $1 - 3\,\mathrm{GeV}$ from data collected by the Fermi Large Area Telescope (LAT) [250] in the Milky Way [251, 252, 253, 254, 255], with morphology compatible with the dark matter expectations. Possible signals consistent with this gamma ray excess have been reported in M31 [238], and the LMC [240], though with less significance. These excesses can be well-fit by dark matter models with $m_\chi \sim \mathcal{O}(10 - 100\,\mathrm{GeV})$

---

[1] Though model-specific details can easily change these numbers by $\mathcal{O}(1)$ factors or more.

annihilating to either $b\bar{b}$ or $\tau^+\tau^-$ followed by cascade decays which result in the observed photons, with a thermally averaged cross section of $\langle\sigma v\rangle \sim 2 \times 10^{-26}\mathrm{cm}^3/\mathrm{s}$ [252, 253, 254, 255, 240, 256].

However, the ultimate origin of this gamma ray excess remains unclear. An unresolved population of millisecond pulsars (MSPs) in the center of the Milky Way has been suggested as an alternate source of this signal [257, 258, 259, 260, 261, 262]. Ref. [263] has argued that the distribution of gamma rays in the Galactic Center excess (GCE) in the Fermi-LAT data contains non-Poissonian statistics, suggestive of a MSP origin. At this time, debate appears to be far from settled, with questions about the spectrum of MSPs [264], morphology and background emission modelling [265, 266, 267], and the non-Poissonian statistics interpretation [268, 269] all remaining open. A recent analysis [270] suggests that the observed excess is best fit by a combination of point sources and a diffuse source, but uncertainties are large enough that either origin could dominate.

In this context, searches for indirect detection signals beyond prompt photons are especially interesting. Dark matter annihilation into Standard Model final states which decay into gamma rays will necessarily also have significant branching ratios into electrons and positrons. These $e^\pm$ will interact with galactic magnetic fields, ambient photons (from starlight, dust and the Cosmic Microwave Background (CMB)) and interstellar gas, losing energy and emitting a range of secondary photons ranging in energy from radio up to X-rays. These signals depend on the properties of the target beyond the dark matter distribution, introducing uncertainties that do not exist in prompt photon searches; however the systematics and backgrounds are largely distinct as well.

In this work, we set constraints on dark matter annihilation by analyzing a 3.6 cm radio map of the Andromeda galaxy (M31) by the Effelsberg telescope [271]. M31 has been a common target for dark matter indirect detection searches using radio emission from the center of the galaxy [272, 273, 274, 275]; though the resulting constraints are sensitive to assumptions made about the astrophysical characteristics of the galaxy and the dark matter distribution.

The $e^\pm$ injection rate (and the associated radio signal) at the center of M31 is dependent on the slope of the dark matter density distribution, which has considerable uncertainties [276]. The galactic center radio signal is also dependent on assumptions of the diffusion coefficient. For example, Refs. [272, 273, 274] assume electrons and positrons lose all of their energy before diffusing a measurable distance, predicting larger signals in this region than analyses which assume greater diffusion (as considered in as Ref. [256]).

In order to set robust limits which are less sensitive to reasonable variations of the astrophysical parameters, we consider the morphology and intensity of the radio emission from the region of M31 between 0.9–6.9 kpc from the galactic center. We compute the expected synchrotron emission from electrons and positrons in M31 produced through dark matter in the mass range $6 - 500\mathrm{GeV}$ annihilating to $b\bar{b}$ while varying the diffusion coefficient over the range of experimentally allowed values [277, 278, 279, 271]. Commonly used tools for modeling the transport of $e^{\pm}$ (such as `galprop` [280] and `rx-dmfit` [281]) use a uniform diffusion coefficient. For modeling the relatively large region of interest for our analysis, this assumption is insufficient. We develop a numerical solution that allows for radial dependence in all transport coefficients – including the diffusion coefficient. Using our numerical method, we solve for the spherically averaged electron-positron phase space density and compute the radio emission from this phase space density and an axisymmetric model of the magnetic field. We then set exclusion limits on the annihilation cross section of dark matter, while varying the diffusion coefficient normalization.

The remainder of this paper is organized as follows. In Section 4.2, we describe the radio observations of M31 used in the analysis. Section 4.3 describes the spectrum and morphology of electrons and positrons injected into M31 through the annihilation of dark matter. We construct our models of the magnetic fields, interstellar radiation field (ISRF), and thermal gas density using a variety of relevant data in Section 4.4. The transport of electrons and positrons within M31 is described in Section 4.5. In this section, we include a discussion of the physics of charged particle transport in a galaxy and our numerical method for solving the transport equation for systems with position-dependent energy loss and diffusion. In Section 4.6, we calculate the intensity and morphology of the resulting synchrotron emission. Our statistical method for determining a data-driven background model and setting exclusion limits is described in Section 4.7. In Section 4.8, we present our results. Finally, we conclude in Section 4.9.

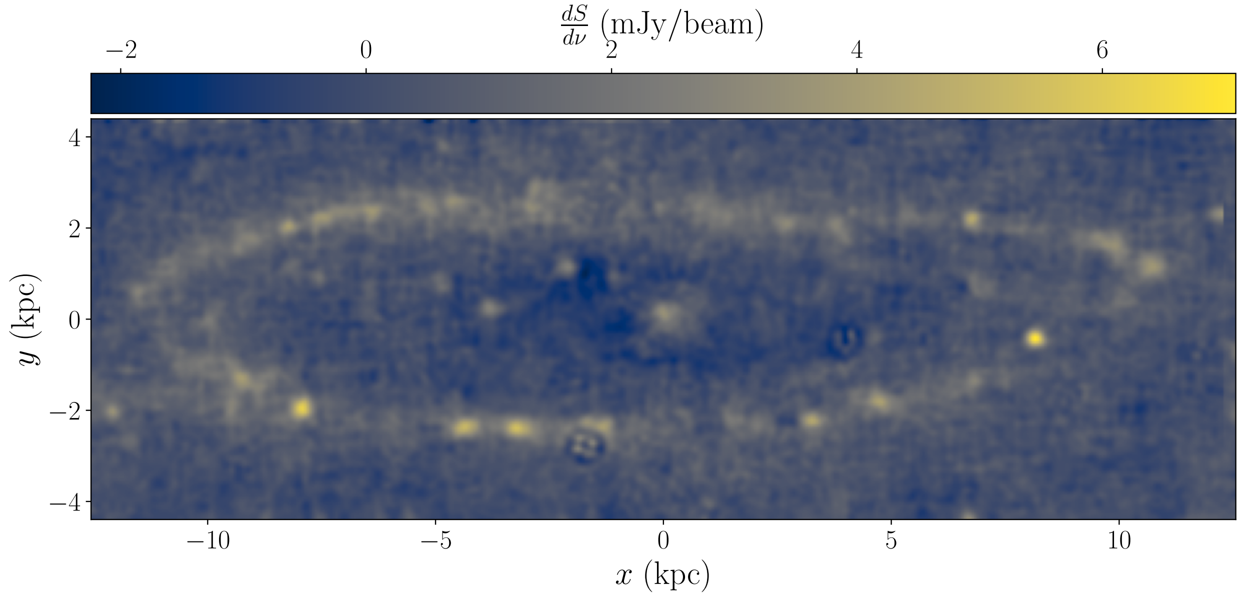

Figure 4.1: Smoothed non-thermal radio intensity map of M31 from Ref. [271], showing the flux per unit frequency per beam averaged over a frequency bandwidth of $1.1\mathrm{GHz}$. The HPBW projected into the plane of M31 is $0.340\mathrm{kpc}$ and the rms noise is given by $\sigma_{\mathrm{rms}} = 0.25\mathrm{mJy/beam}$ in the inner $9.13\mathrm{kpc} \times 9.13\mathrm{kpc}$ region and $\sigma_{\mathrm{rms}} = 0.3\mathrm{mJy/beam}$ in the rest of the map. Digitized data for this figure was provided by the authors of Ref. [271].

4.2 Radio Observations of M31

To constrain dark matter annihilation into high-energy electrons and positrons in M31, we use the non-thermal radio flux per unit frequency per beam $dS/d\nu$ from a survey of $\nu = 8.35\mathrm{GHz}$ emission in M31 [271] using the Effelsberg 100-m telescope. Our data has the thermal emission subtracted, along with 38 point sources which are not associated with M31. This is the highest frequency, and therefore highest resolution, intensity map of M31 measured by the Effelsberg telescope. The frequency bandwidth is $\Delta\nu = 1.1\mathrm{GHz}$, while the half-power beam-width (HPBW) is $1.5'$ (corresponding to a physical size of $0.34\,\mathrm{kpc}$ at the distance of M31). The root-mean-squared (rms) noise of the data is $\sigma_{\mathrm{rms}} = 0.25\,\mathrm{mJy/beam}$ in the inner $9.13\,\mathrm{kpc} \times 9.13\,\mathrm{kpc}$ region and $\sigma_{\mathrm{rms}} = 0.3\,\mathrm{mJy/beam}$ elsewhere.

In Figure 4.1, we show the intensity map of the data.[2] The reported intensity at each pixel is the radio emission measured by the Effelsberg telescope from that location on the sky; this corresponds

---

[2] Note that our vertical axis in Figure 4.1 is inverted compared to Figure 9 of Ref. [271].

to the true differential flux convolved with the frequency band and the angular beam centered on that location. Our x and y coordinates are oriented so that the x axis is aligned with the semimajor axis of M31, converting angular coordinates to lengths assuming a distance to M31 of 785 kpc [282].

We note that the observations of M31 have significant negative values, well in excess of statistical expectations given the rms noise. Most notably, the data has a large negative excursion located near the center of M31, at $(x, y) \sim (-2, 1)\,\mathrm{kpc}$. This may be due to over-subtraction of one of the point sources identified by Ref. [271] These negative values suggest that pixels labeled as having a flux of 0 mJy/beam actually may have a significant (unknown) positive flux. This in part motivates our choice to set limits using *morphology* of the expected dark matter-induced radio signal, rather than overall intensity.

Like the Milky Way, M31 is a spiral galaxy with approximate axisymmetry around a rotating stellar disk. We adopt cylindrical coordinates with the origin at the center of M31, the cylindrical radius R and the height away from the midplane of the disk z. The assumption of axisymmetry implies there is no dependence on the angle around the disk ϕ. We will refer to the spherical radius from the center of M31 as r. Note that we observe M31 at an angle of inclination given by $\beta = 77.5^\circ$ [283], and so the cylindrical (R, z, ϕ) coordinates are projected on to the $x - y$ coordinate system of Figure 4.1.

4.3 Dark Matter Production of $e^\pm$ in M31

Dark matter annihilation to unstable Standard Model particles such as b-quarks, τ leptons, or W bosons will result in cascade decays involving large numbers of leptons and QCD bound states, many of which themselves will decay into prompt photons and $e^\pm$. Though the exact spectrum of stable final-state particles that result from these decay showers of course depends on the initial Standard Model pair produced in the annihilation, there are also broad similarities regardless of the progenitors. As explicit calculation of the showers show (using a particle hadronization and decay package such as `pythia8` [284]), the final state particles will have energies in the $\mathcal{O}(0.1 -$

$10\,\mathrm{GeV}$) range for dark matter with the weak-scale masses typically expected for thermal relics. In this section, we calculate the injection morphology and spectrum of electrons and positrons produced in M31 due to dark matter annihilation, assuming weak-scale masses and annihilation into $b\bar{b}$ pairs.

While the flux on Earth of prompt photons from dark matter annihilation involves the integration of the dark matter density squared along the line of sight, electrons and positrons generated far from the Earth do not propagate to detectors here. Instead, we must track the evolution of the $e^{\pm}$ phase space density as the particles diffuse and energy is lost – a task we will take up in Section 4.5. For now, we will quantify the rate of production of the $e^{\pm}$ with a source term, which depends on the local dark matter density, $\rho_\chi(\boldsymbol{x})$, at every location within M31 and the particle physics model of the dark matter candidate. The source term or injection density rate of $e^{\pm}$ due to dark matter self-annihilation is given by

$$Q_e(\boldsymbol{x}, E) = \frac{\langle \sigma v \rangle}{2m_\chi^2} \frac{dN_e}{dE} \rho_\chi(\boldsymbol{x})^2, \tag{4.1}$$

where $\langle \sigma v \rangle$ is the thermally averaged annihilation cross section, m_χ is the dark matter particle mass, dN_e/dE is the injection spectrum of $e^{\pm}$ per annihilation in terms of the total energy[3] $E = (m_e^2 + p^2)^{1/2}$ of the $e^{\pm}$. Here and throughout this work, we have assumed that dark matter is its own antiparticle. If it is not and the abundance of dark matter particles and anti-particles is symmetric, there is an additional factor of $1/2$ in Eq. (4.1).

The energy spectrum of the $e^{\pm}$ source is determined by dN_e/dE which is influenced by the dark matter mass and the annihilation channel. Our choices for these parameters are motivated by fits of dark matter annihilation to the gamma ray excess in the Milky Way's Galactic center [255, 254, 253, 252]. In the Milky Way, the dark matter candidates that best fit the gamma ray excesses have $m_\chi \sim 30 - 50$ GeV annihilating to $b\bar{b}$ or $m_\chi \sim 10$ GeV annihilating to $\tau^+\tau^-$ [252, 253, 254, 255, 240]. A similar signal in M31 has a best fit of dark matter with mass $m_\chi \sim 10$ GeV annihilating to $b\bar{b}$, or $m_\chi \sim 5$ GeV annihilating to $b\bar{b}$ and $\tau^+\tau^-$ democratically [256].

In part motivated by these fits, in this work we consider dark matter annihilation into $b\bar{b}$ with

---

[3] Here and throughout this work we will use units where $c = \hbar = 1$.

m_χ in the range $6 - 500\,\mathrm{GeV}$. We scan in dark matter mass from $6 - 500\,\mathrm{GeV}$, and use `pythia8` to decay, shower, and hadronize the $b\bar{b}$ annihilations to calculate dN_e/dE for each choice of m_χ.[4] We show in Figure 4.2 the resulting $e^\pm$ spectra for a sample of representative dark matter masses. All spectra are cut off at low energy by $E = m_e$.

The morphology of the source is determined by the dark matter distribution of M31. This can be fit by a modified Navarro-Frenk-White (NFW) profile [285, 286, 287]

$$\rho_\chi = \frac{\rho_0}{(r/r_s)^{\gamma_{\mathrm{NFW}}}\,(1 + r/r_s)^{3-\gamma_{\mathrm{NFW}}}} \tag{4.2}$$

where γ_{NFW} is the logarithmic inner-slope, ρ_0 is the scale density and r_s is the scale radius. In the Milky Way, the gamma ray excess favors an inner slope of $\gamma_{\mathrm{NFW}} \sim 1.25$ [252, 253, 254, 255]. This slope is adopted by Ref. [256] for the dark matter distribution of M31. However, there is considerable uncertainty in the M31 dark matter distribution. In keeping with available kinematic fits to the rotation curve, we use a standard NFW with $\gamma_{\mathrm{NFW}} = 1$. For the scale density and the scale radius, we use the best-fit values from analysis of kinematic data [279]:

$$\begin{aligned} \rho_0 &= (0.418 \pm 0.068)\,\mathrm{GeV/cm^3}, \\ r_s &= (16.5 \pm 1.5)\,\mathrm{kpc}. \end{aligned} \tag{4.3}$$

4.4 Astrophysical Model of M31

The intensity and morphology of a radio signal which originates from electrons and positrons in a galaxy depends greatly on how the charged particles propagate. In M31, the most important propagation effects are diffusion and energy loss [256]. To calculate the effects of these, we must first model the properties of the interstellar medium.

In this section, we present our models for the magnetic field, the interstellar radiation field

---

[4] The `pythia` shower was modified to allow decays of Standard Model particles which are meta-stable on detector timescales, but whose decays would be astrophysically relevant, e.g., μ, π^0, $\pi^\pm$, and neutrons.

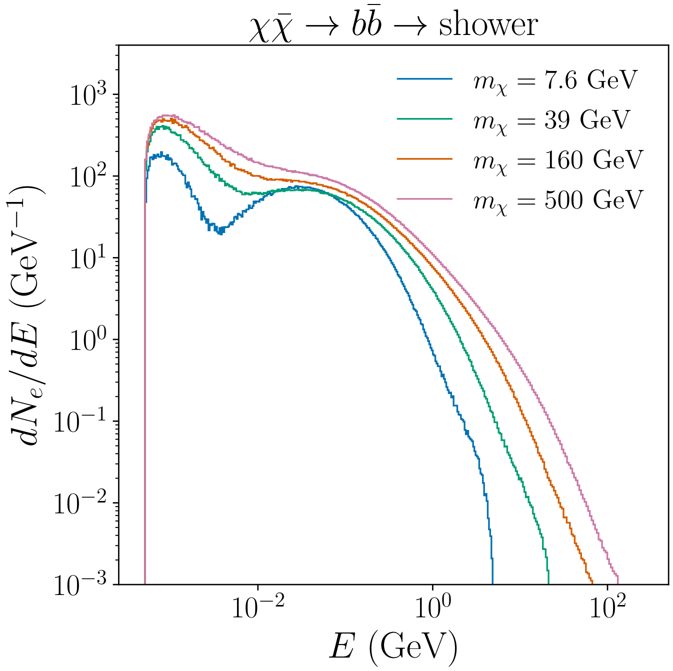

Figure 4.2: The number of $e^{\pm}$ in final states per unit energy per annihilation of dark matter into $b\bar{b}$ for a representative sample of dark matter masses m_χ.

(ISRF), and the various components of thermal gas within M31. As relativistic $e^{\pm}$ propagate, the interstellar magnetic field causes them undergo synchrotron energy loss, emitting photons at radio frequencies. Random fluctuations in the magnetic field also diffuse the charged particles through space. The ISRF causes the $e^{\pm}$ to lose energy through inverse-Compton scattering. Lastly, the various components of gas cause energy loss through bremsstrahlung and Coulomb scattering.

The measured distance to M31 has varied considerably in the literature. Early measurements found a value of 690kpc [288], but modern techniques and measurements prefer $760 - 785\text{kpc}$ [282, 289, 290]. As a result, the references we used to construct our astrophysical models assume a variety of distances to the galaxy. Throughout this work, we use a distance to M31 of 785 kpc [282, 289] obtained using measurements of tip of the red giant branch stars. When necessary, we scale the results of previous works used in our model of M31.

4.4.1 Magnetic Fields of M31

The magnetic field $\boldsymbol{B}$ in M31 is turbulent, with fluctuations on many length-scales, ranging from the size of the galaxy down to far below the resolution limit of our experimental probes. The details of small-scale fluctuations are not observationally accessible, but the expectation value of $\boldsymbol{B}^2$ and the power spectrum of fluctuations of the magnetic field at different locations in the galaxy can be measured though radio polarization and cosmic ray propagation observations, respectively. These observationally accessible features of the galactic magnetic field suffice for our purposes.

We write the magnetic field as the product of an axi-symmetric field magnitude and a random dimensionless vector-field that depends on location $\boldsymbol{x}$:

$$\boldsymbol{B}(\boldsymbol{x}) = \bar{B}(R,z)\boldsymbol{b}(\boldsymbol{x}). \tag{4.4}$$

The vector $\boldsymbol{b}$ contains the local fluctuations in the field, and

$$\bar{B}(R,z)^2 \equiv \langle \boldsymbol{B}(\boldsymbol{x})^2 \rangle \tag{4.5}$$

is the expectation value of the magnitude of the field squared, which we assume is independent of ϕ. Formally, this is an ensemble average with respect to the probability distribution that the magnetic field is sampled from.

As is conventional [291, 292, 293, 294, 256], we characterize the magnetic field fluctuations in terms of a power spectrum normalized as

$$\langle \boldsymbol{b}(\boldsymbol{x})^2 \rangle = \int\limits_{k_0}^{\infty} dk P_b(k) = 1, \tag{4.6}$$

where k_0 is the minimum wavenumber for which the power spectrum applies. The length-scale $1/k_0$ is typically assumed to be a factor of $\mathcal{O}(10-100)$ smaller than of the characteristic length-scale of the galaxy [291]. For M31, this implies $\mathcal{O}(0.1\text{kpc}) \lesssim 1/k_0 \lesssim \mathcal{O}(1\text{kpc})$ (though when setting limits we will vary this parameter over a much more conservative range). Observations of the propagation of cosmic rays in the Galaxy [295] find a diffusion coefficient of the form $D \propto E^{\delta}$ with $\delta \simeq 1/3$. This is consistent with magnetic field fluctuations that follow a Kolmogrov spectrum [296], $P_b \propto k^{-5/3}$. The diffusion of charged particles moving in a magnetic field with fluctuations obeying a Kolmogrov spectrum will be discussed in detail in Section 4.5.1.

We determine the R dependence of $\bar{B}$ from measurements of the M31 magnetic field (taken to be the root-mean-squared (RMS) field strength) in the disk in three regions: within the inner $1\mathrm{kpc}$ [297], in the range $6-14\mathrm{kpc}$ [298], and in intergalactic space [299]. The measurements from Refs. [297, 298] are shown in Figure 4.3. The intergalactic magnetic field has been measured to be at most $0.3\mu\mathrm{G}$ [299], which we take to be the 1σ upper bound of the field strength outside of M31. To require our fit to the M31 field strength to agree with this upper bound, we include $\bar{B} = 0.15 \pm 0.15\mu\mathrm{G}$ at $R = 300\mathrm{kpc}$ (though it is not shown in Figure 4.3) in addition to the measurements from Refs. [297, 298].

We fit the RMS magnetic field measurements to the functional form

$$\bar{B}(R,z) = \left(B_0 e^{-R/R_{B,0}} + B_1 e^{-R/R_{B,1}}\right) e^{-|z|/h_B(R)}. \tag{4.7}$$

which has sufficient flexibility to fit the available data. Our best-fit parameters of Eq. (4.7) are shown in Table 4.1.

Magnetic Field	
$B_0(\mu\mathrm{G})$	11.2 ± 2.9
$B_1(\mu\mathrm{G})$	7.2 ± 1.9
$R_{B,0}(\mathrm{kpc})$	3.5 ± 2.6
$R_{B,1}(\mathrm{kpc})$	77.6 ± 21

Table 4.1: Parameter values of Eq. (4.7), fit to the data at $|z| = 0$ (shown in Figure 4.3).

Assuming equipartition between the cosmic ray and magnetic field energy density, the vertical scale height of the magnetic field is approximately four times the scale height of the disk of synchrotron emission [300], which itself is approximated by the scale height of the HI disk [298]. The

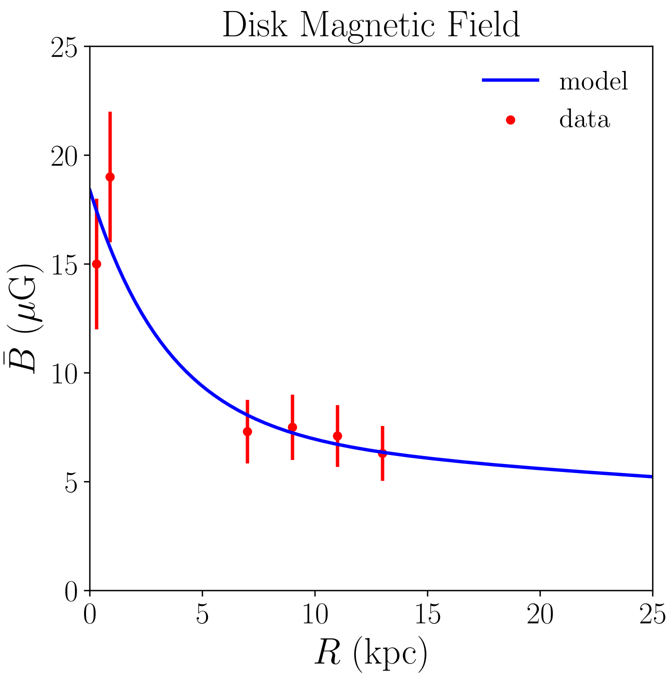

Figure 4.3: RMS magnetic field strength in the disk of M31, as measured by Refs. [297, 298] (red). Our double-exponential fit Eq. (4.7) (with the parameters of Table 4.1) is shown in blue.

HI disk scale height as a function of R was measured by Ref. [301]; rescaling from the distance to M31 assumed in that work (690kpc), the magnetic field scale height is

$$\begin{aligned} h_B(R) =& 4h_{\text{syn}} = 4h_{\text{HI}} \\ =& (0.83 \pm 0.17\,\text{kpc}) + (0.064 \pm 0.012) \times R. \end{aligned} \tag{4.8}$$

4.4.2 Interstellar Radiation Fields of M31

The ISRF of M31 has contributions from the CMB, starlight, and infrared emission from dust. We model each component, and sum the results to obtain the total energy density of radiation within M31. Most straightforward is the energy density of the CMB, which is (for our purposes) uniform and given by

$$\rho_{\text{CMB}} = \frac{\pi^2 (k_B T_{\text{CMB}})^4}{15} = 0.26\text{eV}/\text{cm}^3, \tag{4.9}$$

where $k_B T_{\text{CMB}} = 2.3 \times 10^{-4}\text{eV}$ [302].

We determine the energy density from stars and dust from the measured luminosity distribution of M31. The energy density of stellar radiation ρ_* in M31 is related to the bolometric luminosity density Q_* by

$$\rho_*(\boldsymbol{x}) = \frac{1}{4\pi}\int d^3x' \frac{Q_*(\boldsymbol{x'})}{|\boldsymbol{x}-\boldsymbol{x'}|^2}. \tag{4.10}$$

In Ref. [303], the extinction-corrected stellar luminosity distribution of M31 was modeled for five different structural components (bulge, disk, nucleus, young disk and stellar halo). As these distributions are extinction corrected, they describe the luminosities that would be observed without dust absorbing stellar emission. Assuming that the dust is in equilibrium with the starlight, the luminosity it emits in IR is equal to the luminosity that it absorbs. Therefore, the extinction-corrected stellar luminosity distribution integrated over all wavelengths approximates the bolometric luminosity from stars and dust combined.

Ref. [303] models the luminosity density Q_j as

$$Q_j(\boldsymbol{x}) = Q_{0,j}\exp\left[\left(\frac{\sqrt{R^2+(z/q_j)^2}}{A_{0,j}}\right)^{1/N_j}\right], \tag{4.11}$$

where $j =$ (bulge, disk, nucleus, young disk, stellar halo) indexes the various components of the luminosity distribution and $(Q_{0,j}, q_j, A_{0,j}, N_j)$ are parameters determined separately for each component. As Ref. [303] finds that the M31 luminosity is dominated by the bulge and disk components, we only include those in our model of the ISRF.

Ref. [303] fits the parameters $q_j, A_{0,j}, N_j$ to data, and provides the extinction corrected total luminosity of each M31 structural component in each of the $ugriz$ filter bands. These luminosities are defined as

$$L_{a,j} \equiv \left.\left(\lambda\frac{dL_j}{d\lambda}\right)\right|_{\lambda_a}, \tag{4.12}$$

where $a = (u, g, r, i, z)$ represents the spectroscopic band of the measurement, and λ_a is the central wavelength of the relevant band.

The $Q_{0,j}$ depend on the total bolometric luminosity of each component $L_{\mathrm{bol},j}$:

$$L_{\mathrm{bol},j} = \int d^3x' Q_j(\boldsymbol{x'}). \tag{4.13}$$

The bolometric luminosity of the j component can be found by integrating

$$L_{\mathrm{bol},j} = \int d\lambda \frac{dL_j}{d\lambda} \tag{4.14}$$

Therefore, we need the luminosity per unit wavelength – or spectral energy distribution (SED) – of each component.

The SED is only available in the inner 1 kpc of M31 [304], but M31's bulge is concentrated in the inner $1-2\mathrm{kpc}$ [303]. Therefore, we use the SED from the inner 1 kpc of M31 [304] as a template for the SED of the bulge, renormalized so that it accounts for the luminosity of the whole bulge. To chose the appropriate normalization we digitize and smoothly interpolate the extinction corrected SED of the inner 1 kpc of M31 from Figure 1 of Ref. [304], and fit the proportionality constant between the inner kpc and the entire bulge by minimizing the χ^2 between the re-normalized SED and the bulge luminosity in each band, derived from the fits of Ref. [303]. Our best fit rescaled SED and the measured luminosities in the $ugriz$ bands for the bulge are shown in Figure 4.4a. Using the best fit rescaled SED, we then integrate $dL_{\mathrm{bulge}}/d\lambda$ over wavelengths λ to obtain the bolometric luminosity of the bulge.

For the functional form of the SED for the disk, we subtract our best-fit SED for the bulge from the extinction corrected SED for the whole galaxy (given in Ref. [305]). Using this functional form, we repeat the procedure that we used for the bulge: we perform a χ^2 minimization to find the proportionality constant that gives the best agreement between the rescaled SED and the luminosity values for the disk, and integrate $dL_{\mathrm{disk}}/d\lambda$ over λ to get the bolometric luminosity of the disk. Our best fit rescaled SED and the measured luminosities in the $ugriz$ bands for the disk are shown in Figure 4.4b.

We use our bolometric luminosity values and Eq. (4.13) to calculate $Q_{0,j}$ for each component.

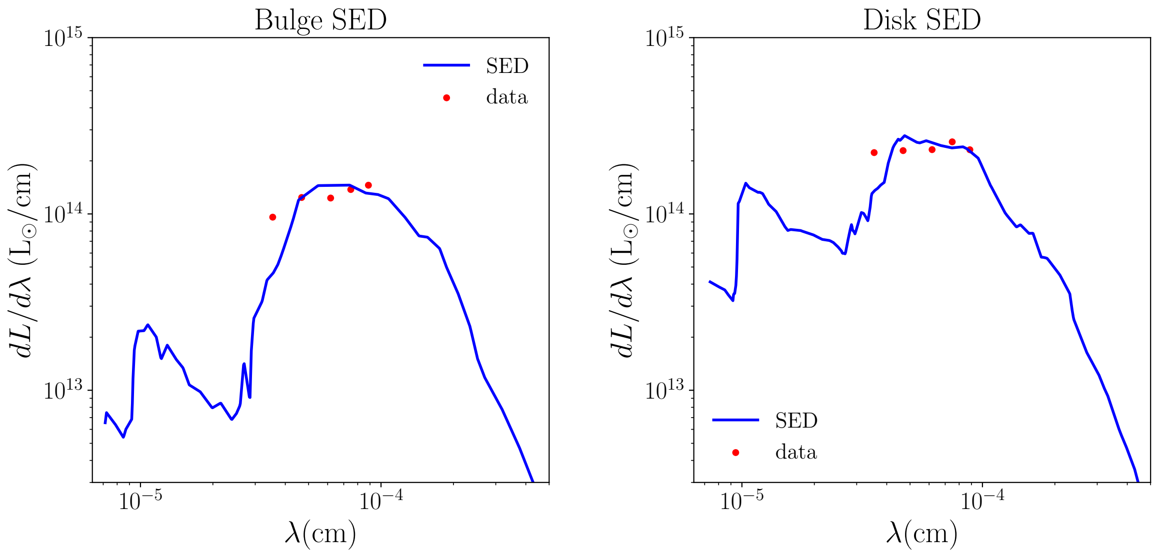

(a) (b)

Figure 4.4: Best-fit rescaled SED models [304, 305] and observed differential luminosities in $ugriz$ filters [303] for (a) the bulge and (b) the disk.

We show the values of the structural parameters $(Q_{0,j}, q_j, A_{0,j}, N_j)$ and luminosities $(L_{u,j}, L_{g,j}, L_{r,j}, L_{i,j}, L_{z,j}, L_{\rm bol}$ in Table 4.2 (for $j = \rm bulge, disk$). We add our results for the luminosity density of the disk and bulge to get $Q_*(\boldsymbol{x})$ and numerically integrate Eq. (4.10) to obtain ρ_*. As we derived our luminosity density distributions from extinction corrected luminosities [303] and SEDs [304, 305], our result for ρ_* contains contributions from starlight and dust. Our model for the ISRF $\rho_{\rm tot} = \rho_* + \rho_{\rm CMB}$ as well as the radiation density from individual components in the plane of the disk are given in Figure 4.5.

It is important to note that our model for the starlight luminosity of the innermost regions of M31 is significantly larger than the equivalent for the Milky Way [306] (shown with the dashed curve in Figure 4.5). Previous dark matter studies of radio emission from the center of M31 used a starlight model scaled with an $\mathcal{O}(1)$ factor from the Milky Way [256, 272, 274, 275]. The higher luminosity in the center of the galaxy that we find in our model leads to greater energy losses into X-rays from $e^{\pm}$ inverse Compton scattering with the starlight photons. As a consequence of this increased energy-loss mechanism, the radio signature of dark matter-produced electrons and positrons in the galactic center is reduced.

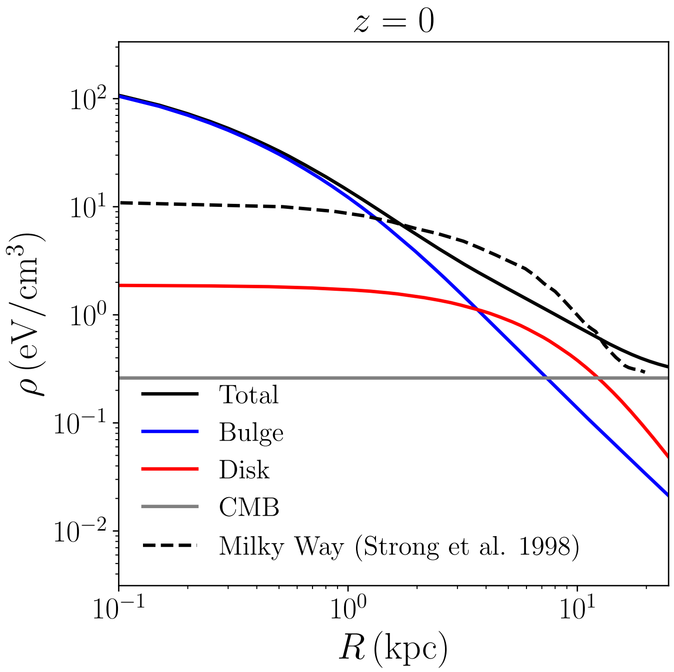

Figure 4.5: The ISRF radiation density for M31 along the disk ($z = 0$). The CMB result is given in Eq. (4.9). The bulge and disk components come from replacing Q_* with Q_{bulge} and Q_{disk}, respectively in Eq. (4.10). The Milky Way ISRF is digitized from Figure 1 of Ref. [306].

At distances further from the center ($\gtrsim 1\,\mathrm{kpc}$), our starlight model more closely matches those previously assumed for M31. As we will describe in detail, our dark matter constraints are obtained from radio emission in this region rather then from the center itself. Consequentially, we are less sensitive to differences in the starlight in the core of M31.

4.4.3 Gas in M31

The thermal gas of M31 can be split into ionized gas and neutral gas, each of which play different roles in the energy loss of relativistic electrons and positrons. Elastic collisions between the ionized gas and the $e^{\pm}$ result in Coulomb losses in the $e^{\pm}$. This leads to a net transfer of energy out of the $e^{\pm}$ and into the gas. Interactions between $e^{\pm}$ and ionized gas also result in bremsstrahlung losses due to inelastic collisions. Neutral gas only causes bremsstrahlung losses. As the rate of energy loss depends on the properties of the ionized and neutral gas, we must model HI, H_2, and ^{4}He gas separately.

Radiation Field		
Parameter	Bulge Value	Disk Value
Structural Parameters		
$Q_0\,(10^{10}\,L_\odot/\mathrm{kpc}^3)$	1.4×10^2	1.9×10^{-2}
$A_0\,(\mathrm{kpc})$	4.6×10^{-3}	2.6
q	0.72	0.17
N	2.7	1.2
Observed Luminosities		
$L_u\,(10^{10}\,L_\odot)$	0.34	0.78
$L_g\,(10^{10}\,L_\odot)$	0.57	1.1
$L_r\,(10^{10}\,L_\odot)$	0.75	1.4
$L_i\,(10^{10}\,L_\odot)$	1.0	1.9
$L_z\,(10^{10}\,L_\odot)$	1.3	2.0
$L_{\mathrm{bol}}\,(10^{10}\,L_\odot)$	2.0	3.0

Table 4.2: Top: best-fit parameters to the extinction-corrected luminosity distribution Eq. (4.11). Bottom: observed extinction-corrected luminosities in $ugriz$ filter bands followed by our derived bolometric luminosities. The bulge values are in the second column while the disk values are in the third column. All values except for L_{bol} and Q_0 are taken from Ref. [303], see text for details of our calculations of L_{bol} and Q_0.

4.4.3.1 Ionized Gas

Due to the difficulty of observing M31 as compared to our own Galaxy, the gas model of M31 is motivated by that of the Milky Way. Following Ref. [307], we model the ionized gas density as

$$\langle n_{\mathrm{ion}} \rangle \equiv \bar{n}_{\mathrm{ion}}(R, z) = \bar{n}_{\mathrm{ion},0}\,\mathrm{sech}^2\,(R/R_{\mathrm{ion}})\,\mathrm{sech}^2\,(z/z_{\mathrm{ion}}) \tag{4.15}$$

where $\langle n_{\mathrm{ion}} \rangle$ is the ion density averaged over scales that are small compared to the galaxy but large compared to fluctuations in the ion density. The parameters $\bar{n}_{\mathrm{ion}}$, R_{ion}, and z_{ion} will be fit to M31 measurements of the ion density from Hα emission [308] and Faraday rotation [298], as we will discuss below.

We first extract the ion density at the mid-plane of M31 at $R \simeq 9\mathrm{kpc}$ from measurements of Hα emission [308]. Here, the observable is the emission measure ($\mathcal{E}$) along the line of sight, which is related to the ion density by

$$\mathcal{E} = \int d\ell \, \langle n_{\rm ion}^2 \rangle, \tag{4.16}$$

Ref. [308] measures the value of $\mathcal{E}$ along a line of sight at $R = 9{\rm kpc}$ and then projects to the result that would be observed if M31 were viewed face-on, finding $\mathcal{E} = 6 - 15{\rm pc}\,{\rm cm}^{-6}$.

The ionized gas inhabits the galaxy in clumps that are small compared to astrophysical scales. These clumps make up a fraction of the volume of the galaxy given by the fill factor ϕ, which Ref. [308] assumes to be the Milky Way value of 0.2. Under this assumption (and taking the maximal value of $\mathcal{E} = 15{\rm pc}\,{\rm cm}^{-6}$ as well as their median scale height of $\hat{z}_{\rm ion} = 500{\rm pc}$), Ref. [308] calculates a mid-plane ion density of $\hat{n}_{\rm ion} = 0.39{\rm cm}^{-3}$ [308]. This is the density in a gas clump corresponding to a density field in the neighborhood of $R = 9{\rm kpc}, z = 0{\rm kpc}$ of

$$n_{\rm ion} = \mathcal{F}(\boldsymbol{x})\hat{n}_{\rm ion} \tag{4.17}$$

where $\mathcal{F}$ is the filling function which varies over short length-scales and is defined to be 1 inside a clump of ionized gas and 0 outside. Its spatial average over astrophysical length-scales is equal to the fill factor ϕ. The result obtained by Ref. [308] for $\hat{n}_{\rm ion}$ is likely an overestimate since they obtained it using their maximal value of $\mathcal{E}$. Therefore, we modify it to the result they would have obtained if they had used their central value of $\mathcal{E}$.

Given Eqs. (4.16) & (4.17), the mid-plane ion density scales with the emission measure and the scale height as

$$\hat{n}_{\rm ion} \propto \sqrt{\frac{\mathcal{E}}{\hat{z}_{\rm ion}}}. \tag{4.18}$$

We can use this dependence to re-scale the results of Ref. [308] for $\hat{n}_{\rm ion}$, as well as propagate uncertainties based on the measured value of $\mathcal{E} \simeq (10 \pm 5){\rm pc}\,{\rm cm}^{-6}$ and the range of assumed values for the scale height $\hat{z}_{\rm ion} \simeq (500 \pm 300){\rm pc}$. After doing so, our re-scaled result for the mid-plane ionized gas density becomes $\hat{n}_{\rm ion} = (0.32 \pm 0.20){\rm cm}^{-3}$. Using Eq. (4.17), and averaging over a small neighborhood around $R = 9{\rm kpc}, z = 0{\rm kpc}$ leads to our inferred value of $\bar{n}_{\rm ion}$ in this neighborhood:

$$\bar{n}_{\text{ion}}^{\text{obs}} = \phi \hat{n}_{\text{ion}} = (0.063 \pm 0.039)\text{cm}^{-3}. \tag{4.19}$$

By observing rotation measures (RM) from Faraday rotation and assuming magnetic field equipartition, Ref. [298] determines $\bar{n}_{\text{ion}}$ in the upper layers of the thermal disk (between $0.3-1\text{kpc}$ from the mid-plane) at three different values of R between $8-14\text{kpc}$. We take the distance of these measurements from the midplane to be the midpoint of the upper layers of the thermal disk ($z = 0.65\text{kpc}$). Errors were not reported for these results; we make the conservative choice to use errors of 50% of the measured value.

Ionized Gas Measurements

R (kpc)	z (kpc)	$\bar{n}_{\text{ion}}$ (cm^{-3})	Ref.
9	0	0.063	[308]
9	0.65	8×10^{-3}	[298]
11	0.65	7×10^{-3}	[298]
13	0.65	4×10^{-3}	[298]

Table 4.3: Values of the ionized gas density derived from observations of Hα emission [308] and Faraday rotation [298]. These derived values are used to fit our model of the ionized gas density given in Eq. (4.15).

We summarize the ionized gas observations from Faraday rotation [298] and our derived value at the midplane from the measurement of emission measure [308] in Table 4.3. Using these observations and our derived value, we perform a χ^2 fit to Eq. (4.15); we show our results in Table 4.4.

4.4.3.2 HI Gas

For the HI gas density, we digitize the radial column density distribution provided by Ref. [309] in the range $R \in [1, 23]\,\text{kpc}$. We then interpolate and extrapolate the digitized column density to get a function valid for all $R \geq 0$. For the extrapolation, we use a growing exponential at small R and a decaying exponential at large R, such that the value and slope of the function are continuous at each boundary. Our interpolation and extrapolation of the fit to the column density of HI within the disk of M31 [309] is shown in Figure 4.6a (see the vertical axis on the right).

Gas Density	
Parameter	Value
Ionized	
$\bar{n}_{\rm ion,0}({\rm cm}^{-3})$	0.14 ± 0.15
$R_{\rm ion}({\rm kpc})$	9.4 ± 5.7
$z_{\rm ion}({\rm kpc})$	0.39 ± 0.09
HI	
$h_{\rm HI,0}({\rm kpc})$	0.21 ± 0.04
S	0.016 ± 0.003
$\rm H_2$	
$h_{\rm H_2,0}({\rm kpc})$	0.15 ± 0.075
$R_{\rm H_2}({\rm kpc})$	13.2 ± 6.6

Table 4.4: Parameter values for our models of interstellar gas in M31. The top panel of the table has the best-fit parameter values for the ionized gas density in M31. The next two panels list parameters for the HI and $\rm H_2$ distributions along the z coordinate given by Eqs. (4.20) and (4.22), respectively.

We assume that the gas density on the disk is proportional to the column density. For the z-dependence of the HI density we assume a decaying exponential with a scale-height of $h_{\rm HI}(R)$ taken from Ref. [301], as previously discussed in Section 4.4.1:

$$h_{\rm HI}(R) = h_{\rm HI,0} + S \times R, \tag{4.20}$$

where $h_{\rm HI,0}$ and S are reported in Table 4.4. We normalize the HI density to the total HI mass reported in Table 1 of [309]. The resulting gas density on the disk is shown in Figure 4.6a (see the vertical axis on the left).

4.4.3.3 H_2 Gas

For the $\rm H_2$ density, we digitize the radial column density distribution provided by Ref. [309] in the range $R \in [2.5, 18]\,{\rm kpc}$. We then repeat our interpolation/extrapolation procedure to obtain a model of the column density of $\rm H_2$ on the disk. The results are shown in Figure 4.6b. We again assume that the density of $\rm H_2$ on the disk is proportional to the column density.

We assume a decaying exponential for the z-dependence, however there is little observational

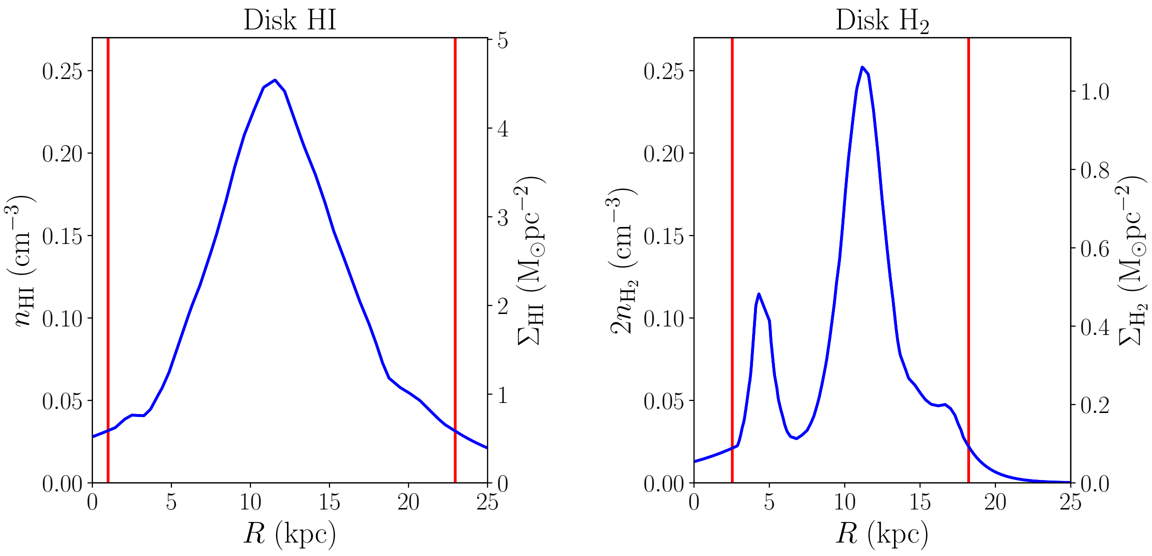

(a) (b)

Figure 4.6: Number density (left axis) and surface density (right axis) of (a) HI and (b) H_2 gas in the plane of the disk. The digitized and interpolated distributions from Ref. [309] are within the two vertical red lines. Outside these regions, we fit exponential extrapolations, matching the function values and first derivatives at the boundaries.

data available for the scale height of H_2 in M31. We therefore use the H_2 scale height in the Milky Way (derived from the data in Ref. [310]), and re-scale to M31 using a comparison of the HI scale heights in the Milky Way and M31. We digitize the fit to the H_2 scale height data in Figure 10 of Ref. [310], and smooth-out the fluctuations by fitting the digitized version of the fit to the functional form

$$h_{\rm H_2}^{\rm MW} = h_{\rm H_2,0}^{\rm MW} e^{-R/R_{\rm H_2}}. \tag{4.21}$$

We compare our model for the scale height in the Milky Way to that of Ref. [310] in Figure 4.7.

To obtain a scale height for H_2 gas in M31 from the scale height of H_2 in the Milky Way, we take the ratio of the average HI scale height for M31 (Eq. (4.20)) to that of the Milky Way (see Figure 6 of Ref. [310]) in the region $R \in [0, 7]$ kpc. We find this ratio is 1.55, and assume this ratio holds for the H_2 gas:

$$h_{\rm H_2} = 1.55 \times h_{\rm H_2}^{\rm MW} = h_{\rm H_2,0} e^{-R/R_{\rm H_2}}. \tag{4.22}$$

The resulting values of $h_{\rm H_2,0}$ and $R_{\rm H_2}$ are given in Table 4.4. The errors in these two parameters

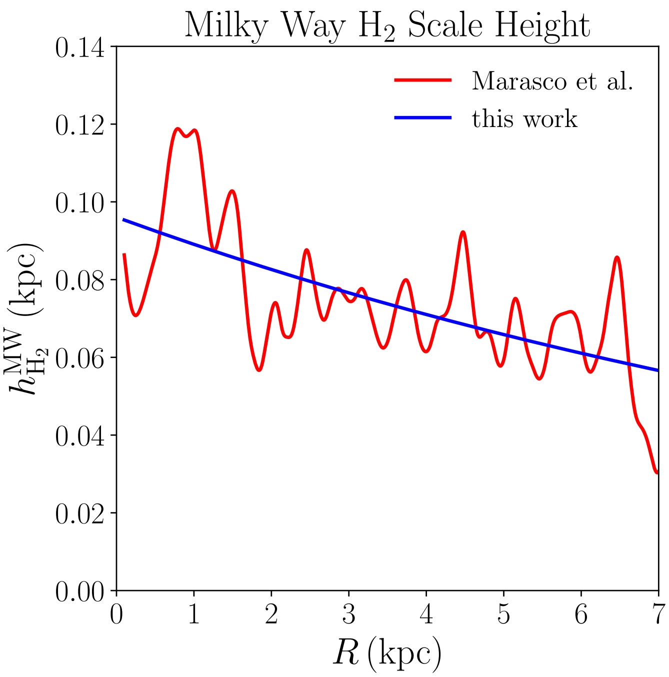

Figure 4.7: Fit to the Milky Way H_2 scale height [310] (red curve). The parameterized fit of Eq. (4.21) is shown in blue.

are dominated by the systematic errors of converting from their values in the Milky Way so we conservatively set their errors to 50% of their values.

Again, we normalize our distribution for the H_2 density based on the measured value for the total H_2 gas mass reported in Table 1 of Ref. [309]. The resulting H_2 density on the disk is shown in Figure 4.6b.

4.4.3.4 ^{4}He Gas

The last significant component of neutral gas that we have to model is $^4\mathrm{He}$. The mass fraction of $^4\mathrm{He}$ in simulated spiral galaxies was found to vary spatially over the range $Y_{\mathrm{He}} \simeq 0.25 - 0.3$ [311]. The lower limit is the primordial value set by Big Bang Nucleosynthesis, and higher values are due to stellar production. For simplicity, we approximate that $^4\mathrm{He}$ production from stars is negligible, so the ratio of $^4\mathrm{He}$ to H is set by Big Bang Nucleosynthesis:

$$N_{\mathrm{He}} = \frac{N_H Y_{\mathrm{He}}}{4(1 - Y_{\mathrm{He}})} \simeq N_H/12. \tag{4.23}$$

The errors in our model for the Helium density from using this approximation are $< 25\%$. As the effects of bremsstrahlung from $^4\mathrm{He}$ are subdominant compared to the other components in our propagation model, the errors in our final results from this approximation will be negligible as well.

Further, we assume that the $^4\mathrm{He}$ density has the same morphology as the total hydrogen density. The local density for ^{4}He is then derived from the HI and H_2 gas:

$$n_{\mathrm{He}} = \left(\frac{1}{12}\right) \times n_H = \left(\frac{1}{12}\right) \times (n_{\mathrm{HI}} + 2n_{\mathrm{H}_2}). \tag{4.24}$$

4.5 Propagation of $e^{\pm}$ in M31

The production of electrons and positrons by dark matter annihilation provides a source Q_e for the phase space-density f_e within a galaxy. From their initial locations, the $e^{\pm}$ will diffuse in turbulent magnetic fields and undergo energy loss from synchrotron radiation as well as inverse Compton, bremsstrahlung and Coulomb scattering. The synchrotron losses lead to the radio signal we will use to constrain dark matter annihilation, but all forms of energy loss must be tracked to determine the evolution of f_e in energy and position.

The evolution of the phase space density f_e is controlled by the diffusion-loss equation:

$$\frac{\partial f_e}{\partial t} = \partial_i[\mathcal{D}_{ij}(\boldsymbol{x}, E)\partial_j f_e] + \frac{\partial}{\partial E}[b(\boldsymbol{x}, E) f_e] + Q_e(\boldsymbol{x}, E). \tag{4.25}$$

where $f_e(\boldsymbol{x}, E) = dn_e/dE$ is the phase space density of electrons at position $\boldsymbol{x}$ and energy E, $\mathcal{D}_{ij}(\boldsymbol{x}, E)$ is the diffusion matrix, and $b(\boldsymbol{x}, E)$ is the energy loss parameter. The position-dependent diffusion matrix depends on both the RMS magnetic field, $\bar{B}$ and the turbulent fluctuations of the field at small scales. The loss parameter depends on $\bar{B}^2$, the ISRF, and the densities of the various gas components, which have been modeled in Section 4.4.

4.5.1 Diffusion Matrix

Fluctuations in the magnetic field cause the relativistic $e^{\pm}$ to exhibit diffusive motion. In a uniform magnetic field with strength B, the motion of $e^{\pm}$ is helical, with a Larmor radius of

$$r_L = \frac{E \sin\alpha}{eB} = (1.1 \times 10^{-7}\mathrm{pc}) \left(\frac{E}{1\mathrm{GeV}}\right) \left(\frac{10\mu\mathrm{G}}{B}\right). \tag{4.26}$$

Here, E is the particle energy and α is the pitch angle, which is defined as the angle of the velocity with respect to the direction of the magnetic field. For a changing magnetic field, the Larmor radius can still be defined, provided the field variations are small over the distance traversed by the particle in the time it takes for its phase to change by $\mathcal{O}(1)$. For the $\mathcal{O}(10\,\mu\mathrm{G})$ magnetic fields in the disk of M31 (see Section 4.4.1), electrons and positrons of the energies expected from the annihilation of dark matter have Larmor radii of $\lesssim \mathcal{O}(10^{-7}\,\mathrm{pc})$. As the fluctuations of the field follow a power law distribution on length-scales smaller than $1/k_0 \sim \mathcal{O}(1\mathrm{kpc})$, the magnetic field is dominated by Fourier modes that are much larger than the Larmor radius. Modes that are of order the Larmor radius and smaller can be treated perturbatively.

The motion of an electron or positron under the influence of the large-scale magnetic field fluctuations is well-described by the adiabatic approximation: the particle exhibits helical motion about the local field with an axis that gradually changes as the particle moves along the slowly changing magnetic field [312]. The magnetic field fluctuations with length-scales below the Larmor radius perturb this adiabatic motion, causing pitch angle scattering which leads to diffusion along the axis of the local magnetic field [313]. Since the direction of the large-scale magnetic field slowly changes over space and time, the diffusion is shared evenly in all directions leading to isotropic diffusion [313].

With these approximations and assuming magnetic field fluctuations characterized by the Kolmogrov spectrum, introduced in Section 4.4.1, the diffusion matrix is [291, 314]

$$\mathcal{D}_{ij} \simeq \left(1.5\times 10^{28}\mathrm{cm}^2/\mathrm{s}\right)\delta_{ij}\left(\frac{d_0}{1\mathrm{kpc}}\right)^{2/3}\left(\frac{10\mu\mathrm{G}}{\bar{B}}\right)^{1/3}\left(\frac{E}{1\mathrm{GeV}}\right)^{1/3} \equiv D_0\delta_{ij}\left(\frac{10\mu\mathrm{G}}{\bar{B}}\right)^{1/3}\left(\frac{E}{1\mathrm{GeV}}\right)^{1/3}, \tag{4.27}$$

where $d_0 = 1/k_0$ is largest length-scale over which the Kolmogrov spectrum of magnetic field fluctuations is valid. Since the diffusion matrix is isotropic, it can be written as

$$\mathcal{D}_{ij} = \delta_{ij}D. \tag{4.28}$$

It is conventional to refer to D the diffusion coefficient. We absorb the uncertainties in the prefactor of Eq. (4.27) and d_0 into the constant D_0. A range of possible values for D_0 (in both the Milky Way and M31) have been suggested in the literature. We review these briefly here.

Ref. [315] infers the diffusion coefficient for $e^{\pm}$ near star-forming regions in M31 from measurements of non-thermal radio emission at $\nu = 1.4\mathrm{GHz}$ and one higher frequency using two methods. The first method infers the diffusion coefficient from the difference in morphology between the two frequencies. The second method uses the difference between non-thermal emission and thermal emission at each of the frequencies, assuming that the thermal emission has a similar morphology to the source distribution of cosmic ray electrons. These methods allow Ref. [315] to extract the diffusion coefficient at two electron and positron energies: 4.1 and $7.5\mathrm{GeV}$.

Rescaling Ref. [315]'s results to the magnetic field parameters of M31, we obtain $D_0 \simeq 1.1\times 10^{28}\mathrm{cm}^2/\mathrm{s}$ using the first method and $D_0 \simeq 3.5\times 10^{27}\mathrm{cm}^2/\mathrm{s}$ using the second. Neither method fully models the propagation of cosmic rays, and the variation between the two results makes it difficult to identify either value as our default D_0 value.

For further guidance about the value of D_0 in M31, we review studies of propagation in the Milky Way. The `galprop` cosmic ray propagation model [292] uses observations of cosmic rays in the Milky Way [316, 317] to determine its best-fit diffusion coefficients [318]. The assumed propagation model includes a uniform diffusion coefficient of the form $D = \tilde{D}_0\left(E/4\mathrm{GeV}\right)^{\delta}$ for which the best-fit parameters were found to be $\tilde{D}_0 = (8.3\pm 1.5)\times 10^{28}\mathrm{cm}^2/\mathrm{s}$ and $\delta = 0.31\pm 0.02$

[318]. Comparing the model of Ref. [318] to our form for the diffusion coefficient, Eq. (4.27), and assuming that the cosmic rays studied were subject to a constant $10\mu\mathrm{G}$ magnetic field, these measurements imply $D_0 = (5.2 \pm 0.9) \times 10^{28}\mathrm{cm}^2/\mathrm{s}$. Ref. [319] constructed MIN, MED and MAX propagation models for $1\mathrm{GeV}$ cosmic ray energies in the Milky Way, which can be interpreted as a range of $D_0 = [5.9 \times 10^{27} - 2.0 \times 10^{28}]\ \mathrm{cm}^2/\mathrm{s}$, assuming the relevant magnetic field is a constant $10\mu\mathrm{G}$.

Underestimating the diffusion coefficient would under-predict how far particles will move before emitting most of their energy, leading to an over-prediction of the signal in regions of high dark matter density. A large value of D_0 will likewise result in a smaller signal flux for a given cross section. Therefore, to set conservative limits on the cross section of dark matter annihilation, we must avoid assuming too small a value for D_0. To set our conservative upper limit on D_0, we select a maximum value of $d_0 \equiv 1/k_0$ in Eq. (4.27) by setting k_0 equal to the wavenumber of a fluctuation with wavelength of $R_{B,1} = 77.6\mathrm{kpc}$ (the longest scale-length in our magnetic field model). This leads to $d_0 \lesssim R_{B,1}/(2\pi) \simeq 12.5\mathrm{kpc}$, implying $D_0 \lesssim 8 \times 10^{28}\mathrm{cm}^2/\mathrm{s}$.

Given the variation in diffusion coefficients in the Milky Way and M31, as well as our conservative upper bound, we consider D_0 in the range

$$3 \times 10^{27}\mathrm{cm}^2/\mathrm{s} \leq D_0 \leq 8 \times 10^{28}\mathrm{cm}^2/\mathrm{s}, \tag{4.29}$$

We select as a default value $D_0 = 1 \times 10^{28}\mathrm{cm}^2/\mathrm{s}$.

Though D_0 is position-independent, the diffusion coefficient D explicitly depends on the magnetic field, and our model for the magnetic field is position dependent (see Section 4.2). As a result, the diffusion coefficient also depends on location within M31. We show the dependence on location within M31 in Figure 4.8 for our default diffusion coefficient normalization ($D_0 = 1 \times 10^{28}\mathrm{cm}^2/\mathrm{s}$) and $E = 1\mathrm{GeV}$. The diffusion coefficient varies more rapidly with z when R is small, as a result of the magnetic field scale height increasing with R.

Prior studies of radio emission from dark matter annihilation in M31 make the approximation

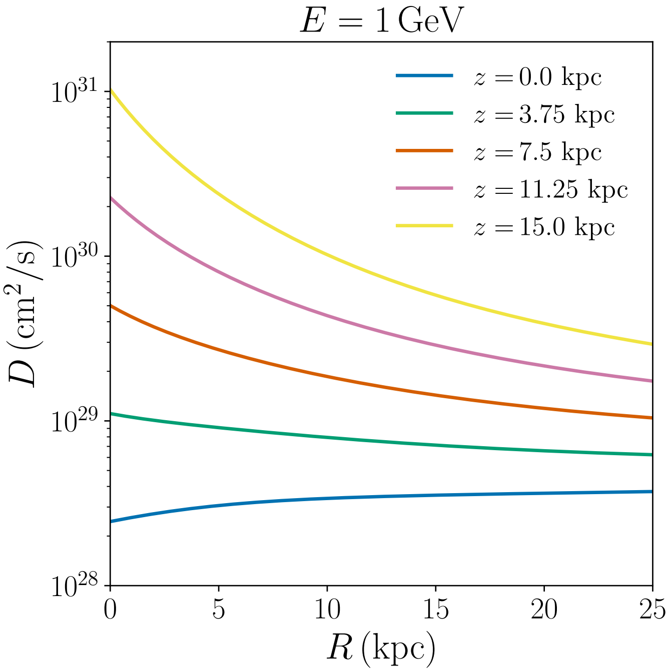

Figure 4.8: Diffusion coefficient as a function of R for $E = 1\mathrm{GeV}$ and various values of z, with $D_0 = 10^{28}$ cm^2/s.

that the diffusion coefficient is zero [272, 273, 274] or position independent [256, 275]. This latter assumption is sufficient when the region of interest is small and the diffusion coefficient is nearly constant over the region. Over the length scales of interest, the variations in the diffusion coefficient must be taken into account, and we develop a numerical method for calculating the evolution of phase space density of the charged particles which can accommodate a position-dependent diffusion coefficient. We describe our numerical solution in Section 4.5.3, after introducing the energy-loss terms that enter into Eq. (4.25) in the next subsection. To our knowledge this is the first study that uses a position-dependent diffusion coefficient to set limits on dark matter annihilation in M31 via radio emission.

4.5.2 Energy Loss due to Radiative Processes

As the electrons and positrons diffuse through the ISM they lose energy through radiative processes. This energy loss is encoded in Eq. (4.25) by the loss parameter b. In M31, the relevant losses are inverse Compton (IC), synchrotron, bremsstrahlung, and Coloumb interactions:

$$-\frac{dE}{dt} \equiv b(\boldsymbol{x}, E) = b_{\rm IC}(\boldsymbol{x}, E) + b_{\rm sync}(\boldsymbol{x}, E) + b_{\rm brem}(\boldsymbol{x}, E) + b_{\rm C}(\boldsymbol{x}, E). \tag{4.30}$$

We treat each of these terms in turn.

The inverse Compton scattering between $e^{\pm}$ and the ambient starlight, rescattered light from dust, and CMB emission will transfer energy from the charged particles into the photons, at a rate [312]

$$b_{\rm IC} = b_{\rm IC}^{(0)} \left(\frac{\rho_\gamma(\boldsymbol{x})}{10{\rm eV/cm}^3}\right)\left(\frac{E}{1{\rm GeV}}\right)^2, \tag{4.31}$$

where $b_{\rm IC}^{(0)} = 1.0\times10^{-15}{\rm GeV/s}$ and ρ_γ is the total radiation energy density, derived in Section 4.4.2.

Synchrotron emission occurs due to the acceleration of charged particles in galactic magnetic fields. As described in Section 4.4.1, the magnetic fields of M31 do not change appreciably over the Larmor radius of the relevant $e^{\pm}$. Additionally, due to pitch angle scattering, the pitch angles are approximately uniformly occupied. Therefore, the energy loss due to synchrotron emission can be determined by assuming a locally constant magnetic field and averaging the energy loss over all pitch angles. The expression for the loss due to synchrotron is given by [312]

$$b_{\rm sync} = b_{\rm sync}^{(0)} \left(\frac{\bar{B}(R,z)}{10\mu{\rm G}}\right)^2\left(\frac{E}{1{\rm GeV}}\right)^2 \tag{4.32}$$

where $b_{\rm sync}^{(0)} = 2.5\times10^{-16}{\rm GeV/s}$.

The third term in Eq. (4.30) is the contribution to the loss from bremsstrahlung emission due to $e^{\pm}$ scattering with neutral hydrogen, neutral helium, and ionized gas:

$$b_{\rm brem} = b_{\rm H}(\boldsymbol{x}, E) + b_{\rm He}(\boldsymbol{x}, E) + b_{\rm ion}(\boldsymbol{x}, E). \tag{4.33}$$

The expressions for these three components of the bremsstrahlung loss are given by [320, 306]

$$\begin{aligned} b_{\rm H} &= b_{\rm H}^{(0)} \left(\frac{n_{\rm H}(\boldsymbol{x})}{1{\rm cm}^{-3}}\right) \left(\frac{E}{1{\rm GeV}}\right), \\ b_{\rm He} &= b_{\rm He}^{(0)} \left(\frac{n_{\rm He}(\boldsymbol{x})}{1{\rm cm}^{-3}}\right) \left(\frac{E}{1{\rm GeV}}\right), \\ b_{\rm ion} &= b_{\rm ion}^{(0)} \left(\frac{n_{\rm ion}(\boldsymbol{x})}{1{\rm cm}^{-3}}\right) \left(\frac{E}{1{\rm GeV}}\right) \left[1 + \frac{1}{7.94} \ln\left(\frac{E}{1{\rm GeV}}\right)\right], \end{aligned} \tag{4.34}$$

where $b_{\rm H}^{(0)} = 1.22 \times 10^{-16}{\rm GeV/s}$, $b_{\rm He}^{(0)} = 3.61 \times 10^{-16}{\rm GeV/s}$ and $b_{\rm ion}^{(0)} = 1.74 \times 10^{-16}{\rm GeV/s}$. Our models for the density of each gas component were presented in Section 4.4.3.

Lastly, the fourth contribution to the loss parameter is from Coulomb interactions with ionized gas and is given by [321, 322]

$$b_{\rm C} = b_{\rm C}^{(0)} \left(\frac{n_{\rm ion}(\boldsymbol{x})}{1{\rm cm}^{-3}}\right) \left[1 + \frac{1}{82} \ln\left(\frac{E}{1{\rm GeV}} \frac{1{\rm cm}^{-3}}{n_{\rm ion}}\right)\right], \tag{4.35}$$

where $b_{\rm C}^{(0)} = 6.2 \times 10^{-16}{\rm GeV/s}$. Note that Coulomb losses are not radiative processes involving the loss of energy from the charged particles into photons, but rather are due to an energy transfer from the relativistic $e^{\pm}$ to non-relativistic ions in the interstellar plasma.

We show the resulting loss coefficient as a function of energy in Figure 4.9. Figure 4.9a shows the total loss coefficient given by Eq. (4.30) for various values of R on the disk. Figure 4.9b shows the total loss coefficient at the origin and the contributions to it from the individual processes discussed in this subsection. Coulomb losses dominate at low energy, inverse Compton and synchrotron losses dominate at high energy, and bremsstrahlung only becomes marginally important at intermediate energies for $R \simeq 10\,{\rm kpc}$ due to the large concentration of interstellar gas in the ring-like structure (discussed in Section 4.7.2).

4.5.3 Solving the Diffusion Loss Equation

We now turn to the numerical solution to the diffusion loss equation (Eq. (4.25)) in M31, assuming the electron and positron injection from dark matter from Section 4.3 and the astrophysical model

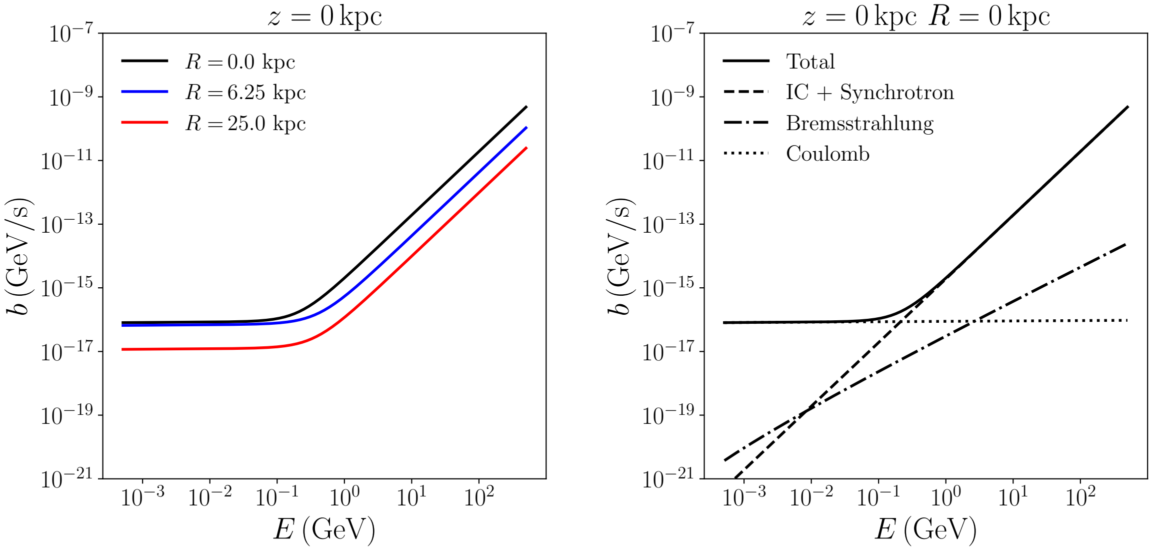

(a) (b)

Figure 4.9: (a) The energy dependence of the loss coefficient for various values of R at $z = 0$. (b) The energy dependence of the total loss coefficient (solid line) and its subcomponents at $R = z = 0$. Inverse Compton and synchrotron losses, which have the same energy dependence, are shown as the dashed line, bremsstrahlung as dot-dashed, and Coulomb losses as the dotted line.

of M31 from Section 4.4.

To motivate our approach, it is useful to consider the two dynamic time scales which characterize the diffusion (τ_D) and energy loss (τ_b), defined implicitly through rewriting Eq. (4.25) as

$$\frac{\partial f_e}{\partial t} = -\frac{f_e}{\tau_D} - \frac{f_e}{\tau_b} + Q_e(\boldsymbol{x}, E). \tag{4.36}$$

These timescales depend on R, z, E and derivatives of f_e over f_e. As a result, τ_b and τ_D are independent of the overall magnitude of f_e.

The timescale for diffusion is

$$\tau_D^{-1} = -\left(\partial_i D\right) \frac{\partial_i f_e}{f_e} - D \frac{\nabla^2 f_e}{f_e}. \tag{4.37}$$

In the approximation that f_e depends on position only as a power-law in r,

$$\begin{aligned} \tau_D &\sim \frac{r^2}{D}\left[1 + z\frac{\partial_z D}{D} + R\frac{\partial_R D}{D}\right]^{-1} \equiv \frac{L(\boldsymbol{x})^2}{D} \\ &\sim (2\times 10^{16}\mathrm{s})\left(\frac{L(\boldsymbol{x})}{5\mathrm{kpc}}\right)^2\left(\frac{1\times 10^{28}\mathrm{cm}^2/\mathrm{s}}{D}\right). \end{aligned} \tag{4.38}$$

where $L(\boldsymbol{x})$ is a length-scale that determines the rate that diffusion causes the phase space density to change. Assuming f_e is a power law in E, the characteristic timescale for energy loss can be approximated by

$$\tau_b \simeq \frac{E}{b} = (1\times 10^{16}\mathrm{s})\left(\frac{E}{1\mathrm{GeV}}\right)\left(\frac{1\times 10^{-16}\mathrm{GeV/s}}{b}\right). \tag{4.39}$$

The propagation is dominated by diffusion when $\tau_D \ll \tau_b$ and dominated by energy loss when $\tau_D \gg \tau_b$. Both diffusion and loss will dominate at different values of E and $\boldsymbol{x}$. In Figure 4.10 we plot the inverse timescales for diffusion and loss over a range of R and z. Along the disk, loss tends to dominate (Figure 4.10a), whereas diffusion becomes the more important term off of the disk (Figure 4.10b).

In regions of phase space where $\tau \equiv (\tau_b^{-1} + \tau_D^{-1})^{-1} \ll T_{\mathrm{M31}}$ (where $T_{\mathrm{M31}} \simeq 3\times 10^{17}\,\mathrm{s}$ is the approximate age of M31), the phase space density f_e today will be well-approximated by the equilibrium density. In Figure 4.11, we show τ for $E = 0.5\,\mathrm{GeV}$, $R \in [0,25]\mathrm{kpc}$ and $z \in [0,15]\mathrm{kpc}$ assuming our lowest diffusion coefficient normalization, $D_0 = 3\times 10^{27}\mathrm{cm}^2/\mathrm{s}$. $E = 0.5\mathrm{GeV}$ is a lower bound on the range of energies that contribute significantly to $\nu = 8.35\mathrm{GHz}$ radio emission in M31. Due to the energy dependence of the diffusion and loss coefficients, τ decreases as E increases for $E \gtrsim 0.1\mathrm{GeV}$. As larger D_0 also makes τ smaller, the combination of D_0 and E shown in Figure 4.11 provides an upper bound on τ.

As can be seen in Figure 4.11, within $R < 25\,\mathrm{kpc}$ and $|z| < 15\,\mathrm{kpc}$, we find $\tau < T_{\mathrm{M31}}$. Near the center of the galaxy and for higher $e^{\pm}$ energies, τ decreases. Though some regions at large R have timescales comparable to the age of M31, these regions are far from the inner part of the

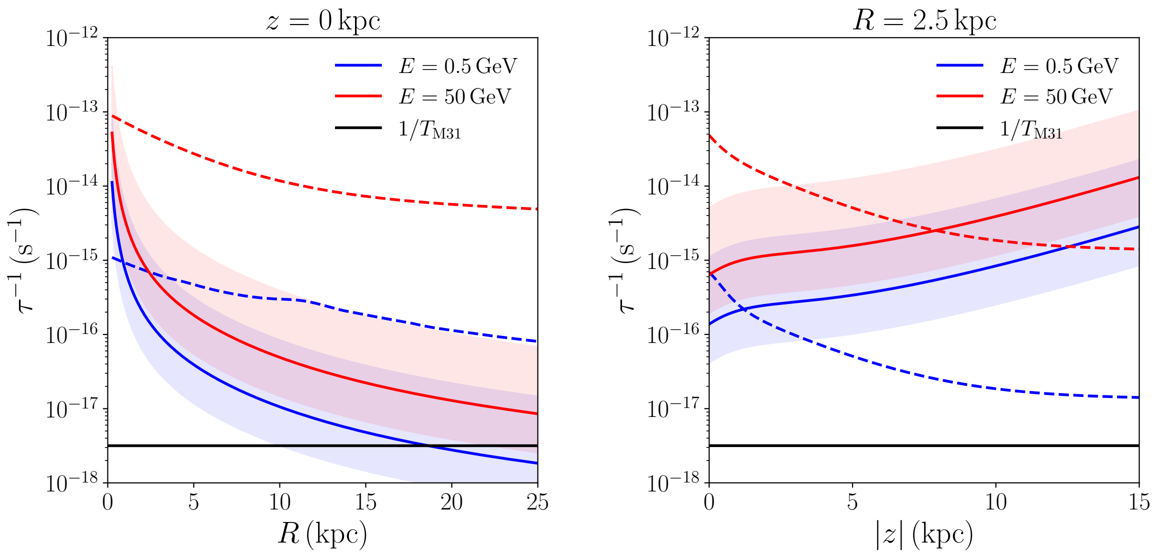

(a)

(b)

Figure 4.10: The inverse timescales for diffusion (solid lines) and loss (dashed lines), Eqs. (4.38) and (4.39). We show for comparison the inverse of the age of M31 (solid black), $T_{\mathrm{M31}} = 10^{10}$ years. The shaded regions around each solid line shows the variation of the inverse timescales for diffusion as D_0 is varied within the range given in Eq. (4.29).

galaxy where the Effelsberg radio data will be used to set limits. We are therefore justified in following the general approach of the literature [272, 273, 256, 274] by approximating the phase space density f_e of $e^{\pm}$ in M31 today as the equilibrium density.

If b and D do not depend on $\boldsymbol{x}$, a semi-analytic solution exists for the equilibrium density (see e.g., Ref. [281]). When the region of interest is small, homogeneous coefficients can be obtained by averaging the diffusion and loss coefficients over the relevant volume [281, 256]. However, our goal in this paper is to compute the synchrotron distribution over the field of view of the radio data in Figure 4.1, that is, most of the galactic disk of M31. Based on the astrophysical models (described in Section 4.4), the diffusion and loss coefficients will vary significantly over this region. We must therefore solve Eq. (4.25) in the case of non-homogeneous coefficients.

While the source term is spherically symmetric, the diffusion and loss coefficients are axially symmetric, implying that the solution to Eq. (4.25) depends on R, z and E. However, a fully axially symmetric numeric solution is intractable given our numeric approach. To overcome this

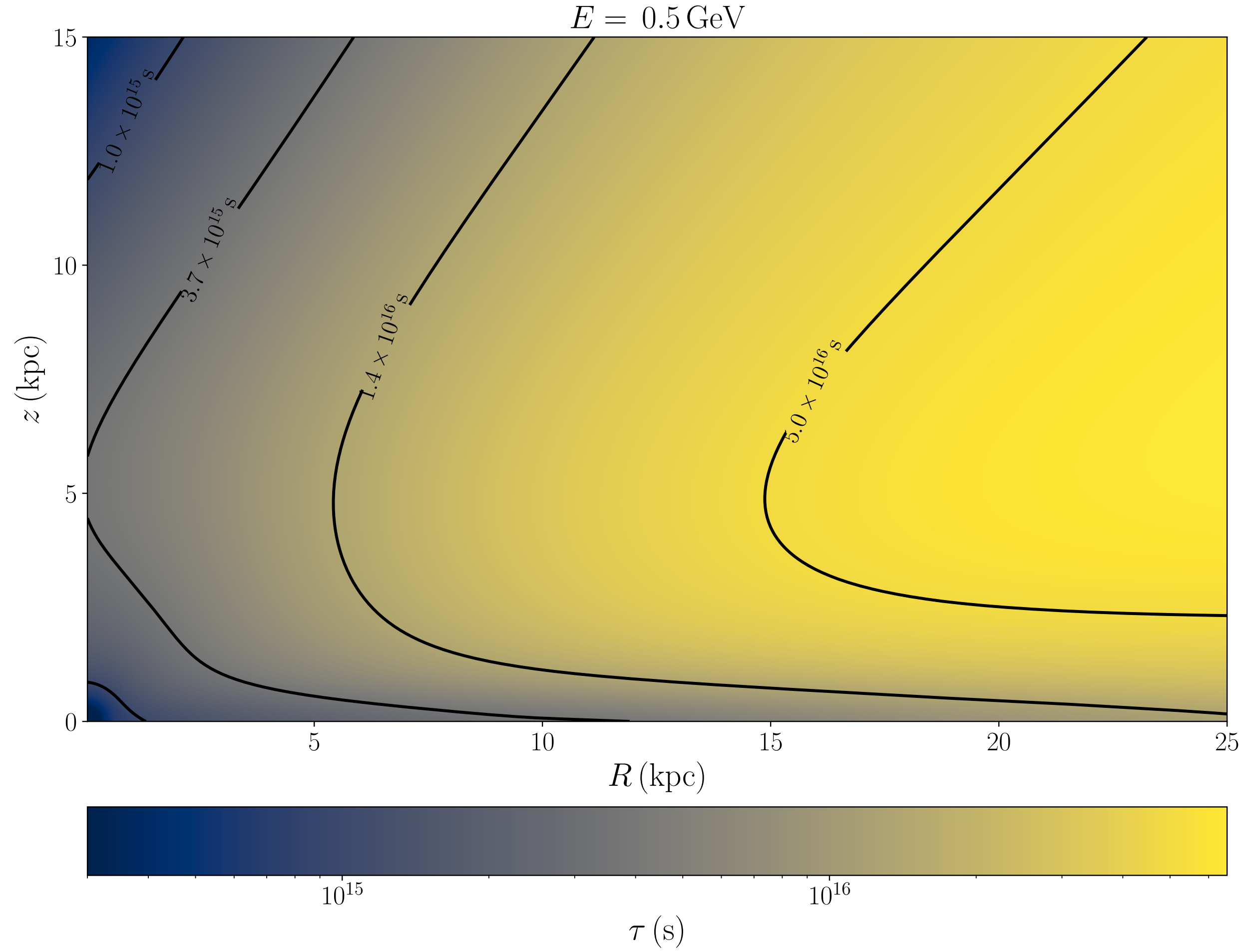

Figure 4.11: Dynamic timescale τ of M31 as a function of R and z for $E = 0.5\,\mathrm{GeV}$ (the minimum energy contributing significantly to the $8.35\,\mathrm{GHz}$ synchrotron signal) and $D_0 = 3 \times 10^{27}\mathrm{cm}^2/\mathrm{s}$ (the lower bound on the diffusion coefficient).

problem, we average Eq. (4.25) over solid angle Ω:

$$\frac{\partial\langle f_e\rangle}{\partial t} = \frac{\partial}{\partial r}\langle D\left(\partial_r f_e\right)\rangle + \frac{2}{r}\langle D\left(\partial_r f_e\right)\rangle + \frac{\partial}{\partial E}\langle bf\rangle + Q_e, \tag{4.40}$$

where (for an arbitrary function $g(E, \boldsymbol{x})$),

$$\langle g\rangle(E, r) \equiv \frac{1}{4\pi}\int d\Omega g(E, \boldsymbol{x}). \tag{4.41}$$

Spherically averaging Eq. (4.40), we find

$$\frac{\partial\langle f_e\rangle}{\partial t} = \left[\frac{\partial}{\partial r} + \frac{2}{r}\right]\left(\bar{D}\partial_r\langle f_e\rangle\right) + \frac{\partial}{\partial E}\left(\bar{b}\langle f_e\rangle\right) + Q_e \tag{4.42}$$

where

$$\bar{D} \equiv \frac{\langle D\partial_r f_e\rangle}{\langle\partial_r f_e\rangle}, \quad \bar{b} \equiv \frac{\langle bf_e\rangle}{\langle f_e\rangle}. \tag{4.43}$$

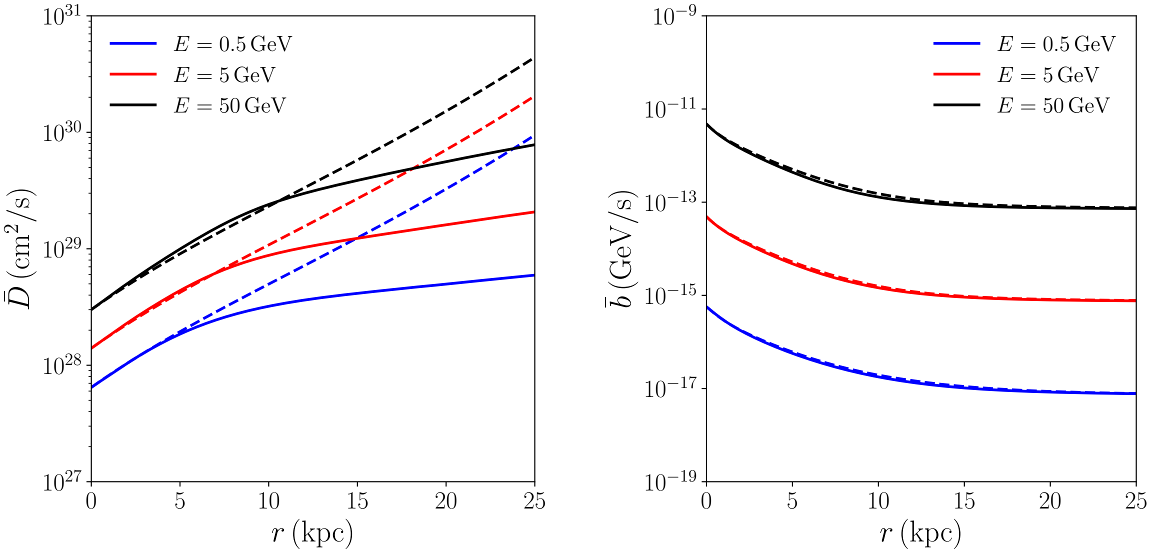

(a) (b)

Figure 4.12: Spherically averaged diffusion coefficient (left) and loss coefficient (right) using the unweighted average (dashed) and the weighted average (solid) for a range of energies. We use our default value of $D_0 = 1 \times 10^{28}\mathrm{cm}^2/\mathrm{s}$.

The averaged coefficients $\bar{D}$ and $\bar{b}$ required to solve for $\langle f_e\rangle$ in Eq. (4.42) themselves depend on

f_e. To calculate $\bar{D}$ and $\bar{b}$, we use approximate solutions for f_e, then use these averaged coefficients to numerically solve the spherically averaged diffusion loss equation for $\langle f_e \rangle$.

We calculate these approximate solutions for $\bar{D}$ and $\bar{b}$ in two different ways: first by assuming that f_e is approximately spherically symmetric, and in the second approach taking into account approximate deviations from spherical symmetry. For the region of M31 of interest for our analysis of the radio data (namely, the region inside $\sim 10\,\mathrm{kpc}$), the resulting solutions for $\langle f_e \rangle$ (and the resulting synchrotron emission) are similar regardless of our assumptions.

Our first approximate solution – the “unweighted" solution – assumes that deviations from spherical symmetry for f_e are small. If this is the case,

$$\begin{aligned} \bar{D} &\simeq \langle D \rangle \\ \bar{b} &\simeq \langle b \rangle, \end{aligned} \tag{4.44}$$

and we can numerically average over solid angles our models for D and b given in Sections 4.5.1 and 4.5.2.

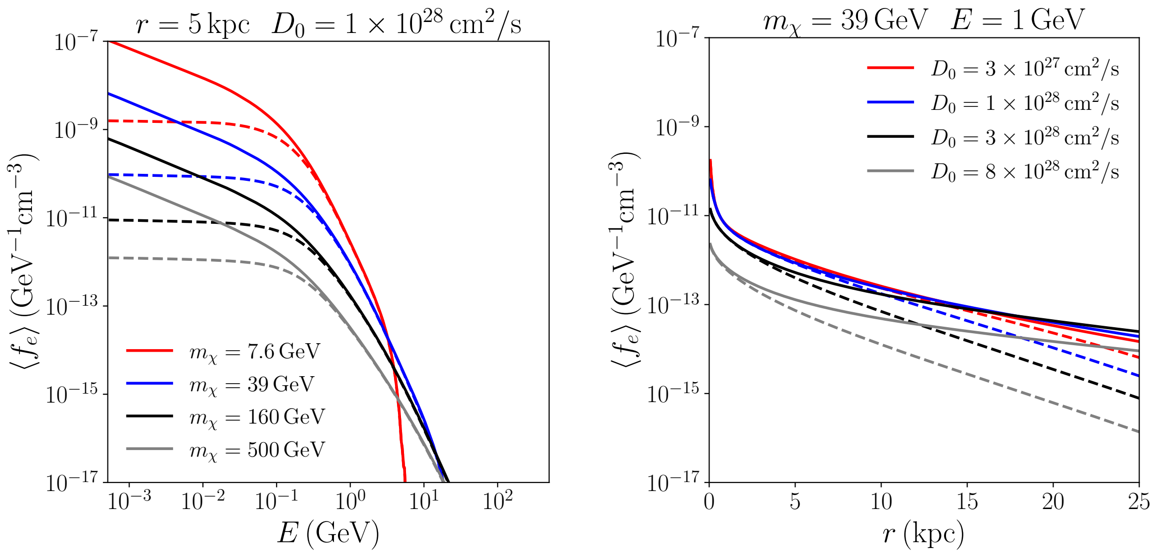

(a) (b)

Figure 4.13: Spherically averaged equilibrium phase space density of $e^{\pm}$ as a function of (a) E and (b) r from dark matter with an annihilation cross-section of $\langle \sigma v \rangle = 2.2\times10^{-25}\mathrm{cm^3/s}$. In (a) we keep r and D_0 constant for various values of m_χ. In (b) we hold E and m_χ constant and vary D_0. Dashed and solid lines are as in Figure 4.12.

For our second solution for the diffusion and loss coefficients, we calculate the spherically-averaged $\bar{D}$ and $\bar{b}$ parameters by substituting into Eq. (4.43) the approximate equilibrium solution for f_e obtained from solving Eq. (4.36) with $\partial f_e/\partial t = 0$:

$$f_e \simeq Q_e \tau, \tag{4.45}$$

where $\tau^{-1} \equiv \tau_b^{-1} + \tau_D^{-1}$. We refer to this as the "weighted" solution, as $\bar{D}$ and $\bar{b}$ are obtained as averages of D and b weighted by $\partial_r f_e$ and f_e, respectively.

Figure 4.12 shows the spherically averaged diffusion and loss coefficients for the unweighted (dashed) and weighted (solid) averaging schemes. The two methods give very similar results for the loss coefficient across all of phase space and galactic radii. For the diffusion coefficient, the two calculations agree for the inner part of M31, $r \lesssim 10\text{kpc}$. As we will show, the disagreement at large radii in the diffusion coefficients does not result in significant differences in the predicted synchrotron emission from the region of M31 that we will use to set limits. As a result, the constraints derived from radio observations are robust across these different solutions.

Using either the weighted or unweighted solutions for $\bar{D}$ and $\bar{b}$, we must solve the diffusion loss equation for $\langle f_e \rangle$. Defining $u \equiv r\langle f_e \rangle$, Eq. (4.42) becomes

$$\frac{\partial u}{\partial t} = \frac{\partial}{\partial r}\left[\bar{D}(r,E)\frac{\partial u}{\partial r}\right] - \frac{\partial \bar{D}}{\partial r}\frac{u}{r} + \frac{\partial}{\partial E}\left[\bar{b}(r,E)u\right] + rQ(r,E) \tag{4.46}$$

Under this redefinition, the boundary condition at $r = 0$ can be easily written as $u(0, E) = 0$, as long as f_e does not diverge faster than $1/r$. This is satisfied if the inner slope of the dark matter density has a power law index $\gamma_{\text{NFW}} < 1.5$. The other required boundary conditions are $u(49.9\text{kpc}, E) = 0$ and $u(r, m_\chi) = 0$. To solve Eq. (4.46), we discretize r, E and t and use finite differences to approximate the derivatives. This leads to a recursive equation for u at the next time-step in t, given its value at the current t.

Forward difference schemes for solving Eq. (4.46) are only stable if the time-step satisfies $\Delta t \lesssim (\Delta r)^2/D$ over the whole domain [323], where Δr is the grid-spacing. Given the approximate age of M31 and our grid-spacing $\Delta r = 62\,\mathrm{pc}$, $\mathcal{O}(10^7)$ time-steps would be needed to reach the equilibrium solution using a forward difference method. Backward differences, on the other hand, are unconditionally stable [323] for any size of time-step. We therefore use backward differences to approximate the derivatives on the right-hand-side, leading to an implicit equation for u at the next time-step, which can be solved with a sparse matrix method. We choose the time-step to be much larger than the maximum timescale in the problem to minimize the number of iterations required. Further details about our numerical method for solving the diffusion-loss equation are provided in Appendix C.1.

The results for the equilibrium solutions of $\langle f_e \rangle$ are shown in Figure 4.13. Figure 4.13a shows the energy dependence of $\langle f_e \rangle$ at $r = 5\mathrm{kpc}$ for a representative set of values of m_χ and our default value of D_0. Figure 4.13b shows the dependence on r for each value of D_0 and $E = 1\mathrm{GeV}$. The results become more sensitive to changes in D_0 for $D_0 \gtrsim 3 \times 10^{28}\mathrm{cm}^2/\mathrm{s}$. In both panels, the solid curves represent the weighted solution while the dashed curves represent the unweighted solution.

4.6 Synchrotron Spectrum and Morphology

Relativistic electrons and positrons in M31 accelerate in the galactic magnetic field, leading to synchrotron emission. The power emitted per unit frequency from an electron or positron at pitch angle α and energy E is [324]

$$\frac{dP}{d\nu}(\nu, \alpha, E) = 2\pi\sqrt{3}e^2\gamma\nu_0 x \int\limits_{x/\sin\alpha}^{\infty} d\xi K_{5/3}(\xi), \tag{4.47}$$

where $\nu_0 \equiv e\bar{B}/(2\pi\gamma m_e)$, $x = 2\nu/(3\gamma^3\nu_0)$, γ is the Lorentz factor and K_n is the n^{th}-order modified Bessel function of the second kind. The differential flux can therefore be obtained by averaging Eq. (4.47) over uniformly distributed pitch angles, and convolving with the spherically-averaged phase space density of electrons leading to:

$$\begin{aligned}\frac{d^2S}{d\Omega d\nu} =& \frac{1}{4\pi}\int\limits_{\text{los}} dl \int\limits_{m_e}^{\infty} dE \langle f_e\rangle(r(l,\Omega),E)\langle dP/d\nu\rangle_\alpha \\ \langle dP/d\nu\rangle_\alpha \equiv& \frac{1}{2}\int\limits_{-1}^{1} d(\cos\alpha)\frac{dP}{d\nu},\end{aligned} \tag{4.48}$$

where $\Omega = (\theta, \phi)$ is the location on the sky.

For $\sin\alpha \sim \mathcal{O}(1)$ and $x \gg 1$, $dP/d\nu$ is exponentially suppressed at low energies [324], so most of the power is radiated by $e^{\pm}$ with energies satisfying

$$E \gtrsim 10\text{GeV}\left(\frac{\nu}{8.35\text{GHz}}\right)^{1/2}\left(\frac{10\mu\text{G}}{\bar{B}}\right)^{1/2}. \tag{4.49}$$

As the Effelsberg radio telescope data used in this study is at frequencies around 8.35GHz, we are most interested in the $e^{\pm}$ produced through dark matter annihilation with energies of $\sim 10\text{GeV}$ and higher. This is shown in Figure 4.14 where we plot the dependence of $\langle dP/d\nu\rangle_\alpha$ on E for a variety of fixed values of $\bar{B}$.

In Figure 4.15, we show the 8.35GHz radio emission resulting from dark matter of mass $m_\chi = 39\text{GeV}$ annihilating with a cross section of $\langle\sigma v\rangle = 2.2 \times 10^{-25}\text{cm}^3/\text{s}$, assuming $D_0 = 1 \times 10^{28}\text{cm}^2/\text{s}$. In Figure 4.16, we show the signal along the semi-major axis (a) for a variety of values of m_χ, holding D_0 constant and (b) for a variety of values of D_0 holding m_χ constant.

4.7 Statistical Methodology

Having developed a numeric method to calculate the radio emission induced by dark matter annihilation in M31, we can now compare our predicted signal with data to set limits on the annihilation cross section to $\bar{b}b$ as a function of dark matter mass. Though the dark matter annihilation will be brightest in the center of the galaxy, this region also has significant baryonic sources whose intensities cannot be easily modelled. In addition, the flux near the center of M31 is sensitive to

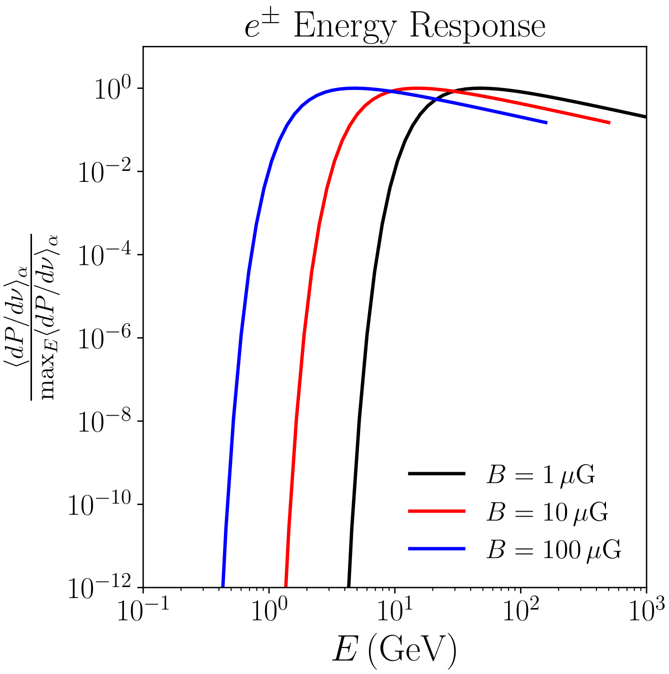

Figure 4.14: Energy response of $e^{\pm}$ producing synchrotron emission of frequency $\nu = 8.35$GHz for a variety of magnetic field strength values.

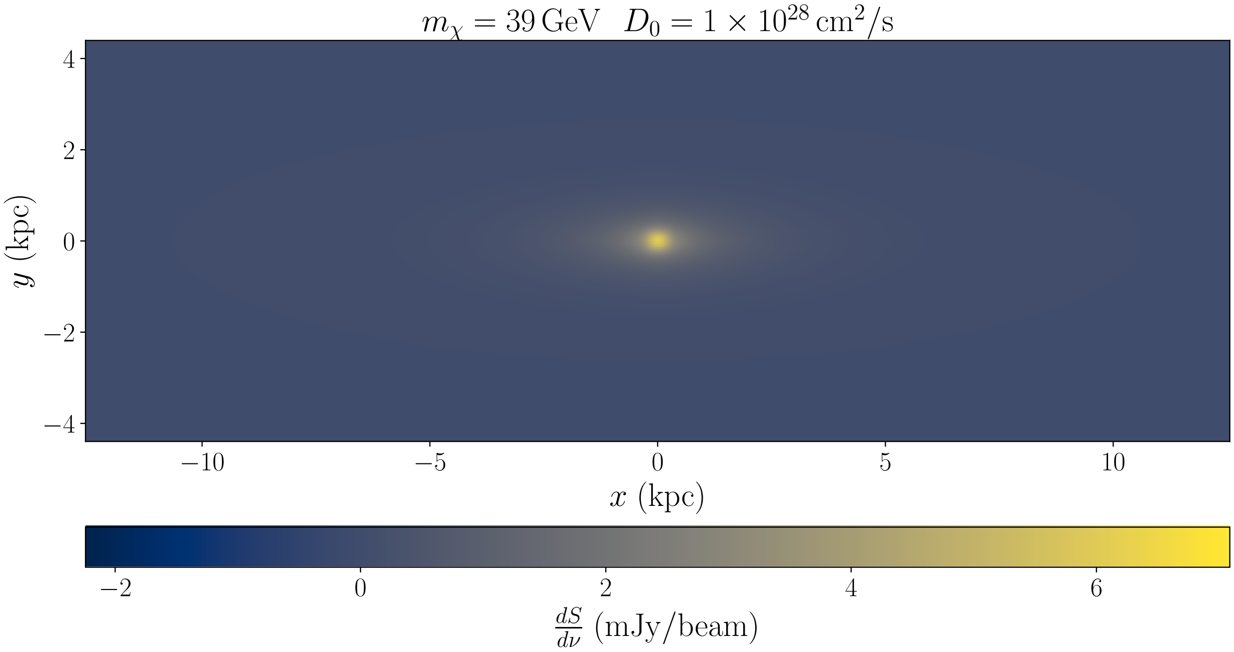

Figure 4.15: Predicted synchrotron emission at a frequency of $\nu = 8.35$GHz from dark matter with $m_\chi = 39$GeV annihilating with a cross-section of $\langle \sigma v \rangle = 2.2 \times 10^{-25}\,\mathrm{cm}^3/\mathrm{s}$. In calculating this synchrotron map, we used our default value of D_0 and our weighted averaging scheme.

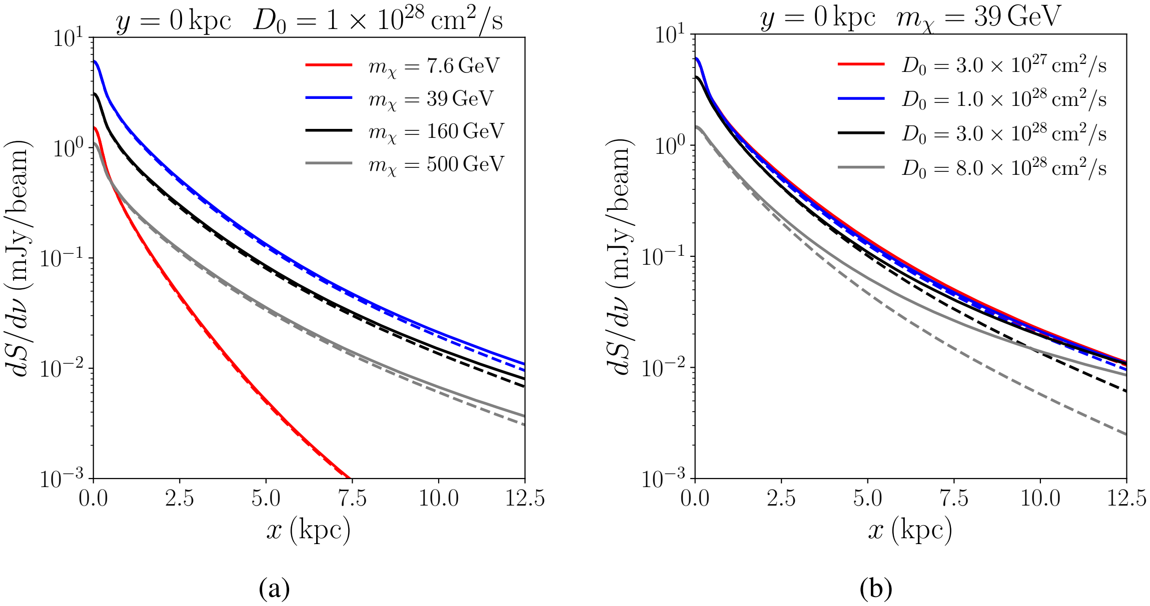

(a)

(b)

Figure 4.16: Predicted synchrotron emission at a frequency of $\nu = 8.35$GHz from dark matter annihilating with a cross-section of $\langle\sigma v\rangle = 2.2 \times 10^{-25}\,\mathrm{cm}^3/\mathrm{s}$. The emission is shown as a function of x, the distance from the center of M31 in the plane of the sky along the semi-major axis. The flux is integrated over the effective beam size of the data, $\Omega_{\mathrm{beam}} = 2.157 \times 10^{-7}\,\mathrm{sr}$. In (a) we fix D_0 to the default value of $1 \times 10^{28}\mathrm{cm}^2/\mathrm{s}$ and vary m_χ. In (b) we set $m_\chi = 39$GeV and vary D_0. The solid curves show the emission using our weighted numerical solutions, dashed curves use the unweighted approach.

the value of D_0 for $D_0 \gtrsim 1 \times 10^{28}\mathrm{cm}^2/\mathrm{s}$ (as seen in Figure 4.16b). For these reasons we set limits using the expected *morphology* of the dark matter signal outside of the center, rather than the total intensity. This also makes our constraints insensitive to possible mismeasurement of the overall zero-level of the radio data.

This approach requires data-driven modeling of the backgrounds within the galaxy. The background emission in M31 is complicated, with numerous point sources and a prominent ring feature (see Figure 4.1). None of these features are morphologically consistent with the expectations of dark matter annihilation, and can safely be attributed to baryonic physics. Even so, a multi-step process is required to define a search region and construct a background model within that region that does not risk fitting-away any potential signal.

In Section 4.7.1, we first describe how we mask the point sources, the ring of radio emission in the disk, and the bright center of M31. This will allow us to define a search region interior to the ring, where the background can be approximated as the residual emission from the ring plus a constant. In the end, the radio emission from this search region will be used to set limits on the dark matter model.

Next in Section 4.7.2, we describe how we determine the background model within the search region using the data itself – without absorbing dark matter emission (potentially present in the data) into the model. We introduce a background model with five free parameters: three morphological parameters (μ_1, μ_2, μ_3) controlling the shape of the residual background from the elliptical ring, and two coefficients (w_1, w_2) which determine the intensity of each component of the background. The morphological parameters are fixed based on the data independent of the signal hypothesis, while the intensity coefficients are adjusted to their most likely values for each hypothesis.

Fixing the morphological parameters must be done carefully to avoid absorbing any signal present in the data into the background model. We leverage the fact that the signal peaks toward the center of M31, while the emission from the ring is dominant away from the center. We therefore can fix the morphological parameters by using the data away from the center of the intensity map (exterior to the dark matter-rich "signal region"). The size of this signal region is determined by comparing fits of the morphological parameters of the background model assuming the presence or absence of a dark matter signal.

After defining the search region and fixing the morphology of our background model within this region, we set statistical limits on specific signal models. We use a CL_s test, described in Section 4.7.3. CL_s works by building distributions of test-statistics from synthetic observations generated from background-only and signal-plus background hypotheses. This test-statistic is sensitive to the morphology of the signal in addition to the amplitude, making this ideal for the distributed signal of dark matter in M31. Our full set of limits varying over astrophysical model parameters and using the methodology we describe here will be shown in Section 4.8.

4.7.1 Background Masks

The baryonic sources of radio emission in M31 are complicated and difficult to model from first principles. Overall, we expect relatively uniform background emission across the interior of the galaxy, overlaid with significant emission from the galactic center due to baryonic processes, as well as point sources throughout the galaxy. In addition, M31 contains a prominent elliptical ring-shaped structure in radio with a semi-major axis of approximately $10\mathrm{kpc}$, due to significant star formation in this region [325, 326]. All of these features can clearly be seen in the radio map of Figure 4.1. The location of the ring correlates with the highest densities of gas in our astrophysical models from Section 4.4.

Notably, other than the emission at the center of the galaxy, the spatial distribution of all of these sources of radio emission is inconsistent with emission sourced by dark matter. Rather than attempting to model these baryonic sources from first principles, we mask and remove them from our statistical analysis. As the emission at the center and the point sources are localized, we are able to completely remove them using masks. The ring of bright emission is broad enough that it cannot be removed completely. Instead, we model it as a Gaussian ring and mask its brightest emission.

4.7.1.1 Point Source Masks

Ref. [271] has removed 38 point sources unrelated to M31. However, many point sources within the galaxy remain in the data. We locate point sources algorithmically by identifying circular regions (with a diameter of 0.75 times the HPBW of the beam) that are over-bright compared to the concentric annulus with inner and outer diameter of 2.25 and 2.75 times the HPBW, respectively. We classify a circular region centered on pixel i a point-source at high ($\sim 4\sigma$) confidence if

$$\langle d\rangle_i^{(\mathrm{cir})} > \langle d\rangle_i^{(\mathrm{ann})} + 4\sigma_{\mathrm{rms}} \tag{4.50}$$

where $\langle d\rangle_i^{(\mathrm{cir})}$ and $\langle d\rangle_i^{(\mathrm{ann})}$ are the flux per beam averaged over the circle and annulus centered at the pixel i, respectively (the noise σ_{rms} is defined in Section 4.2). For each pixel in the radio map that passes this criteria, we mask a circular region (of diameter 0.75 times the HPBW) centered on the pixel.

In addition to these conventional point sources, there is a feature (located near $x = 4\mathrm{kpc}$, $y = 0\mathrm{kpc}$ in Figure 4.1) that is likely an artifact of the imaging process. As this feature does not have the intensity distribution of a point source, it was not identified by our point source algorithm, and we mask it by hand.[5]

4.7.1.2 Center Mask

The center of M31 is the brightest source of radio emission in the galaxy. While dark matter-induced emission would also peak in this region, much of the observed emission is likely due to difficult-to-model baryonic processes. Limits on annihilation can be set by using only this central emission [272, 274, 275], but the intensity of the dark matter signal here is sensitive to the diffusion parameter for $D_0 \gtrsim 1 \times 10^{28}\mathrm{cm}^2/\mathrm{s}$ (as shown in Figure 4.16b). For these reasons, we also mask the center of M31 in our analysis and set limits on dark matter using the region outside the center. Here, the lower signal rate is off-set by the lower background, and the differing morphologies of

---

[5] There is a similar feature near $x = -2\mathrm{kpc}$, $y = -2.5\mathrm{kpc}$. As this feature will not be in the search region (defined in Section 4.7.1.3), we do not mask it manually.

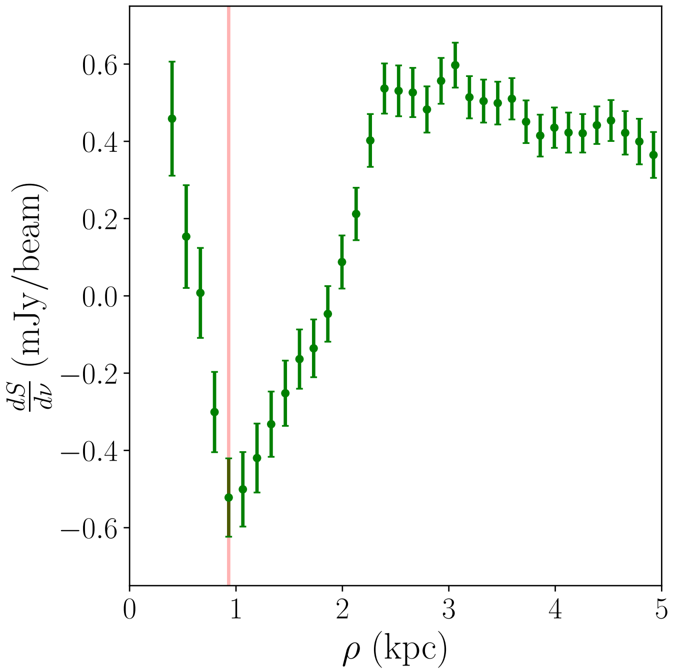

Figure 4.17: Observed flux averaged over concentric circular annuli of radius ρ in the plane of the sky, not including pixels that are in the point source mask. The errors in the annulus averaged flux in a particular bin are found by averaging the rms noise over the bin and dividing by the square root of the number of beams in the bin. The radius of the center circular mask is shown with a red vertical line.

the signal and background can be used to set limits less sensitive to uncertainties in the diffusion coefficient.

Our point-source masking technique also identifies a source at the center of M31, but the default point-source mask is too small to cover the entire bright center region. To determine the size of the central circular mask, we plot the intensity, averaged over concentric circular annuli (excluding pixels in point-source masks), as a function of 2D radius $\rho = (x^2 + y^2)^{1/2}$ in Figure 4.17. We mask the central region out to the minimum of this averaged flux, at $\rho = 0.93\text{kpc}$. The intensity map with point sources and the center masked is shown in Figure 4.18a.

4.7.1.3 Ring and Outside Masks

Finally, we must construct a mask for the elliptical ring of bright emission in the star forming region of the M31 disk [325, 326]. Given the morphology of this feature, it cannot be due to dark

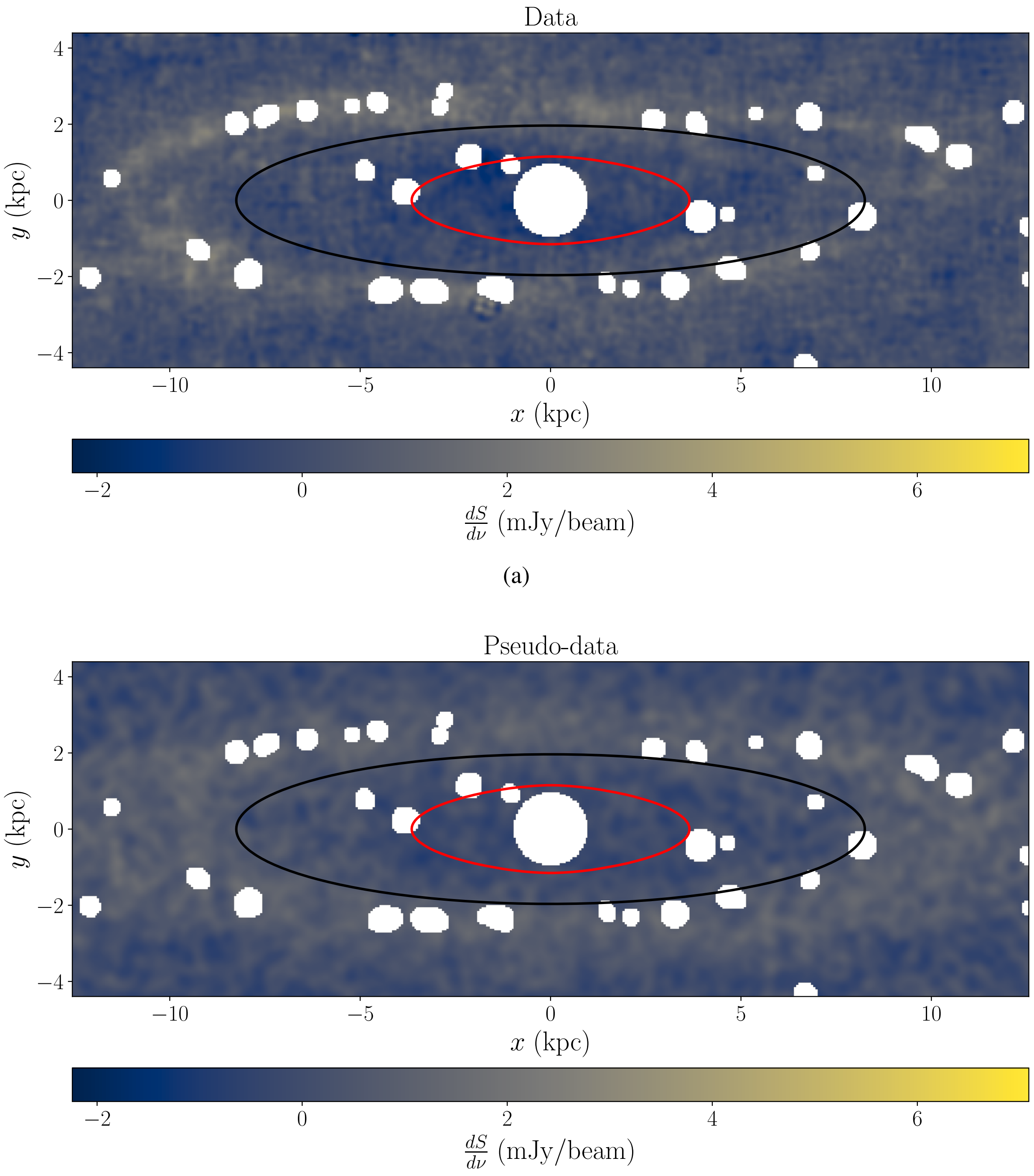

(a)

(b)

Figure 4.18: Intensity maps of the (a) radio data and (b) simulated pseudo-data using the globally-fit background model, with point source and center masks (described in Sections 4.7.1.1 and 4.7.1.2, respectively) applied. The method of simulating the pseudo-data is described in Appendix C.2. The search region (used to set limits on dark matter annihilation, see Section 4.7.1.3) consists of the unmasked pixels within the black contour. The signal region, masked when defining signal-independent background templates (see Section 4.7.2), is interior to the red contour.

matter annihilation. Masking it therefore does not risk removing a potential signal and setting overly-strong constraints.

To construct the mask, we first fit the data to a sum of a uniform template and a Gaussian elliptical ring template which have the forms

$$\begin{aligned}\Phi^u(\boldsymbol{x}; w_1) &= w_1, \\ \Phi^r(\boldsymbol{x}; w_2, \boldsymbol{\mu}) &= w_2 \exp\left[-\frac{\left(R_e(\boldsymbol{x}, \mu_1) - \mu_2\right)^2}{2\mu_3^2}\right],\end{aligned} \tag{4.51}$$

where

$$R_e(\boldsymbol{x}, \mu_1) = \sqrt{x^2 + \mu_1^2 y^2} \tag{4.52}$$

is the elliptical radius, $\boldsymbol{\mu} = (\mu_1, \mu_2, \mu_3)$ are free parameters of the model that control the shape and size of the ring, and $\boldsymbol{w} = (w_1, w_2)$ control the intensity of each component of the background. For the remainder of the paper, we will refer to $\boldsymbol{\mu}$ as the background morphological parameters and $\boldsymbol{w}$ as the background coefficients. The total background model is

$$\Phi^b(\boldsymbol{x}; \boldsymbol{w}, \boldsymbol{\mu}) = \Phi^u(\boldsymbol{x}; w_1) + \Phi^r(\boldsymbol{x}; w_2, \boldsymbol{\mu}) \tag{4.53}$$

As the dark matter-induced annihilation signal is expected to be small at the radius of the ring, we can fit our model to the ring independent of the signal model. We minimize the χ^2 statistic between the observed flux (d_i in pixel i at location $\boldsymbol{x}_i$) and the ring plus uniform background model

$$\chi^2 = \sum_{i=1}^{N_{\text{pix}}} \frac{\left[d_i - \Phi^b(\boldsymbol{x}_i; \boldsymbol{w}, \boldsymbol{\mu})\right]^2}{\sigma^2_{\text{rms,i}}}. \tag{4.54}$$

with respect to all components of $\boldsymbol{w}$ and $\boldsymbol{\mu}$. The resulting best fit values for the morphological parameters are listed in Table 4.5 in the first section (labeled "Full Map Analysis") and second column (labeled "Global Fit"). Figure 4.19 shows the radio data (with point sources and galactic center masked) and the globally fit background model averaged over concentric elliptical annuli (with the same eccentricity as the globally fit ring model) as a function of R_e.

Parameter	Global Fit	Signal-Region Masked
Full Map Analysis		
μ_1	4.20	4.28
$\mu_2(\text{kpc})$	11.1	11.1
$\mu_3(\text{kpc})$	2.88	2.42
Right-Only Analysis		
μ_1	3.63	3.63
$\mu_2(\text{kpc})$	9.30	9.17
$\mu_3(\text{kpc})$	2.39	2.15

Table 4.5: Best-fit morphological parameters for the ring. The Global Fit has the parameter values fit to the data with the center and point sources masked, while the Signal-Region Masked fit is over data with the additional mask over the central signal-rich region applied. We separately show the parameters after fitting to the entire M31 data set (labeled "Full Map Analysis"), and the data in the $x > 0$ right-hand side of Figure 4.1 (labeled "Right-Only Analysis," see Section 4.8).

We show a heatmap of the globally-fit background model superimposed with simulated errors in Figure 4.18b. Our method for simulating random errors correlated over the beam size (which is much larger than the pixel size) is explained in Appendix C.2.

It is clear from Figure 4.19 that the emission outside of the ring ($R_e \gtrsim 15\text{kpc}$) is significantly brighter than the emission inside ($R_e \lesssim 5\text{kpc}$). As the dark matter signal is expected to drop with distance from the center, it cannot be responsible for this excess emission outside the ring. Therefore, we mask exterior to the ring. The width of the best-fit Gaussian is too broad to completely mask the emission out to the level of statistical noise in the region interior to the ring. We instead mask the ring inward to 1 standard deviation from the peak of the Gaussian ring model. That is, we mask all pixels satisfying

$$R_e(\boldsymbol{x}, \mu_1) > \mu_2 - \mu_3, \tag{4.55}$$

using the globally-fit values for the morphological parameters $\boldsymbol{\mu}$.

The inner boundary of the ring mask is shown in black contours in each panel of Figure 4.18. The interior of this contour (minus the center and pixels masked as part of point sources) is the search region that will be used to constrain dark matter annihilation.

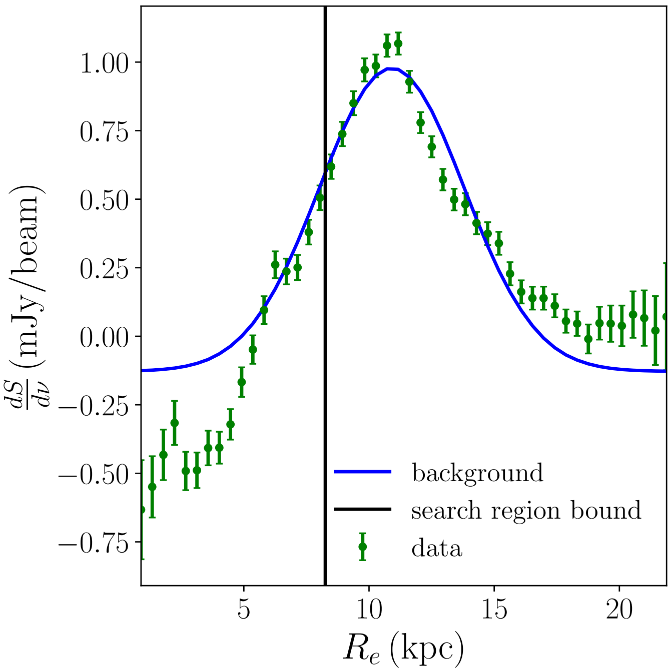

Figure 4.19: Synchrotron data and globally fit background model (parameters given in the "Full Map Analysis" section of Table 4.5) averaged over elliptical annuli as a function of $R_e(\boldsymbol{x}, \mu_1)$ where μ_1 is taken to be the globally fit value.

4.7.2 Background Model of the Search Region

Having selected our search region, we must now define our background model that we will use to construct our background-only and signal plus background hypotheses. The model has the functional form of Eq. (4.53) (used to define the ring and outside-region mask in Section 4.7.1.3), but as the intensity map has the potential to be signal-rich, we must fix the morphological parameters when calculating our limits more carefully than when we initially defined the search region.

If there was a (known) dark matter signal in the data, the parameters of the background model would be most accurately found by subtracting that signal from the data and then fitting our background model to the result. Alternatively, if there is no dark matter signal in the data, the parameters of the background model would be most accurately found by fitting the background model to the data itself. With only the point-source and circular center masks applied, the best fit parameters for the background model are sensitive to the (unknown) presence of signal in the data. We avoid the risk of the background model absorbing any signal present in the data by leveraging the morphology of the signal maps, which peak towards the center of M31.

Unlike the procedure for constructing the globally-fit background model, if we fit the background model only using data outside the center of M31 (where dark matter contributes less to the radio flux), then fits with and without signal subtracted will be more in agreement. The level of statistical agreement will increase as we mask more of an assumed signal. To maximize the amount of signal masked for a given area masked, the mask should have the shape of a region bounded by a contour of constant signal intensity. We will call the inner signal-rich region the “signal region," and the mask that covers it the “signal-region mask."

Our strategy then is to mask the signal region, and fit the parameters of Φ^b to the data exterior to the mask (including data outside the search region). This fit will allow us to define

$$\hat{\Phi}^b(\boldsymbol{x};\boldsymbol{w}) = \Phi^b(\boldsymbol{x};\boldsymbol{w},\hat{\boldsymbol{\mu}}) \tag{4.56}$$

where $\hat{\boldsymbol{\mu}}$ are the morphological parameters, fit outside the signal region and fixed for the rest of the analysis, while $\boldsymbol{w}$ are free parameters which set the amplitude of the various components of the background. These free parameters will be fit to the data (or pseudo-data) in the search region when we set limits on the presence of a dark matter signal. The region exterior to the signal-region mask, used to find $\hat{\boldsymbol{\mu}}$, must be sufficiently signal-poor so that statistical tests that distinguish between signal plus background and background-only hypotheses obtain the same results regardless of whether $\hat{\boldsymbol{\mu}}$ is determined by assuming the presence or absence of signal in the data.

To identify this signal-poor region, we use as a benchmark signal the flux from dark matter with $m_\chi = 38.6\mathrm{GeV}$, $\langle\sigma v\rangle = 2.2\times10^{-25}\mathrm{cm}^3/\mathrm{s}$ and a diffusion normalization of $D_0 = 1\times10^{28}\mathrm{cm}^2/\mathrm{s}$. As the leakage out of the masked signal region is minimal and the signal morphology depends only weakly on the choice of mass and diffusion parameters, the resulting fits can be applied to signals with other values of m_χ and D_0. The cross-section is chosen to be approximately an order of magnitude larger than the best fit value from the GCE [255, 254, 253, 252] and existing limits from dwarf galaxies [243, 242, 244, 245, 246, 248]. Our fitting procedure will ensure that the background model is not significantly influenced by the presence of dark matter signals of this intensity and weaker in the data.

We make a series of candidate signal-region masks that intersect the semi-major axis at x values between $[1.0 - 8.8]\,\mathrm{kpc}$. For each of these masks, we fit our background model (Eq. (4.53)) to the remaining unmasked data with signal subtracted (defined as "Fit A") or without signal subtracted ("Fit B") by minimizing Eq. (4.54) with respect to all components of $\boldsymbol{w}$ and $\boldsymbol{\mu}$. We take the sum in Eq. (4.54) to be over pixels not covered by the candidate signal region mask, the center mask, or point source masks.

For each candidate signal-region mask, we determine if Fits A and B of the morphological parameters lead to statistically indistinguishable results when testing for the presence of signal. To compare the background-only and signal plus background hypotheses, we introduce a test statistic, defined as

$$\begin{aligned}\lambda_{\langle\sigma v\rangle,\boldsymbol{\theta}}(\{d_i\}) =& \Delta\chi^2 = \chi^2_{s+b} - \chi^2_b \\ =& \sum_i \frac{\left[d_i - \hat{\Phi}_i^{s+b}(\langle\sigma v\rangle, \boldsymbol{\theta}, \boldsymbol{w^{s+b}})\right]^2}{\sigma^2_{\mathrm{rms},i}} \\ &- \sum_i \frac{\left[d_i - \hat{\Phi}_i^{b}(\boldsymbol{w^{b}})\right]^2}{\sigma^2_{\mathrm{rms},i}},\end{aligned} \tag{4.57}$$

This statistic will also be used in our methodology for setting limits on dark matter (see Section 4.8). In Eq. (4.57), $\{d_i\}$ are the differential flux values in each pixel of the intensity map, and the sum runs over pixels i that are in the search region (defined in Section 4.7.1). $\boldsymbol{w^b}$ ($\boldsymbol{w^{s+b}}$) are the most-likely values of the background coefficients, $\boldsymbol{w} = (w_1, w_2)$, under the background-only (signal plus background) hypothesis and are determined analytically for each intensity map. The test statistic is constructed such that higher test statistic values imply that the intensity map is more background-like.

The test statistic depends on the signal hypothesis being tested through the signal plus background model

$$\hat{\Phi}_i^{s+b}(\langle\sigma v\rangle, \boldsymbol{\theta}, \boldsymbol{w^{s+b}}) = \Phi_i^s(\langle\sigma v\rangle, \boldsymbol{\theta}) + \hat{\Phi}_i^b(\boldsymbol{w^{s+b}}), \tag{4.58}$$

where the signal flux at the pixel centered at solid angle Ω_i is given by

$$\Phi_i^s(\langle\sigma v\rangle, \boldsymbol{\theta}) \equiv \Omega_{\text{beam}} \left.\frac{d^2S}{d\Omega d\nu}\right|_{\Omega_i, \langle\sigma v\rangle, \boldsymbol{\theta}} \tag{4.59}$$

using the differential flux calculated in Section 4.6. The signal hypothesis is parameterized by the cross section $\langle\sigma v\rangle$ and a vector $\boldsymbol{\theta}$, containing m_χ, D_0 and all other default astrophysical parameters, given in Section 4.4.

For a given candidate signal-region mask, we calculate distributions of test statistics from ensembles of pseudo-data using background models with morphological parameters fixed by Fits A and B. These ensembles are drawn using the methods described in Appendix C.2, using the $\hat{\Phi}_i^b$ appropriate for each fit, summing over pixels in the search region for each calculation of $\lambda_{\langle\sigma v\rangle, \boldsymbol{\theta}}$. As the test statistic requires a choice of signal parameters, we use as our reference signal model $m_\chi = 38.6\,\text{GeV}$, $D_0 = 1 \times 10^{28}\,\text{cm}^2/\text{s}$, and a cross-section for which the signal plus background hypothesis is easily distinguished from the background hypothesis: $\langle\sigma v\rangle = 1.1 \times 10^{-25}\,\text{cm}^3/\text{s}$. If – for a given signal mask – the distribution of test-statistics is indistinguishable between background Fits A and B, then the same will be true for the result of a statistical test for distinguishing signal plus background from background. This means the morphological parameters can be fit to the data using that signal region mask without absorbing potential signal from the data.

Figure 4.20 shows the mean test statistic using candidate Fits A and B as a function of the distance from the origin that the signal region mask intersects the semi-major axis. For a mask which intersects the semi-major axis at $x = 3.65\text{kpc}$, the means of the distributions of the test statistic from Fits A and B agree within statistical noise. Selecting this signal region mask (shown with a red contour in Figure 4.18), we set $\hat{\boldsymbol{\mu}}$ to the best-fit morphological parameters of Fit B. The values of the morphological parameters from this fit are shown in Table 4.5 (the “Signal-Region Masked" column of the “Full Map Analysis" section). To construct our signal plus background

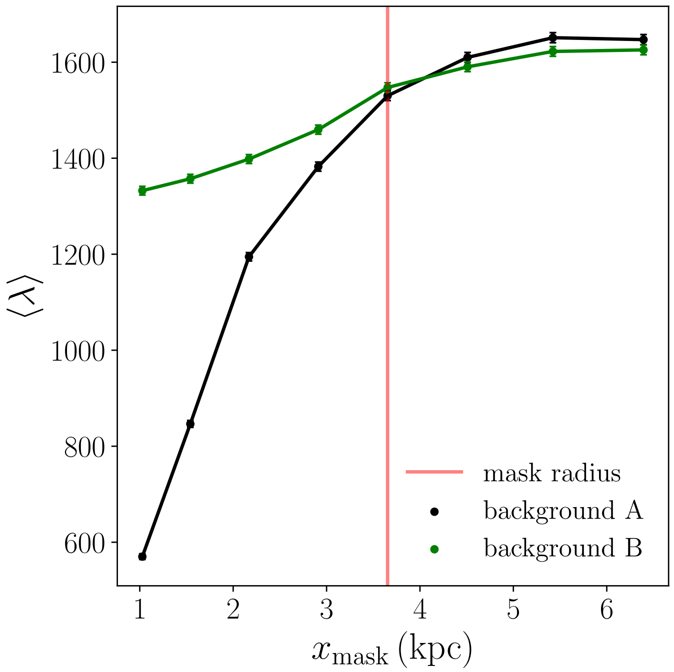

Figure 4.20: Mean test statistics from background-only pseudo-data for a series of candidate fits of the morphological parameters of the background model. Each fit comes from minimizing Eq. (4.54) outside of the candidate signal region mask that intersects the semi-major axis of M31 at $x_{\rm mask}$, assuming the presence (green) or absence (black) of dark matter signal in the data. The distributions of test statistics are constructed for a signal from dark matter with $m_\chi = 38.6 \text{GeV}$ and $\langle\sigma v\rangle = 1.1 \times 10^{-25} \text{cm}^3/\text{s}$ and default diffusion normalization of $D_0 = 1 \times 10^{28} \text{cm}^2/\text{s}$. The size of the signal-region mask that we select is shown with the red vertical line.

and background-only hypotheses, we will use the background model with the morphological parameters fixed to $\hat{\boldsymbol{\mu}}$ and the coefficients $\boldsymbol{w} = (w_1, w_2)$ free to float to their most likely values for each hypothesis.

4.7.3 Limits on a Signal Model

Having fixed our background model morphology, we now describe our statistical approach to setting limits on dark matter annihilation in M31, using the data in the entire search region. In order to maximize the statistical power in the morphology of the signal when setting limits, we use the CL_s method [327] with pixel-level radio data and templates.

As in Section 4.7.2, we parameterize our signals using the cross section $\langle \sigma v \rangle$, and the parameter vector $\boldsymbol{\theta}$ which includes the dark matter mass m_χ and diffusion coefficient D_0. We will use the test statistic $\lambda_{\langle \sigma v \rangle, \boldsymbol{\theta}}$ from Eq. (4.57) to distinguish between background-like and signal plus background-like intensity maps.

Statistical inference for a signal parameterized by $\langle \sigma v \rangle$ and $\boldsymbol{\theta}$ requires the probability distributions of $\lambda_{\langle \sigma v \rangle, \boldsymbol{\theta}}$ under our background-only and signal plus background hypotheses. We construct these probability distributions by generating an ensemble of simulated observations of M31 under each hypothesis and calculating $\lambda_{\langle \sigma v \rangle, \boldsymbol{\theta}}$ for each simulated observation. The simulated observations are generated under the background (signal plus background) hypothesis by superimposing $\hat{\Phi}^b$ ($\hat{\Phi}^{s+b}$) with randomly drawn noise maps. The probability distribution from which the noise maps are drawn has correlations between nearby pixels, as expected due to the Gaussian beam of the observations (described in Section 4.2). More details on our procedure for producing pseudodata are described in Appendix C.2.

In Figure 4.21, we show sample distributions of $\lambda_{\langle \sigma v \rangle, \boldsymbol{\theta}}$ for $m_\chi = 38.6\,\mathrm{GeV}$, $D_0 = 1 \times 10^{28}\,\mathrm{cm}^2/\mathrm{s}$ and two choices of $\langle \sigma v \rangle$ ($1.1 \times 10^{-26}\mathrm{cm}^3/\mathrm{s}$ and $4.6 \times 10^{-26}\mathrm{cm}^3/\mathrm{s}$). In these examples, the blue and red histograms are the distributions of the test statistic assuming background and signal plus background (respectively) in arbitrary units. The solid curves are the Gaussian approximations of each distribution. The vertical green line in each plot is the value

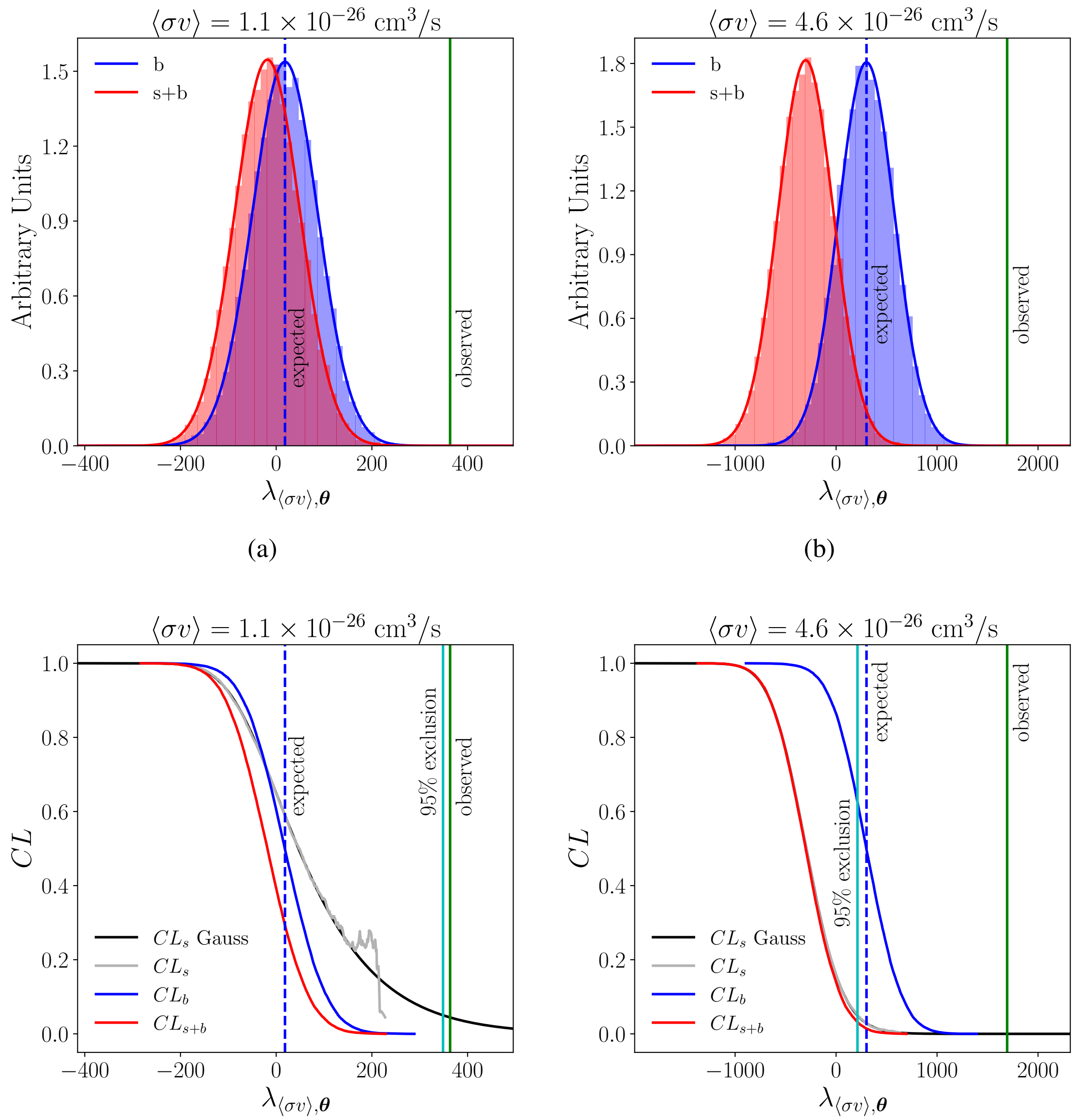

(a)

(b)

(c)

(d)

Figure 4.21: Top row: example histograms of $\lambda_{\langle\sigma v\rangle,\boldsymbol{\theta}}$ for background and signal plus background hypotheses for a signal parameterized by $m_\chi = 38.6$GeV and $D_0 = 1\times10^{28}$cm^2/s. Plot (a) has $\langle\sigma v\rangle = 1.1\times10^{-26}$cm^3/s and (b) has $\langle\sigma v\rangle = 4.6\times10^{-26}$cm^3/s. The value of $\lambda_{\langle\sigma v\rangle,\boldsymbol{\theta}}$ for the data is shown with the vertical green lines and the median expected test statistics from the background only hypothesis are shown with the dashed blue vertical lines. Each distribution is constructed from $N = 20000$ independent simulated maps. The smooth curves are Gaussian approximations of the distributions. Bottom row: example CL curves for the signal models shown above. The black curve is an approximation of CL_s derived from the Gaussian approximations of the distributions of the test statistic. The test statistic that is excluded at 95% confidence according to the Gaussian approximation of CL_s is shown with a vertical cyan line.

of $\lambda^{(\mathrm{obs})}_{\langle\sigma v\rangle,\boldsymbol{\theta}} \equiv \lambda_{\langle\sigma v\rangle,\boldsymbol{\theta}}(\{d_i^{(\mathrm{obs})}\})$, evaluated on the actual M31 radio data.

For an arbitrary signal hypothesis parameterized by $\langle\sigma v\rangle$ and $\boldsymbol{\theta}$, our distributions of $\lambda_{\langle\sigma v\rangle,\boldsymbol{\theta}}$ can be used to approximate the probability distribution of $\lambda_{\langle\sigma v\rangle,\boldsymbol{\theta}}$ assuming background:

$$p_{\langle\sigma v\rangle,\boldsymbol{\theta}}(\lambda|b) \equiv p(\lambda_{\langle\sigma v\rangle,\boldsymbol{\theta}} = \lambda|b), \tag{4.60}$$

and signal plus background:

$$p_{\langle\sigma v\rangle,\boldsymbol{\theta}}(\lambda|s+b,\langle\sigma v\rangle,\boldsymbol{\theta}) \equiv p\left(\lambda_{\langle\sigma v\rangle,\boldsymbol{\theta}} = \lambda|s+b,\langle\sigma v\rangle,\boldsymbol{\theta}\right). \tag{4.61}$$

A given observation with test-statistic $\lambda^{(\mathrm{obs})}_{\langle\sigma v\rangle,\boldsymbol{\theta}}$ then has a CL_b value given by the probability of seeing data more background-like than observed, assuming the background-only hypothesis is correct:

$$CL_b\left(\lambda^{(\mathrm{obs})}_{\langle\sigma v\rangle,\boldsymbol{\theta}},\langle\sigma v\rangle,\boldsymbol{\theta}\right) = \int\limits_{\lambda^{(\mathrm{obs})}_{\langle\sigma v\rangle,\boldsymbol{\theta}}}^{\infty} d\lambda\; p_{\langle\sigma v\rangle,\boldsymbol{\theta}}(\lambda|b). \tag{4.62}$$

Similarly, the CL_{s+b} value for the observation is the probability of seeing a more background-like intensity map than that observed, assuming that the signal plus background hypothesis is correct:

$$CL_{s+b}\left(\lambda^{(\mathrm{obs})}_{\langle\sigma v\rangle,\boldsymbol{\theta}},\langle\sigma v\rangle,\boldsymbol{\theta}\right) = \int\limits_{\lambda^{(\mathrm{obs})}_{\langle\sigma v\rangle,\boldsymbol{\theta}}}^{\infty} d\lambda\; p_{\langle\sigma v\rangle,\boldsymbol{\theta}}(\lambda|s+b,\langle\sigma v\rangle,\boldsymbol{\theta}). \tag{4.63}$$

The ratio $CL_s\left(\lambda^{(\mathrm{obs})}_{\langle\sigma v\rangle,\boldsymbol{\theta}},\langle\sigma v\rangle,\boldsymbol{\theta}\right) \equiv CL_{s+b}/CL_b$ can then be interpreted as the probability of signal parameters greater than $\langle\sigma v\rangle$, given data. A 95% confidence level exclusion therefore corresponds to a signal for which

$$CL_s(\lambda^{(\mathrm{obs})}_{\langle\sigma v\rangle,\boldsymbol{\theta}},\langle\sigma v\rangle,\boldsymbol{\theta}) = \frac{CL_{s+b}(\lambda^{(\mathrm{obs})}_{\langle\sigma v\rangle,\boldsymbol{\theta}},\langle\sigma v\rangle,\boldsymbol{\theta})}{CL_b(\lambda^{(\mathrm{obs})}_{\langle\sigma v\rangle,\boldsymbol{\theta}},\langle\sigma v\rangle,\boldsymbol{\theta})} = 0.05. \tag{4.64}$$

The expected 95% confidence limits correspond to signal parameters for which the median test statistic under the background hypothesis ($CL_b = 0.5$) leads to $CL_s = 0.05$. The 1 and 2σ errors of this expected limit are calculated using the corresponding percentiles of the background distribution.

Example CL curves are shown in Figures Figure 4.21c and Figure 4.21d (corresponding to the distributions of the test statistics in Figures Figure 4.21a and Figure 4.21b, respectively). The CL_s curve of each plot (shown in grey) is dominated by statistical noise in the simulated intensity maps when CL_b and CL_s are small. As seen in this example, we generically find that $\lambda^{(\mathrm{obs})}_{\langle\sigma v\rangle,\boldsymbol{\theta}}$ is $5-6\sigma$ larger than the mean of the background-only distribution for our search region,[6] implying that CL_b of the observed test statistic is $\sim 2\times 10^{-8}$.

The fact that the *observed* test statistics are located on the tail of the CL_b distributions is a consequence of observed radio intensities that are much less signal-like than the signal-free background model. We confirmed that this issue exists for all values of m_χ and D_0 studied in this work. This means that while the background model does not describe the observations well, the observed deviations away from the background-only model are not compatible with the morphology of any signal. This will lead to limits that are much stronger than expected.

This issue requires further investigation. In Figure 4.22a, we show our best fit background model and signal plus background model with $\langle\sigma v\rangle = 1.1\times 10^{-26}\mathrm{cm}^3/\mathrm{s}$ for $m_\chi = 38.6\mathrm{GeV}$ and $D_0 = 1\times 10^{28}\mathrm{cm}^2/\mathrm{s}$ along with the data in the search region as a function of elliptical distance from the center of the map (note that this choice of signal parameters is excluded at 95% confidence).[7] As can be seen, the residuals of the data with respect to the background-only model are negative for $R_e \lesssim 4\mathrm{kpc}$, but the signal plus background model predicts a larger flux than the background-only model in this region.

In Figures Figure 4.22c and Figure 4.22b we show elliptically averaged radio emission as well as best fit models in the left search region (masking the $x > 0$ data) and right search region

---

[6] To obtain CL values not dominated by the finite statistics in our simulated intensity maps would require $\sim 10^9$ maps. Instead, we set limits in this regime by extrapolating the test statistic distributions by fitting them to Gaussians and calculating an approximation of CL_s using these extrapolations (shown in black in Figures Figure 4.21c and Figure 4.21d).

[7] To produce this plot, we compute the average flux per beam in pixels in the search region in concentric elliptical annuli with the same eccentricity as the globally fit ring model.

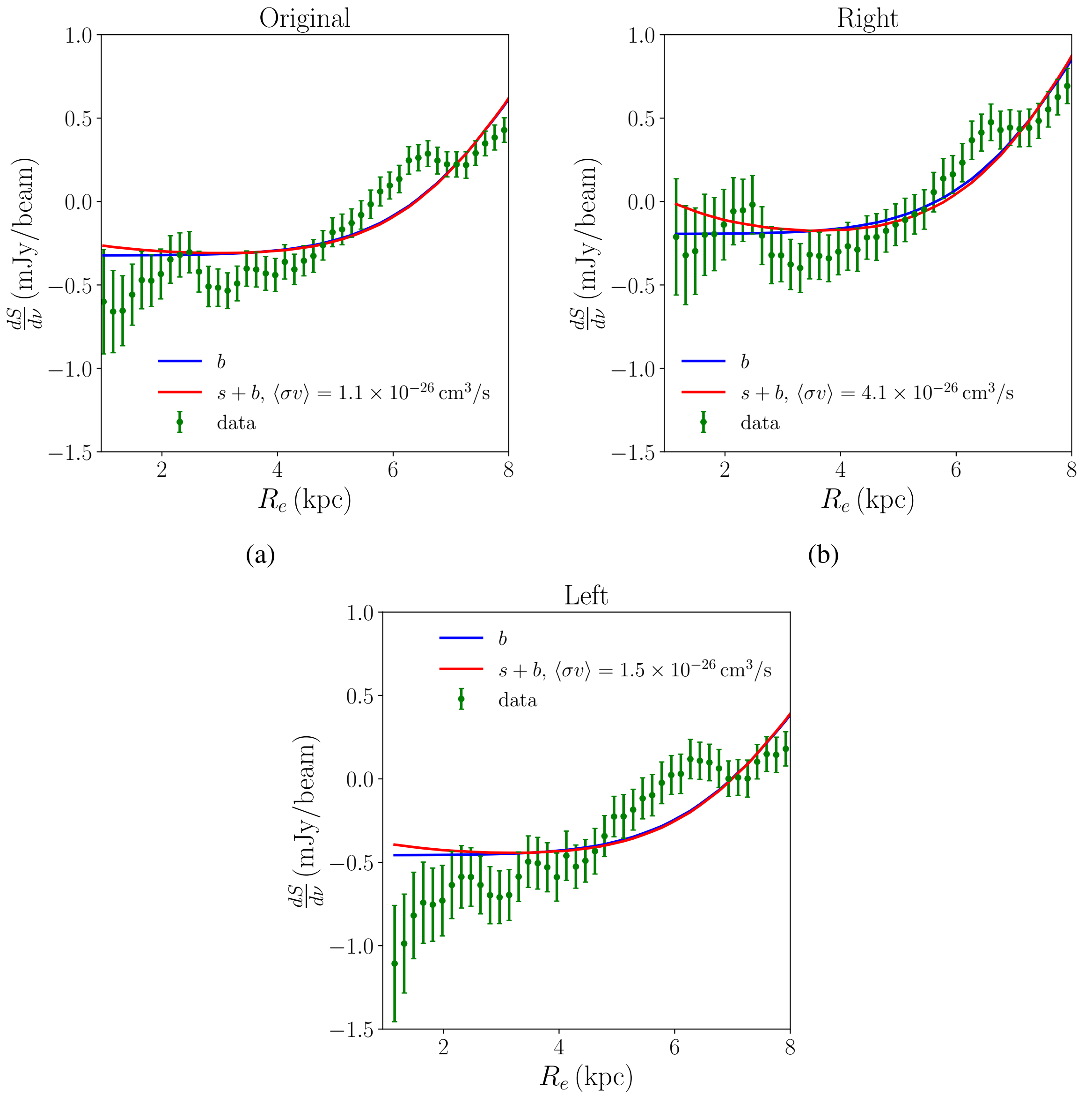

(a)

(b)

(c)

Figure 4.22: Radio Flux averaged over concentric elliptical annuli as function of $R_e(\boldsymbol{x}, \mu_1)$ (with μ_1 given by the global fit of the Full Map analysis) along with the best fit background model and the excluded signal plus background model for (a) the original search region, (b) the left half search region, and (c) the right half search region. All signal plus background models shown have $m_\chi = 38.6\text{GeV}$ and $D_0 = 1 \times 10^{28}\text{cm}^2/\text{s}$. For the excluded signal plus background model, we take the lowest value of $\langle\sigma v\rangle$ that leads to 95% exclusion for the values of mass and diffusion normalization plotted.

(masking $x < 0$), respectively. As can be seen, the large negative excursion in the left search region is the source of the negative residuals we identified in Fig. Figure 4.22a and can be traced specifically to the large negative observed flux located around $(x, y) \sim (-2, 1)\,\mathrm{kpc}$. This negative flux is clearly visible in Figures Figure 4.1 and Figure 4.18a. The low flux measurement (well in excess of a 2σ deviation given the expected measurement errors) may be due to the over-subtraction of a point source external to M31.

Critically, given our understanding of the dark matter distribution within M31, dark matter emission cannot create such a region of low emission close to the center of M31, even if the overall baseline of zero radio flux was mismeasured. Thus, considering only the part of the data without this region of anomalously low emission will not set overly-optimistic limits on dark matter annihilation. Indeed, we will see in the next section that it sets more conservative and weaker bounds.

4.8 Constraints on Annihilating Dark Matter in M31

In light of the findings from last section, we first calculate limits for the original search region (within the black contour in Fig. Figure 4.18a) and compare them to the limits from the right and left search regions. We set $95\%\, CL_s$ exclusion limits for dark matter with mass in the range $[6 - 500]$ GeV, annihilating to $b\bar{b}$. In Figure 4.23 we show the limits on $\langle \sigma v \rangle$ as a function of m_χ, assuming the default diffusion parameter normalization $D_0 = 1 \times 10^{28}\mathrm{cm}^2/\mathrm{s}$. This includes the observed limits for the original, right and left search regions with black curves of various styles, alongside the 1 and 2σ variation around the expected limits for the original search region. As expected, the observed limit for the original search region is far stronger than the 2σ variation assuming the background hypothesis. The limits from the left search region are nearly as strong as those from the original search region while the limits from the right search region are approximately as strong as expected, confirming that the stronger-than-expected limits come entirely from the left-hand side of the M31 emission, where the region of negative flux is located.

To get the most accurate limits using only the right side of the map, we recalculate the search

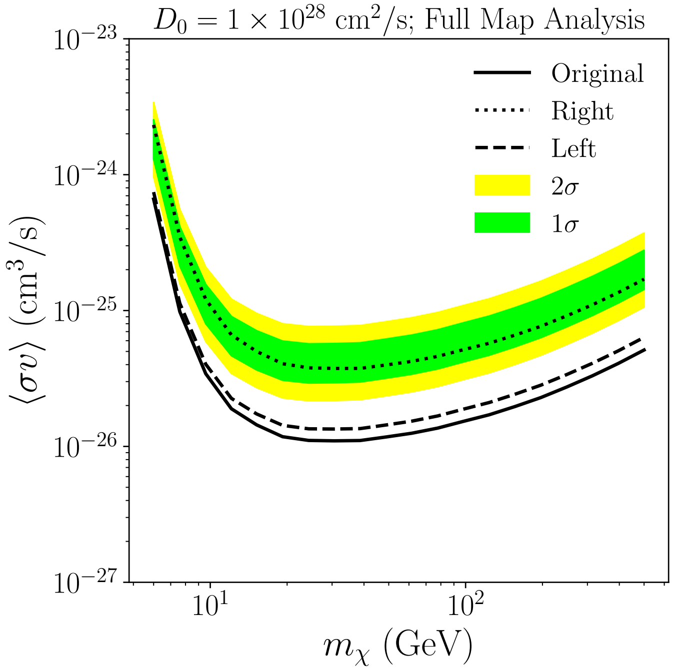

Figure 4.23: 95% confidence limits on dark matter annihilation assuming $D_0 = 1 \times 10^{28}\mathrm{cm}^2/\mathrm{s}$ from our Full Map analysis. The 1σ and 2σ expected limits from the original search region are shown in green and yellow, with the observed limits for this search region shown with a solid line (labeled “original”). The dotted and dashed lines are the actual limits from the data in the right ($x > 0$) and left ($x < 0$) half of the search region, respectively.

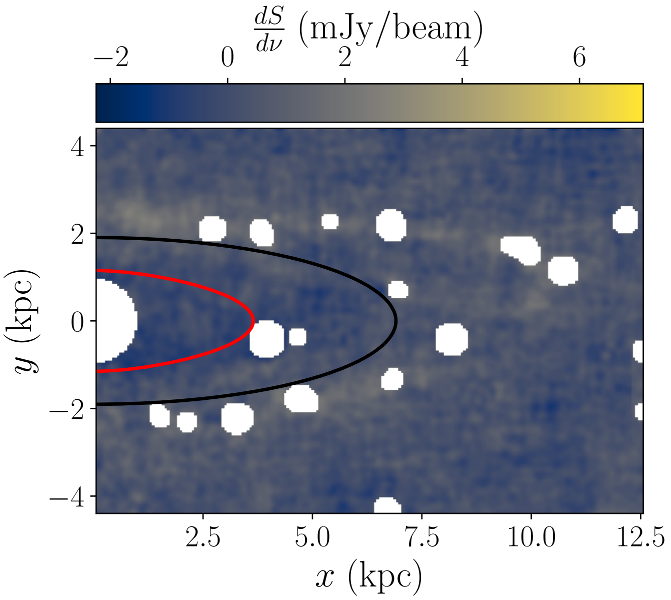

Figure 4.24: As Figure 4.18a but for the right-only analysis. The search region contour is recalculated with the left side of the image masked, and thus differs slightly from the search region of the full map analysis.

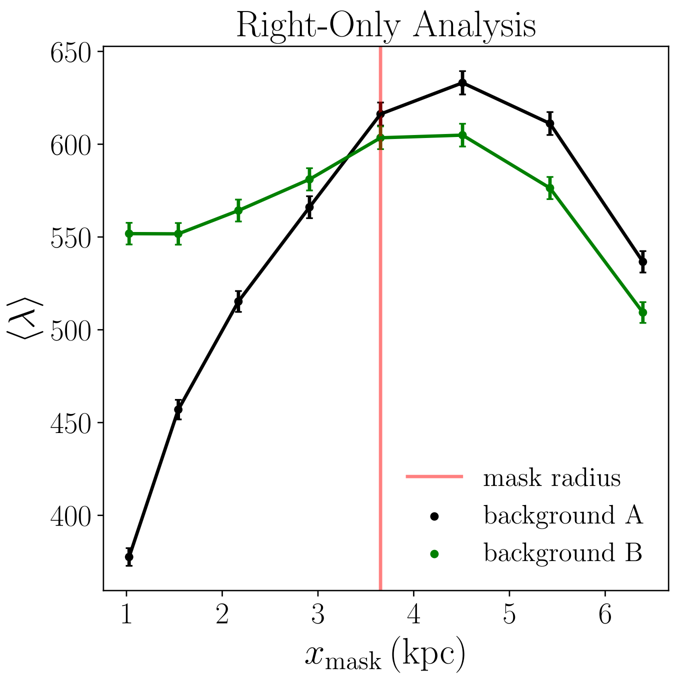

Figure 4.25: As Figure 4.20, but for our analysis with the left side of the data masked.

region and re-fix the background morphological parameters with the left side of the data masked, using the steps described in Sections 4.7.1 and 4.7.2. The resulting morphological parameter values used to recalculate the search region are shown in the “Right-Only Analysis" section of Table 4.5 in the second column (labeled “Global Fit"). The new search region is bounded by the black contour in Figure 4.24. We show the resulting test statistics as a function of candidate signal region mask size for background Fits A and B in Figure 4.25. Based on this, we select the signal region mask for the right-only analysis which intersects the semi-major axis at $x = 3.65\text{kpc}$, where the mean test statistics from Fits A and B agree within statistical error. This turns out to be the same signal region mask that we found for our full map analysis. This signal region mask is bounded by the red contour in Figure 4.24. We fix the morphological parameters of the background model $\boldsymbol{\mu}$ to the best fit values from background model B with this signal region mask. The resulting values for the morphological parameters are shown in the third column (labeled “Signal-Region Masked") of the second half (labeled “Right-Only Analysis") of Table 4.5.

Using this background model for the right-only analysis, we show in Figures Figure 4.26a and Figure 4.26b examples of the test statistic distributions and CL curves for pseudo-data in the right search region and show sample distributions, for $m_\chi = 38.6\text{GeV}$, $D_0 = 1 \times 10^{28}\text{cm}^2/\text{s}$, and $\langle \sigma v \rangle = 7.4 \times 10^{-26}\text{cm}^3/\text{s}$. This is the cross section that is excluded at approximately 95% confidence for these values of m_χ and D_0.

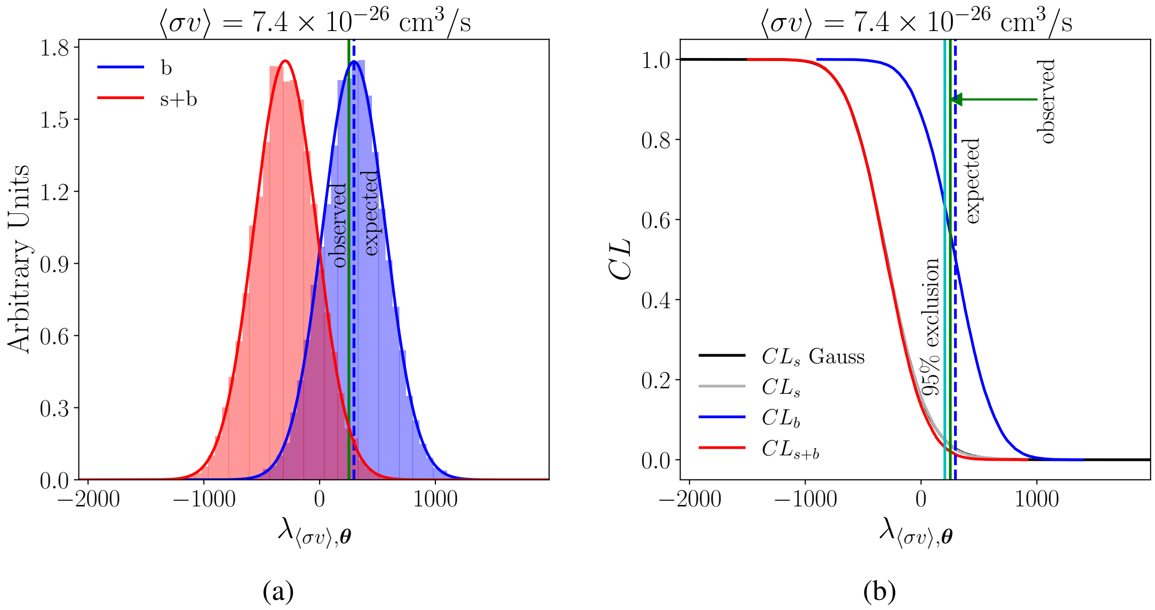

(a)

(b)

Figure 4.26: Same as Figure 4.21 but for the right-only analysis. The cross-section shown here is close to the expected and actual 95% confidence limit. The expected limit is almost the same as the actual limit since the test statistic from the data is very close to the 50th percentile test statistic from background pseudo-data.

In Figure 4.27, we show our limits on $\langle \sigma v \rangle$ as a function of m_χ, using the right-only analysis. These results constitute our most conservative and robust limits on dark matter annihilation using the radio observations of M31. In both panels, the green and yellow bands quantify the 1 and 2σ statistical error of our expected limits for our default value of D_0 and for the weighted averaging scheme, introduced in Section 4.5.3 (and otherwise default parameters). Each panel quantifies the effects of different systematics on our results. In Figure 4.27a we show the observed 95% confidence exclusion limit from each spherically averaging procedure for our default value of D_0. As can be seen, the limits do not depend on the averaging scheme used. In Figure 4.27b, we show the observed limits as D_0 is varied. The limits are relatively insensitive to variations of the diffusion coefficient in the range $3 \times 10^{27}\text{cm}^2/\text{s} \leq D_0 \leq 3 \times 10^{28}\text{cm}^2/\text{s}$. The limits become about

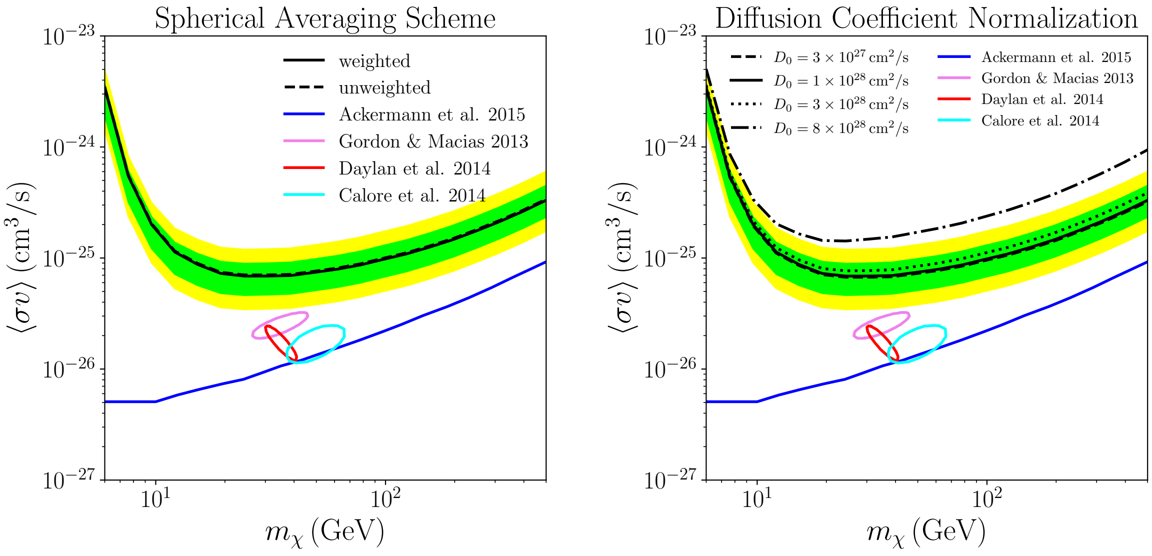

(a) (b)

Figure 4.27: Expected and actual 95% confidence limits from the right-only analysis, using the data from the search region shown in Figure 4.24. The two panels show the variation of the observed limits due to (a) changes in the averaging procedure (introduced in Section 4.5.3) for our default diffusion coefficient normalization and (b) changes in the diffusion coefficient normalization, D_0 for our weighed averaging scheme. Both panels have the expected limits obtained using the default value of D_0 ($1 \times 10^{28}\text{cm}^2/\text{s}$) and the weighted averaging scheme. The contours show best fits to the GCE [252, 253, 255] and the solid blue lines show limits from dwarfs using *Fermi* Pass 8 data [248].

a factor of three weaker when D_0 changes from $3 \times 10^{28}\mathrm{cm}^2/\mathrm{s}$ to $8 \times 10^{28}\mathrm{cm}^2/\mathrm{s}$ for $m_\chi \gtrsim 10\mathrm{GeV}$. We also show best fit contours to the GCE from previous analyses [252, 253, 255], as well as limits from Milky Way dwarfs using *Fermi* Pass 8 data [248]. Our limits do not exclude parameters that fit the GCE. Although our limits are weaker than the dwarf limits, they are robust to astrophysical uncertainties.

4.9 Conclusion

In this work, we have set robust and conservative limits on dark matter annihilation to $b\bar{b}$ using the $8.35\,\mathrm{GHz}$ Effelsberg radio map of M31, which is sensitive to the predicted synchrotron emission of the $e^{\pm}$ produced in the cascade b decays. These limits are based on a numeric solution to the diffusion-loss equation that accommodates non-uniform parameters, and an astrophysical model that uses observations of the gas, dust, starlight, and magnetic fields of M31. Our ISRF model for the starlight is derived directly from *ugriz* luminosity data, which led to notably larger values for ρ_* in the center of M31 compared to previous works.

Unlike previous studies, our numerical solution to the diffusion-loss equation allows for position dependent diffusion and loss coefficients. Our method still requires spherical averaging of the background model. Though we have shown that our final limits are insensitive to the averaging procedure, additional work is needed to develop a numeric solution which is adapted to the axisymmetry of M31.

Our limits are based on the morphology of the observed flux, and our results are independent of the true zero-flux level of the intensity map. The limits are based on the radio flux only interior to the bright ring of radio emission in M31, allowing us to use data-driven models of the background based on signal-poor regions of the observed intensity map. Due to a localized anomaly of low radio flux in the search region, we choose conservatively to select only the half of the dataset without this anomaly with which to set our limits.

Our limits on dark matter annihilation in M31 do not exclude best-fit models to the GCE (shown as contours in Figures Figure 4.27a& Figure 4.27b) and are weaker than those found in previous radio studies [272, 273, 274, 275]. These weaker limits are due in part to the fact that in our analysis we mask the center of the galaxy, where the signal intensity is maximum – however, this choice minimizes the sensitivity to unknown astrophysical parameters at the galactic center. The weaker limits are also likely due to the differences in our astrophysical model of M31 compared to previous work. In particular, the core of M31 is much more luminous in starlight than a simple scaling of the comparable region of the Milky Way would suggest. This increased starlight flux results in increased energy losses of $e^{\pm}$ into X-rays through inverse Compton scattering, reducing the flux of dark matter-induced radio waves. Though beyond the scope of this work, this suggests that an analysis of constraints from X-ray emission in the center of M31 from dark matter annihilation may set interesting limits.

The sensitivity of the limits to the astrophysical conditions within M31 are notable; though in this work we have taken care to construct an accurate model of M31 based on observations, future measurements and astronomical input would likely improve the model and the resulting limits. Similar analysis is likely necessary for constraints on dark matter annihilation via radio waves in other systems beyond M31.

CHAPTER 5

CONCLUSION

In this thesis we set constraints on new physics using cosmological and astrophysical observations, providing insights far beyond the reach of laboratory experiments. In Chapter 2, we showed that generic isocurvature initial conditions can be stringently bound over a large range of scales by the CMB, BAO and Ly-α forest datasets. The δ function parameterization allowed us to parse the sensitivity of these datasets over a range of wavenumbers. The broken power-law has features in common with the power spectrum predicted by a range of cosmological phenomena. In Chapter 3 we focused on a class of cosmological phase transitions that produced dark radiation with a pattern of perturbations that are statistically independent from those of the adiabatic mode. These perturbations in dark radiation can last until reheating sourcing an isocurvature mode with a power spectrum given by the generic broken power law of Chapter 2.

In Chapter 4, we developed observation-driven models of the astrophysical environment of Andromeda and a radially dependent diffusion-loss solver to calculate the propagation and resulting synchrotron radiation from high energy $e^{\pm}$ produced in dark matter annihilation. Using this numerical pipeline, we simulated radio signals from dark matter annihilation in M31 and extracted robust morphology-driven 95% CL upper limits on $\langle\sigma v\rangle$ for dark matter masses in the range $6-500\,\mathrm{GeV}$. These results are not the strongest reported limits but they are fairly robust to astrophysical uncertainties such as the diffusion coefficient and magnetic field structure.

The results presented here motivate several potential directions for future research. For the isocurvature constraints derived in Chapter 2, additional improvements could come from analyzing forthcoming cosmological datasets, especially those sensitive to smaller scales, such as deeper measurements of the Ly-α forest and higher-resolution observations of the CMB. In Chapter 3, we noted that a full treatment of gravitational wave signatures arising from cosmological phase transitions could complement isocurvature constraints, potentially allowing more stringent lower bounds on the energy scale of inflation. Regarding the dark matter analysis in Chapter 4, future sensitivity improvements could result from incorporating data in multiple frequency bands, as well as refining models of cosmic-ray propagation and diffusion parameters within galaxies. These directions highlight an example of the continued potential for cosmological and astrophysical data to sharpen our understanding of fundamental physics.

Taken together, the results presented in this dissertation demonstrate how precision cosmology and targeted astrophysical observations can work in concert to interrogate physics far beyond the reach of terrestrial experiments. By pushing generic, model-agnostic limits on isocurvature and by developing data-driven techniques for diffuse-emission searches, I have shown that even null detections are extraordinarily informative. The coming decade—marked by CMB-S4 [56], PTA gravitational-wave detections [328, 329] and ultra-deep radio surveys [330, 331]—will provide us with opportunities to discover new physics or tighten constraints even more. The results presented in this thesis and those attained by other contemporary scientists will provide a strong foundation for taking the next steps.

REFERENCES

[1] M. R. Buckley, P. Du, N. Fernandez, and M. J. Weikert, "Dark radiation isocurvature from cosmological phase transitions," *JCAP*, vol. 07, p. 031, 2024. arXiv: `2402.13309 [hep-ph]`.

[2] M. R. Buckley, P. Du, N. Fernandez, and M. J. Weikert, "General Constraints on Isocurvature from the CMB and Ly-α Forest," Feb. 2025. arXiv: 2502.20434 `[astro-ph.CO]`.

[3] M. J. Weikert and M. R. Buckley, "Limits on dark matter annihilation from the shape of radio emission in M31," *JHEP*, vol. 02, p. 029, 2024. arXiv: 2303.11354 `[hep-ph]`.

[4] R. Beck, E. M. Berkhuijsen, R. Gießübel, and D. D. Mulcahy, "Magnetic fields and cosmic rays in m 31. i. spectral indices, scale lengths, faraday rotation, and magnetic field pattern," vol. 633, A5, 2020.

[5] D. J. Gross and F. Wilczek, "Ultraviolet Behavior of Nonabelian Gauge Theories," *Phys. Rev. Lett.*, vol. 30, J. C. Taylor, Ed., pp. 1343–1346, 1973.

[6] H. D. Politzer, "Reliable Perturbative Results for Strong Interactions?" *Phys. Rev. Lett.*, vol. 30, J. C. Taylor, Ed., pp. 1346–1349, 1973.

[7] K. Eguchi et al., "First results from KamLAND: Evidence for reactor anti-neutrino disappearance," *Phys. Rev. Lett.*, vol. 90, p. 021 802, 2003. arXiv: hep-ex/0212021.

[8] D. Adey et al., "Measurement of the Electron Antineutrino Oscillation with 1958 Days of Operation at Daya Bay," *Phys. Rev. Lett.*, vol. 121, no. 24, p. 241 805, 2018. arXiv: 1809.02261 `[hep-ex]`.

[9] K. Abe et al., "Indication of Electron Neutrino Appearance from an Accelerator-produced Off-axis Muon Neutrino Beam," *Phys. Rev. Lett.*, vol. 107, p. 041 801, 2011. arXiv: 1106.2822 `[hep-ex]`.

[10] D. G. Michael et al., "Observation of muon neutrino disappearance with the MINOS detectors and the NuMI neutrino beam," *Phys. Rev. Lett.*, vol. 97, p. 191 801, 2006. arXiv: hep-ex/0607088.

[11] S. Bose and A. Raychaudhuri, "A Note on the neutrino mass implications of the K2K experiment," *J. Phys. G*, vol. 29, pp. 1069–1074, 2003. arXiv: hep-ph/0303229.

[12] S. Weinberg, "Baryon and Lepton Nonconserving Processes," *Phys. Rev. Lett.*, vol. 43, pp. 1566–1570, 1979.

[13] P. Minkowski, “$\mu \to e\gamma$ at a Rate of One Out of 10^9 Muon Decays?” *Phys. Lett. B*, vol. 67, pp. 421–428, 1977.

[14] M. Gell-Mann, P. Ramond, and R. Slansky, “Complex Spinors and Unified Theories,” *Conf. Proc. C*, vol. 790927, pp. 315–321, 1979. arXiv: 1306.4669 `[hep-th]`.

[15] G. W. Bennett et al., “Final Report of the Muon E821 Anomalous Magnetic Moment Measurement at BNL,” *Phys. Rev. D*, vol. 73, p. 072 003, 2006. arXiv: hep-ex/0602035.

[16] D. P. Aguillard et al., “Measurement of the Positive Muon Anomalous Magnetic Moment to 0.20 ppm,” *Phys. Rev. Lett.*, vol. 131, no. 16, p. 161 802, 2023. arXiv: 2308.06230 `[hep-ex]`.

[17] T. Aaltonen et al., “High-precision measurement of the W boson mass with the CDF II detector,” *Science*, vol. 376, no. 6589, pp. 170–176, 2022.

[18] N. Aghanim et al., “Planck 2018 results. VI. Cosmological parameters,” *Astron. Astrophys.*, vol. 641, A6, 2020, [Erratum: Astron.Astrophys. 652, C4 (2021)]. arXiv: 1807.06209 `[astro-ph.CO]`.

[19] F. Beutler et al., “The 6dF Galaxy Survey: Baryon Acoustic Oscillations and the Local Hubble Constant,” *Mon. Not. Roy. Astron. Soc.*, vol. 416, pp. 3017–3032, 2011. arXiv: 1106.3366 `[astro-ph.CO]`.

[20] A. J. Ross, L. Samushia, C. Howlett, W. J. Percival, A. Burden, and M. Manera, “The clustering of the SDSS DR7 main Galaxy sample – I. A 4 per cent distance measure at $z = 0.15$,” *Mon. Not. Roy. Astron. Soc.*, vol. 449, no. 1, pp. 835–847, 2015. arXiv: 1409.3242 `[astro-ph.CO]`.

[21] S. Alam et al., “The clustering of galaxies in the completed SDSS-III Baryon Oscillation Spectroscopic Survey: cosmological analysis of the DR12 galaxy sample,” *Mon. Not. Roy. Astron. Soc.*, vol. 470, no. 3, pp. 2617–2652, 2017. arXiv: 1607.03155 `[astro-ph.CO]`.

[22] A. A. Starobinsky, “A New Type of Isotropic Cosmological Models Without Singularity,” *Phys. Lett. B*, vol. 91, I. M. Khalatnikov and V. P. Mineev, Eds., pp. 99–102, 1980.

[23] A. H. Guth, “The Inflationary Universe: A Possible Solution to the Horizon and Flatness Problems,” *Phys. Rev. D*, vol. 23, L.-Z. Fang and R. Ruffini, Eds., pp. 347–356, 1981.

[24] D. Clowe et al., “A direct empirical proof of the existence of dark matter,” *Astrophys. J. Lett.*, vol. 648, pp. L109–L113, 2006. arXiv: astro-ph/0608407.

[25] P. J. E. Peebles, “Large scale background temperature and mass fluctuations due to scale invariant primeval perturbations,” *Astrophys. J. Lett.*, vol. 263, M. A. Srednicki, Ed., pp. L1–L5, 1982.

[26] E. Aver, K. A. Olive, and E. D. Skillman, “The effects of He I λ10830 on helium abundance determinations,” *JCAP*, vol. 07, p. 011, 2015. arXiv: 1503.08146 `[astro-ph.CO]`.

[27] R. J. Cooke, M. Pettini, and C. C. Steidel, “One Percent Determination of the Primordial Deuterium Abundance,” *Astrophys. J.*, vol. 855, no. 2, p. 102, 2018. arXiv: 1710.11129 `[astro-ph.CO]`.

[28] A. G. Riess et al., “Observational evidence from supernovae for an accelerating universe and a cosmological constant,” *Astron. J.*, vol. 116, pp. 1009–1038, 1998. arXiv: astro-ph/9805201.

[29] S. Perlmutter et al., “Measurements of Ω and Λ from 42 High Redshift Supernovae,” *Astrophys. J.*, vol. 517, pp. 565–586, 1999. arXiv: astro-ph/9812133.

[30] E. Hubble, “A Relation between Distance and Radial Velocity among Extra-Galactic Nebulae,” *Proceedings of the National Academy of Science*, vol. 15, no. 3, pp. 168–173, Mar. 1929.

[31] H. Shapley and A. Ames, “A Survey of the External Galaxies Brighter than the Thirteenth Magnitude,” *Annals of Harvard College Observatory*, vol. 88, pp. 41–76, Jan. 1932.

[32] E. P. Hubble, *Realm of the Nebulae*. 1936.

[33] E. L. Scott, C. D. Shane, and M. D. Swanson, “Comparison of the Synthetic and Actual Distribution of Galaxies on a Photographic Plate.,” *APJ*, vol. 119, p. 91, Jan. 1954.

[34] A. Friedmann, “Über die Möglichkeit einer Welt mit konstanter negativer Krümmung des Raumes,” *Zeitschrift fur Physik*, vol. 21, no. 1, pp. 326–332, Dec. 1924.

[35] G. Lemaıˆtre, “Un Univers homogène de masse constante et de rayon croissant rendant compte de la vitesse radiale des nébuleuses extra-galactiques,” *Annales de la Société Scientifique de Bruxelles*, vol. 47, pp. 49–59, Jan. 1927.

[36] H. P. Robertson, “Kinematics and World-Structure,” *APJ*, vol. 82, p. 284, Nov. 1935.

[37] A. G. Walker, “On Milne’s Theory of World-Structure,” *Proc. Lond. Math. Soc. s*, vol. 2-42, no. 1, pp. 90–127, 1937.

[38] A. A. Penzias and R. W. Wilson, “A Measurement of excess antenna temperature at 4080-Mc/s,” *Astrophys. J.*, vol. 142, pp. 419–421, 1965.

[39] D. Baumann, *Cosmology*. Cambridge University Press, Jul. 2022, ISBN: 978-1-108-93709-2, 978-1-108-83807-8.

[40] C. L. Bennett et al., “Four year COBE DMR cosmic microwave background observations: Maps and basic results,” *Astrophys. J. Lett.*, vol. 464, pp. L1–L4, 1996. arXiv: astro-ph/9601067.

[41] D. N. Spergel et al., “Wilkinson Microwave Anisotropy Probe (WMAP) three year results: implications for cosmology,” *Astrophys. J. Suppl.*, vol. 170, p. 377, 2007. arXiv: astro-ph/0603449.

[42] G. F. Smoot et al., “Structure in the COBE differential microwave radiometer first year maps,” *Astrophys. J. Lett.*, vol. 396, pp. L1–L5, 1992.

[43] S. D. M. White and M. J. Rees, “Core condensation in heavy halos: A Two stage theory for galaxy formation and clusters,” *Mon. Not. Roy. Astron. Soc.*, vol. 183, pp. 341–358, 1978.

[44] J. R. Bond and G. Efstathiou, “Cosmic background radiation anisotropies in universes dominated by nonbaryonic dark matter,” *Astrophys. J. Lett.*, vol. 285, pp. L45–L48, 1984.

[45] J. M. Bardeen, J. R. Bond, N. Kaiser, and A. S. Szalay, “The Statistics of Peaks of Gaussian Random Fields,” *Astrophys. J.*, vol. 304, pp. 15–61, 1986.

[46] M. Davis, J. Huchra, D. W. Latham, and J. Tonry, “A survey of galaxy redshifts. II. The large scale space distribution.,” *APJ*, vol. 253, pp. 423–445, Feb. 1982.

[47] D. N. Spergel et al., “First year Wilkinson Microwave Anisotropy Probe (WMAP) observations: Determination of cosmological parameters,” *Astrophys. J. Suppl.*, vol. 148, pp. 175–194, 2003. arXiv: astro-ph/0302209.

[48] M. A. Strauss et al., “Spectroscopic Target Selection in the Sloan Digital Sky Survey: The Main Galaxy Sample,” *Astron. J.*, vol. 124, p. 1810, 2002. arXiv: astro-ph/0206225.

[49] D. J. Eisenstein et al., “Spectroscopic Target Selection for the Sloan Digital Sky Survey: The Luminous Red Galaxy Sample,” *Astron. J.*, vol. 122, p. 2267, 2001. arXiv: astro-ph/0108153.

[50] K. S. Dawson et al., “The Baryon Oscillation Spectroscopic Survey of SDSS-III,” *Astron. J.*, vol. 145, p. 10, 2013. arXiv: 1208.0022 `[astro-ph.CO]`.

[51] C.-T. Chiang, C. Wagner, A. G. Sánchez, F. Schmidt, and E. Komatsu, “Position-dependent correlation function from the SDSS-III Baryon Oscillation Spectroscopic Survey Data Release 10 CMASS Sample,” *JCAP*, vol. 09, p. 028, 2015. arXiv: 1504.03322 `[astro-ph.CO]`.

[52] D. G. York et al., “The Sloan Digital Sky Survey: Technical Summary,” *Astron. J.*, vol. 120, pp. 1579–1587, 2000. arXiv: astro-ph/0006396.

[53] N. Aghanim et al., "Planck 2018 results. VIII. Gravitational lensing," *Astron. Astrophys.*, vol. 641, A8, 2020. arXiv: 1807.06210 `[astro-ph.CO]`.

[54] Y. Akrami et al., "Planck 2018 results. X. Constraints on inflation," *Astron. Astrophys.*, vol. 641, A10, 2020. arXiv: 1807.06211 `[astro-ph.CO]`.

[55] P. A. R. Ade et al., "BICEP2 / Keck Array x: Constraints on Primordial Gravitational Waves using Planck, WMAP, and New BICEP2/Keck Observations through the 2015 Season," *Phys. Rev. Lett.*, vol. 121, p. 221 301, 2018. arXiv: 1810.05216 `[astro-ph.CO]`.

[56] K. Abazajian et al., "CMB-S4 Science Case, Reference Design, and Project Plan," Jul. 2019. arXiv: 1907.04473 `[astro-ph.IM]`.

[57] F. Zwicky, "Die Rotverschiebung von extragalaktischen Nebeln," *Helv. Phys. Acta*, vol. 6, pp. 110–127, 1933.

[58] F. Zwicky, "On the Masses of Nebulae and of Clusters of Nebulae," *Astrophys. J.*, vol. 86, pp. 217–246, 1937.

[59] V. C. Rubin and W. K. Ford Jr., "Rotation of the Andromeda Nebula from a Spectroscopic Survey of Emission Regions," *APJ*, vol. 159, p. 379, Feb. 1970.

[60] V. C. Rubin, W. K. Ford Jr., and N. Thonnard, "Extended rotation curves of high-luminosity spiral galaxies. IV. Systematic dynamical properties, Sa -> Sc.," *APJl*, vol. 225, pp. L107–L111, Nov. 1978.

[61] J. P. Ostriker and P. J. E. Peebles, "A Numerical Study of the Stability of Flattened Galaxies: or, can Cold Galaxies Survive?" *Astrophys. J.*, vol. 186, pp. 467–480, 1973.

[62] J. P. Ostriker, P. J. E. Peebles, and A. Yahil, "The size and mass of galaxies, and the mass of the universe," *Astrophys. J. Lett.*, vol. 193, pp. L1–L4, 1974.

[63] G. R. Blumenthal, S. M. Faber, J. R. Primack, and M. J. Rees, "Formation of Galaxies and Large Scale Structure with Cold Dark Matter," *Nature*, vol. 311, M. A. Srednicki, Ed., pp. 517–525, 1984.

[64] P. J. E. Peebles, "Dark matter and the origin of galaxies and globular star clusters," *Astrophys. J.*, vol. 277, pp. 470–477, 1984.

[65] E. Corbelli and P. Salucci, "The Extended Rotation Curve and the Dark Matter Halo of M33," *Mon. Not. Roy. Astron. Soc.*, vol. 311, pp. 441–447, 2000. arXiv: astro-ph/9909252.

[66] J. F. Navarro, C. S. Frenk, and S. D. M. White, "The Structure of cold dark matter halos," *Astrophys. J.*, vol. 462, pp. 563–575, 1996. arXiv: astro-ph/9508025.

[67] J. F. Navarro, C. S. Frenk, and S. D. M. White, “A Universal density profile from hierarchical clustering,” *Astrophys. J.*, vol. 490, pp. 493–508, 1997. arXiv: astro-ph/9611107.

[68] M. Persic, P. Salucci, and F. Stel, “The Universal rotation curve of spiral galaxies: 1. The Dark matter connection,” *Mon. Not. Roy. Astron. Soc.*, vol. 281, p. 27, 1996. arXiv: astro-ph/9506004.

[69] P. Salucci and M. Persic, “Dark matter halos around galaxies,” *ASP Conf. Ser.*, vol. 117, p. 1, 1997. arXiv: astro-ph/9703027.

[70] W. J. Percival et al., “The 2dF Galaxy Redshift Survey: The Power spectrum and the matter content of the Universe,” *Mon. Not. Roy. Astron. Soc.*, vol. 327, p. 1297, 2001. arXiv: astro-ph/0105252.

[71] S. Cole, S. Hatton, D. H. Weinberg, and C. S. Frenk, “Mock 2dF and SDSS galaxy redshift surveys,” *Mon. Not. Roy. Astron. Soc.*, vol. 300, pp. 945–966, 1998. arXiv: astro-ph/9801250.

[72] M. Markevitch et al., “A Textbook example of a bow shock in the merging galaxy cluster 1E0657-56,” *Astrophys. J. Lett.*, vol. 567, p. L27, 2002. arXiv: astro-ph/0110468.

[73] M. C. Weisskopf, H. D. Tananbaum, L. P. van Speybroeck, and S. L. O’Dell, “Chandra x-ray observatory (cxo):overview,” *Proc. SPIE Int. Soc. Opt. Eng.*, vol. 4012, p. 2, 2000. arXiv: astro-ph/0004127.

[74] J. Lesgourgues, “The Cosmic Linear Anisotropy Solving System (CLASS) I: Overview,” Apr. 2011. arXiv: 1104.2932 `[astro-ph.IM]`.

[75] Z. Ahmed et al., “Dark Matter Search Results from the CDMS II Experiment,” *Science*, vol. 327, pp. 1619–1621, 2010. arXiv: 0912.3592 `[astro-ph.CO]`.

[76] G. Angloher et al., “Results on light dark matter particles with a low-threshold CRESST-II detector,” *Eur. Phys. J. C*, vol. 76, no. 1, p. 25, 2016. arXiv: 1509.01515 `[astro-ph.CO]`.

[77] C. Amole et al., “Dark Matter Search Results from the PICO-60 C_3F_8 Bubble Chamber,” *Phys. Rev. Lett.*, vol. 118, no. 25, p. 251 301, 2017. arXiv: 1702.07666 `[astro-ph.CO]`.

[78] E. Aprile et al., “Excess electronic recoil events in XENON1T,” *Phys. Rev. D*, vol. 102, no. 7, p. 072 004, 2020. arXiv: 2006.09721 `[hep-ex]`.

[79] V. Khachatryan et al., “Search for dark matter, extra dimensions, and unparticles in monojet events in proton–proton collisions at $\sqrt{s} = 8$ TeV,” *Eur. Phys. J. C*, vol. 75, no. 5, p. 235, 2015. arXiv: 1408.3583 `[hep-ex]`.

[80] D. Abercrombie et al., “Dark Matter benchmark models for early LHC Run-2 Searches: Report of the ATLAS/CMS Dark Matter Forum,” *Phys. Dark Univ.*, vol. 27, A. Boveia, C. Doglioni, S. Lowette, S. Malik, and S. Mrenna, Eds., p. 100 371, 2020. arXiv: 1507.00966 `[hep-ex]`.

[81] G. Aad et al., “Search for new phenomena in final states with an energetic jet and large missing transverse momentum in pp collisions at $\sqrt{s}$ =8 TeV with the ATLAS detector,” *Eur. Phys. J. C*, vol. 75, no. 7, p. 299, 2015, [Erratum: Eur.Phys.J.C 75, 408 (2015)]. arXiv: 1502.01518 `[hep-ex]`.

[82] R. Aaij et al., “Search for Dark Photons Produced in 13 TeV pp Collisions,” *Phys. Rev. Lett.*, vol. 120, no. 6, p. 061 801, 2018. arXiv: 1710.02867 `[hep-ex]`.

[83] Y. Du, F. Huang, H.-L. Li, Y.-Z. Li, and J.-H. Yu, “Revisiting dark matter freeze-in and freeze-out through phase-space distribution,” *JCAP*, vol. 04, no. 04, p. 012, 2022. arXiv: 2111.01267 `[hep-ph]`.

[84] G. Jungman, M. Kamionkowski, and K. Griest, “Supersymmetric dark matter,” *Phys. Rept.*, vol. 267, pp. 195–373, 1996. arXiv: hep-ph/9506380.

[85] G. Bertone, D. Hooper, and J. Silk, “Particle dark matter: Evidence, candidates and constraints,” *Phys. Rept.*, vol. 405, pp. 279–390, 2005. arXiv: hep-ph/0404175.

[86] B. W. Lee and S. Weinberg, “Cosmological Lower Bound on Heavy Neutrino Masses,” *Phys. Rev. Lett.*, vol. 39, M. A. Srednicki, Ed., pp. 165–168, 1977.

[87] G. Steigman, “Cosmology Confronts Particle Physics,” *Ann. Rev. Nucl. Part. Sci.*, vol. 29, pp. 313–338, 1979.

[88] M. Srednicki, R. Watkins, and K. A. Olive, “Calculations of Relic Densities in the Early Universe,” *Nucl. Phys. B*, vol. 310, M. A. Srednicki, Ed., p. 693, 1988.

[89] P. Gondolo and G. Gelmini, “Cosmic abundances of stable particles: Improved analysis,” *Nucl. Phys. B*, vol. 360, pp. 145–179, 1991.

[90] G. Steigman, B. Dasgupta, and J. F. Beacom, “Precise Relic WIMP Abundance and its Impact on Searches for Dark Matter Annihilation,” *Phys. Rev. D*, vol. 86, p. 023 506, 2012. arXiv: 1204.3622 `[hep-ph]`.

[91] L. J. Hall, K. Jedamzik, J. March-Russell, and S. M. West, “Freeze-In Production of FIMP Dark Matter,” *JHEP*, vol. 03, p. 080, 2010. arXiv: 0911.1120 `[hep-ph]`.

[92] F. Elahi, C. Kolda, and J. Unwin, “UltraViolet Freeze-in,” *JHEP*, vol. 03, p. 048, 2015. arXiv: 1410.6157 `[hep-ph]`.

[93] N. Bernal, M. Heikinheimo, T. Tenkanen, K. Tuominen, and V. Vaskonen, "The Dawn of FIMP Dark Matter: A Review of Models and Constraints," *Int. J. Mod. Phys. A*, vol. 32, no. 27, p. 1 730 023, 2017. arXiv: 1706.07442 `[hep-ph]`.

[94] D. J. E. Marsh, "Axion Cosmology," *Phys. Rept.*, vol. 643, pp. 1–79, 2016. arXiv: 1510.07633 `[astro-ph.CO]`.

[95] A. Mazumdar and J. Rocher, "Particle physics models of inflation and curvaton scenarios," *Phys. Rept.*, vol. 497, pp. 85–215, 2011. arXiv: 1001.0993 `[hep-ph]`.

[96] K. Freese and M. W. Winkler, "Dark matter and gravitational waves from a dark big bang," *Phys. Rev. D*, vol. 107, no. 8, p. 083 522, 2023. arXiv: 2302.11579 `[astro-ph.CO]`.

[97] G. Elor, R. Jinno, S. Kumar, R. McGehee, and Y. Tsai, "Finite Bubble Statistics Constrain Late Cosmological Phase Transitions," Nov. 2023. arXiv: 2311.16222 `[hep-ph]`.

[98] D. J. H. Chung, E. W. Kolb, A. Riotto, and L. Senatore, "Isocurvature constraints on gravitationally produced superheavy dark matter," *Phys. Rev. D*, vol. 72, p. 023 511, 2005. arXiv: astro-ph/0411468.

[99] D. J. H. Chung, H. Yoo, and P. Zhou, "Fermionic Isocurvature Perturbations," *Phys. Rev. D*, vol. 91, no. 4, p. 043 516, 2015. arXiv: 1306.1966 `[astro-ph.CO]`.

[100] D. J. H. Chung, H. Yoo, and P. Zhou, "Quadratic Isocurvature Cross-Correlation, Ward Identity, and Dark Matter," *Phys. Rev. D*, vol. 87, p. 123 502, 2013. arXiv: 1303.6024 `[astro-ph.CO]`.

[101] P. W. Graham, J. Mardon, and S. Rajendran, "Vector Dark Matter from Inflationary Fluctuations," *Phys. Rev. D*, vol. 93, no. 10, p. 103 520, 2016. arXiv: 1504.02102 `[hep-ph]`.

[102] E. W. Kolb and A. J. Long, "Completely dark photons from gravitational particle production during the inflationary era," *JHEP*, vol. 03, p. 283, 2021. arXiv: 2009.03828 `[astro-ph.CO]`.

[103] E. W. Kolb and A. J. Long, "Cosmological gravitational particle production and its implications for cosmological relics," *Rev. Mod. Phys.*, vol. 96, no. 4, p. 045 005, 2024. arXiv: 2312.09042 `[astro-ph.CO]`.

[104] M. A. Amin and M. Mirbabayi, "A Lower Bound on Dark Matter Mass," *Phys. Rev. Lett.*, vol. 132, no. 22, p. 221 004, 2024. arXiv: 2211.09775 `[hep-ph]`.

[105] M. A. G. Garcia, M. Pierre, and S. Verner, "New window into gravitationally produced scalar dark matter," *Phys. Rev. D*, vol. 108, no. 11, p. 115 024, 2023. arXiv: 2305.14446 `[hep-ph]`.

[106] G. Sato-Polito, E. D. Kovetz, and M. Kamionkowski, “Constraints on the primordial curvature power spectrum from primordial black holes,” *Phys. Rev. D*, vol. 100, p. 063 521, 6 Sep. 2019.

[107] B. Carr, M. Raidal, T. Tenkanen, V. Vaskonen, and H. Veermäe, “Primordial black hole constraints for extended mass functions,” *Phys. Rev. D*, vol. 96, no. 2, p. 023 514, 2017. arXiv: 1705.05567 `[astro-ph.CO]`.

[108] J. Barir, M. Geller, C. Sun, and T. Volansky, “Gravitational waves from incomplete inflationary phase transitions,” *Phys. Rev. D*, vol. 108, no. 11, p. 115 016, 2023. arXiv: 2203.00693 `[hep-ph]`.

[109] D. J. H. Chung, M. Münchmeyer, and S. C. Tadepalli, “Search for isocurvature with large-scale structure: A forecast for Euclid and MegaMapper using EFTofLSS,” *Phys. Rev. D*, vol. 108, no. 10, p. 103 542, 2023. arXiv: 2306.09456 `[astro-ph.CO]`.

[110] J. de Kruijf, E. Vanzan, K. K. Boddy, A. Raccanelli, and N. Bartolo, “Searching for blue in the dark,” Aug. 2024. arXiv: 2408.04991 `[astro-ph.CO]`.

[111] T. Sekiguchi, H. Tashiro, J. Silk, and N. Sugiyama, “Cosmological signatures of tilted isocurvature perturbations: reionization and 21cm fluctuations,” *JCAP*, vol. 03, p. 001, 2014. arXiv: 1311.3294 `[astro-ph.CO]`.

[112] D. Blas, J. Lesgourgues, and T. Tram, “The Cosmic Linear Anisotropy Solving System (CLASS) II: Approximation schemes,” *JCAP*, vol. 07, p. 034, 2011. arXiv: `1104.2933` `[astro-ph.CO]`.

[113] P. McDonald et al., “The Observed probability distribution function, power spectrum, and correlation function of the transmitted flux in the Lyman-alpha forest,” *Astrophys. J.*, vol. 543, pp. 1–23, 2000. arXiv: astro-ph/9911196.

[114] C. Pedersen et al., “Massive neutrinos and degeneracies in Lyman-alpha forest simulations,” *JCAP*, vol. 04, p. 025, 2020. arXiv: 1911.09596 `[astro-ph.CO]`.

[115] C. Pedersen et al., “An emulator for the Lyman-α forest in beyond-ΛCDM cosmologies,” *JCAP*, vol. 05, p. 033, 2021. arXiv: 2011.15127 `[astro-ph.CO]`.

[116] C. Pedersen, A. Font-Ribera, and N. Y. Gnedin, “Compressing the cosmological information in one-dimensional correlations of the Lyman-α forest,” Sep. 2022. arXiv: 2209.09895 `[astro-ph.CO]`.

[117] D. J. Fixsen, E. S. Cheng, J. M. Gales, J. C. Mather, R. A. Shafer, and E. L. Wright, “The Cosmic Microwave Background spectrum from the full COBE FIRAS data set,” *Astrophys. J.*, vol. 473, p. 576, 1996. arXiv: astro-ph/9605054.

[118] V. Iršič, H. Xiao, and M. McQuinn, "Early structure formation constraints on the ultralight axion in the postinflation scenario," *Phys. Rev. D*, vol. 101, no. 12, p. 123 518, 2020. arXiv: 1911.11150 `[astro-ph.CO]`.

[119] M. Feix, S. Hagstotz, A. Pargner, R. Reischke, B. M. Schäfer, and T. Schwetz, "Post-inflationary axion isocurvature perturbations facing CMB and large-scale structure," *JCAP*, vol. 11, p. 046, 2020. arXiv: 2004.02926 `[astro-ph.CO]`.

[120] M. Redi and A. Tesi, "Meso-inflationary QCD axion," *Phys. Rev. D*, vol. 107, no. 9, p. 095 032, 2023. arXiv: 2211.06421 `[hep-ph]`.

[121] P. W. Graham and H. Ramani, "Constraints on dark matter from dynamical heating of stars in ultrafaint dwarfs. II. Substructure and the primordial power spectrum," *Phys. Rev. D*, vol. 110, no. 7, p. 075 012, 2024. arXiv: 2404.01378 `[hep-ph]`.

[122] M. Bucher, K. Moodley, and N. Turok, "The General primordial cosmic perturbation," *Phys. Rev. D*, vol. 62, p. 083 508, 2000. arXiv: astro-ph/9904231.

[123] D. Wands, K. A. Malik, D. H. Lyth, and A. R. Liddle, "A New approach to the evolution of cosmological perturbations on large scales," *Phys. Rev. D*, vol. 62, p. 043 527, 2000. arXiv: astro-ph/0003278.

[124] C. Gordon, D. Wands, B. A. Bassett, and R. Maartens, "Adiabatic and entropy perturbations from inflation," *Phys. Rev. D*, vol. 63, p. 023 506, 2000. arXiv: astro-ph/0009131.

[125] D. H. Lyth, C. Ungarelli, and D. Wands, "The Primordial density perturbation in the curvaton scenario," *Phys. Rev. D*, vol. 67, p. 023 503, 2003. arXiv: astro-ph/0208055.

[126] K. A. Malik and D. Wands, "Adiabatic and entropy perturbations with interacting fluids and fields," *JCAP*, vol. 02, p. 007, 2005. arXiv: astro-ph/0411703.

[127] D. Wands, "Multiple field inflation," *Lect. Notes Phys.*, vol. 738, pp. 275–304, 2008. arXiv: astro-ph/0702187.

[128] S. Ghosh, S. Kumar, and Y. Tsai, "Free-streaming and coupled dark radiation isocurvature perturbations: constraints and application to the Hubble tension," *JCAP*, vol. 05, no. 05, p. 014, 2022. arXiv: 2107.09076 `[astro-ph.CO]`.

[129] M. Savelainen, J. Valiviita, P. Walia, S. Rusak, and H. Kurki-Suonio, "Constraints on neutrino density and velocity isocurvature modes from WMAP-9 data," *Phys. Rev. D*, vol. 88, p. 063 010, 2013. arXiv: 1307.4398 `[astro-ph.CO]`.

[130] D. Baumann, D. Green, J. Meyers, and B. Wallisch, "Phases of New Physics in the CMB," *JCAP*, vol. 01, p. 007, 2016. arXiv: 1508.06342 `[astro-ph.CO]`.

[131] T. Brinckmann and J. Lesgourgues, “MontePython 3: boosted MCMC sampler and other features,” *Phys. Dark Univ.*, vol. 24, p. 100 260, 2019. arXiv: 1804.07261 `[astro-ph.CO]`.

[132] S. Chabanier et al., “The one-dimensional power spectrum from the SDSS DR14 Lyα forests,” *JCAP*, vol. 07, p. 017, 2019. arXiv: 1812.03554 `[astro-ph.CO]`.

[133] S. Goldstein, J. C. Hill, V. Iršič, and B. D. Sherwin, “Canonical Hubble-Tension-Resolving Early Dark Energy Cosmologies Are Inconsistent with the Lyman-α Forest,” *Phys. Rev. Lett.*, vol. 131, no. 20, p. 201 001, 2023. arXiv: 2303.00746 `[astro-ph.CO]`.

[134] M. A. Fernandez, S. Bird, and M.-F. Ho, “Cosmological constraints from the eBOSS Lyman-α forest using the PRIYA simulations,” *JCAP*, vol. 07, p. 029, 2024. arXiv: 2309.03943 `[astro-ph.CO]`.

[135] A. He, M. M. Ivanov, S. Bird, R. An, and V. Gluscevic, “A Fresh Look at Neutrino Self-Interactions With the Lyman-α Forest: Constraints from EFT and PRIYA,” Mar. 2025. arXiv: 2503.15592 `[astro-ph.CO]`.

[136] J. Chluba and R. A. Sunyaev, “The evolution of CMB spectral distortions in the early Universe,” *Mon. Not. Roy. Astron. Soc.*, vol. 419, pp. 1294–1314, 2012. arXiv: 1109.6552 `[astro-ph.CO]`.

[137] J. B. Dent, D. A. Easson, and H. Tashiro, “Cosmological constraints from CMB distortion,” *Phys. Rev. D*, vol. 86, p. 023 514, 2012. arXiv: 1202.6066 `[astro-ph.CO]`.

[138] J. Chluba, R. Khatri, and R. A. Sunyaev, “CMB at 2x2 order: The dissipation of primordial acoustic waves and the observable part of the associated energy release,” *Mon. Not. Roy. Astron. Soc.*, vol. 425, pp. 1129–1169, 2012. arXiv: 1202.0057 `[astro-ph.CO]`.

[139] R. Khatri, R. A. Sunyaev, and J. Chluba, “Mixing of blackbodies: entropy production and dissipation of sound waves in the early Universe,” *Astron. Astrophys.*, vol. 543, A136, 2012. arXiv: 1205.2871 `[astro-ph.CO]`.

[140] J. Chluba and D. Grin, “CMB spectral distortions from small-scale isocurvature fluctuations,” *Mon. Not. Roy. Astron. Soc.*, vol. 434, pp. 1619–1635, 2013. arXiv: 1304.4596 `[astro-ph.CO]`.

[141] J. Chluba, “Distinguishing different scenarios of early energy release with spectral distortions of the cosmic microwave background,” *Mon. Not. Roy. Astron. Soc.*, vol. 436, pp. 2232–2243, 2013. arXiv: 1304.6121 `[astro-ph.CO]`.

[142] G. Arsenadze, A. Caputo, X. Gan, H. Liu, and J. T. Ruderman, “Shaping Dark Photon Spectral Distortions,” Sep. 2024. arXiv: 2409.12940 `[astro-ph.CO]`.

[143] A. Kogut et al., "The Primordial Inflation Explorer (PIXIE): A Nulling Polarimeter for Cosmic Microwave Background Observations," *JCAP*, vol. 07, p. 025, 2011. arXiv: 1105.2044 `[astro-ph.CO]`.

[144] J. Chluba, "Refined approximations for the distortion visibility function and μ-type spectral distortions," *Mon. Not. Roy. Astron. Soc.*, vol. 440, no. 3, pp. 2544–2563, 2014. arXiv: 1312.6030 `[astro-ph.CO]`.

[145] W. Hu and N. Sugiyama, "Small scale cosmological perturbations: An Analytic approach," *Astrophys. J.*, vol. 471, pp. 542–570, 1996. arXiv: astro-ph/9510117.

[146] P. Adshead, G. Holder, and P. Ralegankar, "BBN constraints on dark radiation isocurvature," *JCAP*, vol. 09, p. 016, 2020. arXiv: 2006.01165 `[astro-ph.CO]`.

[147] G. Domènech, S. Passaglia, and S. Renaux-Petel, "Gravitational waves from dark matter isocurvature," *JCAP*, vol. 03, no. 03, p. 023, 2022. arXiv: 2112.10163 `[astro-ph.CO]`.

[148] G. Domènech, "Cosmological gravitational waves from isocurvature fluctuations," *AAPPS Bull.*, vol. 34, no. 1, p. 4, 2024. arXiv: 2311.02065 `[gr-qc]`.

[149] S. Passaglia and M. Sasaki, "Primordial black holes from CDM isocurvature perturbations," *Phys. Rev. D*, vol. 105, no. 10, p. 103 530, 2022. arXiv: 2109.12824 `[astro-ph.CO]`.

[150] V. Kuzmin, V. Rubakov, and M. Shaposhnikov, "On anomalous electroweak baryon-number non-conservation in the early universe," *Physics Letters B*, vol. 155, no. 1, pp. 36–42, 1985.

[151] M. E. Shaposhnikov, "Possible Appearance of the Baryon Asymmetry of the Universe in an Electroweak Theory," *JETP Lett.*, vol. 44, pp. 465–468, 1986.

[152] M. E. Shaposhnikov, "Baryon Asymmetry of the Universe in Standard Electroweak Theory," *Nucl. Phys. B*, vol. 287, pp. 757–775, 1987.

[153] A. G. Cohen, D. B. Kaplan, and A. E. Nelson, "Progress in electroweak baryogenesis," *Ann. Rev. Nucl. Part. Sci.*, vol. 43, pp. 27–70, 1993. arXiv: hep-ph/9302210.

[154] M. Trodden, "Electroweak baryogenesis," *Rev. Mod. Phys.*, vol. 71, pp. 1463–1500, 1999. arXiv: hep-ph/9803479.

[155] A. Riotto and M. Trodden, "Recent progress in baryogenesis," *Ann. Rev. Nucl. Part. Sci.*, vol. 49, pp. 35–75, 1999. arXiv: hep-ph/9901362.

[156] M. Dine and A. Kusenko, "The Origin of the matter - antimatter asymmetry," *Rev. Mod. Phys.*, vol. 76, p. 1, 2003. arXiv: hep-ph/0303065.

[157] D. E. Morrissey and M. J. Ramsey-Musolf, "Electroweak baryogenesis," *New J. Phys.*, vol. 14, p. 125 003, 2012. arXiv: 1206.2942 `[hep-ph]`.

[158] P. Creminelli, A. Nicolis, and R. Rattazzi, "Holography and the electroweak phase transition," *JHEP*, vol. 03, p. 051, 2002. arXiv: hep-th/0107141.

[159] L. Randall and G. Servant, "Gravitational waves from warped spacetime," *JHEP*, vol. 05, p. 054, 2007. arXiv: hep-ph/0607158.

[160] G. Nardini, M. Quiros, and A. Wulzer, "A Confining Strong First-Order Electroweak Phase Transition," *JHEP*, vol. 09, p. 077, 2007. arXiv: 0706.3388 `[hep-ph]`.

[161] T. Konstandin, G. Nardini, and M. Quiros, "Gravitational Backreaction Effects on the Holographic Phase Transition," *Phys. Rev. D*, vol. 82, p. 083 513, 2010. arXiv: 1007.1468 `[hep-ph]`.

[162] T. Konstandin and G. Servant, "Cosmological Consequences of Nearly Conformal Dynamics at the TeV scale," *JCAP*, vol. 12, p. 009, 2011. arXiv: 1104.4791 `[hep-ph]`.

[163] D. Bunk, J. Hubisz, and B. Jain, "A Perturbative RS I Cosmological Phase Transition," *Eur. Phys. J. C*, vol. 78, no. 1, p. 78, 2018. arXiv: 1705.00001 `[hep-ph]`.

[164] P. Baratella, A. Pomarol, and F. Rompineve, "The Supercooled Universe," *JHEP*, vol. 03, p. 100, 2019. arXiv: 1812.06996 `[hep-ph]`.

[165] S. Bruggisser, B. Von Harling, O. Matsedonskyi, and G. Servant, "Electroweak Phase Transition and Baryogenesis in Composite Higgs Models," *JHEP*, vol. 12, p. 099, 2018. arXiv: 1804.07314 `[hep-ph]`.

[166] E. Megías, G. Nardini, and M. Quirós, "Cosmological Phase Transitions in Warped Space: Gravitational Waves and Collider Signatures," *JHEP*, vol. 09, p. 095, 2018. arXiv: 1806.04877 `[hep-ph]`.

[167] K. Agashe, P. Du, M. Ekhterachian, S. Kumar, and R. Sundrum, "Cosmological Phase Transition of Spontaneous Confinement," *JHEP*, vol. 05, p. 086, 2020. arXiv: 1910.06238 `[hep-ph]`.

[168] K. Fujikura, Y. Nakai, and M. Yamada, "A more attractive scheme for radion stabilization and supercooled phase transition," *JHEP*, vol. 02, p. 111, 2020. arXiv: 1910.07546 `[hep-ph]`.

[169] K. Agashe, P. Du, M. Ekhterachian, S. Kumar, and R. Sundrum, "Phase Transitions from the Fifth Dimension," *JHEP*, vol. 02, p. 051, 2021. arXiv: 2010.04083 `[hep-th]`.

[170] F. R. Ares, M. Hindmarsh, C. Hoyos, and N. Jokela, "Gravitational waves from a holographic phase transition," *JHEP*, vol. 21, p. 100, 2020. arXiv: 2011.12878 `[hep-th]`.

[171] P. Agrawal and M. Nee, "Avoided deconfinement in Randall-Sundrum models," *JHEP*, vol. 10, p. 105, 2021. arXiv: 2103.05646 `[hep-ph]`.

[172] N. Levi, T. Opferkuch, and D. Redigolo, "The supercooling window at weak and strong coupling," *JHEP*, vol. 02, p. 125, 2023. arXiv: 2212.08085 `[hep-ph]`.

[173] C. Csáki, M. Geller, Z. Heller-Algazi, and A. Ismail, "Relevant dilaton stabilization," *JHEP*, vol. 06, p. 202, 2023. arXiv: 2301.10247 `[hep-ph]`.

[174] C. Eröncel, J. Hubisz, S. J. Lee, G. Rigo, and B. Sambasivam, "New Horizons in the Holographic Conformal Phase Transition," May 2023. arXiv: 2305.03773 `[hep-ph]`.

[175] R. K. Mishra and L. Randall, "Consequences of a Stabilizing Field's Self-Interactions for RS Cosmology," Sep. 2023. arXiv: 2309.10090 `[hep-ph]`.

[176] R. K. Mishra and L. Randall, "Phase Transition to RS: Cool, not Supercool," Jan. 2024. arXiv: 2401.09633 `[hep-ph]`.

[177] Y. Bai and P. Schwaller, "Scale of dark QCD," *Phys. Rev. D*, vol. 89, no. 6, p. 063 522, 2014. arXiv: 1306.4676 `[hep-ph]`.

[178] G. D. Kribs and E. T. Neil, "Review of strongly-coupled composite dark matter models and lattice simulations," *Int. J. Mod. Phys. A*, vol. 31, no. 22, p. 1 643 004, 2016. arXiv: 1604.04627 `[hep-ph]`.

[179] J. M. Cline, "Dark atoms and composite dark matter," *SciPost Phys. Lect. Notes*, vol. 52, p. 1, 2022. arXiv: 2108.10314 `[hep-ph]`.

[180] J. Shelton and K. M. Zurek, "Darkogenesis: A baryon asymmetry from the dark matter sector," *Phys. Rev. D*, vol. 82, p. 123 512, 2010. arXiv: 1008.1997 `[hep-ph]`.

[181] B. Dutta and J. Kumar, "Asymmetric dark matter from hidden sector baryogenesis," *Physics Letters B*, vol. 699, no. 5, pp. 364–367, 2011.

[182] M. Holthausen, J. Kubo, K. S. Lim, and M. Lindner, "Electroweak and Conformal Symmetry Breaking by a Strongly Coupled Hidden Sector," *JHEP*, vol. 12, p. 076, 2013. arXiv: 1310.4423 `[hep-ph]`.

[183] P. Schwaller, "Gravitational Waves from a Dark Phase Transition," *Phys. Rev. Lett.*, vol. 115, no. 18, p. 181 101, 2015. arXiv: 1504.07263 `[hep-ph]`.

[184] E. Hall, T. Konstandin, R. McGehee, and H. Murayama, "Asymmetric matter from a dark first-order phase transition," *Phys. Rev. D*, vol. 107, no. 5, p. 055 011, 2023. arXiv: 1911.12342 `[hep-ph]`.

[185] Y. Bai and M. Korwar, "Cosmological constraints on first-order phase transitions," *Phys. Rev. D*, vol. 105, no. 9, p. 095 015, 2022. arXiv: 2109.14765 `[hep-ph]`.

[186] S. Bottaro, M. Costa, and O. Popov, "Asymmetric accidental composite dark matter," *JHEP*, vol. 11, p. 055, 2021. arXiv: 2104.14244 `[hep-ph]`.

[187] R. Pasechnik, M. Reichert, F. Sannino, and Z.-W. Wang, "Gravitational Waves from Composite Dark Sectors," Sep. 2023. arXiv: 2309.16755 `[hep-ph]`.

[188] T. Karwal and M. Kamionkowski, "Dark energy at early times, the Hubble parameter, and the string axiverse," *Phys. Rev. D*, vol. 94, no. 10, p. 103 523, 2016. arXiv: 1608.01309 `[astro-ph.CO]`.

[189] E. Mörtsell and S. Dhawan, "Does the Hubble constant tension call for new physics?" *JCAP*, vol. 09, p. 025, 2018. arXiv: 1801.07260 `[astro-ph.CO]`.

[190] V. Poulin, T. L. Smith, T. Karwal, and M. Kamionkowski, "Early Dark Energy Can Resolve The Hubble Tension," *Phys. Rev. Lett.*, vol. 122, no. 22, p. 221 301, 2019. arXiv: 1811.04083 `[astro-ph.CO]`.

[191] A. G. Riess et al., "A Comprehensive Measurement of the Local Value of the Hubble Constant with 1 km s^{-1} Mpc^{-1} Uncertainty from the Hubble Space Telescope and the SH0ES Team," *Astrophys. J. Lett.*, vol. 934, no. 1, p. L7, 2022. arXiv: 2112.04510 `[astro-ph.CO]`.

[192] F. Niedermann and M. S. Sloth, "New early dark energy," *Phys. Rev. D*, vol. 103, no. 4, p. L041303, 2021. arXiv: 1910.10739 `[astro-ph.CO]`.

[193] F. Niedermann and M. S. Sloth, "Resolving the Hubble tension with new early dark energy," *Phys. Rev. D*, vol. 102, no. 6, p. 063 527, 2020. arXiv: 2006.06686 `[astro-ph.CO]`.

[194] F. Niedermann and M. S. Sloth, "Hot new early dark energy," *Phys. Rev. D*, vol. 105, no. 6, p. 063 509, 2022. arXiv: 2112.00770 `[hep-ph]`.

[195] A. Kosowsky, M. S. Turner, and R. Watkins, "Gravitational waves from first order cosmological phase transitions," *Phys. Rev. Lett.*, vol. 69, pp. 2026–2029, 1992.

[196] A. Kosowsky, M. S. Turner, and R. Watkins, "Gravitational radiation from colliding vacuum bubbles," *Phys. Rev. D*, vol. 45, pp. 4514–4535, 1992.

[197] A. Kosowsky and M. S. Turner, "Gravitational radiation from colliding vacuum bubbles: envelope approximation to many bubble collisions," *Phys. Rev. D*, vol. 47, pp. 4372–4391, 1993. arXiv: astro-ph/9211004.

[198] M. Kamionkowski, A. Kosowsky, and M. S. Turner, "Gravitational radiation from first order phase transitions," *Phys. Rev. D*, vol. 49, pp. 2837–2851, 1994. arXiv: astro-ph/9310044.

[199] C. Caprini et al., "Science with the space-based interferometer eLISA. II: Gravitational waves from cosmological phase transitions," *JCAP*, vol. 04, p. 001, 2016. arXiv: 1512.06239 `[astro-ph.CO]`.

[200] C. Caprini et al., "Detecting gravitational waves from cosmological phase transitions with LISA: an update," *JCAP*, vol. 03, p. 024, 2020. arXiv: 1910.13125 `[astro-ph.CO]`.

[201] R. Caldwell et al., "Detection of early-universe gravitational-wave signatures and fundamental physics," *Gen. Rel. Grav.*, vol. 54, no. 12, p. 156, 2022. arXiv: 2203.07972 `[gr-qc]`.

[202] P. Athron, C. Balázs, A. Fowlie, L. Morris, and L. Wu, "Cosmological phase transitions: From perturbative particle physics to gravitational waves," *Prog. Part. Nucl. Phys.*, vol. 135, p. 104 094, 2024. arXiv: 2305.02357 `[hep-ph]`.

[203] G. Agazie et al., "The NANOGrav 15 yr Data Set: Evidence for a Gravitational-wave Background," *Astrophys. J. Lett.*, vol. 951, no. 1, p. L8, 2023. arXiv: 2306.16213 `[astro-ph.HE]`.

[204] A. Afzal et al., "The NANOGrav 15 yr Data Set: Search for Signals from New Physics," *Astrophys. J. Lett.*, vol. 951, no. 1, p. L11, 2023. arXiv: 2306.16219 `[astro-ph.HE]`.

[205] J. Antoniadis et al., "The second data release from the European Pulsar Timing Array III. Search for gravitational wave signals," Jun. 2023. arXiv: 2306.16214 `[astro-ph.HE]`.

[206] D. J. Reardon et al., "Search for an Isotropic Gravitational-wave Background with the Parkes Pulsar Timing Array," *Astrophys. J. Lett.*, vol. 951, no. 1, p. L6, 2023. arXiv: 2306.16215 `[astro-ph.HE]`.

[207] H. Xu et al., "Searching for the Nano-Hertz Stochastic Gravitational Wave Background with the Chinese Pulsar Timing Array Data Release I," *Res. Astron. Astrophys.*, vol. 23, no. 7, p. 075 024, 2023. arXiv: 2306.16216 `[astro-ph.HE]`.

[208] P. Amaro-Seoane et al., "Laser Interferometer Space Antenna," Feb. 2017. arXiv: 1702.00786 `[astro-ph.IM]`.

[209] P. Auclair et al., "Cosmology with the Laser Interferometer Space Antenna," *Living Rev. Rel.*, vol. 26, no. 1, p. 5, 2023. arXiv: 2204.05434 `[astro-ph.CO]`.

[210] S. Kawamura et al., “The Japanese space gravitational wave antenna DECIGO,” *Class. Quant. Grav.*, vol. 23, N. Mio, Ed., S125–S132, 2006.

[211] S. Kawamura et al., “Current status of space gravitational wave antenna DECIGO and B-DECIGO,” *PTEP*, vol. 2021, no. 5, 05A105, 2021. arXiv: 2006.13545 `[gr-qc]`.

[212] G. M. Harry, P. Fritschel, D. A. Shaddock, W. Folkner, and E. S. Phinney, “Laser interferometry for the big bang observer,” *Class. Quant. Grav.*, vol. 23, pp. 4887–4894, 2006, [Erratum: Class.Quant.Grav. 23, 7361 (2006)].

[213] T. L. Smith, E. Pierpaoli, and M. Kamionkowski, “A new cosmic microwave background constraint to primordial gravitational waves,” *Phys. Rev. Lett.*, vol. 97, p. 021 301, 2006. arXiv: astro-ph/0603144.

[214] J. Froustey, C. Pitrou, and M. C. Volpe, “Neutrino decoupling including flavour oscillations and primordial nucleosynthesis,” *JCAP*, vol. 12, p. 015, 2020. arXiv: 2008.01074 `[hep-ph]`.

[215] J. J. Bennett et al., “Towards a precision calculation of $N_{\rm eff}$ in the Standard Model II: Neutrino decoupling in the presence of flavour oscillations and finite-temperature QED,” *JCAP*, vol. 04, p. 073, 2021. arXiv: 2012.02726 `[hep-ph]`.

[216] K. Akita and M. Yamaguchi, “A precision calculation of relic neutrino decoupling,” *JCAP*, vol. 08, p. 012, 2020. arXiv: 2005.07047 `[hep-ph]`.

[217] M. Kawasaki, K. Miyamoto, K. Nakayama, and T. Sekiguchi, “Isocurvature perturbations in extra radiation,” *JCAP*, vol. 02, p. 022, 2012. arXiv: 1107.4962 `[astro-ph.CO]`.

[218] A. H. Guth and E. J. Weinberg, “Could the universe have recovered from a slow first-order phase transition?” *Nuclear Physics B*, vol. 212, no. 2, pp. 321–364, 1983.

[219] A. R. Liddle and D. Wands, “Microwave background constraints on extended inflation voids,” *Monthly Notices of the Royal Astronomical Society*, vol. 253, no. 4, pp. 637–648, Dec. 1991.

[220] M. S. Turner, E. J. Weinberg, and L. M. Widrow, “Bubble nucleation in first order inflation and other cosmological phase transitions,” *Phys. Rev. D*, vol. 46, pp. 2384–2403, 1992.

[221] E. J. Copeland, A. R. Liddle, D. H. Lyth, E. D. Stewart, and D. Wands, “False vacuum inflation with Einstein gravity,” *Phys. Rev. D*, vol. 49, pp. 6410–6433, 1994. arXiv: astro-ph/9401011.

[222] C. Baccigalupi and F. Perrotta, “Effects of inflationary bubbles on the polarization and temperature anisotropies of the cosmic microwave background,” *Mon. Not. Roy. Astron. Soc.*, vol. 314, p. 1, 2000. arXiv: astro-ph/9911530.

[223] J. Lesgourgues and T. Tram, "The Cosmic Linear Anisotropy Solving System (CLASS) IV: efficient implementation of non-cold relics," *JCAP*, vol. 09, p. 032, 2011. arXiv: 1104.2935 `[astro-ph.CO]`.

[224] Y. Akrami et al., "Planck 2018 results. IX. Constraints on primordial non-Gaussianity," *Astron. Astrophys.*, vol. 641, A9, 2020. arXiv: 1905.05697 `[astro-ph.CO]`.

[225] T. Montandon, G. Patanchon, and B. van Tent, "Isocurvature modes: joint analysis of the CMB power spectrum and bispectrum," *JCAP*, vol. 01, p. 004, 2021. arXiv: 2007.05457 `[astro-ph.CO]`.

[226] E. Kawakami, M. Kawasaki, K. Miyamoto, K. Nakayama, and T. Sekiguchi, "Non-Gaussian isocurvature perturbations in dark radiation," *JCAP*, vol. 07, p. 037, 2012. arXiv: 1202.4890 `[astro-ph.CO]`.

[227] M. Kierkla et al., "From Hubble to Bubble," *JHEP*, vol. 11, p. 077, 2023. arXiv: 2309.08530 `[astro-ph.CO]`.

[228] A. D. Linde, "Decay of the False Vacuum at Finite Temperature," *Nucl. Phys.*, vol. B216, p. 421, 1983, [Erratum: Nucl. Phys.B223,544(1983)].

[229] S. R. Coleman, "The Fate of the False Vacuum. 1. Semiclassical Theory," *Phys. Rev.*, vol. D15, pp. 2929–2936, 1977, [Erratum: Phys. Rev.D16,1248(1977)].

[230] C. G. Callan Jr. and S. R. Coleman, "The Fate of the False Vacuum. 2. First Quantum Corrections," *Phys. Rev. D*, vol. 16, pp. 1762–1768, 1977.

[231] S. Coleman and F. De Luccia, "Gravitational effects on and of vacuum decay," *Phys. Rev. D*, vol. 21, pp. 3305–3315, 12 Jun. 1980.

[232] C.-P. Ma and E. Bertschinger, "Cosmological perturbation theory in the synchronous and conformal Newtonian gauges," *Astrophys. J.*, vol. 455, pp. 7–25, 1995. arXiv: astro-ph/9506072.

[233] B. Audren, J. Lesgourgues, K. Benabed, and S. Prunet, "Conservative Constraints on Early Cosmology: an illustration of the Monte Python cosmological parameter inference code," *JCAP*, vol. 02, p. 001, 2013. arXiv: 1210.7183 `[astro-ph.CO]`.

[234] A. Gelman and D. B. Rubin, "Inference from Iterative Simulation Using Multiple Sequences," *Statist. Sci.*, vol. 7, pp. 457–472, 1992.

[235] A. Lewis, "GetDist: a Python package for analysing Monte Carlo samples," Oct. 2019. arXiv: 1910.13970 `[astro-ph.IM]`.

[236] N. Schöneberg, G. Franco Abellán, A. Pérez Sánchez, S. J. Witte, V. Poulin, and J. Lesgourgues, “The H0 Olympics: A fair ranking of proposed models,” *Phys. Rept.*, vol. 984, pp. 1–55, 2022. arXiv: 2107.10291 `[astro-ph.CO]`.

[237] J. Petrović, P. D. Serpico, and G. Zaharijas, “Millisecond pulsars and the galactic center gamma-ray excess: The importance of luminosity function and secondary emission,” *JCAP*, p. 023, 2015.

[238] T. Jeltema and S. Profumo, “Searching for dark matter with x-ray observations of local dwarf galaxies,” *Astrophys.J.*, p. 1045, 2008.

[239] T. Jaffe, A. Banday, J. Leahy, S. Leach, and A. Strong, “Connecting synchrotron, cosmic rays, and magnetic fields in the plane of the galaxy,” *Mon.Not.Roy.Astron.Soc.*, p. 1152, 2011.

[240] H. Zhao, “Analytical models for galactic nuclei,” *Mon.Not.Roy.Astron.Soc.*, p. 488, 1996.

[241] J. Yin et al., “Milky way versus andromeda: A tale of two disks,” vol. 505, p. 497, 2009.

[242] R. L. Jaffe, “Multi-quark hadrons. 2. methods,” *Phys.Rev.D*, p. 281, 1977.

[243] J. Jauch and F. Rohrlich, “The theory of photons and electrons. the relativistic quantum field theory of charged particles with spin one-half,”

[244] F. C. Jones, “Calculated spectrum of inverse-compton-scattered photons,” *Phys.Rev.*, p. 1159, 1968.

[245] E. W. Kolb and M. S. Turner, “The early universe,” vol. 69, 1990.

[246] T. Linden, D. Hooper, and F. Yusef-Zadeh, “Dark matter and synchrotron emission from galactic center radio filaments,” *Astrophys.J.*, p. 95, 2011.

[247] S. Mao et al., “Magnetic field structure of the large magellanic cloud from faraday rotation measures of diffuse polarized emission,” *Astrophys.J.*, p. 25, 2012.

[248] M. Viel, G. D. Becker, J. S. Bolton, and M. G. Haehnelt, “Warm dark matter as a solution to the small scale crisis: New constraints from high redshift lyman-α forest data,” *Phys.Rev.D*, 2013.

[249] B. Moore, “Evidence against dissipationless dark matter from observations of galaxy haloes,” *Nature*, p. 629, 1994.

[250] S. Rahmani, S. Lianou, and P. Barmby, “Star formation laws in the andromeda galaxy: Gas, stars, metals and the surface density of star formation,” vol. 456, p. 4128, 2016.

[251] V. Petrosian, “On the non thermal emission and acceleration of electrons in coma and other clusters of galaxies,” *Astrophys.J.*, p. 560, 2001.

[252] R. A. M. Walterbos and R. Braun, “Diffuse ionized gas in the spiral galaxy m31,” vol. 431, p. 156, 1994.

[253] M. Fukugita, T. Ichikawa, J. E. Gunn, M. Doi, K. Shimasaku, and D. P. Schneider, “The sloan digital sky survey photometric system,” vol. 111, p. 1748, 1996.

[254] U. Heinbach and M. Simon, “Propagation of galactic cosmic rays under diffusive reacceleration,” vol. 441, p. 209, 1995.

[255] J. F. Navarro, C. S. Frenk, and S. D. M. White, “The structure of cold dark matter halos,” vol. 462, p. 563, 1996.

[256] J. D. Jackson, “Classical electrodynamics,” 1975.

[257] C. Bierlich et al., “A comprehensive guide to the physics and usage of pythia 8.3,” arXiv:2203.11601, 2022.

[258] N. Mirabal, “Dark matter vs. pulsars: Catching the impostor,” *Mon.Not.Roy.Astron.Soc.*, p. 2461, 2013.

[259] J. F. Navarro, C. S. Frenk, and S. D. White, “A universal density profile from hierarchical clustering,” *Astrophys.J.*, p. 493, 1997.

[260] R. Beck, “Magnetic fields in galaxies,” vol. 166, p. 215, 2012.

[261] M. Cirelli, P. D. Serpico, and G. Zaharijas, “Bremsstrahlung gamma rays from light dark matter,” *JCAP*, p. 035, 2013.

[262] E. M. Berkhuijsen, R. Beck, and F. S. Tabatabaei, “How cosmic ray electron propagation affects radio-far-infrared correlations in m 31 and m 33,” vol. 435, p. 1598, 2013.

[263] A. Geringer-Sameth, S. M. Koushiappas, and M. G. Walker, “Comprehensive search for dark matter annihilation in dwarf galaxies,” vol. 91, p. 083 535, 2015.

[264] V. Gammaldi et al., “Dark matter search in dwarf irregular galaxies with the fermi large area telescope,” vol. 104, p. 083 026, 2021.

[265] I. V. Moskalenko et al., “Galprop code for galactic cosmic ray propagation and associated photon emissions,” vol. 33, p. 698, 2013.

[266] F. Calore, I. Cholis, and C. Weniger, “Background model systematics for the fermi gev excess,” *JCAP*, p. 038, 2015.

[267] S. K. Lee, M. Lisanti, and B. R. Safdi, “Distinguishing dark matter from unresolved point sources in the inner galaxy with photon statistics,” *JCAP*, p. 056, 2015.

[268] A. Geringer-Sameth et al., “Indication of gamma-ray emission from the newly discovered dwarf galaxy reticulum ii,” vol. 115, p. 081 101, 2015.

[269] M. R. Buckley et al., “Search for gamma-ray emission from dark matter annihilation in the large magellanic cloud with the fermi large area telescope,” *Phys.Rev.D*, 2015.

[270] M. Ackermann et al., “Searching for dark matter annihilation from milky way dwarf spheroidal galaxies with six years of fermi large area telescope data,” vol. 115, p. 231 301, 2015.

[271] A. Drlica-Wagner et al., “Search for gamma-ray emission from des dwarf spheroidal galaxy candidates with fermi-lat data,” vol. 809, p. L4, 2015.

[272] A. Strong and I. Moskalenko, “Propagation of cosmic-ray nucleons in the galaxy,” *Astrophys.J.*, p. 212, 1998.

[273] C. Gordon and O. Macias, “Dark matter and pulsar model constraints from galactic center fermi-lat gamma ray observations,” *Phys.Rev.D*, 2013.

[274] R. Gießübel and R. Beck, “The magnetic field structure of the central region in m 31,” vol. 571, A61, 2014.

[275] K. Boshkayev et al., “Numerical analyses of m31 dark matter profiles,” vol. 33, p. 2 450 016, 2024.

[276] M. Regis, S. Colafrancesco, S. Profumo, W. de Blok, M. Massardi, and L. Richter, “Local group dsph radio survey with atca (iii): Constraints on particle dark matter,” *JCAP*, p. 016, 2014.

[277] Y. Sofue and H. Nakanishi, “Three-dimensional distribution of the ism in the milky way galaxy. iv. 3d molecular fraction and galactic-scale h i-to-h₂ transition,” vol. 68, p. 63, 2016.

[278] D. Hooper, I. Cholis, T. Linden, J. Siegal-Gaskins, and T. Slatyer, “Pulsars cannot account for the inner galaxy’s gev excess,” *Phys.Rev.D*, 2013.

[279] A. Egorov and E. Pierpaoli, “Constraints on dark matter annihilation by radio observations of m31,” *Phys.Rev.D*, 2013.

[280] A. E. Egorov, “Updated constraints on wimp dark matter annihilation by radio observations of m31,” vol. 106, p. 023 023, 2022.

[281] B. Groves and O. Krause, “Hot & cold dust in m31: The resolved sed of andromeda,” vol. 284, p. 112, 2012.

[282] B. Carr, K. Kohri, Y. Sendouda, and J. Yokoyama, “Constraints on primordial black holes,” vol. 84, p. 116 902, 2021.

[283] J. Steinacker, W. Dröge, and R. Schlickeiser, “Particle acceleration in impulsive solar flares - part one,” vol. 115, p. 313, 1988.

[284] N. Aghanim et al., “Planck 2018 results. vi. cosmological parameters,” *Astron.Astrophys.*, A6, 2020.

[285] G. C. Gómez, R. A. Benjamin, and D. P. Cox, “A reexamination of the distribution of galactic free electrons,” vol. 122, p. 908, 2001.

[286] N. E. Yanasak et al., “Measurement of the secondary radionuclides ¹⁰be, ²⁶al, ³⁶cl, ⁵⁴mn, and ¹⁴c and implications for the galactic cosmic-ray age,” vol. 563, p. 768, 2001.

[287] J. Ma, “Structure and inclination angle of the spiral galaxy m31,” vol. 18, p. 1420, 2001.

[288] W. Baade and H. H. Swope, “Variable star field 96’ south preceeding the nucleous of the andromeda galaxy.,” vol. 68, p. 435, 1963.

[289] E. Corbelli, S. Lorenzoni, R. Walterbos, R. Braun, and D. Thilker, “A wide-field h i mosaic of messier 31. ii. the disk warp, rotation, and the dark matter halo,” vol. 511, A89, 2010.

[290] S. Li, A. G. Riess, M. P. Busch, S. Casertano, L. M. Macri, and W. Yuan, “A sub-2% distance to m31 from photometrically homogeneous near-infrared cepheid period-luminosity relations measured with the hubble space telescope,” vol. 920, p. 84, 2021.

[291] D. Hooper and L. Goodenough, “Dark matter annihilation in the galactic center as seen by the fermi gamma ray space telescope,” vol. 697, p. 412, 2011.

[292] A. Geringer-Sameth and S. M. Koushiappas, “Exclusion of canonical weakly interacting massive particles by joint analysis of milky way dwarf galaxies with data from the fermi gamma-ray space telescope,” vol. 107, p. 241 303, 2011.

[293] R. J. Hamilton and V. Petrosian, “Stochastic acceleration of electrons. i. effects of collisions in solar flares,” vol. 398, p. 350, 1992.

[294] H. Collaboration et al., “Hi4pi: A full-sky h i survey based on ebhis and gass,” vol. 594, A116, 2016.

[295] M. Aartsen et al., “Search for neutrinos from dark matter self-annihilations in the center of the milky way with 3 years of icecube/deepcore,” *Eur.Phys.J.C*, p. 627, 2017.

[296] K. N. Abazajian, “The consistency of fermi-lat observations of the galactic center with a millisecond pulsar population in the central stellar cluster,” *JCAP*, p. 010, 2011.

[297] T. Daylan et al., “The characterization of the gamma-ray signal from the central milky way: A case for annihilating dark matter,” *Phys.Dark Univ.*, p. 1, 2016.

[298] R. Caputo et al., “Search for gamma-ray emission from dark matter annihilation in the small magellanic cloud with the fermi large area telescope,” *Phys.Rev.D*, 2016.

[299] A. Bajkova and V. Bobylev, “Rotation curve and mass distribution in the galaxy from the velocities of objects at distances up to 200 kpc,” *Astron.Lett.*, p. 567, 2016.

[300] S. Mishra-Sharma and K. Cranmer, “Neural simulation-based inference approach for characterizing the galactic center γ -ray excess,” vol. 105, p. 063 017, 2022.

[301] K. Azizi, S. Agaev, and H. Sundu, “The scalar hexaquark $uuddss$: A candidate to dark matter?” *J.Phys.G*, 2020.

[302] J. Binney and S. Tremaine, “Galactic dynamics,” 1987.

[303] K. K. Boddy, J. Kumar, A. B. Pace, J. Runburg, and L. E. Strigari, “Effective J-factors for milky way dwarf spheroidal galaxies with velocity-dependent annihilation,” *Phys.Rev.D*, 2020.

[304] M. Ackermann et al., “Searching for dark matter annihilation from milky way dwarf spheroidal galaxies with six years of fermi large area telescope data,” *Phys.Rev.Lett.*, 2015.

[305] T. Dame, D. Hartmann, and P. Thaddeus, “The milky way in molecular clouds: A new complete co survey,” *Astrophys.J.*, p. 792, 2001.

[306] A. Marasco, F. Fraternali, J. M. van der Hulst, and T. Oosterloo, “Distribution and kinematics of atomic and molecular gas inside the solar circle,” vol. 607, A106, 2017.

[307] A. Boveia and C. Doglioni, “Dark matter searches at colliders,” *Ann.Rev.Nucl.Part.Sci.*, p. 429, 2018.

[308] G. Fragione, F. Antonini, and O. Y. Gnedin, “Millisecond pulsars and the gamma-ray excess in andromeda,” vol. 871, p. L8, 2019.

[309] R. Braun and R. A. M. Walterbos, “Physical properties of neutral gas in m31 and the galaxy,” vol. 386, p. 120, 1992.

[310] S. Abdollahi et al., “$Fermi$ large area telescope fourth source catalog,” *Astrophys.J.Suppl.*, p. 33, 2020.

[311] F. Vincenzo, A. Miglio, C. Kobayashi, J. T. Mackereth, and J. Montalban, “He abundances in disc galaxies. i. predictions from cosmological chemodynamical simulations,” vol. 630, A125, 2019.

[312] R. Trotta, G. Jóhannesson, I. Moskalenko, T. Porter, R. d. Austri, and A. Strong, “Constraints on cosmic-ray propagation models from a global bayesian analysis,” *Astrophys.J.*, p. 106, 2011.

[313] B. B. Siffert, A. Limone, E. Borriello, G. Longo, and G. Miele, “Radio emission from dark matter annihilation in the large magellanic cloud,” *Mon.Not.Roy.Astron.Soc.*, p. 2463, 2011.

[314] A. Tamm, E. Tempel, P. Tenjes, O. Tihhonova, and T. Tuvikene, “Stellar mass map and dark matter distribution in m31,” *Astron.Astrophys.*, A4, 2012.

[315] T. A. Porter, G. Johannesson, and I. V. Moskalenko, “High-energy gamma rays from the milky way: Three-dimensional spatial models for the cosmic-ray and radiation field densities in the interstellar medium,” *Astrophys.J.*, p. 67, 2017.

[316] E. Carlson, T. Linden, and S. Profumo, “Cosmic-ray injection from star-forming regions,” *Phys.Rev.Lett.*, 2016.

[317] S. K. Lee, M. Lisanti, B. R. Safdi, T. R. Slatyer, and W. Xue, “Evidence for unresolved γ-ray point sources in the inner galaxy,” *Phys.Rev.Lett.*, 2016.

[318] M. H. Chan, “Revisiting the constraints on annihilating dark matter by the radio observational data of m31,” *Phys.Rev.D*, 2016.

[319] M. Cirelli et al., “Pppc 4 dm id: A poor particle physicist cookbook for dark matter indirect detection,” vol. 2011, p. 051, 2011.

[320] R. M. Crocker, D. I. Jones, F. Melia, J. Ott, and R. J. Protheroe, “A lower limit of 50 microgauss for the magnetic field near the galactic centre,” vol. 463, p. 65, 2010.

[321] R. K. Leane and T. R. Slatyer, “Revival of the dark matter hypothesis for the galactic center gamma-ray excess,” *Phys.Rev.Lett.*, 2019.

[322] O. Macias, S. Horiuchi, M. Kaplinghat, C. Gordon, R. M. Crocker, and D. M. Nataf, “Strong evidence that the galactic bulge is shining in gamma rays,” *JCAP*, p. 042, 2019.

[323] M. Di Mauro, “Characteristics of the galactic center excess measured with 11 years of $Fermi$-lat data,” *Phys.Rev.D*, 2021.

[324] F. S. Tabatabaei and E. M. Berkhuijsen, “Relating dust, gas, and the rate of star formation in m 31,” vol. 517, A77, 2010.

[325] A. Genina et al., “The core-cusp problem: A matter of perspective,” vol. 474, p. 1398, 2018.

[326] C. Frenk and S. D. White, “Dark matter and cosmic structure,” *Annalen Phys.*, p. 507, 2012.

[327] Y. Génolini et al., “New minimal, median, and maximal propagation models for dark matter searches with galactic cosmic rays,” vol. 104, p. 083 005, 2021.

[328] T. Liu, T. Cohen, C. McGrath, P. B. Demorest, and S. J. Vigeland, “Multi-messenger Approaches to Supermassive Black Hole Binary Detection and Parameter Estimation. II. Optimal Strategies for a Pulsar Timing Array,” *Astrophys. J.*, vol. 945, no. 1, p. 78, 2023. arXiv: 2301.07135 `[astro-ph.HE]`.

[329] D. J. Wilner et al., “Key Science Goals for the Next Generation Very Large Array (ngVLA): Update from the ngVLA Science Advisory Council (2024),” Aug. 2024. arXiv: 2408.14497 `[astro-ph.IM]`.

[330] I. Heywood et al., “MIGHTEE: total intensity radio continuum imaging and the COSMOS/XMM-LSS Early Science fields,” *MNRAS*, vol. 509, no. 2, pp. 2150–2168, Jan. 2022. arXiv: 2110.00347 `[astro-ph.GA]`.

[331] D. J. Bacon et al., “Cosmology with Phase 1 of the Square Kilometre Array: Red Book 2018: Technical specifications and performance forecasts,” *Publ. Astron. Soc. Austral.*, vol. 37, e007, 2020. arXiv: 1811.02743 `[astro-ph.CO]`.

[332] A. Mégevand and F. A. Membiela, “Thin and thick bubble walls. Part I. Vacuum phase transitions,” *JCAP*, vol. 06, p. 007, 2023. arXiv: 2302.13349 `[gr-qc]`.

[333] K. A. Malik and D. Wands, “Cosmological perturbations,” *Phys. Rept.*, vol. 475, pp. 1–51, 2009. arXiv: 0809.4944 `[astro-ph]`.

[334] J. Liu, L. Bian, R.-G. Cai, Z.-K. Guo, and S.-J. Wang, “Constraining First-Order Phase Transitions with Curvature Perturbations,” *Phys. Rev. Lett.*, vol. 130, no. 5, p. 051 001, 2023. arXiv: 2208.14086 `[astro-ph.CO]`.

APPENDIX A

GENERAL CONSTRAINTS ON ISOCURVATURE FROM THE CMB AND LY-α FOREST

A.1 Adiabatic and Isocurvature initial conditions

In this section, we will present the full set of initial conditions for perturbations in adiabatic and four isocurvature (CDI, BDI, NDI and DRDI) modes in the synchronous gauge and in terms of the conformal time τ (see [232, 122, 128]). Other than DRDI, we assume no dark radiation present in these modes. In the synchronous gauge, the perturbed FRW metric is written as

$$ds^2 = a(\tau)^2 \left[-d\tau^2 + (\delta_{ij} + h_{ij})dx^i dx^j\right] . \tag{A.1}$$

The metric perturbation h_{ij} can be written in Fourier space as

$$h_{ij}(\mathbf{k},\tau) = \left[\hat{k}_i \hat{k}_j h(\mathbf{k},\tau) + \left(\hat{k}_i \hat{k}_j - \frac{1}{3}\delta_{ij}\right) 6\eta(\mathbf{k},\tau)\right] , \tag{A.2}$$

where h and η denote the trace and traceless longitudinal part of h_{ij} respectively.

We will then show initial conditions for metric perturbations h, η, as well as first three moments of density perturbations of each species (denoted as δ, θ, σ).

A.1.1 Adiabatic modes

The set of adiabatic modes are given by

$$\begin{aligned}
\eta^{\mathrm{ad}} &= 1 - \frac{5+4R_\nu}{12(15+4R_\nu)}(k\tau)^2 \\
h^{\mathrm{ad}} &= \frac{1}{2}k^2\tau^2 \\
\delta_\gamma^{\mathrm{ad}} &= -\frac{1}{3}k^2\tau^2 \\
\delta_c^{\mathrm{ad}} &= \delta_b^{\mathrm{ad}} = \frac{3}{4}\delta_\gamma^{\mathrm{ad}} = \frac{3}{4}\delta_\nu^{\mathrm{ad}} \\
\theta_c^{\mathrm{ad}} &= 0 \\
\theta_\gamma^{\mathrm{ad}} &= \theta_b^{\mathrm{ad}} = -\frac{1}{36}k^4\tau^3 \\
\theta_\nu^{\mathrm{ad}} &= \frac{23+4R_\nu}{15+4R_\nu}\theta_\gamma^{\mathrm{ad}} \\
\sigma_\nu^{\mathrm{ad}} &= \frac{2}{3(15+4R_\nu)}k^2\tau^2. \qquad \text{(A.3)}
\end{aligned}$$

A.1.2 CDI and BDI modes

The set of CDI and BDI modes are given by

$$
\begin{aligned}
\eta^{\rm CDI} &= -\frac{1}{6}\frac{\Omega_c}{\Omega_m}\omega_m\tau + \frac{1}{16}\frac{\Omega_c}{\Omega_m}\omega_m^2\tau^2 \\
h^{\rm CDI} &= \frac{\Omega_c}{\Omega_m}\omega_m\tau - \frac{3}{8}\frac{\Omega_c}{\Omega_m}\omega_m^2\tau^2 \\
\delta_\gamma^{\rm CDI} &= \delta_\nu^{\rm CDI} = -\frac{2}{3}\frac{\Omega_c}{\Omega_m}\omega_m\tau + \frac{1}{4}\frac{\Omega_c}{\Omega_m}\omega_m^2\tau^2 \\
\delta_c^{\rm CDI} - 1 &= \delta_b^{\rm CDI} = \frac{3}{4}\delta_\gamma^{\rm CDI} \\
\theta_c^{\rm CDI} &= 0 \\
\theta_\gamma^{\rm CDI} &= \theta_b^{\rm CDI} = \theta_\nu^{\rm CDI} = -\frac{1}{12}\frac{\Omega_c}{\Omega_m}\omega_m k^2\tau^2 \\
\sigma_\nu^{\rm CDI} &= \frac{-1}{6(15+2R_\nu)}\frac{\Omega_c}{\Omega_m}\omega_m k^2\tau^3, \qquad \text{(A.4)} \\
\eta^{\rm BDI} &= -\frac{1}{6}\frac{\Omega_b}{\Omega_m}\omega_m\tau + \frac{1}{16}\frac{\Omega_b}{\Omega_m}\omega_m^2\tau^2 \\
h^{\rm BDI} &= \frac{\Omega_b}{\Omega_m}\omega_m\tau - \frac{3}{8}\frac{\Omega_b}{\Omega_m}\omega_m^2\tau^2 \\
\delta_\gamma^{\rm BDI} &= \delta_\nu^{\rm BDI} = -\frac{2}{3}\frac{\Omega_b}{\Omega_m}\omega_m\tau + \frac{1}{4}\frac{\Omega_b}{\Omega_m}\omega_m^2\tau^2 \\
\delta_b^{\rm BDI} - 1 &= \delta_c^{\rm BDI} = \frac{3}{4}\delta_\gamma^{\rm BDI} \\
\theta_c^{\rm BDI} &= 0 \\
\theta_\gamma^{\rm BDI} &= \theta_b^{\rm BDI} = \theta_\nu^{\rm BDI} = -\frac{1}{12}\frac{\Omega_b}{\Omega_m}\omega_m k^2\tau^2 \\
\sigma_\nu^{\rm BDI} &= \frac{-1}{6(15+2R_\nu)}\frac{\Omega_b}{\Omega_m}\omega_m k^2\tau^3, \qquad \text{(A.5)}
\end{aligned}
$$

where $\omega_m \equiv \sqrt{8\pi G/3}\, a(\tau_{\rm ini})\bar{\rho}_m(\tau_{\rm ini})/\sqrt{\bar{\rho}_r(\tau_{\rm ini})}$ and $\bar{\rho}_m$,$\bar{\rho}_r$ is the background matter and radiation density respectively. Ω_b (Ω_m) is the factional energy density in baryons (total matter) today. At the time initial conditions are set, $\omega_m\tau \ll 1$ can be treated as an expansion parameter.

A.1.3 NDI

The set of the NDI mode is given by

$$
\begin{aligned}
\eta^{\mathrm{NDI}} &= \frac{-R_\nu}{6(15+4R_\nu)}(k\tau)^2 \\
h^{\mathrm{NDI}} &= \frac{R_\nu}{40(1-R_\nu)}\frac{\Omega_b}{\Omega_m}\omega_m k^2\tau^3 \\
\delta_\gamma^{\mathrm{NDI}} &= \frac{-R_\nu}{1-R_\nu}\left(1-\frac{1}{6}(k\tau)^2\right) \\
\delta_b^{\mathrm{NDI}} &= \frac{R_\nu}{8(1-R_\nu)}(k\tau)^2 \\
\delta_c^{\mathrm{NDI}} &= \frac{-R_\nu}{80(1-R_\nu)}\frac{\Omega_b}{\Omega_m}\omega_m k^2\tau^3 \\
\delta_\nu^{\mathrm{NDI}} &= 1-\frac{1}{6}(k\tau)^2 \\
\theta_\gamma^{\mathrm{NDI}} &= \theta_b^{\mathrm{NDI}} = \frac{-R_\nu}{4(1-R_\nu)}k^2\tau + \frac{3\Omega_b}{16\Omega_m(1-R_\nu)^2}\omega_m k^2\tau^2 \\
\theta_c^{\mathrm{NDI}} &= 0 \\
\theta_\nu^{\mathrm{NDI}} &= \frac{1}{4}k^2\tau \\
\sigma_\nu^{\mathrm{NDI}} &= \frac{1}{2(15+4R_\nu)}k^2\tau^2,
\end{aligned}
\tag{A.6}
$$

where $R_\nu \equiv \bar{\rho}_\nu/\bar{\rho}_r$.

A.1.4 DRDI

We assume DR is free-streaming, analogous to Standard Model neutrinos. We keep terms up to $\mathcal{O}((k\tau)^2)$. For terms that are zero up to this order, we retain the leading non-vanishing term. The initial conditions are

$$\begin{aligned}
\eta^{\rm DRDI} &= \frac{-R_{\rm dr} + R_{\rm dr}^2 + R_{\rm dr}R_\nu}{6(1-R_{\rm dr})(15+4R_{\rm dr}+4R_\nu)}(k\tau)^2 \\
h^{\rm DRDI} &= \frac{R_{\rm dr}}{40(1-R_{\rm dr})}\frac{\Omega_b}{\Omega_m}\omega_m k^2\tau^3 \\
\delta_\gamma^{\rm DRDI} &= \delta_\nu^{\rm DRDI} = \frac{-R_{\rm dr}}{1-R_{\rm dr}}\left(1-\frac{1}{6}(k\tau)^2\right) \\
\delta_b^{\rm DRDI} &= \frac{R_{\rm dr}}{8(1-R_{\rm dr})}(k\tau)^2 \\
\delta_c^{\rm DRDI} &= \frac{-R_{\rm dr}}{80(1-R_{\rm dr})}\frac{\Omega_b}{\Omega_m}\omega_m k^2\tau^3 \\
\delta_{\rm dr}^{\rm DRDI} &= 1-\frac{1}{6}(k\tau)^2 \\
\theta_\gamma^{\rm DRDI} &= \theta_b^{\rm DRDI} = \frac{-R_{\rm dr}}{4(1-R_{\rm dr})}k^2\tau \\
\theta_c^{\rm DRDI} &= 0 \qquad\qquad\qquad\qquad\qquad\qquad\qquad\qquad\qquad\qquad\qquad\qquad\qquad\qquad\text{(A.7)} \\
\theta_{\rm dr}^{\rm DRDI} &= \frac{1}{4}k^2\tau \\
\sigma_\nu^{\rm DRDI} &= \frac{-19R_{\rm dr}}{30(1-R_{\rm dr})(15+4R_{\rm dr}+4R_\nu)}k^2\tau^2 \\
\sigma_{\rm dr}^{\rm DRDI} &= \frac{15-15R_{\rm dr}+4R_\nu}{30(1-R_{\rm dr})(15+4R_{\rm dr}+4R_\nu)}k^2\tau^2,
\end{aligned}$$

where $R_{\rm dr} \equiv \bar{\rho}_{\rm dr}/\bar{\rho}_r$.

APPENDIX B
DARK RADIATION ISOCURVATURE FROM COSMOLOGICAL PHASE TRANSITIONS

B.1 Bubble Wall Dynamics

As the χ field tunnels to the true vacuum in a region of spacetime, a wall forms as χ smoothly varies from χ_- inside the region to χ_+ outside. We follow the approach of Ref. [332] to calculate the field profile and dynamics inside the wall, working in the thin wall approximation which assumes that the wall thickness is smaller than any other length scale in the problem.

For this calculation, it is convenient to work in Gaussian-normal coordinates adapted to a hypersurface Σ along the wall. On the hypersurface, the field takes on a constant value $\chi(x^\mu) = \chi_\Sigma \in (\chi_-, \chi_+)$. Points on Σ are parameterized as $x^\mu = X^\mu(\xi^a)$ for three coordinates $\xi^a = (\xi^0, \xi^1, \xi^2)$. The fourth coordinate n measures the proper distance along a geodesic that originates from $X^\mu(\xi^a)$ with a tangent vector that is orthogonal to Σ. In this coordinate system, an arbitrary point near Σ has Gaussian-normal coordinates which can be related to the original coordinates by

$$x^\mu = X^\mu(\xi^a) + nN^\mu(\xi^a) + \mathcal{O}(n^2) \tag{B.1}$$

where $N^\mu(\xi^a)$ is a unit normal vector satisfying

$$\begin{aligned} N_\mu N^\mu &= 1 \\ N_\mu \partial_a X^\mu &= 0. \end{aligned} \tag{B.2}$$

On the hypersurface Σ, $n = 0$.

The scalar field χ obeys the standard equation of motion:

$$g^{\mu\nu}\left[\partial_\mu \partial_\nu \chi - \Gamma^\rho_{\mu\nu}\partial_\rho \chi\right] = V'(\chi). \tag{B.3}$$

In the thin-wall approximation, $\partial_n \chi \gg \partial_a \chi$, allowing us to drop derivatives other than those with respect to n. Thus, in Gaussian-normal coordinates, the equations of motion are approximately[1]

$$\partial_n^2 \chi - K(n)\partial_n \chi = V'(\chi(n)), \tag{B.4}$$

where $K(n)$ is the mean extrinsic curvature of the hypersurface at n. In the thin wall approximation, $K(n)$ does not vary considerably over the width of the wall, so we can replace $K(n) \to K(0) \equiv K$. Multiplying Eq. (B.4) by $\partial_n \chi$ and integrating, we obtain

$$\frac{1}{2}(\partial_n \chi)^2 - K \int\limits_{-\infty}^{n} dn (\partial_n \chi)^2 = V(\chi(n)), \tag{B.5}$$

where $V(\chi)$ is the potential defined in Eq. (3.2) with an appropriate constant added such that V is positive definite. Here we have defined n such that $\chi(n) \to \chi_-$ as $n \to -\infty$. Taking $n \to \infty$ in Eq. (B.5) gives

$$-K\sigma = \Delta V \tag{B.6}$$

where σ is the surface tension, defined as

$$\sigma \equiv \int dn (\partial_n \chi)^2. \tag{B.7}$$

This is equivalent to the radial bounce action S_1, introduced in Section 3.2. Since K can be written in terms of the shape and dynamics of the wall, Eq. (B.6) can be used as a dynamic equation for the wall after we calculate σ.

To determine the surface tension σ, we solve Eq. (B.5). To do so, it is useful to consider the

---

[1] This equation is exact at $n = 0$ as, in the Gaussian normal coordinates, $\partial_a \chi|_{n=0} = 0$.

order of magnitude of the terms in the equation for values of n inside the wall:

$$\begin{aligned} K \int_{-\infty}^{n} dn(\partial_n \chi)^2 \sim & \mathcal{O}\left(\Delta V\right) \\ V(\chi) \sim & \mathcal{O}\left(V_{\max}\right), \end{aligned} \tag{B.8}$$

where $V_{\max}$ is the maximum potential value between the two minima. The thin-wall approximation requires that $\Delta V \ll V_{\max}$. Therefore, an approximate solution for the profile of the bubble wall can be found by setting $K = 0$ in Eq. (B.5). However, from Eq. (B.6) this solution is only consistent if we set $\Delta V = 0$ as well. We find a self-consistent approximate solution by splitting the potential into two parts:

$$\begin{aligned} V =& V_0 + V_1 \\ V_0 \equiv& \frac{\lambda}{4}\left(\chi^2 - \frac{m^2}{\lambda}\right)^2 \\ V_1 \equiv& \frac{\mu}{3}\chi^3 + \text{const.} \end{aligned} \tag{B.9}$$

where V_0 is the Z_2 symmetric part of the potential and the constant on the last line makes $V_1(\chi_-) \approx 0$.

Therefore, an approximate solution for the bubble wall profile can be found by solving

$$\frac{1}{2}(\partial_n \chi)^2 \approx V_0(\chi(n)). \tag{B.10}$$

subject to boundary conditions $\chi(\pm\infty) = \pm m/\sqrt{\lambda}$. The solution is

$$\chi = \frac{m}{\sqrt{\lambda}} \tanh\left(\frac{n}{\ell}\right), \tag{B.11}$$

where $\ell \equiv \sqrt{2}/m$. This allows us to calculate σ explicitly:

$$\sigma = \frac{2\sqrt{2}}{3}\frac{m^3}{\lambda}. \tag{B.12}$$

Having calculated the surface tension, we next consider the mean extrinsic curvature of the surface Σ:

$$K = -(g^{\mu\nu}\nabla_\mu \tilde{N}_\nu)|_{n=0}. \tag{B.13}$$

Here $\tilde{N}_\nu(n, \xi^a)$ is an arbitrary extension of N_ν to a unit vector field that agrees with N_ν on Σ. In our case, Σ is the surface of a spherical bubble nucleated at some time t_I with a radius

$$r(t, t_I) = \int\limits_{t_I}^{t} \frac{dt' v_w(t')}{a(t')} + \frac{r_c}{a(t_I)} \tag{B.14}$$

where the critical radius r_c is the initial physical radius of the bubble as mentioned in Section 3.2. Points $x^\mu = (t, r, \theta, \phi)$ on Σ satisfy

$$0 = F(x^\mu) \equiv r - r(t, t_I) \tag{B.15}$$

The unit normal vector N_μ is then given by

$$N_\mu = \frac{\partial_\mu F}{\sqrt{|\partial_\mu F \partial^\mu F|}} = \gamma_w(-v_w, a(t)\hat{\mathbf{r}}). \tag{B.16}$$

and

$$n = (x^\mu - X^\mu)N_\mu = \frac{F(x^\mu)}{\sqrt{|\partial_\mu F \partial^\mu F|}} = a(t)\gamma_w(r - r(t, t_I)). \tag{B.17}$$

Using Eqs. (B.13) and (B.16), we calculate the mean curvature of Σ. Since N_μ does not depend explicitly on r but n depends on t and r, we can extend the domain of N_μ away from $n = 0$ and take $\tilde{N}_\mu \equiv N_\mu$. Then the mean curvature can be written as

$$K = -\partial_t(\gamma_w v_w) - 3H\gamma_w v_w - \frac{2\gamma_w}{a(t) r(t, t_I)}. \tag{B.18}$$

Substituting this result into Eq. (B.6) leads to a dynamic equation for the expansion of the bubble wall

$$\partial_t(\gamma_w v_w) + 3H\gamma_w v_w + \frac{2\gamma_w}{a(t)r(t,t_I)} = \frac{\Delta V}{\sigma}. \tag{B.19}$$

When a bubble first nucleates its physical size is the critical radius $r_c \equiv 3S_1/\Delta V = 3\sigma/\Delta V$ and its wall is at rest [229, 228]. Putting $a(t_I)r(t_I,t_I) = r_c$ and $v_w = 0$ in Eq. (B.19), we can see that, the bubble wall will accelerate and expand until it reaches the terminal velocity given by

$$(\gamma_w v_w)|_\infty = \frac{\Delta V}{3\sigma H_{\text{inf}}} = \frac{1}{r_c H_{\text{inf}}} \gg 1, \tag{B.20}$$

where we have used the condition in Eq. (3.5). This implies the terminal wall velocity is $v_w \approx 1$, with $\gamma_w \approx 1/(r_c H_{\text{inf}})$, after a time $t - t_I \sim H_{\text{inf}}^{-1}$.

B.2 Two-Bubble Terms

Here we quantify the errors from our calculation of the power spectrum of δ_χ in Section 3.3. The power spectrum is determined by the two-point function which can be written as the double sum over bubbles given in Eq. (3.17). The double sum can be split up as

$$\langle\delta_\chi(\mathbf{k})\delta_\chi(\mathbf{k}')\rangle = \langle\delta_\chi(\mathbf{k})\delta_\chi(\mathbf{k}')\rangle^{(1)} + \langle\delta_\chi(\mathbf{k})\delta_\chi(\mathbf{k}')\rangle^{(2)} \tag{B.21}$$

where the first term on the right is the contribution from terms where $I = J$ and the second term is the contribution from terms where $I \neq J$. In Section 3.3, we calculated the power spectrum from the $I = J$ terms only and here we will approximate the correction from including the $I \neq J$ terms.

The correction to the 2-point function from the $I \neq J$ terms can be written as

$$\langle\delta_\chi(\mathbf{k})\delta_\chi(\mathbf{k}')\rangle^{(2)} = e^{2t_e/\tau_{\text{PT}}}\frac{(4\pi)^2}{k^3k'^3}(N^2 - N)\int d^4x d^4x' p_2(x,x') e^{-i(\mathbf{k}\cdot\mathbf{x}+\mathbf{k}'\cdot\mathbf{x}')}\mathcal{A}(kr(t))\mathcal{A}(k'r(t')) \tag{B.22}$$

where $p_2(x,x')$ is the joint probability density function for bubbles nucleated at space-time coordinates x and x'. For $t < t'$, we will write the joint probability density function as

$$p_2(x, x') = p(x|x')p_1(x') \tag{B.23}$$

where

$$p_1(x') = \frac{1}{N}\Gamma a(t')^3 p_{\text{false}}(t') \tag{B.24}$$

and the conditional probability can be written as

$$p(x|x') = \frac{1}{N}\Gamma a(t)^3 \Theta(\Delta x - r(t)) p_{\text{false}}(t|t', \Delta x) \qquad t < t'. \tag{B.25}$$

Here, $\Delta x \equiv |\mathbf{x} - \mathbf{x}'|$ and

$$\begin{aligned} p_{\text{false}}(t|t', \Delta x) =& e^{-J(t,\Delta x)} \qquad t < t' \\ J(t, \Delta x) =& \int_0^t dt'' \Gamma a(t'')^3 \left[\mathcal{V}_{\mathcal{H}}(t'') - \mathcal{V}_{\mathcal{O}}(t'', \Delta x)\right] \end{aligned} \tag{B.26}$$

where $\mathcal{V}_{\mathcal{H}}(t'')$ is the comoving Hubble volume at t'' and $\mathcal{V}_{\mathcal{O}}(t'', \Delta x)$ is the overlap volume between two spheres of comoving radius $r(t'')$ at $\mathbf{x}$ and $\mathbf{x}'$. $J(t, \Delta x) \leq t/\tau_{\text{PT}}$ where equality is acheived if $\mathcal{V}_{\mathcal{O}}(t'', \Delta x) = 0$ for $t'' \in [0, t]$. The Θ function in Eq. (B.25) ensures that the probability goes to zero for a bubble nucleated at coordinates $\mathbf{x}, t$ that encloses the point $\mathbf{x}'$. For $t > t'$ we use $p_2(x, x') = p(x'|x)p_1(x)$ rather than Eq. (B.23) and exchange $x \leftrightarrow x'$ in Eq. (B.25).

Since $p_2(x, x')$ only depends on $\mathbf{x}$ and $\mathbf{x}'$ through Δx, we change integration variables to

$$\begin{aligned} \mathbf{X} \equiv& \frac{\mathbf{x} + \mathbf{x}'}{2} \\ \mathbf{\Delta x} \equiv& \mathbf{x} - \mathbf{x}' \end{aligned} \tag{B.27}$$

and write $\mathbf{k} \cdot \mathbf{x} + \mathbf{k}' \cdot \mathbf{x}' = (\mathbf{k} + \mathbf{k}') \cdot \mathbf{X} + (\mathbf{k} - \mathbf{k}') \cdot \mathbf{\Delta x}/2$. Integration over $\mathbf{X}$ is then trivial. If $t_e/\tau_{\text{PT}} \ll 1$, we can safely set $\exp\left[-J(t, \Delta x)\right] \to 1$ and $\exp\left(-t/\tau_{\text{PT}}\right) \to 1$, leading to the expression

$$\langle\delta_\chi(\mathbf{k})\delta_\chi(\mathbf{k}')\rangle^{(2)} = 2\frac{(4\pi)^2}{k^6}(2\pi)^3\delta^3(\mathbf{k}+\mathbf{k}')\Gamma^2\int_0^{t_e} dt\int_t^{t_e} dt' a(t)^3 a(t')^3 \mathcal{A}(kr(t))\mathcal{A}(kr(t'))\int d^3(\Delta x)e^{-i\mathbf{k}\cdot\mathbf{\Delta x}}\Theta(\Delta x- \tag{B.28}$$

The $\mathbf{\Delta x}$ integral leads to a term proportional to $\delta^3(\mathbf{k})$ and a finite term. We ignore the term proportional to the delta function and change to dimensionless integration variables $u \equiv kr(t)$ and $u' \equiv kr(t')$ to obtain

$$\langle\delta_\chi(\mathbf{k})\delta_\chi(\mathbf{k}')\rangle^{(2)} = -\frac{128\pi^3}{k^3}(2\pi)^3\delta^3(\mathbf{k}+\mathbf{k}')\gamma_{\rm PT}^2\int_{kr_e}^{kr_i} du u^{-4}\mathcal{A}(u)^2\int_{kr_e}^{u} du' u'^{-4}\mathcal{A}(u') + (\propto \delta^3(\mathbf{k})) \tag{B.29}$$

This contribution to the two point function is proportional to $\gamma_{\rm PT}^2$ so it is suppressed by an extra factor of $\gamma_{\rm PT}$ compared to the result found in Section 3.3. We checked numerically that this term can be neglected for all values of $\gamma_{\rm PT}$ considered in this work.

B.3 Curvature Produced by FOPT

In the main text we calculated the contribution of the FOPT to the isocurvature power spectrum. In this section we will show that the FOPT can also source curvature perturbations during inflation due to non-adiabatic pressure in bubble walls. We will start by calculating the components of the stress-energy tensor for the χ field and extract the non-adiabatic pressure. We will then use our expression for the non-adiabatic pressure to calculate the evolution of the comoving curvature perturbation during inflation.

B.3.1 Stress-Energy Tensor

The stress-energy tensor for the χ field is given by the standard expression for a scalar field

$$T^\mu{}_\nu = g^{\mu\rho}\partial_\rho\chi\partial_\nu\chi - \delta^\mu_\nu\left(\frac{1}{2}g^{\rho\sigma}\partial_\rho\chi\partial_\sigma\chi + V(\chi)\right) \tag{B.30}$$

As discussed in Appendix B.1, when a bubble is nucleated, χ only depends on the coordinate n orthogonal to the wall (with unit vector N_ν). As a result, the stress-energy tensor for a single bubble can be written as

$$T^\mu{}_\nu = \left[N^\mu N_\nu - \frac{1}{2}\delta^\mu_\nu\right](\partial_n\chi)^2 - \delta^\mu_\nu V(\chi). \tag{B.31}$$

The definition of n for a bubble nucleated at the origin at time t_I is given in Eq. (B.17). We split the potential into its two components $V = V_0 + V_1$ and substitute Eq. (B.10) for V_0. Then the stress energy tensor can be written as

$$T^\mu{}_\nu = \left[N^\mu N_\nu - \delta^\mu_\nu\right](\partial_n\chi)^2 - \delta^\mu_\nu V_1(\chi) \tag{B.32}$$

The term proportional to $(\partial_n\chi)^2$ vanishes everywhere except on the wall. The term proportional to V_1 is negligible inside the wall compared to the first term but switches from 0 for $n \lesssim 0$ to $+\Delta V$ for $n \gtrsim 0$. This motivates us to define “wall" and “bulk" contributions to the stress energy tensor

$$\begin{aligned}(T_\text{wall})^\mu{}_\nu =& \left[N^\mu N_\nu - \delta^\mu_\nu\right](\partial_n\chi)^2 \\ (T_\text{bulk})^\mu{}_\nu =& V_1(\chi(n))\end{aligned} \tag{B.33}$$

where the full tensor is the sum of the two:

$$T^\mu{}_\nu = (T_\text{wall})^\mu{}_\nu + (T_\text{bulk})^\mu{}_\nu \tag{B.34}$$

In this work, the most important properties of the stress tensor are the energy density ρ and the pressure p. Using Eq. (B.16), we can write the “wall" and “bulk" components of the single bubble energy density as

$$\begin{aligned}\rho_\text{wall} =& -(T_\text{wall})^0{}_0 = \gamma_w^2(\partial_n\chi)^2 \\ \rho_\text{bulk} =& -(T_\text{bulk})^0{}_0 = V_1(\chi(n))\end{aligned} \tag{B.35}$$

and of the pressure as

$$\begin{aligned} p_{\text{wall}} =& \frac{1}{3}\left(T_{\text{wall}}\right)^{i}{}_{i} = \gamma_w^2(v_w^2 - 2/3)(\partial_n \chi)^2 = (v_w^2 - 2/3)\rho_{\text{wall}} \\ p_{\text{bulk}} =& \frac{1}{3}\left(T_{\text{bulk}}\right)^{i}{}_{i} = -V_1(\chi(n)) = -\rho_{\text{bulk}} \end{aligned} \tag{B.36}$$

B.3.1.1 Wall Energy Density

We next calculate $\bar{\rho}_{\text{wall}}$ and $\delta\rho_{\text{wall}}(\mathbf{k}, t)$ for the whole Universe at time t. To do so, we will sum the first line of Eq. (B.35) over bubbles nucleated before t

$$\rho_{\text{wall}}(\mathbf{x}, t) = \gamma_w^2 \sum_{I=1}^{N} \Theta(t - t_I)\ (\partial_n \chi)^2\big|_{n=n_I} \tag{B.37}$$

where $n_I \equiv a(t)\gamma_w(|\mathbf{x} - \mathbf{x_I}| - r(t, t_I))$ is the normal coordinate for bubble I, $\mathbf{x_I}$ is the center position of the bubble, and for γ_w we take the terminal value for all bubbles given in Eq. (B.20). Using the solution for the profile of the bubble wall in Eq. (B.11), the wall energy density can be written as

$$\rho_{\text{wall}} = \frac{\gamma_w \Delta V}{4\ell} \sum_{I} \Theta(t - t_I)\,\text{sech}^4\left(n_I/\ell\right) \tag{B.38}$$

The spatial average of the wall energy is

$$\begin{aligned} \bar{\rho}_{\text{wall}} =& \frac{1}{\mathcal{V}} \int_{\mathcal{V}} d^3x \rho_g \\ =& \frac{4\pi}{3} \frac{\Delta V}{\mathcal{V} a(t)} \sum_{I=1}^{N} \Theta(t - t_I) r(t, t_I)^2. \end{aligned} \tag{B.39}$$

We substitute Eq. (3.8) for $r(t, t_I)$ and use the probability density in Eq. (3.19) to convert the sum over bubbles into an integral over time

$$\bar{\rho}_{\text{wall}} = \frac{4\pi}{3} \gamma_{\text{PT}} \Delta V e^{-t/\tau_{PT}}. \tag{B.40}$$

The perturbation $\rho_{\text{wall}} - \bar{\rho}_{\text{wall}}$ of the wall's energy density in Fourier space is

$$\delta\rho_{\text{wall}} = \int d^3x \rho_{\text{wall}}(\mathbf{k}) e^{-i\mathbf{k}\cdot\mathbf{x}} + \text{const.} \times \delta^3(\mathbf{k}), \tag{B.41}$$

where the second term is only non-zero for $\mathbf{k} = 0$. This term can be dropped, as only the non-zero wavenumbers enter our analysis. Assuming that $r_I \gg \ell/(\gamma_w a)$ for all relevant bubbles, and that we are interested in modes such that $k\ell/(\gamma_w a) \ll 1$, the integral over $\mathbf{x}$ results in the closed form solution

$$\delta\rho_{\text{wall}} = \frac{4\pi}{3} \frac{\Delta V}{Ha(t) v_w k^2} \sum_I \Theta(t - t_I) \mathcal{B}(kr(t_I)) e^{-i\mathbf{k}\cdot\mathbf{x_I}}, \tag{B.42}$$

where

$$\mathcal{B}(y) \equiv y \sin y. \tag{B.43}$$

B.3.1.2 Bulk Energy Density

The bulk energy density is given by the point-wise function of χ in the second line of Eq. (B.35). In a region of space where bubble I is the only bubble, the behavior of χ is given by Eq. (B.11) with $n \to n_I$. Since we only care about the bulk energy density on scales much larger than the thickness of the wall, we can approximate

$$\begin{aligned} \chi(n_I) \approx& \frac{2m}{\sqrt{\lambda}} \left[\Theta(n_I) - \frac{1}{2}\right] \\ =& \frac{2m}{\sqrt{\lambda}} \left[\Theta(|\mathbf{x} - \mathbf{x_I}| - r(t, t_I)) - \frac{1}{2}\right], \end{aligned} \tag{B.44}$$

leading to

$$\rho_{\text{bulk},I} = V_1(\chi(n_I)) \approx \Delta V \left[1 - \Theta(r(t, t_I) - |\mathbf{x} - \mathbf{x_I}|)\right]. \tag{B.45}$$

where $\Delta V \equiv 2\mu m^3/(3\lambda^{3/2})$. The fraction of space in true vacuum by the end of inflation is $\sim \gamma_{\text{PT}} H_{\text{inf}} t_e \ll 1$. As a result, most bubbles do not overlap and the bulk energy density for the whole Universe can be approximated as

$$\rho_{\text{bulk}} = \Delta V \left[1 - \sum_I \Theta(t - t_I)\Theta(r(t, t_I) - |\mathbf{x} - \mathbf{x_I}|) \right]. \tag{B.46}$$

Spatially averaging this bulk density results in

$$\bar{\rho}_{\text{bulk}} = \Delta V p_{\text{false}}(t) = \Delta V e^{-t/\tau_{PT}}, \tag{B.47}$$

which dominates over the wall contribution, Eq. (B.47). The density perturbation for the bulk contribution is

$$\begin{aligned} \delta\rho_{\text{bulk}}(\mathbf{k}, t) = & -\Delta V \sum_I \Theta(t - t_I) \\ & \times \int d^3x e^{-i\mathbf{k}\cdot\mathbf{x}} \Theta(r(t, t_I) - |\mathbf{x} - \mathbf{x_I}|) \\ & + \text{const.} \times \delta^3(\mathbf{k}). \end{aligned} \tag{B.48}$$

Again dropping the second term and performing the integral over $\mathbf{x}$

$$\delta\rho_{\text{bulk}}(\mathbf{k}, t) = \frac{4\pi\Delta V}{k^3} \sum_I \Theta(t - t_I) \mathcal{A}(kr(t, t_I)) e^{-i\mathbf{k}\cdot\mathbf{x_I}}, \tag{B.49}$$

where we have defined

$$\mathcal{A}(y) \equiv y \cos y - \sin y. \tag{B.50}$$

B.3.2 Curvature Power Spectrum

In the standard inflationary model, the inflaton field produces subhorizon quantum fluctuations in the comoving curvature perturbation (denoted as $\mathcal{R}$) with a power spectrum given by [333]

$$P_{\mathcal{R}_\phi}(k) \equiv P_{\mathcal{R}}(k, t_k) = \left. \frac{H^4}{4\pi^2 \dot{\bar{\phi}}^2} \right|_{t_k}, \tag{B.51}$$

where t_k is the time that wave-number k exits the horizon $(a(t_k)H_{\rm inf} \sim k)$. In the class of models of FOPT considered in this paper, bubbles from the FOPT quickly become larger than the horizon. As a result, their effect on the subhorizon dynamics is mostly from modifying the background energy density $\bar{\rho}_\chi$, which can be neglected since we work in the region $\bar{\rho}_\chi \ll (\bar{\rho}_\chi + \bar{\rho}_\phi)$. Thus, the subhorizon dynamics are almost unaltered from standard inflation.

Outside of the horizon, the curvature perturbation evolves according to [124, 126]

$$\dot{\mathcal{R}} = \frac{H}{\bar{\rho} + \bar{p}} \delta p_{\rm nad} + \mathcal{O}\left(\frac{k^2}{a^2 H^2}\right), \tag{B.52}$$

where $\delta p_{\rm nad}$ is the non-adiabatic pressure perturbation

$$\delta p_{\rm nad} \equiv \delta p - \frac{\dot{\bar{p}}}{\dot{\bar{\rho}}} \delta\rho. \tag{B.53}$$

The non-adiabatic pressure of the inflaton is suppressed outside the horizon [127], while for the χ field it is sourced by the energy of the bubble wall. Setting $v_w = 1$ and using results in Appendix B.3.1, the superhorizon evolution of $\mathcal{R}$ is

$$\dot{\mathcal{R}} \approx \frac{4}{3}\frac{H}{\dot{\bar{\phi}}^2} \delta\rho_{\rm wall} \quad (t > t_k), \tag{B.54}$$

where $\delta\rho_{\rm wall}$ is defined in Eq. B.41. The curvature $\mathcal{R}$ at the end of inflation ($t = t_e$) is then

$$\begin{aligned} \mathcal{R}(\mathbf{k}, t_e) = \mathcal{R}(\mathbf{k}, t_k) + \frac{16\pi}{9} \frac{\Delta V}{\dot{\bar{\phi}}^2} \frac{1}{k^2} \\ \times \sum_I kr(t_I) \sin\left(kr(t_I)\right) e^{-i\mathbf{k}\cdot\mathbf{x_I}} \int_{t_k}^{t_e} dt \frac{1}{a(t)} \Theta(t - t_I), \end{aligned} \tag{B.55}$$

where I runs over all nucleated bubbles.

To calculate the power spectrum of $\mathcal{R}$ at the end of inflation, we follow the same procedure as in Eq. (3.17): we ignore cross-terms in the double sum, write the ensemble average as an integral, integrate over spatial coordinates, and change the t integration variable to $u \equiv kr(t)$. The curvature power spectrum is then given as:

$$P_{\mathcal{R}}(k,t_e) - P_{\mathcal{R}}(k,t_k) = \frac{128}{81}\left(\frac{\Delta V}{\dot{\phi}^2}\right)^2 \gamma_{\mathrm{PT}} \times \left[\frac{1}{2}\left(kr(t_k) - \frac{1}{2}\sin\left(2kr(t_k)\right)\right) + \int\limits_{kr(t_k)}^{kr_i} du \frac{\sin^2 u}{u^2}\right]. \tag{B.56}$$

The first term in the square brackets comes from bubbles nucleated after t_k while the second term comes from bubbles nucleated before t_k. If FOPT starts after t_k ($t_i > t_k$), the second term in the brackets of Eq. (B.56) is absent since there are no bubbles nucleated before t_k. The power spectrum in this case is simply given by the first term with $t_k \to t_i$. Since $r(t)$ is the radius of the horizon at t, then the definition of t_k implies $r(t_k) \sim 1/k$ so the first term in the brackets is independent of k.

Given our definition of $P_{\mathrm{ad}}(k)$ in Eq. 3.27, we find that $P_{\mathrm{ad}}(k) = P_{\mathcal{R}}(k,t_e)$. There is also a contribution to the curvature power spectrum from bubble percolation when the phase transition completes around T_* [96, 334, 97]. As mentioned in section 3.4.1, we can neglect those contributions when studying CMB observables since we consider scenarios where $T_* \gg T_{\mathrm{CMB}}$. Bringing all of this together, we can obtain $P_{\mathrm{ad}}(k)$:

$$P_{\mathrm{ad}}(k) \approx P_{\mathcal{R}_\phi}(k) + \frac{128}{81}\left(\frac{\Delta V}{\dot{\phi}^2}\right)^2 \gamma_{\mathrm{PT}} \begin{cases} \frac{1}{3}(kr_i)^3 & kr_i \ll 1 \\ 0.95 & kr_i \gg 1 \end{cases}. \tag{B.57}$$

Here the inflaton contribution $P_{\mathcal{R}_\phi}(k)$ is usually parameterized as $P_{\mathcal{R}_\phi}(k) = A_s(k/k_{\mathrm{pivot}})^{n_s-1}$, where A_s and n_s are the amplitude and spectral index respectively. The contribution from FOPT has a distinct k dependence: for $kr_i \ll 1$ it goes as $(kr_i)^3$ and for $kr_i \to \infty$ it approaches a constant.

Since we focus on isocurvature effects of the FOPT in this work, we choose the model parameters such that the contribution of FOPT to $P_{\mathrm{ad}}(k)$ (second term of Eq. (B.57)) is negligible. This translates to the requirement that:

$$\left(\frac{\Delta V}{\dot{\phi}^2}\right)^2 \gamma_{\rm PT} \ll A_s. \tag{B.58}$$

Moreover, we also require the effect of FOPT on CMB angular power spectrum (e.g., C_ℓ^{TT}) is dominantly from isocurvature. Given the scaling of the isocurvature effects at the end of Section 3.4.1, this condition is given as:

$$\left(\frac{\Delta V}{\dot{\phi}^2}\right)^2 \ll R_{\rm dr}^2. \tag{B.59}$$

B.4 Initial Conditions for the Dark Radiation Isocurvature Mode

In this section, we will present the full set of initial conditions for perturbations in the DR isocurvature mode in the synchronous gauge and in terms of the conformal time τ (see also [128]). We assume DR is free-streaming, analogous to Standard Model neutrinos. We keep terms up to $\mathcal{O}((k\tau)^2)$. For terms that are zero up to this order, we retain the leading non-vanishing term. The initial conditions are

$$
\begin{aligned}
\eta^{\text{iso}} &= \frac{-R_{\text{dr}} + R_{\text{dr}}^2 + R_{\text{dr}} R_\nu}{6(1-R_{\text{dr}})(15+4R_{\text{dr}}+4R_\nu)}(k\tau)^2 \\
h^{\text{iso}} &= \frac{R_{\text{dr}}}{40(1-R_{\text{dr}})}\omega_b k^2 \tau^3 \\
\delta_\gamma^{\text{iso}} = \delta_\nu^{\text{iso}} &= \frac{-R_{\text{dr}}}{1-R_{\text{dr}}}\left(1 - \frac{1}{6}(k\tau)^2\right) \\
\delta_b^{\text{iso}} &= \frac{R_{\text{dr}}}{8(1-R_{\text{dr}})}(k\tau)^2 \\
\delta_c^{\text{iso}} &= \frac{-R_{\text{dr}}}{80(1-R_{\text{dr}})}\omega_b k^2 \tau^3 \\
\delta_{\text{dr}}^{\text{iso}} &= 1 - \frac{1}{6}(k\tau)^2 \\
\theta_\gamma^{\text{iso}} = \theta_b^{\text{iso}} &= \frac{-R_{\text{dr}}}{4(1-R_{\text{dr}})}k^2\tau \\
\theta_{\text{dr}}^{\text{iso}} &= \frac{1}{4}k^2\tau \\
\sigma_\nu^{\text{iso}} &= \frac{-19R_{\text{dr}}}{30(1-R_{\text{dr}})(15+4R_{\text{dr}}+4R_\nu)}k^2\tau^2 \\
\sigma_{\text{dr}}^{\text{iso}} &= \frac{15 - 15R_{\text{dr}} + 4R_\nu}{30(1-R_{\text{dr}})(15+4R_{\text{dr}}+4R_\nu)}k^2\tau^2,
\end{aligned}
\tag{B.60}
$$

where $\omega_b \equiv \sqrt{8\pi G/3}\, a(\tau_{\text{ini}})\bar{\rho}_b(\tau_{\text{ini}})/\sqrt{\bar{\rho}_r(\tau_{\text{ini}})}$ and $\bar{\rho}_b$,$\bar{\rho}_r$ is the background baryon and radiation density respectively. At the time initial conditions are set, $\omega_b\tau \ll 1$ can be treated as an expansion parameter.

APPENDIX C

LIMITS ON DARK MATTER ANNIHILATION FROM THE SHAPE OF RADIO EMISSION IN M31

C.1 Solving the Diffusion Equation through the Method of Backwards Differences

In this Appendix, we describe our numeric method for solving for the spherically averaged electron phase space density that satisfies Eq. (4.42). Using forward differences, the large time-steps required to numerically solve the diffusion-loss equation over the relevant timescales of M31 result in unstable solutions. Backward differences, on the other hand, are unconditionally stable [323]. Since we are only interested in the equilibrium solution and not the details of the approach to equilibrium, we use backward differences with time-steps large enough that the solution converges only after two time steps.

It is more convenient to work with $u \equiv r\langle f_e \rangle$, which converts to Eq. (4.42) to Eq. (4.46). The discretized form of Eq. (4.46) with backward differences is

$$\begin{aligned}\frac{u_{ij}^{n+1}-u_{ij}^{n}}{\Delta t} =&D(r_i,E_j)\frac{u_{i+1,j}^{n+1}-2u_{ij}^{n+1}+u_{i-1,j}^{n+1}}{\Delta r^2}+\left.\frac{\partial D}{\partial r}\right|_{r_i,E_j}\left[\frac{u_{i+1,j}^{n+1}-u_{i-1,j}^{n+1}}{2\Delta r}-\frac{u_{ij}^{n+1}}{r}\right]\\ &+\frac{b(r_i,E_{j+1})u_{i,j+1}^{n+1}-b(r_i,E_j)u_{ij}^{n+1}}{\Delta E_i}+r_iQ_e(r_i),\end{aligned} \tag{C.1}$$

where $u_{ij}^n = u(r_i, E_j, t_n)$ and Δt, Δr and $\Delta E_i = E_{i+1} - E_i$ are the grid spacings for each coordinate. We use $n_E = 400$ logarithmically spaced steps for E and $n_r = 800$ linearly spaced steps for r.

Combining all terms from Eq. (C.1) evaluated at time-step t_{n+1} gives

$$\left[\delta_{ik}\delta_{jl}-A_{ik}(E_j)\delta_{jl}-\delta_{ik}B_{jl}(r_i)\right]u_{kl}^{n+1}=u_{ij}^{n}+C(r_i,E_j). \tag{C.2}$$

Here, A and B are given by

$$A(E_j) = \begin{pmatrix} \alpha_0(r_1, E_j) & \alpha_1(r_1, E_j) & 0 & \dots & 0 & 0 \\ \alpha_{-1}(r_2, E_j) & \alpha_0(r_2, E_j) & \alpha_1(r_2, E_j) & \dots & 0 & 0 \\ 0 & \alpha_{-1}(r_3, E_j) & \alpha_0(r_3, E_j) & \dots & 0 & 0 \\ \vdots & \vdots & \vdots & \ddots & \vdots & \vdots \\ 0 & 0 & 0 & \dots & \alpha_0(r_{n_r-1}, E_j) & \alpha_1(r_{n_r-1}, E_j) \\ 0 & 0 & 0 & \dots & \alpha_{-1}(r_{n_r}, E_j) & \alpha_0(r_{n_r}, E_j) \end{pmatrix}, \quad \text{(C.3)}$$

$$B(r_i) = \begin{pmatrix} \beta_0(r_i, E_1) & \beta_1(r_i, E_1) & 0 & \dots & 0 & 0 \\ \beta_{-1}(r_i, E_2) & \beta_0(r_i, E_2) & \beta_1(r_i, E_2) & \dots & 0 & 0 \\ 0 & \beta_{-1}(r_i, E_3) & \beta_0(r_i, E_3) & \dots & 0 & 0 \\ \vdots & \vdots & \vdots & \ddots & \vdots & \vdots \\ 0 & 0 & 0 & \dots & \beta_0(r_i, E_{n_E-1}) & \beta_1(r_i, E_{n_E-1}) \\ 0 & 0 & 0 & \dots & \beta_{-1}(r_i, E_{n_E}) & \beta_0(r_i, E_{n_E}) \end{pmatrix}, \quad \text{(C.4)}$$

$$\alpha_{-1}(r_i, E_j) = \left(\frac{D(r_i, E_j)}{\Delta r^2} - \frac{1}{2\Delta r} \left.\frac{\partial D}{\partial r}\right|_{r_i, E_j} \right) \Delta t \qquad 2 \le i \le n_r \quad 1 \le j \le n_E \qquad \text{(C.5)}$$

$$\alpha_0(r_i, E_j) = \left(-\frac{2D(r_i, E_j)}{\Delta r^2} - \frac{1}{r} \left.\frac{\partial D}{\partial r}\right|_{r_i, E_j} \right) \Delta t \qquad 1 \le i \le n_r \quad 1 \le j \le n_E \qquad \text{(C.6)}$$

$$\alpha_1(r_i, E_j) = \left(\frac{D(r_i, E_j)}{\Delta r^2} + \frac{1}{2\Delta r} \left.\frac{\partial D}{\partial r}\right|_{r_i, E_j} \right) \Delta t \quad 1 \le i \le n_r - 1 \quad 1 \le j \le n_E \qquad \text{(C.7)}$$

$$\beta_{-1}(r_i, E_j) = 0 \qquad 1 \le i \le n_r \quad 2 \le j \le n_E \qquad \text{(C.8)}$$

$$\beta_0(r_i, E_j) = -\frac{b(r_i, E_j)}{\Delta E} \Delta t \qquad 2 \le i \le n_r \quad 1 \le j \le n_E \qquad \text{(C.9)}$$

$$\beta_1(r_i, E_j) = \frac{b(r_i, E_{j+1})}{\Delta E} \Delta t \qquad 1 \le i \le n_r \quad 1 \le j \le n_E - 1, \quad \text{(C.10)}$$

and the function C is given by

$$C(r_i, E_j) = r_i Q_e(r_i, E_j)\Delta t. \tag{C.11}$$

The matrices in Eq. (C.3) are constructed using the boundary conditions

$$\begin{aligned} u(0, E) &= 0 \\ u(r_{n_r+1}, E) &= 0 \\ u(r, E_{n_E+1}) &= 0, \end{aligned} \tag{C.12}$$

where $r_{n_r+1} = 49.9\,\mathrm{kpc}$ and $E_{n_E+1} = m_\chi$. To update u from time-step n to $n+1$, we must solve Eq. (C.2) for u_{ij}^{n+1} given u_{ij}^n, A, B and C.

It is convenient to flatten the two lower indices in u_{ij}^n into a single lowered index by reshuffling the $i \in [1, n_r]$ and $j \in [1, n_E]$ indices of r and E into a single index $a \in [1, n_r \times n_E]$ as

$$a = i + (j-1) \times n_r.$$

With this reordering, the phase space density can be encoded as a vector at time-step n. Using this redefinition, the vector $\boldsymbol{\mathcal{U}}^n$ at time-step n has components

$$\mathcal{U}_a^n = u_{ij}^n. \tag{C.13}$$

Eq. (C.2) can then be written as a matrix equation in the $n_r \times n_E$ vector indices

$$\mathcal{M}\boldsymbol{\mathcal{U}^{n+1}} = \boldsymbol{\mathcal{U}^{n}} + \boldsymbol{\mathcal{C}}. \tag{C.14}$$

The matrix $\boldsymbol{\mathcal{C}}$ has been redefined from $C_{ij}^n \equiv C(r_i, E_j)$ in a manner identical to u_{ij}^n, with $\mathcal{C}_a^n = C_{ij}^n$,

$a = i + (j-1) \times n_r$. The matrix $\mathcal{M}$ is defined as

$$\mathcal{M} = \mathbb{I} - \mathcal{A} - \mathcal{B} \tag{C.15}$$

The matrices $\mathcal{A}$ and $\mathcal{B}$ are $n_E \times n_E$ block matrices with $n_r \times n_r$ blocks:

$$\mathcal{A} \equiv \begin{pmatrix} A(E_1) & 0 & 0 & \dots & 0 & 0 \\ 0 & A(E_2) & 0 & \dots & 0 & 0 \\ 0 & 0 & A(E_3) & \dots & 0 & 0 \\ \vdots & \vdots & \vdots & \ddots & \vdots & \vdots \\ 0 & 0 & 0 & \dots & A(E_{n_E-1}) & 0 \\ 0 & 0 & 0 & \dots & 0 & A(E_{n_E}) \end{pmatrix} \tag{C.16}$$

where $A(E_j)$ is defined in Eq. (C.3) and

$$\mathcal{B} \equiv \begin{pmatrix} B_0(E_1) & B_1(E_1) & 0 & \dots & 0 & 0 \\ B_{-1}(E_2) & B_0(E_2) & B_1(E_2) & \dots & 0 & 0 \\ 0 & B_{-1}(E_3) & B_0(E_3) & \dots & 0 & 0 \\ \vdots & \vdots & \vdots & \ddots & \vdots & \vdots \\ 0 & 0 & 0 & \dots & B_0(E_{n_E-1}) & B_1(E_{n_E-1}) \\ 0 & 0 & 0 & \dots & B_{-1}(E_{n_E}) & B_0(E_{n_E}) \end{pmatrix}. \tag{C.17}$$

The block submatrices are

$$B_m(E_j) = \begin{pmatrix} \beta_m(r_1, E_j) & 0 & 0 & \dots & 0 & 0 \\ 0 & \beta_m(r_2, E_j) & 0 & \dots & 0 & 0 \\ 0 & 0 & \beta_m(r_3, E_j) & \dots & 0 & 0 \\ \vdots & \vdots & \vdots & \ddots & \vdots & \vdots \\ 0 & 0 & 0 & \dots & \beta_m(r_{n_r-1}, E_j) & 0 \\ 0 & 0 & 0 & \dots & 0 & \beta_m(r_{n_r}, E_j) \end{pmatrix} \quad m = -1, 0, 1. \tag{C.18}$$

Starting from the first row, we reduce $\mathcal{M}$ to upper-echelon form. The components of $\boldsymbol{\mathcal{U}}^{n+1}$ can then be solved for, starting from the final component and recursively solving for the other components in reverse order. For the most general matrix, this procedure would require $\mathcal{O}(n_E \times n_r)^3$ operations, which would be computationally prohibitive. In our case, the matrix $\mathcal{M}$ is tridiagonal with a fringe, which requires only $\mathcal{O}(n_r^2 \times n_E)$ operations.

Initially, we set the time-step to an approximation of the maximum timescale of the problem:

$$\Delta t = \Delta t_0 = \max\left(\tau_D^{\max}, \tau_b^{\max}\right), \tag{C.19}$$

where $\tau_D^{\max}$ and $\tau_b^{\max}$ are the maximum diffusion and loss time-scales:

$$\begin{aligned} \tau_b^{\max} &\simeq \max_{ij} \tau_b(r_i, E_j) \\ \tau_D^{\max} &\simeq \max_{ij} \tau_D(r_i, E_j) \end{aligned} \tag{C.20}$$

As we need only a rough estimate of the time scales for our initial time-step, we use simplified equations for τ_b and τ_D:

$$\begin{aligned} \tau_b =& \frac{m_\chi}{b} > \frac{\max E}{b}, \\ \tau_D =& \frac{r_s^2}{\bar{D}}, \end{aligned} \tag{C.21}$$

where r_s is the scale radius of the dark matter distribution, given in Section 4.3.

Using $\Delta t = \Delta t_0$, we iteratively solve for $\boldsymbol{\mathcal{U}}^{n+1}$ from $\boldsymbol{\mathcal{U}}^{n}$ until each component of the two vectors is different by less than 1 part in 10^3. We then reduce the time-step by a factor of 2 and repeat, starting with the final result from the last time-step and iterating until the same convergence criteria is met. We repeat this procedure – reducing the time-step by a factor of 2, and achieving convergence of the solution – until there have been at least 5 different values of Δt and $\boldsymbol{\mathcal{U}}^{n}$ converges in one step for 3 values of Δt in a row. We find that these convergence criteria are conservative as convergence is achieved after 5 values of Δt for all solutions that we examined.

C.2 Simulating Intensity Maps

To generate synthetic data from our background and signal plus background models of M31, correlations between pixels due to the beam size must be correctly modelled. The rms noise is given by $\sigma_{\rm rms} = 0.25 {\rm mJy/beam}$ in the central region of the radio map of M31 and $\sigma_{\rm rms} = 0.3 {\rm mJy/beam}$ towards the outside of the map [271] (see Section 4.2). This noise level is independent of the total flux, thus the simulated measurements in pixel i for an intensity model with flux Φ_i is given by

$$s_i = \Phi_i + r_i \tag{C.22}$$

where r_i is the flux from noise in pixel i. These values can be positive or negative. The number of photons collected per beam is large enough that Poisson noise is negligible compared to the rms noise.

In general, the expected observed noise in pixel i can be written as

$$r_i = \int dxdyK(x - x_i, y - y_i)\tilde{r}(x, y) \tag{C.23}$$

where $K(x - x_i, y - y_i)$ is the shape of the beam centered at pixel i and $\tilde{r}(x, y)$ is the noise before convolution with the beam. We assume that the beam is a Gaussian, given by

$$K(\Delta x, \Delta y) = \frac{1}{2\pi\sigma_b^2} \exp\left[-\frac{\Delta x^2 + \Delta y^2}{2\sigma_b^2}\right], \tag{C.24}$$

where

$$\sigma_b = \frac{(HPBW)}{2\sqrt{2\ln(2)}} \tag{C.25}$$

and $HPBW$ is the half-power beam-width projected onto the plane of the sky and is given by $0.34\mathrm{kpc}$.

We assume that the noise before convolution is Gaussian distributed and only correlated over length scales much smaller than the size of the beam. Under these conditions the integral in Eq. (C.23) can be discretized as

$$r_i = \delta x \delta y \sum_\alpha K(x_\alpha - x_i, y_\alpha - y_i)\tilde{r}(x_\alpha, y_\alpha) \tag{C.26}$$

where we have denoted the discretized coordinates with Greek indices and δx and δy are the grid-spacing for these coordinates (chosen to have the same value). These spacings are chosen to be much smaller than the beam but larger than the correlation length of $\tilde{r}$ so that

$$\langle \tilde{r}_\alpha \tilde{r}_\beta \rangle = \delta_{\alpha\beta}\tilde{\sigma}_\alpha^2 \tag{C.27}$$

where $\tilde{r}_\alpha \equiv \tilde{r}(x_\alpha, y_\alpha)$ and $\tilde{\sigma}_\alpha$ is related to $\sigma_{\mathrm{rms},i}$ through

$$\sigma_{\mathrm{rms},i}^2 = \langle r_i^2 \rangle = \delta x^2 \delta y^2 \sum_\alpha \tilde{\sigma}_\alpha^2 K(x_\alpha - x_i, y_\alpha - y_i)^2. \tag{C.28}$$

To solve for $\tilde{\sigma}_\alpha^2$, we make the approximation that $\tilde{\sigma}_\alpha$ is constant over the relevant regions of K leading to

$$\tilde{\sigma}_\alpha^2 = \frac{4\pi\sigma_b^2}{\delta x \delta y}\sigma_{\mathrm{rms},i}^2. \tag{C.29}$$

for $\boldsymbol{x_\alpha}$ near pixel i. To generate noise for our synthetic data, we randomly sample each $\tilde{r}_\alpha$ from a

Gaussian with a standard deviation given by $\tilde{\sigma}_\alpha$ and substitute the result into Eq. (C.26). For $\tilde{\sigma}_\alpha$, we use Eq. (C.29) where i is the pixel closest to the point $\boldsymbol{x_\alpha}$. To avoid edge effects, we allow x_α and y_α to vary beyond the boundaries of the field of view by $5\sigma_b$.

To make an ensemble of pseudo-data assuming a particular hypothesis, we generate an ensemble of random noise maps and add them to a map of the intensity predicted by the hypothesis. For each combination of signal parameters that we test, we construct an ensemble of background-only maps from a set of 2×10^4 random noise maps and we make an equal sized ensemble of signal plus background maps from an independent set of 2×10^4 random noise maps. For each combination of signal parameters, we use the same set of random noise maps to construct our signal plus background pseudo-data, as we do not need to compare the ensembles of pseudo-data from one signal hypothesis to another.